INVESTIGATION OF THE DYNAMICS OF RAILWAY BOGIES SUBJECTED TO TRACTION / BRAKING TORQUE

Yunendar Aryo Handoko

A Thesis Submitted in Partial Fulfilment for the Award
of the Degree of Doctor of Philosophy (PhD)

Centre for Railway Engineering
Central Queensland University
Australia

September 2006

ABSTRACT

The limitations of current simulation packages in addressing the true longitudinal behaviour of railway bogie dynamics during braking/traction has prompted the development of a Rail Bogie Dynamics (RBD) program in this thesis. The RBD program offers novel features for the calculation of the speed profile as a function of the brake torque as well as explicitly determining wheelset angular velocity. With such capability, the speed profile is no longer treated as an input calculated as a priori as required by most of the current simulation systems. The RBD program has been developed using a formulation that includes the wheelset pitch degree of freedom explicitly with a coordinate reference system that is fixed in space and time. The formulation has made the simulation of the bogie dynamics during braking/traction possible in a natural way using the brake/traction torque as the input and the resulting speed profile as the output without any need for working out the speed profile as a priori. Consequently, severe dynamics during braking such as the wheelset skid and the onset of wheel climb derailment can be modelled and critical parameters investigated using the RBD program.

The RBD program has been validated, where possible, through a series of simulations using a commercial software package (VAMPIRE). For cases which cannot be simulated by VAMPIRE such as the wheelset skid, a novel experimental program has been designed and commissioned in the Heavy Testing Laboratory of the Central Queensland University as reported in this thesis. One of the possible applications of the RBD program in examining the effect of asymmetric brake shoe force in bogies equipped with one-side push brake shoe arrangement is illustrated in this thesis. It is believed that the model and RBD program will have significant benefit in understanding the true longitudinal behaviour of wagons in suburban passenger trains that operate under braking/ traction torques for most of their travel. Similar studies will also be useful to freight train wagon dynamics during entry and exit of speed restriction zones and tight curves.

TABLE OF CONTENTS

LIST OF FIGURES

LIST OF TABLES

LIST OF SYMBOLS

Scalar Symbols

a_e	Longitudinal semi axis of the contact ellipse
b_e	Lateral semi axis of the contact ellipse
a_a	Acceleration (magnitude)
a_b	Deceleration (magnitude)
b_a	Half of the distance between accelerometers in the left and the right axle boxes
C	Proportionality constant of Polach's formulation
c_{11}, c_{22}, c_{23}	Kalker's coefficient
c	Damping constant
c_r	Rotational damping constant
dv_{sensor}	Resolution tolerance of the sensor measuring longitudinal movement
$d\Omega_{sensor}$	Resolution tolerance of the sensor measuring the wheelset rotation
D	Effective diameter of brake piston
F_B	Brake shoe force (magnitude)
F_{Beff}	Effective brake shoe force (magnitude)
F_{CR}	The creep forces resultant (magnitude)
F_{CT}	Brake cylinder piston thrust (magnitude)
F_R	Magnitude of counter force exerted by slack adjuster
F_s	Magnitude of spring-damper force
F_T	Brake shoe tangential force (magnitude)
F_x	Magnitude of longitudinal force at contact point
F_Z	Magnitude of vertical force at contact point

g	Constant of gravitation
i_t	Total brake rigging ratio
i_b	Bogie brake rigging ratio
J_y	Polar moment of inertia
k_s	Spring constant
k_r	Rotational spring constant
k_{ir}	Parameter of track irregularities
k_{y_rail}	Rail lateral stiffness
L_H	Klingel hunting wavelength
l	Current spring length
l_o	Undeformed length of the spring
m	Body mass
N_w	Wheel load
n	Number of system coordinates
n_c	Number of constraint equations
p_c	Air pressure in the brake cylinder
Q	Normal load
R	Radius of curve
r_w	Nominal wheel radius
s_1^w, s_2^w	Surface parameters of the wheel
s_1^r, s_2^r	Surface parameters of the rail
s_a	Longitudinal distance travelled during acceleration
s_b	Longitudinal distance travelled during braking
T_B	Brake Torque (magnitude)
T^{ij}	Magnitude of the torque exerted by rotation spring element between body i and body j
V^i	Volume of the rigid body i

v	Longitudinal velocity
v_C	Circumferential velocity
y_f	Flange clearance
y_w	Wheelset lateral displacement
Δ_{ir}	Amplitude of track irregularities
$\xi_{analytical}$	Analytical value of longitudinal creepage
ξ_x	Longitudinal creepage
$\xi_{\exp}$	Longitudinal creepage measured during experiment
ξ_y	Lateral creepage
ξ_{yc}	Lateral creepage after incorporation of spin
ξ_{sp}	Spin creepage
ξ_t	Total creepage (resultant of lateral and longitudinal creepages)
ω	Angular velocity (magnitude)
λ_w	Wheel conicity
η	Brake rigging efficiency
ρ	mass density
μ_b	Brake shoe friction coefficient
μ_r	Wheel-rail friction coefficient
θ^{ij}	Magnitude of relative rotation between body i and body j
$\theta_0^i, \theta_1^i, \theta_2^i, \theta_3^i$	Euler parameters
ψ	Yaw rotation
ϕ	Roll rotation
τ	Tangential stress
σ	Normal stress
φ	Gradient of tangential stress curve in the area of adhesion

Vector-Matrix Symbols

$\mathbf{A}^i$	Transformation matrix of the rigid body i
$\mathbf{A}^j$	Transformation matrix of the rigid body j
$\mathbf{C}$	Contact constraint (set of equations)
$\mathbf{C_q}$	Sub-Jacobian matrix of constraint equation associated with generalised coordinates
$\mathbf{C_s}$	Sub-Jacobian matrix of constraint equation associated with surface parameters
$\mathbf{F}_1^i, \mathbf{F}_2^i, \ldots \mathbf{F}_{n_f}^i$	Set of forces acting on the rigid body i
$\mathbf{G}^i$	Matrix that relates the angular velocity vector of body i and time derivatives of Euler parameters of the body
$\mathbf{G}^j$	Matrix that relates the angular velocity vector of body j and time derivatives of Euler parameters of the body
$\bar{\mathbf{I}}_{\theta\theta}^i$	Inertia tensor of the rigid body i
$\mathbf{M}^i$	Mass matrix of the rigid body i
$\mathbf{M}_1^i, \mathbf{M}_2^i, \ldots \mathbf{M}_{n_m}^i$	Set of moments acting on the rigid body i
$\mathbf{m}_{RR}^i$	Inertia matrix of body i associated with the translation of the body reference
$\mathbf{m}_{\theta\theta}^i$	Inertia matrix of body i associated with the rotation of the body reference
$\mathbf{m}_{\theta\theta}^i$	Inertia coupling between the translation and rotation of the body i reference
$\bar{\mathbf{n}}^{ik}$	Normal vectors to the surface of body i at contact point k
$\bar{\mathbf{n}}^{jk}$	Normal vectors to the surface of body j at contact point k
$\mathbf{Q}$	Sum of the vectors of generalized applied forces and quadratic velocity vector

$\mathbf{Q_d}$	Vector that absorbs the quadratic term in the first order time-derivatives of the generalised coordinates
$\mathbf{Q}_e$	Vector of generalized applied force
$\mathbf{Q}_R^i$	Vector of generalised forces associated with translational coordinates of body i
$\mathbf{Q}_\theta^i$	Vector of generalised forces associated with rotational coordinates of body i
$\mathbf{Q}_v$	Quadratic velocity vector
$\mathbf{q}$	Vector of generalised coordinates
$\mathbf{q}_d$	Vector of dependent generalised coordinates
$\mathbf{q}_i$	Vector of independent generalised coordinates
$\mathbf{R}^i$	Global position vector of the origin of the body i reference frame
$\mathbf{R}^j$	Global position vector of the origin of the body j reference frame
$\mathbf{r}_p^{ij}$	Vector position of point P^i at body i with respect to point P^j at body j
$\mathbf{s}$	Vector of surface parameters
$\mathbf{s}_d$	Vector of dependent surface parameters
$\mathbf{s}_i$	Vector of independent surface parameters
$\overline{\mathbf{t}}_l^{ik}$	Tangent vectors to the surface of body i at contact point k, $(l = 1,2)$
$\overline{\mathbf{t}}_l^{jk}$	Tangent vectors to the surface of body j at contact point k, $(l = 1,2)$
$\overline{\mathbf{u}}_p^i$	Position vector of the point P^i with reference to the body i coordinate system
$\overline{\mathbf{u}}^{ik}$	Position vector of the contact point k with reference to the rigid body i coordinate system

$\bar{\mathbf{u}}^{jk}$	Position vector of the contact point k with reference to the rigid body j coordinate system
$\boldsymbol{\lambda}$	Vector of Lagrange multiplier
$\boldsymbol{\omega}^{i}$	Angular velocity vector of the rigid body i
$\boldsymbol{\omega}^{j}$	Angular velocity vector of the rigid body j

LIST OF ABREVIATIONS

AAR	Association of American Rail Roads
ABS	Anti-lock Braking System
BR	British Railway
BS	British Standard
CQU	Central Queensland University
CRE	Centre for Railway Engineering
DAQ	Data Acquisition
HTL	Heavy Testing Laboratory
INKA	Industri Kereta Api (Indonesian Railway Industry)
IRF	Inertial Reference Frame
RBD	Rail Bogie Dynamic
SHE	Shen-Hedrick-Elkins (theory of wheel-rail rolling contact)
TRF	Track-following Reference Frame
TTL Signal	Transistor - Transistor Logic Signal
UIC	Union Internationale des Chemins de fer (International Union of Railways)
3D-WTSD	Three Dimensional Wagon Track System Dynamic (a 3D model of wagon-track interaction by Sun & Dhanasekar (2001))

ACKNOWLEDGEMENT

It is my pleasure to acknowledge those who have encouraged and supported me in many ways during my PhD research studies.

Firstly I would like to express my earnest gratitude to my supervisor Dr. Manicka Dhanasekar, Associate Professor and Director, Centre for Railway Engineering (CRE), Central Queensland University (CQU) for his valuable discussion and guidance throughout the three and half years for enabling me to write this thesis. He has supported me both in the technical and personal matters during my stay with the CRE.

I should thank Ir. Roos Diatmoko, Director of Indonesian Railway Industry (PT INKA), for his support and continuous encouragement since I started working there in 1996. I also thank the management board and my colleagues in PT INKA for their support.

I also record my special thanks to Florian Sumpf, an exchange student from The University of Aachen, Germany who actively participated in the designing of the bogie braking experiment. The technical assistance related to experimental work in the Heavy Testing Laboratory was thankfully received from a range of technical staff of CQU, Bernard Jansen, Gary Hoare, Ian Major, Grant Caynes, Trevor Ashman, Ken Morrison and Dr. Marcel Frank.

The support from Queensland Railway (QR) that enabled me to carry out the full scale bogie brake experiment is thankfully acknowledged. Special thanks are due to QR Engineers Andrew Nelmes and Bruce Brymer, and a range of other QR staff who installed the track, and also measured various parameters both of the track and bogie components. Without QR support this experiment would not have been possible.

I also thank Dr. Fuji Xia, Dr. Yan Quan Sun, Dr. Colin Cole, Dr. Jian Jun Han, Mitch McClanachan and Scott Simson for valuable technical discussions provided on many occasions. Special thanks to Tim McSweeney and Scott Simson for spending their valuable time for providing very useful suggestions for improvement of my PhD thesis.

Finally, I should thank my family, especially my parents and my wife, Sari Wulandari, for their encouragement, patience and support; and also to my children, Dhila, Hanif and Syifa, as they are my inspiration.

I acknowledge the financial support offered by the CRE, and PT INKA.

DECLARATION

The work contained in this thesis is a direct result of the original work carried out by me and has not been submitted for the award of a degree or diploma at any other tertiary institution in Australia or overseas.

Signed:_____ Date_____

Yunendar Aryo Handoko

Author

PUBLISHED WORK

As a direct result of the research reported in this thesis the following papers have either been published or are under review:

1. Yunendar Handoko and Manicka Dhanasekar (2006), An Inertial Reference Frame Method for the Simulation of the Effect of Longitudinal Force to the Dynamics of Railway Wheelsets, (Accepted to be published in *International Journal of Non Linear Dynamics*).
2. Yunendar Handoko and Manicka Dhanasekar (2006), Simulation of Railway Bogie Skid, (*Journal of Rail and Rapid Transit, Proceedings of Institution of Mechanical Engineer, Part F*, under review)
3. Yunendar Handoko and Manicka Dhanasekar (2006), Simulation of Bogie Dynamics under Heavy Braking, (Accepted to be published and presented in the *Proceedings of the Conference on Railway Engineering* in Melbourne)

During the completion of the research higher degree program at Central Queensland University the author has also co-authored the following papers:

1. Y. Handoko, F. Xia, and M. Dhanasekar, Effect of Asymmetric Brake Shoe Force Application on Wagon Curving Performance, *Vehicle System Dynamic Supplement 41, Proceeding of IAVSD Conference* in Japan, 2004, p113-122.
2. M. McClanachan, Y. Handoko, M. Dhanasekar, D. Skerman, and J. Davey, Modelling Freight Wagon Dynamics, *Vehicle System Dynamic Supplement 41, Proceeding of IAVSD Conference* in Japan, 2004, p438-447.

1. INTRODUCTION

Suburban passenger trains operate under braking / traction condition during most of their travel. Most heavy haul and long haul trains are also operated under similar condition when they enter and exit speed restriction zones and/or tight curves. Although braking/ traction torques modify the operating speed in a complex manner, which could only be realistically evaluated using rigorous calculations, current simulations are routinely carried out for constant speed conditions with the speed profile input as a priori.

With a view to providing a simulation platform which truly accounts for traction/braking torque induced dynamics of wagons, this thesis formulates a model that explicitly accounts for the wheelset pitch degree of freedom. The formulation is provided with reference to a coordinate system that is fixed in space and time. The formulation enables the simulation to be performed in a natural way using the brake/traction torque as the input and the resulting speed profile as the output without any need for working out the speed profile as a priori. A MATLAB computer program titled Rail Bogie Dynamics (RBD) program which uses the formulation is developed and reported in this thesis.

1.1. AIM AND OBJECTIVES

The aim of the thesis is to formulate a model with the potential for simulating true longitudinal dynamics of bogies under braking/traction torque. This aim is achieved through the enabling objectives listed below:

1. Review the dynamics of rail bogies including the effect of braking/traction through literature study.
2. Review the theory of wheel-rail rolling contact available in the literature to incorporate suitable criteria in the model developed.
3. Formulate the system dynamic equations and their solution technique capable of truly modelling the longitudinal dynamics of bogies subjected to braking/traction torque.
4. Develop the Rail Bogie Dynamics (RBD) program based on the formulation and solution technique as per objective 3.
5. Validate the RBD program against VAMPIRE where possible
6. Validate the other and most severe cases using a full-scale laboratory test.
7. Apply the RBD program to evaluate the severe dynamics of bogies induced due to asymmetric brake shoe forces.

1.2. SCOPE AND LIMITATION

The scope of this thesis is to investigate the dynamics of railway bogies subjected to traction/braking torque. The severe bogie dynamics involving wheelset skid will be investigated through simulation and experiments. The effect of the asymmetric braking due to error in the distribution of the brake shoe normal force within a single wheelset in bogies equipped with one-side push brake shoe will also be examined.

The limitations are:

i. Only tangent track will be considered.
ii. Only simple and most common bogies will be considered.
iii. Whole wagon dynamics will not be considered.

1.3. OUTLINE OF THE THESIS

This thesis contains 10 chapters that cover the formulation, validation, and application of the RBD program.

Chapter 1 outlines the aim, objectives, scope and limitation of the thesis.

In Chapter 2, the basic terminologies used in wagon and bogie dynamics are reviewed. The mechanics of wheel-rail contact, which is fundamental to the bogie and wagon dynamics, is discussed. The wagon braking and traction systems and their principle of working are reviewed briefly for completeness. In the last part of this chapter, a review of the current railway wagon simulation software systems and their limitations to perform true longitudinal dynamics of wagon simulation is presented.

Chapter 3 describes in detail the formulation of the RBD program. The coordinates of reference and the formulation of multibody system equations are presented in detail. The law of contact between rigid bodies contact and its mathematical formulation applied to the wheel-rail contact patch are described. The calculation of creep forces using the Polach formulation is presented. The technique for solving the system equations that involves the differential equilibrium equations and algebraic constraint equations in the augmented form is exhibited. Finally, the algorithm for the railway bogie dynamic analysis is presented in a flow chart.

Validation of the RBD program against VAMPIRE, where possible, is contained in Chapters 4 and 5. The simulations in Chapter 4 deals with the dynamics of the wheelset within a bogie frame whilst Chapter 5 deals with the dynamics of simplified two axle bogies. A series of simulations with or without the application of braking/traction torque with various track irregularities are presented.

Chapter 6 describes the design of an experimental program to validate the novel features of the RBD program for the calculation of the speed profile as a function of the brake torque as well as explicitly determining wheelset angular velocity. The concept of the measurement system and the specification of measurement devices used in the experiments are presented. The modifications of the bogie used in the experiment to suit the mounting of the measurement devices and the construction of the test track are also explained.

Chapter 7 presents the results of the experimental program described in Chapter 6. For convenience, the data obtained from the experiments is categorised into two parts. The first part presents the primary data which is gathered directly from the measurement devices and the second part presents the derived data which is manipulated from the primary data. Three brake cylinder pressure cases have been examined from the experimental data; they are 130 kPa, 150 kPa, and 180 kPa. These cases represent the condition below the skid limit, at the skid limit, and above the skid limit respectively.

The comparison of the experimental results with the results obtained through the simulation using the RBD program is exhibited in Chapter 8. The input for the simulation is the measured experimental brake torque and the output is the longitudinal acceleration / deceleration, speed profile, angular velocity and slip.

Chapter 9 presents the application of the RBD program to simulate the severe bogie dynamics due to application of asymmetric brake normal forces within a single wheelset in bogies equipped with a one-side push brake shoe arrangement. The effect of various levels of asymmetric brake shoe forces and application time is examined and reported in this chapter.

Chapter 10 provides the summary of the thesis and lists the conclusions that have emerged from this research. Some recommendations for further research are also offered in this chapter.

2. LONGITUDINAL DYNAMICS OF RAILWAY BOGIES: A LITERATURE REVIEW

2.1. INTRODUCTION

Railway bogies are often subjected to longitudinal forces due to a number of train related dynamics including braking and traction. These longitudinal forces affect the dynamics of bogies in a complex manner. Severe braking or traction may affect the safety and stability of bogies adversely. Thus, there is a need to study the bogie dynamics as a function of the longitudinal forces with a view to minimising the risk to railway transportation.

For the proper analysis of the dynamic performance of bogies under braking or traction, basic understanding of the vertical and lateral dynamics of the wagon is required. The first part of this chapter introduces some important terms that relate to the dynamics of wagons. The mechanics of wheel-rail contact, which is fundamental to the bogie and wagon dynamics, is also discussed in this chapter. The wagon braking and traction systems and their principle of working are reviewed briefly for completeness. In the last part of this chapter, a review of the current railway wagon simulation software systems and their limitation to perform wagon longitudinal dynamics simulation is presented.

2.1.1. Basic Axis System and Terminologies

To discuss the dynamics of the wagon a coordinate system containing six degrees of freedom as shown in Fig 2.1 is normally used. Linear motion along the X, Y and Z axes are termed as longitudinal, lateral, and vertical translations respectively.

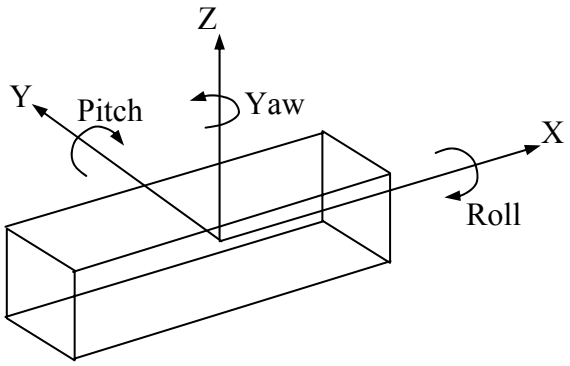

Figure 2.1. Six degrees of freedom of wagon movement

The rotations are defined in accordance to the right hand screw rule where the positive rotation is seen as clockwise if the observer is stationed at the origin and looks at the axes in the positive direction. Rotary motions about the X, Y and Z axes are termed as roll, pitch and yaw respectively (see Fig.2.1).

2.1.2. Wagon Assembly and Tracks Construction

Wagon components and assembly

Most wagons that are currently in use consist of a body and two bogies that provide the necessary suspension. Each bogie basically consists of two wheelsets, a bogie frame consisting of two side frames and one bolster, as well as spring nests. A few commonly available bogies are exhibited in Fig.2.2 - 2.4.

Two common types of bogies widely used in freight trains are three-piece bogies and Y25 bogies. The first is widely used in the United States, Australia, and Asia while the second in Europe (Harder (2000), Bosso et al. (2000)). Fig.2.2 shows a typical three-piece bogie and Fig.2.3 shows a typical Y25 bogie.

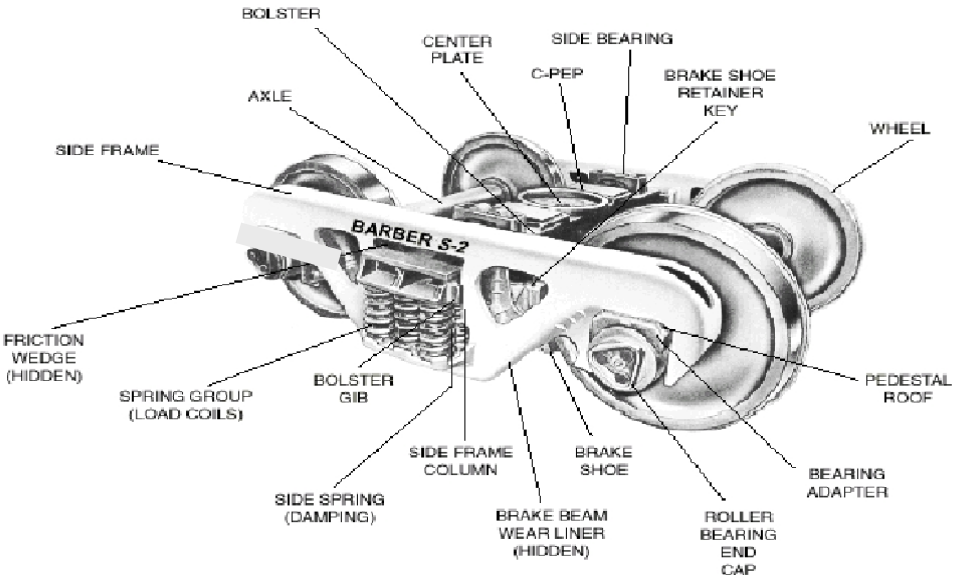

Figure 2.2. Typical design of three-piece bogie (Company Standard Car Truck (2000))

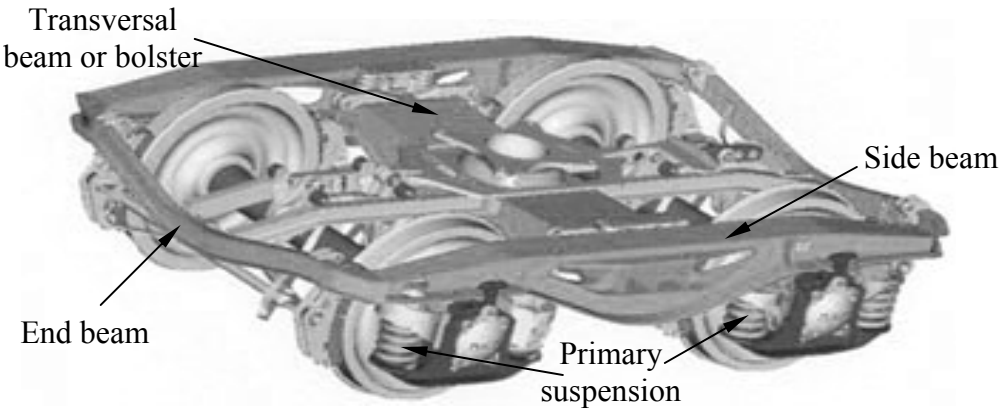

Figure 2.3. Typical design of Y25 bogie (Website K. Industrier. AB (2005))

Three-piece bogies consist of a bolster, two side frames and two wheelsets. This type of bogie does not have primary suspension while the secondary suspension is made from coil springs that connect the bolster with the side frame. Damping is provided by friction wedges, which are placed between the side frame and the bolster.

In contrast to the three-piece bogies, Y25 bogies do not have secondary suspension. They have only primary suspensions that connect the wheelsets and the side frame. The primary suspensions are formed from coil springs and *Lenoir links* which provide friction damping. The bogie frame is constructed from two side beams, one transverse beam or bolster and two end beams.

The three-piece bogies and the Y25 bogies are very popular as they are cheap to purchase and maintain. However, their simple design leads to low levels of lateral stability and ride quality, and higher levels of track forces due to vertical and lateral impacts as well as the angle of attack in curved tracks (Stichel (1999)). Although the performance of both bogies fulfils most of the requirements for freight wagon operations, in some cases a higher performance bogie will be needed. In such cases, at the expense of initial cost, bogies containing both primary and secondary suspensions are used. An example of this type of bogie is shown in Fig 2.4.

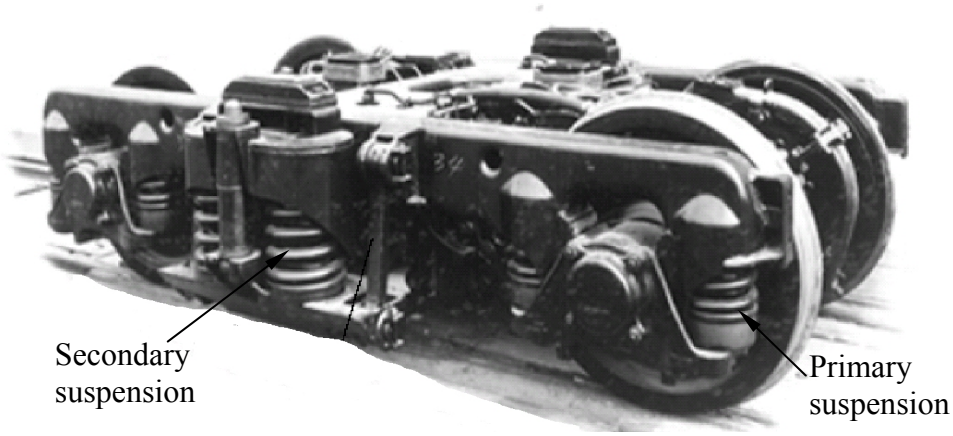

Figure 2.4. Bogie with primary and secondary suspension (Ikamoto (1998))

Track construction

Track is one of the most important technical elements required for the railway operation. Its main function is to provide guidance for the wagons in addition to supporting the heavy mass of the running train and absorbing the induced vibration. Track possesses a complex structure with elastic and dissipative properties. Fig. 2.5 (Profilidis (2000)) exhibits the basic construction of a traditional railway track that consists of a pair of rails, sleepers and track support.

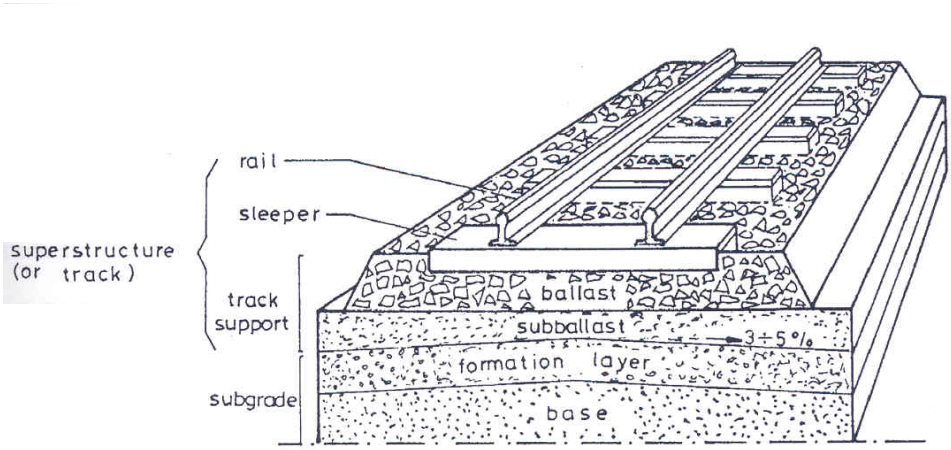

Figure 2.5. A Typical Track Structure (Profilidis (2000))

The requirements for the strength and quality of the track depend to a large extent on the following load parameters (Esveld (2001)):

– axle load: static vertical load per axle
– tonnage borne: sum of the axle loads
– dynamic and / or impact load

The static axle load level, to which the dynamic increment is added, in principle determines the required strength of the track. The dynamic load components, which depend on the operational speed and horizontal and vertical track geometry, are also essential factors in the track structure design.

2.2. DYNAMICS OF THE BOGIES

Train-track dynamics is largely due to the interaction between the complex geometries of the wheel and the rail within the contact patch that generates much high levels of contact forces. It also involves many degrees of freedom and forces that change rapidly and act at the same time at many points in the suspension system and couplers between wagons. The existence of track irregularities and wheel defects makes the problem more challenging to mathematically formulate. Hence an in depth understanding of the subject of the dynamics of multibody systems is essential.

2.2.1 Principles of Wheelset Dynamics

The dynamic characteristics of a railway bogie are defined by the interaction between the wheel and the rail, the configuration of suspensions and the articulation with adjacent wagons. Among these, the interaction between the wheel and the rail that characterises the dynamic behaviour of the railway wheelset running along the track is the most fundamental factor that affects the bogie dynamics.

The wheelset provides basic guidance of travel to railway bogies. The dynamics of a bogie is primarily affected by the dynamic behaviour of the wheelset and the track characteristics. Fig 2.6 depicts a railway wheelset positioned on the track. It could be seen that the conventional wheelset consisting of two conical wheels separated by a

distance compatible to the gauge width of the track fixed to a common axle. This form has a long history and seems to have evolved by a process of trial and error (Wickens (1998)).

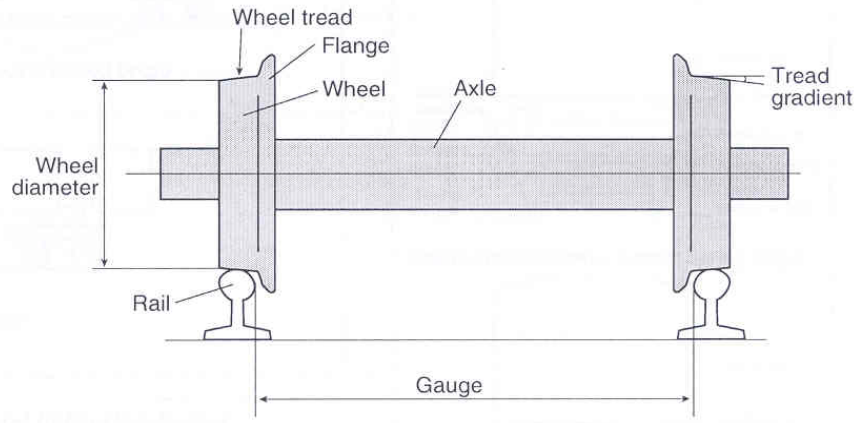

Figure 2.6. Wheelset on the track (Ikamoto (1998))

The observation of the dynamic behaviour of wheelsets has begun since the early years of the railway history. Marshal (1938) has reported that, not long after the conical wheel tread was established in 1821, George Stephenson in his *Observation on Edge and Tram Railway* had stated a very clear description of kinematic oscillation as shown in Fig.2.7. This kinematic oscillation could cause stability problem in the tangent track. The statement of George Stephenson can be found in Wickens (1998) and Wickens (2003).

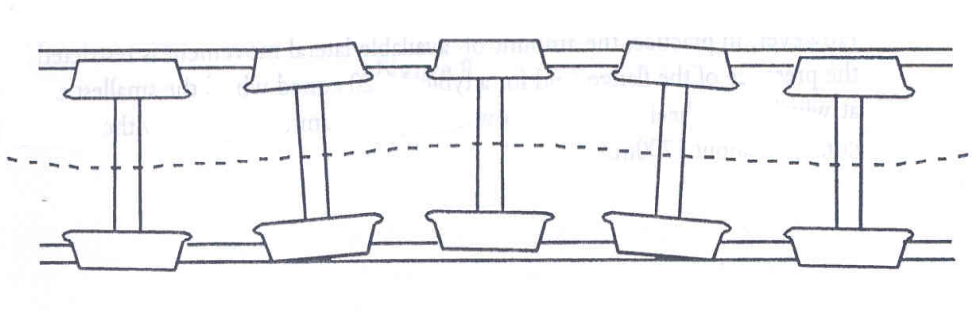

Figure 2.7. Wheelset Kinematic Oscillation (Wickens (2003))

Klingel (1883) formulated the first mathematical relationship for this kinematic oscillation and derived the relationship between the wavelength L_H and the wheelset conicity λ_w, nominal wheel radius r_w and lateral distance between the wheel-rail contact points $2l$ as shown in Eq.2.1.

$$L_H = 2\pi\left(\frac{r_w l}{\lambda_w}\right)^{1/2} \tag{2.1}$$

This simple formula is derived purely from the geometry analysis.

Although the conical wheel causes stability problems in the tangent track, it helps the wheelset to negotiate the curves with ease. A wheelset with conical wheels can maintain a pure rolling motion while running on a curve if it moves outward and takes the radial position. In his book, Wickens (2003) reported that Redtenbacher (1885) had performed a theoretical analysis to improve the understanding of the conical wheelset negotiating curves as illustrated in Fig.2.8.

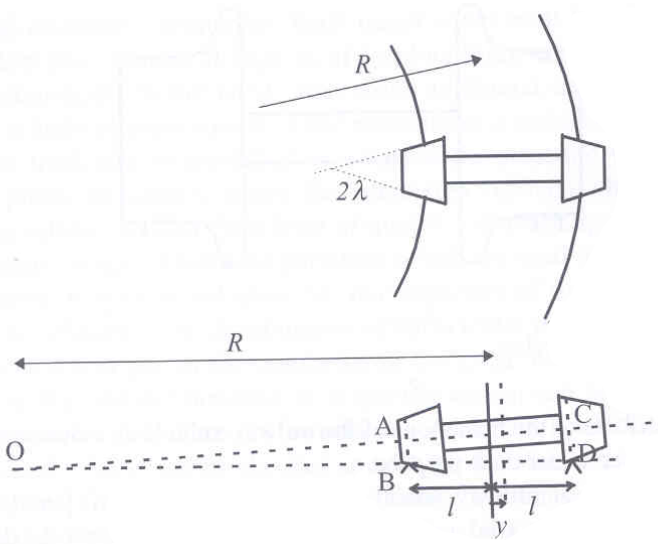

Figure 2.8. Conical wheelset on a curve (Wickens (2003))

From the geometry in Fig. 2.8 it can be seen that there is a simple relationship between the lateral movement of the wheelset y, the radius of curve R, the wheel radius r_w, the lateral distance between the points of contact of the wheels with the rails $2l$, and the conicity λ_w of the wheels in order to sustain pure rolling that is shown in Eq.2.2.

$$\begin{aligned} &OAB = OCD \\ &(r_w - \lambda_w y)/(R-l) = (r_w + \lambda_w y)/(R+l) \\ &y = r_w l / R\lambda_w \end{aligned} \qquad (2.2)$$

As can be seen, the above two analyses of kinematic oscillation and curving are purely based on geometries of the wheel and the track. More detailed analysis of the dynamic behaviour of railway wheelset must be performed if the forces acting at the wheel-rail contact patch are desired.

2.2.2. State-of-the-art of the Study of Wagon and Bogie Dynamics

History and development

The revolution in the analysis of railway wagon dynamics started when the theory of creep (further discussed in Section 2.3) was first introduced by Carter (1926). With this theory, the wheel-rail contact forces can be determined and the equations of motion that describe the wheelset dynamics can also be derived.

Following the development of the creep theory that defines the interaction between the wheel and the rail, extensive studies of wagon dynamics were undertaken. In general the problem of wagon dynamics can be divided into two parts: the hunting or the stability problem which deals with the tangent track, and the curving behaviour which deals with curved track. Unfortunately there is a conflict between stability on the straight track and curving behaviour on the curved track. For example a softer and more flexible primary spring will give a better curving performance but it will reduce the lateral stability in the tangent track. Similarly harder springs will improve the lateral stability but lead to poor curving performance (defined by increase in angle of attack). Gilchrist (1998) has presented a good paper that reviews the history and the development of the research on the optimisation of the hunting and curving problems.

Matsudaira (1952) was the first to solve the complexity of the wheelset equation of motion and concluded that through proper design, a spring-restrained wheelset could be made stable up to any required critical speed as demonstrated by his theoretical work and experiments on a roller rig, where the stability was observed directly. Using his theory, he specified the suspension design parameters for the bogies of the first Shinkansen high speed train that was successfully introduced into service in 1964.

Following Matsudaira's work, from the mid fifties until the mid sixties most of the research on railway wagon dynamics were focused on the subject of stability. For example, de Pater (1956, 1961) investigated the non-linearity of the wheel-rail profile and its effect to wagon stability, and Wickens (1965-6) proved the importance of lateral damping of the primary suspension for the dynamic stability of the wheelset.

However, the more extensive study on wagon dynamics came after Kalker (1967), who studied the rolling contact between two elastic bodies, provided a theory that could be used to calculate forces generated in the wheel-rail rolling contact patch. The work of Kalker and the development in numerical techniques have widely opened the possibility of studying wagon dynamics through computer modelling to obtain better results. Since the pioneering work of Kalker, a large amount of research on wagon dynamics has been reported. It is impossible to present all of them in this review; a brief summary, however, is provided. The research covers the study on stability, curving performance, wagon-track dynamic interaction and control.

Hunting and stability

Rinehart (1978) has examined the hunting stability of three-axle locomotive bogies. Due to symmetry, he has simplified the system using an eleven DOF model representing a "half locomotive" (one bogie only). A set of laboratory test data of natural frequency and mode shapes was used to validate the model. The results showed that a hunting frequency of more than 4 Hz was obtained and the predicted hunting frequency from the mathematical model had good agreement with the measurement.

Tuten et al. (1979) investigated how various wheel profiles and asymmetric loading affected the stability of wagons. The investigation used a nine DOF wagon model. The

results showed that the wagon stability strongly depended on the location of axles having different values of effective conicity and contact angles. The wheel profile mix of a particular bogie was shown to be of much greater importance than whether the bogie was put in the leading or trailing location. The asymmetric loading was also found to affect the lateral stability.

Renger (1984) modelled a railway vehicle with two-axle bogies to examine its lateral stability and ride quality. The vehicle response against the lateral centre line and the cross-level deviations of the track were evaluated. A few important results provided by the simulation are as follow:

(i) The stability and the riding quality could be improved by optimising the secondary lateral damping.

(ii) Instead of using the primary damping, the stability and lateral ride quality could be better improved through the optimisation of the primary stiffness.

De Pater (1989) studied the lateral stability of wagons containing two axle bogies. The study was purely analytical using a mathematical model. He showed that an appropriate choice of the lateral stiffness connecting the two wheelsets could increase the critical speed.

Ahmadian (1998) investigated the non-linear oscillation of the wheelset with flange contact. Bifurcation theory was applied to analyse the instability due to hunting. The studied case was a rail wheelset containing nonlinear primary yaw dampers. The result of the study showed that hunting could occur at speeds below the critical speed

computed through a linear analysis due to nonlinearities caused by flange contact, gauge clearance and yaw dampers.

Yabuno et al. (2001) studied the stabilisation control for the hunting motion of the wheelsets. They proposed a control strategy to limit the hunting motion of the wheelsets. The control method focused on the asymmetry in the stiffness matrix that was the principal cause of hunting. In order to reduce the effect of the asymmetrical component of the matrix, a lateral force proportional to yaw motion was applied. An experimental study was also conducted to validate the theoretical result. It was concluded that the control strategy significantly increased the critical speed.

Mohan (2003) reported an investigation on the nonlinear analysis of the controllable primary suspensions to improve hunting stability of wagons through the use of various primary and secondary stiffness and damping parameters. It was concluded that the critical velocity of wagons was more sensitive to the primary longitudinal stiffness compared to other parameters. He also proposed a method to control hunting stability using semi-active control of the primary longitudinal stiffness.

Curving and derailment

Sweet et al. (1984) studied the running safety of wagons against wheel-climb derailment. The study employed theoretical modelling and experiments. The results showed that the derailment quotient or the ratio of the lateral to the vertical force (L/V ratio) at the wheel-rail interface alone was not sufficient to predict the safety against derailment. Under dynamic conditions, a significantly larger derailment quotient could occur without causing actual derailment if it only occurred for a very short time. Hence

the criterion for derailment was accounted for by both the derailment quotient and the corresponding duration.

Effects of wheel-rail contact geometry to the wheelset steering forces was studied by Mace et al. (1996). The study involved both field experiments and theoretical analysis. It was reported that the hollow worn wheel adversely affected the wheelset steering during negotiating curves, leading to the generation of large negative steering moments. These negative steering moments caused a number of undesirable effects such as the track gauge widening, the rail roll over, the extensive wear of the wheel and the rail, and the increased train rolling resistance.

Haque et al. (1996) reported a non-linear wheelset model for derailment prediction. The modelling provided special emphasis on safety-related behaviour of the wheelset negotiating both the tangent and curved tracks. The wheelset models accounted for non-linearities due to wheel-rail profile geometry and creep force and the longitudinal translation of the contact patch as a function of wheelset yaw angle. The wheelset model was claimed to have lateral, yaw, and spin degrees of freedom and considered single-point and two-point contact as well as transition from one to the other. The authors exhibited that the model was capable of predicting the wheelset dynamic behaviour during wheel climb, wheel lift, steering characteristics during curve negotiation and also limit cycle behaviour on the tangent track.

Nagase et al. (2002) reported experimental results of the wheel climb derailment. The experiment was performed using a model bogie and a model track (1:5 scale). The risk of the derailment was evaluated using Nadal formula (ratio of the lateral force to the vertical force applied to the wheel) as well as by measuring the wheel vertical

displacement using a high-precision laser displacement sensor. As a result, it was found that the adhesion coefficient had a major influence on the occurrence of wheel climb derailment.

Optimisation of hunting and curving behaviour

Wickens (1991) provided a detailed review on optimisation of the hunting and curving behaviour through suspension design using sophisticated mathematical modelling. Current suspension technology has opened possibilities to develop innovative bogie designs with optimal performance in both tangent and curved tracks.

Matsumoto et al. (1999) proposed some methods to optimise the curving behaviour without reducing the hunting speed of the wagon. These methods included optimised worn tread profiles of wheels, independently rotating wheels in the rear axle, and asymmetric arrangement of the longitudinal primary suspension. The third method had earlier been proposed by Suda and Anderson (1994).

The improvement of the compatibility of the lateral stability and the curving performance of a railway passenger bogie was recently reported by Dukkipati and Narayanaswamy (2004). The authors proposed that the stiffness of the primary suspension of the leading axle be set different to the trailing axle.

Wagon and track interaction

All of the above reported research works have been focusing on the study of wagon and/or bogie dynamics without providing much attention to the track structure by assuming the track as a rigid or a simple elastic support. There are several studies, on the other hand, that focus only on the railway track dynamics by simplification of input

disturbance from the measurement or pre-calculated wagon dynamic characteristics (Grassie (1992), Luo et al. (1996), and Kerr (2000)). Some other studies on track dynamics have considered the track and the wagon as a multi-body system but simplified the case to only the vertical interaction between the wagon and the track (Zhai and Sun (1993)and Ripke and Knothe (1995)).

However, sometimes it is necessary to fully describe both the wagon and the track structures in 3D to examine their interaction with each other in all directions. This is because the track structure can affect the wheel rail interaction forces that play an important role in determining the dynamic behaviour of wagons. On the other hand, wagon suspension design can also affect the forces imposed on the track.

Sun and Dhanasekar (2001) introduced a three dimensional wagon track system dynamics (3D-WTSD) model, which fully describes the dynamic behaviour of the wagon and the track when the wagon runs under constant speed on tangent tracks. The 3D-WTSD model can be used, for example, to investigate the effect of track design parameters both on the wagon and the track dynamics or vice versa to investigate the effect of suspension design parameters on both the wagon and the track dynamics. It also can be an effective tool to investigate the effect of track on wagon dynamics and the effect of lateral and vertical impact applied by the wagon to track dynamics (Sun (2002)). From the results of simulations using 3D-WTSD model, Sun and Dhanasekar (2004) also reported the importance of track modelling for the determination of the critical speed of wagons. A similar example of the simulation that takes into account the 3D dynamic behaviour of the wagon and the track was presented by Anderson and Abrahamsson (2002).

In the case of wagon dynamics under traction/braking condition, the vertical and the lateral impact forces applied to the track may not be an issue. However, when the traction/braking force is applied to the wheels a large longitudinal creep force arises in the wheel-rail contact area. This force will dissipate through the structure below the rail such as the sleepers and the ballast. If this longitudinal force is big enough, the sleepers can be displaced from their position. If a train is braked or accelerated on the construction such as the railway bridge, the longitudinal force generated will be also passed through the construction. Therefore, in designing the track structure and the railway bridge this longitudinal force is required to be accounted for.

All of the above described simulation models deal with only *constant speed* without any reference to deceleration or acceleration. The dynamics of wagons under braking/traction is reviewed in Section 2.5.

2.3. THEORY OF WHEEL-RAIL ROLLING CONTACT

This section briefly reviews the development of wheel-rail rolling contact theory, which forms the foundation for determining the wheel-rail interaction forces. The accurate calculation of the wheel-rail interaction forces is very important in the modelling of the railway wagon and bogie dynamics. Kalker (1991) has provided a very good presentation on this subject. Another good reference is a book by Garg and Dukkipati (1984). Details of the mathematical analysis on rolling contact phenomena can be found in Jacobson and Kalker (2000) and Kalker (1990).

2.3.1. The Concept of Creep

Consider two rigid bodies that are in contact at a point. If any one or both of these bodies are rotated and/or moved relative to each other, the contact point will also shift its original position; the resulting velocities of the contact point over each body might or might not be equal to each other. When the velocities are equal, the bodies are said to be undergoing *pure rolling* (with no creep); under unequal velocities, they are said to be undergoing *rolling coupled with sliding (i.e., with creep)*. *Creep* or *creepage* is a dimensionless term (except for spin creepage) defining the deviation of the actual rolling condition between two rigid bodies from pure rolling to rolling coupled with sliding.

In the case of the wheelset running over the rails, creepage is defined in both the longitudinal and the lateral directions and also about the common normal of the contact patch (*spin*) as shown in Fig.2.9 (Dukkipati (2000)). The formulation is provided in Garg and Dukkipati (1984) and Dukkipati (2000) as in Eq.(2.3.a-c).

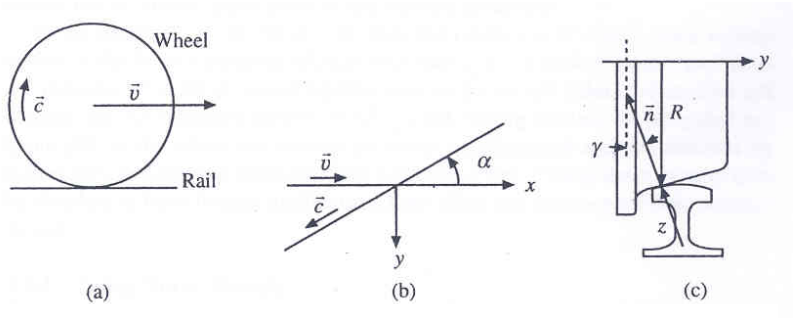

(a) Longitudinal creepage (b) Lateral creepage (c) spin creepage

Figure 2.9. Creepage (Dukkipati (2000))

$$\xi_x = \frac{\text{(longitudinal velocity of wheel – longitudinal velocity of rail) at the point of contact}}{\text{Nominal Velocity}} \quad (2.3.a)$$

$$\xi_y = \frac{\text{(lateral velocity of wheel – lateral velocity of rail) at the point of contact}}{\text{Nominal Velocity}} \quad (2.3.b)$$

$$\xi_{sp} = \frac{\text{(angular velocity of wheel – angular velocity of rail) about normal axis at the point of contact}}{\text{Nominal Velocity}} \quad (2.3.c)$$

where ξ_x , ξ_y , ξ_{sp} are the longitudinal, the lateral and the spin creepages respectively. It is important to note that the longitudinal and the lateral creepages are dimensionless, whereas the spin creepage has the dimension of L^{-1}.

2.3.2. The Development of Wheel-Rail Rolling Contact Theory

The wheel-rail rolling contact theory explains the relationship between the creep forces and the creepage. In general wheel-rail rolling contact theory states that there exists a unique relationship between the creepage and the forces generated at the wheel-rail contact patch. These forces are called creep forces as they are generated due to the existence of the creepage.

The relationship between creepage and creep forces was first defined by Carter (1926) who was concerned with the action of locomotive wheels when large tangential forces were transmitted during acceleration and braking. Carter has shown that the difference between the circumferential velocity of a driven wheel and the translational velocity of the wheel over the rail has a non-zero value as soon as a braking or traction couple is

applied to the wheel. The difference increases if the braking or traction couple increases, which means that there exists a relationship between the couple and the velocity leading to saturation when the Coulomb friction maximal value is reached. However, the formulation given by Carter was based on solving the integral equation of the two dimensional analysis for a cylinder rolling on a plane which only considers the force on the rolling direction. It is clearly *insufficient* for the purpose of rail wagon/ bogie simulation due to the complex geometries of the wheel and the railhead.

Vermeulen and Johnson (1964) proposed a creep-force law, which included the longitudinal and the lateral creepages. However, the spin creep was left out. To calculate the shape and the size of wheel-rail contact, Hertz theory is used. The Hertz theory defines the contact area between the wheel and the rail as elliptical and the ratio of the semi axes of the ellipse as a function of the curvature of the wheel and the railhead. The treatment of the Hertz theory in detail can be seen in Johnson (1985).

The most successful method of calculating the creep force is presented by Kalker (1967) who then wrote the computer program CONTACT, a universal program for all contact problems of bodies that can be described by half-space. He also has written a program called DUVOROL, which efficiently handles all possible rolling contact problems of bodies with identical elastic constants that touch each other according to the Hertz theory. DUVOROL was used by British Rail to construct a book of tables in support of rail vehicle simulation.

The computational time of both CONTACT and DUVOROL, which are based on Kalker's exact theory, is high and hence they are not suitable for real time applications in vehicle simulation (this is the reason why British Rail constructed a book of tables).

Concerned with this, in 1973 Kalker introduced the simplified theory of rolling contact and then used the theory to build a fast algorithm and computer program FASTSIM (Kalker (1982)).

Shen et al. (1983) improved the Vermeulen and Johnson law by including the effect of spin using Kalker's exact linear theory. The model used by Shen et al. is also called the *heuristic model* and is well known as Shen-Hedrick-Elkins or SHE theory. Fig. 2.10 presents the comparison of the creepage – creep force curve produced using FASTSIM, DUVOROL, and the heuristic model of Shen-Hedrick-Elkins for small spin. The figure shows that the three methods agree very closely.

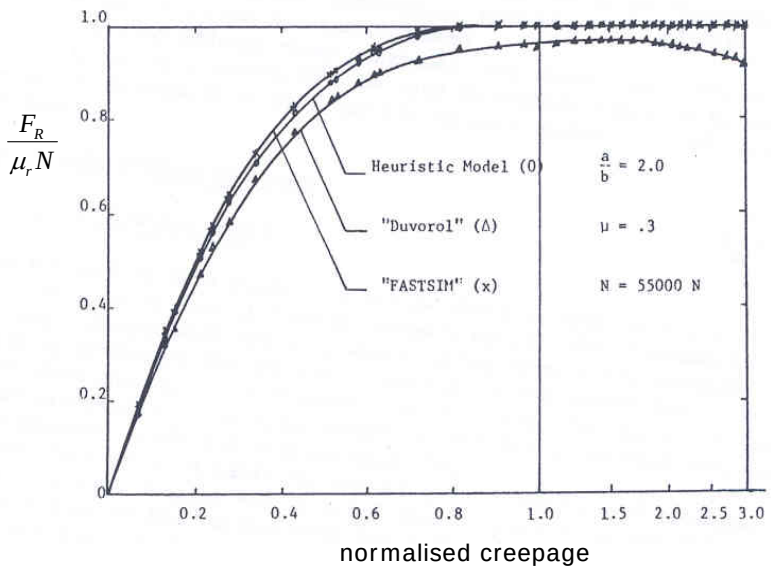

Figure 2.10. Creepage - Creep Force Curves (Shen et al. (1983))

In summary, Kalker (1991) defined the rolling contact theories and their interrelation as shown in Fig 2.11. He also gave a suggestion that the contact mechanics aspect of the wheel and the rail can be treated with the following routines:

Driving/braking wheel action	Shen-Hendrick-Elkins (SHE)
Non flanging vehicle dynamics	BR table book, linear theory, SHE, FASTSIM
Flanging vehicle dynamics	BR table book, FASTSIM
Two-point contact	BR table book, FASTSIM
Wear (profiles)	FASTSIM, CONTACT

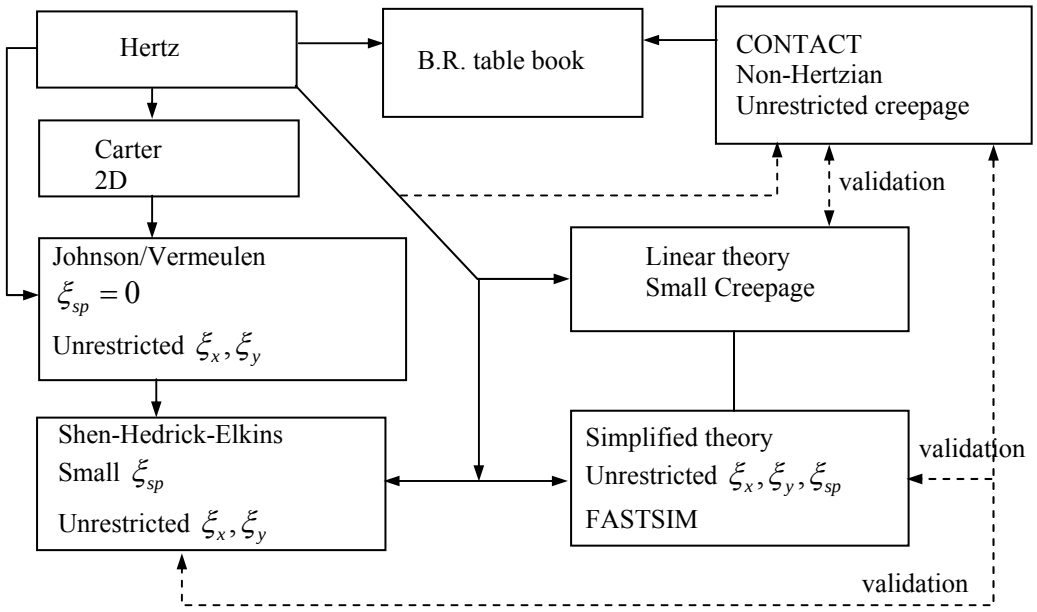

Figure 2.11. Wheel-rail rolling contact theories and their interrelation (Kalker (1991))

To complete our discussion on the development of the wheel-rail rolling contact theory, we should review another method to determine the creep forces which has been recently proposed by Polach (1999). This method is claimed to perform better under high creepage, although it is based on Kalker's work with simplification of the distribution of normal and tangential stresses in the wheel-rail contact patch. According

to this theory the creep forces can be computed efficiently with significant saving in computational effort. Application of this method to wagon dynamics simulation was also reported by the author (Polach (2001, 2005)). Polach also extended his creep force model for large creep application by introducing reduction factors for the Kalker coefficient to differentiate the areas of adhesion and slip.

2.4. FREIGHT WAGON BRAKING AND TRACTION SYSTEM

Traction and braking may be regarded as a process of conversion of energy. If a rail wagon is at rest the kinetic energy remains zero, whilst a moving rail wagon possesses significant kinetic energy. Braking reduces the speed of the wagon which means reducing the wagon kinetic energy, whilst traction does the opposite. However, wagons usually do not have their own traction system but are pulled or pushed by locomotives.

Reducing the speed of the wagon requires significant reduction to kinetic energy. The simplest way of reducing the energy is to convert it into heat by contacting material to the rotating wheels or to discs attached to the axles. The material creates friction and converts the kinetic energy into heat energy. With the reduction in kinetic energy, the wagon slows down and when the kinetic energy is fully nullified, the wagon comes to static equilibrium. The vast majority of freight trains are equipped with braking systems that use compressed air as the force to push blocks on to wheels or pads on to discs. These systems are known as "air brakes" or "pneumatic brakes". There are several types of air brake systems that are currently used in trains, which differ in aspects of their control systems, main control equipment, auxiliary equipments and pressure level. This is due to the different standard operating requirements of various railway networks.

Fig 2.12 shows a typical layout of air brake components of a freight wagon (Bureau (2002)) in North America. A similar system is used in the freight wagons of Australia. In this system the compressed air is transmitted along the train through pipes. A control valve, that is the AB type control valve in the figure, controls the pressure level of compressed air used to produce the braking force.

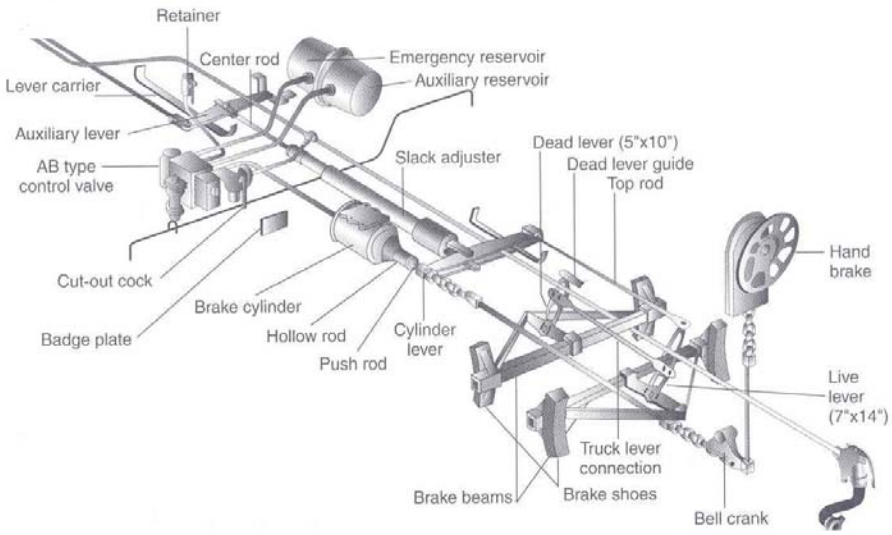

Figure 2.12. Freight wagon air brake system (Bureau (2002))

The braking force produced by the brake cylinder, usually mounted at the wagon underframe, is transmitted through a set of levers and rods to the wagon bogie. The force is then distributed to the wheels through the bogie brake rigging, which consist of levers and brake beams, fitted in each bogie. A slack adjuster is fitted within the mechanical link arrangement. The slack adjuster both takes up and lets out slack in the rods and lever system in order to keep the clearance between the brake shoes and wheels to a specified level.

Fig 2.13 exhibits the typical bogie brake rigging diagram of the three piece bogies that are equipped with one-side push brake shoe arrangement (Handoko et al. (2004)). The link consists of rods and levers suspended from the underframe and bogies, and linked with pins and bushes. The brake rigging requires careful setting up and regular adjustment to ensure the forces are evenly distributed to all wheels.

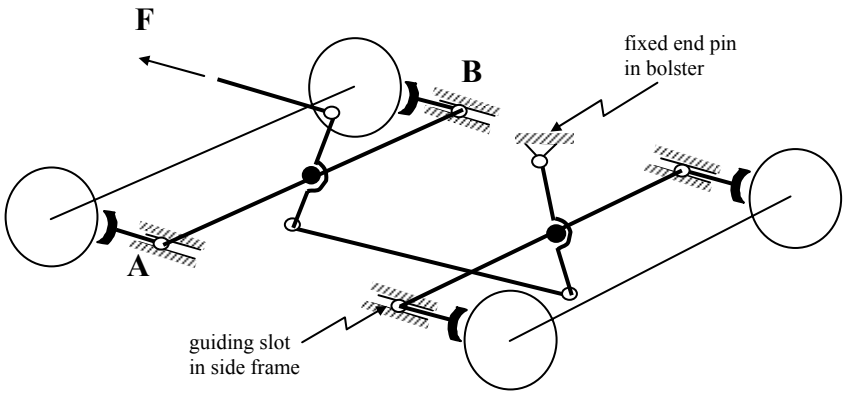

Figure 2.13. Typical bogie brake rigging

It can be seen from the rigging diagram that any bad adjustment of the brake rigging could lead to uneven distribution of braking forces to each wheel. Such a situation can occur when either the centre-pin on rod AB is slightly off-centred or if the fixed-end pin in the bolster is disorientated. The uneven distribution of the braking force to wheels may also occur during curve negotiation if the bogie deforms in shear (warping) mode.

2.4.1. Calculation of Brake Shoe Force

The brake shoe force applied to wheels is calculated from the brake cylinder piston thrust, the total brake rigging ratio (effectively the multiplication factor by which the brake piston force is leveraged by the brake rigging geometry), and the counter-forces

exerted by the brake storage spring of the slack adjuster as shown mathematically in Eq. (2.4).

$$F_B = F_{CT}.i_t - (F_R.i_b) \tag{2.4}$$

where F_B is the brake shoe force, F_{CT} is brake cylinder piston thrust, i_t is total brake rigging ratio, F_R is counter force exerted by slack adjuster, and i_b is the bogie brake rigging ratio. Brake cylinder piston thrust is determined by the cylinder piston area and the pressure in the brake cylinder as shown in Eq.2.5.

$$F_{CT} = \frac{\pi}{4} D^2.p_c \tag{2.5}$$

where D is effective diameter of the piston and p_c is the air pressure in the brake cylinder. The effective brake shoe force that would be actually acting on the wheel is normally less than the calculated brake shoe force above. This is because of power losses in the rigging system due to friction in the pin joints of the brake rigging levers. If we introduce the brake rigging efficiency η to represent these power losses, then the effective brake shoe force can be written as Eq.2.6.

$$F_{Beff} = F_B.\eta \tag{2.6}$$

2.4.2. Brake Application and Release Timing

Brake application time is the time required to build the pressure in the brake cylinder and is opposite to the *brake release time*, which is the time required to empty the cylinder. Ideally, the brake is applied simultaneously at the same time on every wagon of a train. This condition is easy to achieve if the electric brake control system is used.

However it will be difficult for the pure pneumatic brake system where the brake command is conveyed through the brake pipe along the train. This is because the response time is limited by the wave propagation in the compressed air system.

For modern freight traffic, it is required to shorten the application and release timing with greater braking force for efficiency of operation. However for the pure pneumatic brake system, problems will arise if the application time is too short because the front end of the train may reach the maximum brake pressure while the rear end would not have reached the full brake pressure yet. Derailments have occurred in which the rear portion of the train "ran into" the front portion in such circumstances. So there should be an optimum brake application time for a given train.

A similar situation (in reverse) happens with the brake release time. The brake will be released if the brake pipe reaches a certain pressure and all the air in the brake cylinder will be exhausted to the atmosphere. Because of the inertia of the air in the pipe system, the brake pipe pressure in the wagon near to the locomotive, from where the compressed air is supplied, may have reached the required pressure while the rear end would not have yet.

Due to the reasons explained above and also to assure the compatibility among brake systems in use, the UIC, BS, AAR, and other main railway standards have limited the brake application and release times to certain values. This limitation is prescribed for safety reasoning and decided based on experience. For example, the UIC standard prescribes the brake application and release timing for freight cars fitted with single pipe gradual release of brake as follows:

Application time : 0 to 95 % max brake cylinder pressure is 18 sec to 30 sec

Release time : 0 to 95 % max brake cylinder pressure is 45sec to 60 sec

From the application time and release time we can clearly see that, during the braking process, the force applied to the wheel will not be constant; rather it will build up slowly from zero to maximum. This also means that the wagon deceleration will change with time.

2.4.3. Traction

Traction, in general, can be viewed as the reverse process of braking. From this point of view, all parameters that influence the dynamics of wagons during braking can also affect the dynamics of wagons during traction. However, most of the freight wagons are not self-propelled. To accelerate they get the pulling or pushing force from a locomotive. The traction forces in a locomotive are usually generated by diesel engine or electric traction motors that produce torque transmitted to the wheelset using a gear box, whilst the wagons receive the traction force through pulling or pushing action of the mechanical couplers.

2.5. LONGITUDINAL DYNAMICS OF BOGIES AND WAGONS

2.5.1. Basic Principle of Braking Dynamics

During braking, forces or torques are applied to the wheelsets in order to decelerate the wagon. This process also produces reaction force in couplers and pitch torque to the wagon body and bogie. These forces affect the running stability and curving performance of bogies and wagons. On the other hand the dynamic response of the

wagon such as the change of the load distribution to the wheel can also affect the braking performance. The braking performance is usually measured through the stopping distance and also from the occurrence of skidding or wheelslide. With the reduction of the wheel load, the chance of the skid occurrence increases. Braking also involves friction, a complex phenomenon. During the process of braking, friction occurs between the brake shoe and the wheel and between the wheel and the rail as shown in Fig. 2.14.

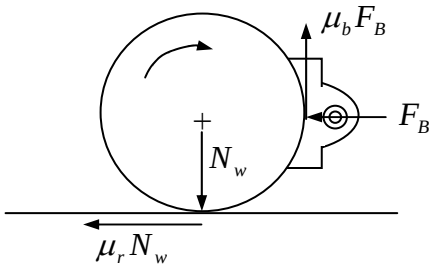

Figure 2.14. Forces at the braked wheel

The brake shoe force applied to the wheel F_B produces tangential force $\mu_b F_B$. If the wheel has radius r_w, a braking torque T_B is generated as shown in Eq.2.7.

$$T_B = \mu_b F_B r_w \tag{2.7}$$

The free body diagram of the braked wheel shown in Fig. 2.15 represents a wheel moving longitudinally in the x-direction at speed V and with angular velocity ω. J_y, r_w and T_B denote the polar moment of inertia, wheel radius and brake torque respectively. At the contact point between the wheel and the rail, longitudinal and vertical forces F_x and F_Z respectively arise as the reaction to the brake torque and the static weight mg.

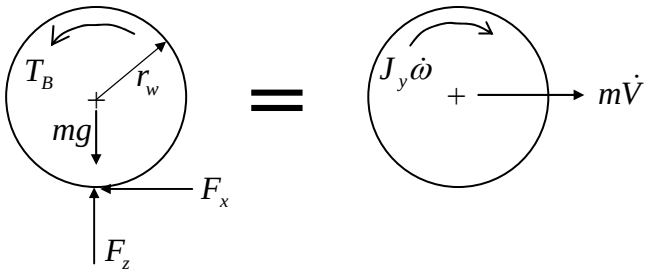

Figure 2.15. Free body diagram of braked wheel

By balancing the forces in the x- and z- directions and moments about the centre of mass of the wheel, three scalar equations of a braked wheel are established:

$$\left.\begin{aligned} m\dot{V} &= -F_x \\ F_z &= mg \\ J_y\dot{\omega} &= F_x r_w - T_B \end{aligned}\right\} \qquad (2.8)$$

where m is the mass of the wheel and wagon supported by the wheel and g is the gravity constant, while over dots denote differentiation with respect to time.

2.5.2. Skid and Friction Coefficient

Severe braking force can cause the wheelset to get locked and slide on the rail. This phenomenon is called skidding. This could lead to geometry damage to the wheels (wheel flat) and the railhead. Skidding also makes the stopping distance longer that would be dangerous to the train operation. Hence skidding should be avoided during braking as a matter of priority.

Skidding occurs when the braking force exceeds the adherence offered by the wheel-rail contact patch. Thus, to avoid skidding of the wheels during brake application the

brake force at the brake shoe must invariably be kept lower than the adhesion at the rail. Skidding does not occur when the relationship in Eq. (2.9) is fulfilled.

$$\mu_b F_B < \mu_r N_W \tag{2.9}$$

Currently many rail wagons are equipped with equipment to prevent skidding. However, there are still many wagons that do not possess this equipment, especially freight wagons, due to costs.

The difficulty in controlling skidding is related to the friction characteristic between materials that vary in nature. For example, friction between the wheel and the rail varies with rail surface condition (Macfarlane (2000)) such as rail corrugations, rail head contamination from oily deposits, leaves, water, ice, sand, etc, and the wheel tread surface condition as the application of the different type of brake shoe on the car (iron block, composition block, disc). Friction between the wheel and the rail also varies with the position of the wheelset along the track. The leading wheelset usually encounters the dirtiest rail and worst adhesion condition, and then cleans it for the wheels that follow. For design purpose, the friction coefficient between the wheel and the rail is usually assumed to be between 0.10 - 0.30.

In Section 2.3, the relation between creepage and the generated creep force has been explained. However, many experiments reported in the literature show that the relation has a peak followed by decay with increase in creepage. To explain this phenomenon, Nielsen and Theiler (1996) proposed the modelling of the friction coefficient as a function of slip velocity. Following the theory of Nielsen and Theiler, the relation between the slip percentage and the friction between wheel and rail was proposed by Ohishi et al. (2000), as exhibited in the adhesion force versus slip velocity curve shown

in Fig.2.16. Because the adhesion forces depend only on the friction coefficient and normal load, it is clear that the friction coefficient is also affected by the slip. The relation between them is not linear and depends on the wheel/rail condition (wet or dry).

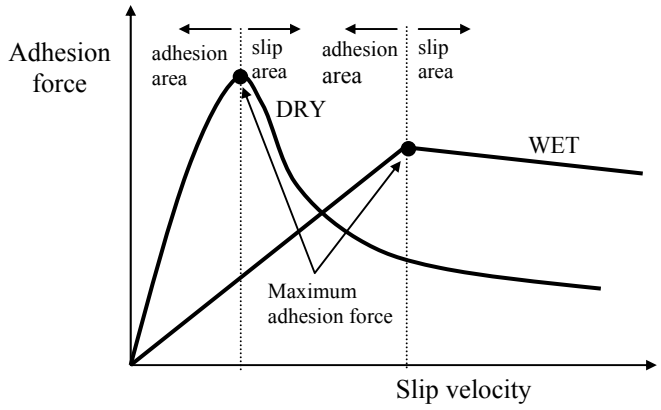

Figure 2.16. Adhesion force against slip velocity (Ohishi et al. (2000))

Coefficient of friction between the brake shoes and the wheel also does not remain constant. It varies with the sliding speed between the brake shoes and the wheal tread that depends on the velocity of the wagons. This also means that it changes continuously during the braking process. Fig 2.17 exhibits a typical plot of kinetic friction coefficient between two surfaces as a function of sliding speed and the Barwel's formula that shows the relationship between the friction coefficient μ_k and sliding speed v_s where the constant c_f depends on the material (Rabinowicz (1995)).

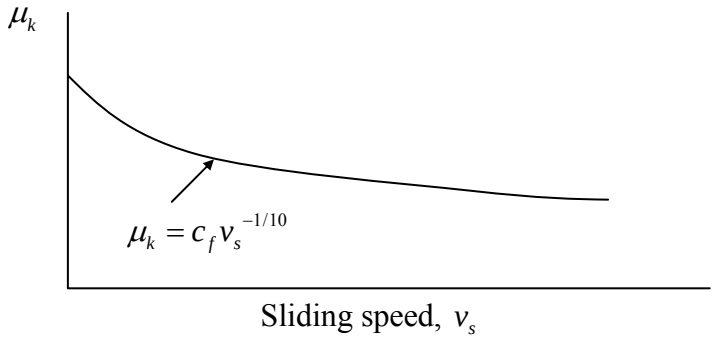

Figure 2.17. Friction coefficient against sliding speed

2.5.3. Dynamics Due to Traction

Because traction can be viewed as the reverse process of braking, the three scalar equations in the Eq. (2.8) are still applicable with only a change of sign (+/-). As a consequence, in the reverse of the skid phenomenon during braking, locomotives exerting excessive traction torque can make the wheelset rotate without any longitudinal motion. This condition is referred to as 'roll-slip' and becomes a subject of interest in the locomotive drive simulation as reported by Muller and Kogel (2000). Roll-slip can lead to railhead damage (engine burn or wheel burn). As for braking, traction can also cause large longitudinal forces in the wheel-rail contact patch.

2.5.4. State-of-the-art of Braking and Traction Dynamics Research

Balas (2001) developed a model for the sliding wheel of a railway car during braking. This work is mainly to assist the study and design of the braking equipment, including the Anti-lock Braking System (ABS). In this model the friction coefficient between the wheel and the rail is considered as a function of the slip of the wheel as shown in Fig 2.18. The slip of the wheel is defined as shown in Eq.2.10.

$$s = (v_{car} - v_w)/v_{car} \tag{2.10}$$

where: s is the slip (always between 0 (no braking) and 1 (locking)), v_{car} is the velocity of the car and v_w is the velocity of the wheel. This concept has been used by Ohishi et al. (2000) to design a control system that would prevent slip during traction of an electric motor coach. The difference is only in the shape of the friction coefficient against slip curve where Balas considers the pseudo sliding due to elasticity of the wheel. If this pseudo sliding is ignored, then the curve in Fig.2.16 used by Ohishi will be obtained.

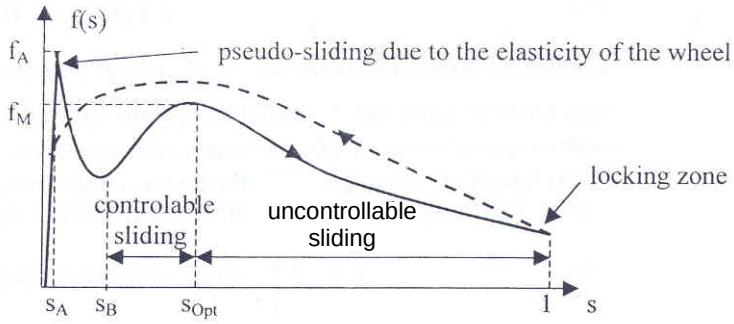

Figure 2.18. Wheel-rail friction coefficient against slip (Balas (2001))

Independently Cocci et al. (2001) presented a railway wagon model with an anti-slip braking system. The model is set up in the ADAMS/Rail and Simulink platform. Similar to Balas, Cocci et al. also considered the friction coefficient between wheel and rail as a function of wheel slip. The bogie suspension is modelled in three dimensions where longitudinal, vertical, and lateral stiffness are considered in the model. However longitudinal dynamics due to the effect of anti-slip control for optimum deceleration was particularly attended. Modelling the complete bogie is required to take into account the effect of load distribution to the wheel due to track geometry and/or track irregularities.

Olson (2001) has studied the longitudinal dynamics of ground vehicles that include non-linear wheel braking and acceleration models. Although his work is focused on road vehicles, it is still appropriate to the study of railway wagon braking. In formulating the equations of motion of wheel under braking condition, Olson considered the slip as a dynamic state variable, replacing the absolute rotational rate of the wheel speed.

Lixin and Haitao (2001) studied the dynamic response of wagons in a heavy haul train during braking mode. For such purpose they have set up a model using ADAMS/Rail software that could predict the three dimensional dynamic response of the wagon under braking conditions. An open-top freight wagon used in China was the case study. From their investigation it was concluded that the application of braking has adversely affected the lateral and vertical dynamic performance of the wagon. However, the investigation was limited to constant brake shoe force that was distributed evenly to the wheels. In actual conditions, the brake force is a time function and may not be symmetric and could be distributed unevenly to the wheels. Lixin and Haitao (2001) *did not* investigate the effect of wheel-lock or skid phenomena. Both of these conditions (asymmetric brake forces and wheel skid) can lead to a more serious situation. This thesis (Chapter 9) describes these phenomena in detail.

Berghuvud (2002) investigated the effect of brake application to wagon curving performance using parameters that define the wagon curving performance such as the wheelset angle of attack, the track forces, and the wear in the contact patch between the wheels and the rails. He found that the wagons with different types of bogies respond in different ways to curving as a function of the applied braking force. However he *did not* consider the effect of variation in speed or deceleration as he examined the wagon

running on downhill slopes while braking was continuously applied to keep its speed constant. The braking force applied also remained constant and symmetric with no wheel skid.

Suda and Grencik (1996) explained the mechanism of deterioration of curving performance under braking conditions where the braking torque reduced the steering torque of the wheelset. This mechanism is explained in Fig.2.19 that shows a free body diagram of a wheelset running along a curved track.

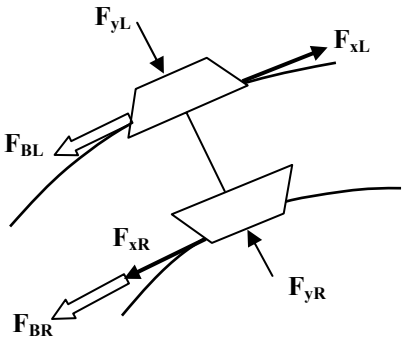

Figure 2.19. Curving diagram of a wheelset (Suda and Grencik (1996))

While negotiating a curve, the rolling radius of the outer wheel becomes larger than that of the inner wheel leading to the generation of longitudinal creep forces F_{xR} and F_{xL}, where in general $F_{xR} \neq F_{xL}$. These creep forces produce a steering torque that guides the wheelset to follow the curve appropriately. Application of brake produces additional longitudinal forces F_{BR} and F_{BL} on the contact points which produce a steering moment as shown in Eq.(2.11).

$$M = a\left[\left(F_{xL} - F_{BL}\right) + \left(F_{xR} + F_{BR}\right)\right], \qquad (2.11)$$

where a is the semi distance between the contact points. However, the resultant of total longitudinal creep force and lateral creep force at the contact points cannot exceed the maximum frictional force between the wheel and the rail. The resultant creep forces are calculated as shown in Eq.(2.12).

$$F_{CR}=\sqrt{\left(F_{xR}+F_{BR}\right)^2+F_{yR}{}^2} \quad ; \; F_{CL}=\sqrt{\left(F_{xL}-F_{BL}\right)^2+F_{yL}{}^2} \tag{2.12}$$

where F_{CR} and F_{CL} are resultant creep forces on the right and left rail respectively. If F_{CR} and F_{CL} exceed the creep condition, they becomes saturated leading to reduction in the longitudinal creep force. The directions of longitudinal creep force and additional force due to braking are the same on the inner wheel, so the reduction in longitudinal force on the inner rail is larger than that on the outer wheel. Because of this reduction of longitudinal forces, the steering moment on the wheelset also reduces.

Malvezzi et al. (2003) carried out an investigation of the braking in trains. They performed probability analysis of train deceleration during braking. The aim of the work was to determine the probability that the real deceleration is lower than the nominal value multiplied by a safety margin.

The analysis of braking in a train was also carried out by Durali and Shadmehri (2003). The authors reported the analysis of train derailment due to severe braking with various wagon weight configurations. From the results, the optimum configuration of wagons and the critical derailment velocity can be determined. The authors also claimed that the results were in excellent agreement with the field experience although they did not present any comparison with the field data in the paper.

Excessive traction torque applied to the locomotive wheels could cause roll-slip. Because this roll-slip reduces the traction power and can damage the locomotive's wheels, it is very important to avoid it during the operation of the motive power. For this reason, studies on the subject of slip controllers have been extensively performed. Among them was the work recently reported by Frylmark and Johnsson (2003). In their thesis Frylmark and Johnsson studied several methods of slip controller such as adhesion observer based controller, fuzzy logic slip controller and hybrid slip control method. As a summary, the authors presented the advantages and disadvantages of each method. They also proposed a few improvements and present ideas that may be interesting in future research.

2.6. WAGON SIMULATION SOFTWARE PACKAGES

The computational simulation of the dynamic behaviour of railway wagons has been a standard design task in the railway industry during recent years (Schupp (2003)). Software packages such as VAMPIRE and NUCARS (Iwnicky (1999)) have been specifically developed for this purpose, while general multibody dynamics software tools such as and ADAMS, SIMPACK and UNIVERSAL MECHANISM have a module which is intended to simulate the railway wagon dynamics. Multibody dynamics computational method has been used as a tool to develop these software packages.

Using VAMPIRE as a tool, McClanachan et al. (2004) have shown that it is possible to adequately model freight wagons containing three piece bogies during constant speed operation. In their paper, the data from field tests were compared with the simulation of roll, bounce and pitch.

Shabana and Sany (2001) reported a survey of rail vehicle track simulations which include flexible multibody dynamics. In their paper they have pointed out that, with the recent development in computational mechanics, it is possible to develop a tool to comprehensively analyse the complex dynamics of railway vehicles and tracks.

Shen and Pratt (2001) developed a railway dynamics modelling and simulation package for current industrial trends. They suggested that the future software tool should adopt the object oriented and knowledge based techniques that aid the human thought process. According to them the new simulation packages should be adaptable to design changes.

2.6.1. Reference Coordinate System and Formulation of Equation of Motion

This section discusses how the multibody system approach is currently used in the formulation of railway vehicle dynamics simulation tools. The review includes the equation of motion and the formulation of the wheel-rail contact problem. These are the specific modelling features that make the railway vehicle dynamic simulation unique. However the review presented here also shows that the current approach is not ideal to simulate railway wagon/ bogie dynamics during braking or traction.

The common method of deriving the equations of motion of the railway wagon is the transfer coordinate (or moving coordinate) system that moves along the track at the speed of the wagon. This coordinate system is referred to as track-based or track-following moving reference system (Zboinski (1999)). With this method it is very convenient to describe the position of the contact point between the wheel and the rail and the direction of wheel-rail contact force. By assuming steady state motion of wagons, a simple form of the equations of motion can be obtained. However, applying

this method to the braking and/ or traction condition is rather cumbersome if not impossible.

Fig 2.20 illustrated this problem where a body i, with body coordinate system ($o_i, \mathbf{x}_i, \mathbf{y}_i, \mathbf{z}_i$) attached to it, is moving with respect to a non-inertial transfer coordinate reference system R ($o_r, \mathbf{x}_r, \mathbf{y}_r, \mathbf{z}_r$). As presented by Schiehlen (1984) and Xia (2002), the Newton-Euler equations of motion for the moving body i with respect to the transfer coordinate system and the inertial reference frame O ($o_o, \mathbf{x}_o, \mathbf{y}_o, \mathbf{z}_o$) are as per detail shown in Eq.(2.13) and Eq.(2.14).

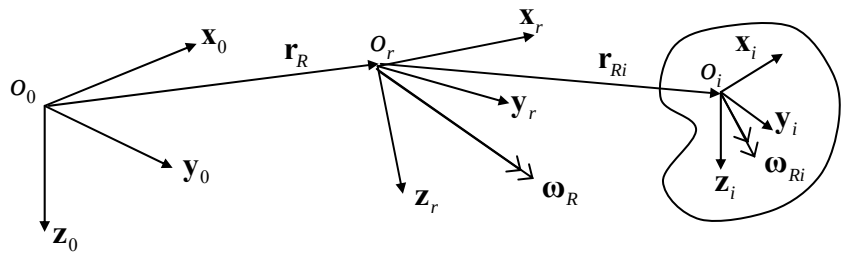

Figure 2.20. The description of the motion of a body in a moving reference frame

$$\mathbf{m}_i\left[\ddot{\mathbf{r}}_R + \tilde{\boldsymbol{\omega}}_R\dot{\mathbf{r}}_R + \left(\dot{\tilde{\boldsymbol{\omega}}}_R + \tilde{\boldsymbol{\omega}}_R^2\right)\mathbf{r}_{Ri} + 2\tilde{\boldsymbol{\omega}}_R\dot{\mathbf{r}}_{Ri} + \ddot{\mathbf{r}}_{Ri}\right] = \mathbf{F}_i \tag{2.13}$$

$$\mathbf{I}_i\dot{\boldsymbol{\omega}}_R + \tilde{\boldsymbol{\omega}}_R\mathbf{I}_i\boldsymbol{\omega}_R + \tilde{\boldsymbol{\omega}}_R\boldsymbol{\omega}_{Ri}(\mathbf{I}_{xi} + \mathbf{I}_{yi} + \mathbf{I}_{zi}) + 2\tilde{\boldsymbol{\omega}}_{Ri}\mathbf{I}_i\boldsymbol{\omega}_R + \mathbf{I}_i\dot{\boldsymbol{\omega}}_{Ri} + \tilde{\boldsymbol{\omega}}_{Ri}\mathbf{I}_i\boldsymbol{\omega}_{Ri} = \mathbf{M}_i \tag{2.14}$$

where $\mathbf{m}_i$ and $\mathbf{I}_i$ are the mass matrix and the inertia tensor of the body respectively, $\mathbf{F}_i$ and $\mathbf{M}_i$ are the external force and moment applied to the body written in the transfer coordinate frame respectively, $\mathbf{r}_R$ and $\boldsymbol{\omega}_R$ are the vector position and the angular velocity of the transfer coordinate system respectively, and $\mathbf{r}_{Ri}$ and $\boldsymbol{\omega}_{Ri}$ are the vector position and angular velocity of the body reference in respect to the transfer coordinate

system respectively. Over dots ($\dot{}$) represent differentiation with respect to time and tildes (~) represent skew symmetric matrix of the vector.

If the transfer coordinate system moves with constant speed along a tangent track, then the Newton-Euler equations of motion reduce to a very simple form as shown in Eq.2.15 and Eq.2.16.

$$\mathbf{m}_i \ddot{\mathbf{r}}_{Ri} = \mathbf{F}_i \tag{2.15}$$

$$\mathbf{I}_i \dot{\boldsymbol{\omega}}_{Ri} + \tilde{\boldsymbol{\omega}}_{Ri} \mathbf{I}_i \boldsymbol{\omega}_{Ri} = \mathbf{M}_i \tag{2.16}$$

The equations will be slightly more complex if the system moves in curving, although it can be handled without much difficulty as long as the speed remains constant because we could pre-define the angular velocity of the transfer coordinate system for the known geometry of the curve.

The problem becomes very complex when we deal with the braking condition where the speed does not remain constant. Currently, the solution to this problem is obtained by pre-guessing the speed profile based on the initial velocity and deceleration and *assuming* the transfer coordinate system to move with this speed profile. This approach *will not provide* an exact solution because the deceleration actually comes from the force applied to the body in the system, or more specifically it is caused by the force generated at the contact points due to brake forces applied to the wheels. To obtain an exact solution, the contact kinematics should be calculated as a function of the variation of the velocity of the moving body and it must be calculated in real time (on line) during the simulation.

Another consequence of using a moving reference frame is that the wheelset rotation with respect to its lateral axis, which is referred to as *wheelset pitch*, is not explicitly included in the formulation. Because the speed of the wagon has been pre-defined and assumed to be the speed of the transfer coordinate system along the track, the nominal wheelset pitch velocity has also to be pre-defined as a function of the speed. Thus, the effect of the severe application of heavy braking and traction such as skid and slip *cannot* be accounted for in the formulation.

Due to the reasons explained above, the best way to treat the dynamics during braking and traction is to describe the absolute body motion in the *fixed inertia coordinate system*. This thesis presents such a formulation which is discussed in Chapter 3.

Another matter that should receive careful attention is the interaction between the wheel and the rail itself. Under braking torque, the locked region in the wheel-rail contact area is moved backward and generates areas of compression and tension as shown in Fig 2.21 (Dukkipati (2000)). In parallel, the forward motion of the wagon is decelerated by the longitudinal creep force developed in the contact area. The larger the longitudinal creep force, the further the zero line of stress is displaced from a line drawn perpendicular to the rail and through the centre of the wheel. If the longitudinal creep force is large enough, all the contact area becomes a slip area or in other words the wheel will purely slide (skid) on the rail. Skidding affects the safety of the wagon so it is important to consider it in the wheelset dynamic model. The problem will be more complicated if the friction coefficients between the wheel and the rail and between the brake shoe and the wheel are treated as dynamic variables.

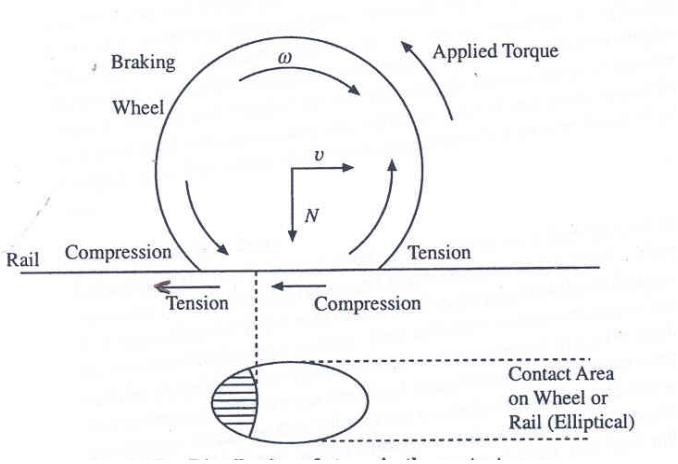

Figure 2.21. Stress distribution in the contact area during braking (Dukkipati (2000))

We should also note that the magnitude of the total creep force is limited by the saturation adhesive force between the wheel and the rail. As the total creep force is the resultant of the longitudinal and lateral creep forces, we can deduce that at saturation the longitudinal creep force could effectively modify the lateral and roll motions between the wheel and the rail. From this fact we can also state that the application of the braking force affects the lateral as well as the longitudinal and the vertical dynamics of the wagon, especially at the onset of and during skidding.

2.7. SUMMARY

Railway wagon, bogie and wheelset dynamics cover the subjects of linear and non-linear stability, curving performance, ride quality and comfort analysis, wagon track interaction, and dynamic control systems. This extensive research is greatly supported by the emergence of wheel-rail rolling contact theory and the improvement of numerical analysis algorithms and computational strategies over the last three decades.

Only limited information on the dynamic behaviour of wagons and bogies under longitudinal forces due to braking and traction are found in the published literature. As wagons are mostly not self-propelled, the interest in the research of the effect of longitudinal forces due to braking is much larger. Much of the research on wagon braking is concerned only with the optimisation of braking distance and to avoid wheel skid. At the onset of and during skidding, the longitudinal creep force affects the lateral creep force at the wheel-rail contact patch as the magnitude of the resultant of the lateral and longitudinal creep force is limited by the saturation adhesive force between the wheel and the rail. The effect of the braking force to the lateral dynamics of the wagon bogie especially at the onset of and during skidding is addressed in this thesis.

The complexity of modelling the dynamics of bogies during traction/braking emerges as we cannot use a transfer coordinate system that moves along the track at the speed of the wagon. The position and orientation of the contact patch, the creepages and creep forces, which are usually defined in the track reference frame, need to be transferred to the absolute reference frame to formulate the equations of motions. A comprehensive explanation of the dynamic behaviour of the bogie under traction/braking condition is undoubtedly required to maximise the efficiency and minimise the risk of railway rollingstock operation. This thesis provides a contribution to this important area.

3. DYNAMICS OF RIGID BODIES - A GENERALISED MODELLING APPROACH

3.1. INTRODUCTION

Many commercially available wagon-track system dynamics software packages adopt the track-following reference (TFR) coordinate frame that moves at predefined wagon speed. Although the TFR coordinate frame simplifies the formulation, it cannot truly account for the effect of the longitudinal traction or braking forces; such effect is indirectly accounted for by inputting variable speed profiles. The inertial reference frame (IFR) that is fixed in space and time with the capability of describing the location and orientation of each moving body in the coordinate system offers an alternative modelling platform. The IRF system is capable of accounting for the large translations and rotations of the wagons due to their operational parameters and track geometry, including the wheelset rotation with respect to its lateral axis (wheelset pitch). The first derivative of this wheelset rotation or the wheelset angular velocity plays a key role in the definition of creepages that are crucial to the calculation of creep forces on the wheel-rail contact patch. In the constant speed simulation this angular velocity is assumed to remain constant and hence, as a simplification, most rail wagon-track system dynamic analysis packages ignore the wheelset pitch degree of freedom. However, during the application of braking or traction torques, the wheelset rotation no longer remains constant; therefore wheelset pitch as a degree of freedom should be included in the modelling. This also implies that the wheel-rail contact parameters should be evaluated as part of the process of simulation and not as a preliminary

calculation as is normally done in constant velocity simulation packages that are commercially available.

As this thesis focuses on the effect of the longitudinal forces to the dynamics of wagons and bogies, the IRF based generalised multibody dynamics approach, especially applied to rigid body systems, is adopted for the modelling. This chapter presents the IRF based generalised rigid body dynamics formulation and its application to the modelling of the wheel-rail contact.

3.2. FORMULATION

Rigid body dynamics is generally expressed in terms of mass matrices as well as the position, velocity, acceleration and force vectors. This section briefly describes the formulation of these vectors and matrices in the IRF Coordinate System. More detailed discussion on the subject of multibody system dynamics can be found in the literature (Shabana (1989), Schiehlen (1997) and Roberson and Schwertassek (1998)).

3.2.1. Coordinate System and Transformation

Fig. 3.1 shows a rigid body i in three-dimensional space. Reference frame **XYZ** is an inertial reference frame (IRF) with its origin fixed in space and time. The unconstrained motion of a rigid body in space can be described using six independent coordinates; namely three independent translation coordinates and three independent rotation coordinates. By measuring the displacement of a selected reference point that is fixed to or forms part of the rigid body, usually its centre of mass, the translational motion of the body can be easily defined. This selected reference point is chosen as the origin of

the body reference frame $\mathbf{X}^i\mathbf{Y}^i\mathbf{Z}^i$. The position of an arbitrary point P^i in the body i with reference to the global IRF system can be written as (see Fig. 3.1)

$$\mathbf{r}^i = \mathbf{R}^i + \mathbf{A}^i\bar{\mathbf{u}}^i \tag{3.1}$$

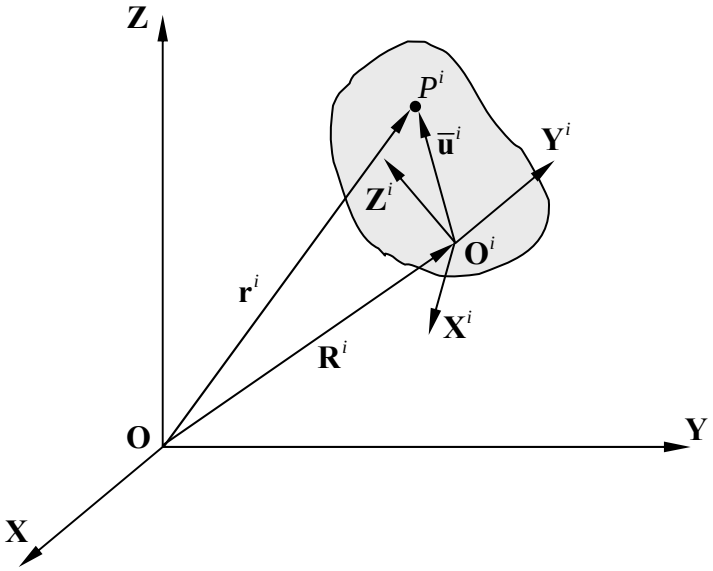

Figure 3.1. Coordinates of rigid body

where $\mathbf{R}^i$ is the global position vector of the origin of the body reference frame, $\mathbf{A}^i$ is the transformation matrix (from the body coordinate system to the global coordinate system), and $\bar{\mathbf{u}}^i$ is the position vector of the same arbitrary point P^i with reference to the body coordinate system. $\mathbf{A}^i$, a 3 x 3 transformation matrix, and $\mathbf{R}^i$ and $\bar{\mathbf{u}}^i$ vectors are respectively given by (Shabana (1989)):

$$\mathbf{A}^i = \begin{bmatrix} 1-2(\theta_2)^2-2(\theta_3)^2 & 2(\theta_1\theta_2-\theta_0\theta_3) & 2(\theta_1\theta_3+\theta_0\theta_2) \\ 2(\theta_1\theta_2+\theta_0\theta_3) & 1-2(\theta_1)^2-2(\theta_3)^2 & 2(\theta_2\theta_3-\theta_0\theta_1) \\ 2(\theta_1\theta_3-\theta_0\theta_2) & 2(\theta_2\theta_3+\theta_0\theta_1) & 1-2(\theta_1)^2-2(\theta_2)^2 \end{bmatrix} \tag{3.2}$$

$$\mathbf{R}^i = \begin{bmatrix} R_1^i & R_2^i & R_3^i \end{bmatrix}^{\mathrm{T}} \tag{3.3}$$

$$\bar{\mathbf{u}}^i = \begin{bmatrix} u_1^i & u_2^i & u_3^i \end{bmatrix}^{\mathrm{T}} \tag{3.4}$$

where $\theta_0^i, \theta_1^i, \theta_2^i, \theta_3^i$ are *Euler parameters* describing rotational coordinates $\boldsymbol{\theta}^i$ that define the body orientation as shown in Eq. (3.5).

$$\boldsymbol{\theta}^i = \begin{bmatrix} \theta_0^i & \theta_1^i & \theta_2^i & \theta_3^i \end{bmatrix} \tag{3.5}$$

The four Euler parameters $\theta_0, \theta_1, \theta_2, \theta_3$ should obey the following condition :

$$\sum_{k=0}^{3} (\theta_k^i)^2 = 1 \tag{3.6}$$

Note: Although the rotational coordinates are represented by four Euler parameters, the number of independent rotational coordinates remains three (represents three rotational degrees of freedom) due to the constraint of Eq. (3.6).

3.2.2. Velocity and Acceleration Analysis

Velocity

By differentiating Eq. (3.1) with respect to time, we obtain the velocity vector:

$$\dot{\mathbf{r}}^i = \dot{\mathbf{R}}^i + \dot{\mathbf{A}}^i \bar{\mathbf{u}}^i \tag{3.7}$$

The vectors $\dot{\mathbf{A}}^i \bar{\mathbf{u}}^i$ can be written as

$$\dot{\mathbf{A}}^i \bar{\mathbf{u}}^i = \mathbf{A}^i \left(\bar{\boldsymbol{\omega}}^i \times \bar{\mathbf{u}}^i \right) \tag{3.8}$$

where $\bar{\boldsymbol{\omega}}^i$ is the angular velocity vector defined with respect to the body coordinate system, shown explicitly as in Eq. (3.9).

$$\bar{\boldsymbol{\omega}}^i = \begin{bmatrix} \bar{\omega}_1^i \\ \bar{\omega}_2^i \\ \bar{\omega}_3^i \end{bmatrix} \tag{3.9}$$

By utilizing the skew symmetric matrix of the vector $\bar{\boldsymbol{\omega}}^i$ (Shabana (1989)) and the identity of the cross product between two vectors (Kreyszig (1999)), the angular velocity and position vector can be evaluated as follows:

$$\bar{\boldsymbol{\omega}}^i \times \bar{\mathbf{u}}^i = \tilde{\bar{\boldsymbol{\omega}}}^i \bar{\mathbf{u}}^i = -\tilde{\bar{\mathbf{u}}}^i \bar{\boldsymbol{\omega}} \tag{3.10}$$

where $\tilde{\bar{\boldsymbol{\omega}}}^i$ and $\tilde{\bar{\mathbf{u}}}^i$ are skew symmetric matrices given by

$$\tilde{\bar{\boldsymbol{\omega}}}^i = \begin{bmatrix} 0 & -\bar{\omega}_3^i & \bar{\omega}_2^i \\ \bar{\omega}_3^i & 0 & -\bar{\omega}_1^i \\ -\bar{\omega}_2^i & \bar{\omega}_1^i & 0 \end{bmatrix} \tag{3.11.a}$$

$$\tilde{\bar{\mathbf{u}}}^i = \begin{bmatrix} 0 & -\bar{u}_3^i & \bar{u}_2^i \\ \bar{u}_3^i & 0 & -\bar{u}_1^i \\ -\bar{u}_2^i & \bar{u}_1^i & 0 \end{bmatrix} \tag{3.11.b}$$

where $\bar{\omega}_1^i, \bar{\omega}_2^i, \bar{\omega}_3^i$ and $\bar{u}_1^i, \bar{u}_2^i, \bar{u}_3^i$ are the components of the vectors $\bar{\boldsymbol{\omega}}^i$ and $\bar{\mathbf{u}}^i$ respectively. Eq. (3.7) can, therefore, be rewritten as

$$\dot{\mathbf{r}}^i = \dot{\mathbf{R}}^i - \mathbf{A}^i \tilde{\bar{\mathbf{u}}}^i \bar{\boldsymbol{\omega}}^i \tag{3.12}$$

The angular velocity vector $\bar{\boldsymbol{\omega}}^i$ can be calculated by using the time derivatives of the rotational coordinate $\boldsymbol{\theta}^i$ of the body reference as

$$\bar{\boldsymbol{\omega}}^i = \bar{\mathbf{G}}^i \dot{\boldsymbol{\theta}}^i \tag{3.13}$$

where $\bar{\mathbf{G}}^i$, in term of Euler parameters, is a 3×4 matrix given by (Shabana (1989))

$$\bar{\mathbf{G}}^i = 2\begin{bmatrix} -\theta_1^i & \theta_0^i & \theta_3^i & -\theta_2^i \\ -\theta_2^i & -\theta_3^i & \theta_0^i & \theta_1^i \\ -\theta_3^i & \theta_2^i & -\theta_1^i & \theta_0^i \end{bmatrix} \tag{3.14}$$

Acceleration

The acceleration can be obtained by differentiating Eq. (3.7) with respect to time. This leads to

$$\ddot{\mathbf{r}}^i = \ddot{\mathbf{R}}^i + \ddot{\mathbf{A}}^i\bar{\mathbf{u}}^i \tag{3.15}$$

The vector $\ddot{\mathbf{A}}^i\bar{\mathbf{u}}^i$ can be written (similar to Eq. (3.8)) as follows:

$$\ddot{\mathbf{A}}^i\bar{\mathbf{u}}^i = \mathbf{A}^i\left[\bar{\boldsymbol{\omega}}^i \times \left(\bar{\boldsymbol{\omega}}^i \times \bar{\mathbf{u}}^i\right)\right] + \mathbf{A}^i\left(\bar{\boldsymbol{\alpha}}^i \times \bar{\mathbf{u}}^i\right) \tag{3.16}$$

where $\bar{\boldsymbol{\alpha}}^{\mathbf{i}} = \begin{bmatrix} \bar{\alpha}_1^i & \bar{\alpha}_2^i & \bar{\alpha}_3^i \end{bmatrix}^{\mathrm{T}}$ is the angular acceleration vector of body i with respect to the body coordinate system.

Eq. (3.16) can also be written as

$$\ddot{\mathbf{A}}^i\bar{\mathbf{u}}^i = \mathbf{A}^i(\tilde{\bar{\boldsymbol{\omega}}}^i)^2\bar{\mathbf{u}}^i + \mathbf{A}^i\tilde{\bar{\boldsymbol{\alpha}}}^i\bar{\mathbf{u}}^i \tag{3.17}$$

where $\tilde{\bar{\boldsymbol{\alpha}}}^i$ is a skew symmetric matrix of the angular acceleration vector given by

$$\tilde{\bar{\boldsymbol{\alpha}}}^i = \begin{bmatrix} 0 & -\bar{\alpha}_3^i & \bar{\alpha}_2^i \\ \bar{\alpha}_3^i & 0 & -\bar{\alpha}_1^i \\ -\bar{\alpha}_2^i & \bar{\alpha}_1^i & 0 \end{bmatrix} \tag{3.18}$$

Thus, Eq. (3.15) can be rewritten as

$$\ddot{\mathbf{r}}^i = \ddot{\mathbf{R}}^{\mathbf{i}} + \mathbf{A}^i(\tilde{\bar{\boldsymbol{\omega}}}^i)^2\bar{\mathbf{u}}^i + \mathbf{A}^i\tilde{\bar{\boldsymbol{\alpha}}}^i\bar{\mathbf{u}}^i \tag{3.19}$$

3.2.3. Mass Matrices

The mass matrix of the rigid body is defined as

$$\mathbf{M}^i = \begin{bmatrix} \mathbf{m}^i_{RR} & \mathbf{m}^i_{R\theta} \\ symmetric & \mathbf{m}^i_{\theta\theta} \end{bmatrix} \tag{3.20}$$

where

$$\mathbf{m}^i_{RR} = \int_{V^i} \rho^i \mathbf{I} dV^i \tag{3.21}$$

$$\mathbf{m}^i_{R\theta} = -\int_{V^i} \rho^i \mathbf{A}^i \tilde{\bar{\mathbf{u}}}^i \bar{\mathbf{G}}^i dV^i \tag{3.22}$$

$$\mathbf{m}^i_{\theta\theta} = \int_{V^i} \rho^i \bar{\mathbf{G}}^{i^{\mathrm{T}}} \tilde{\bar{\mathbf{u}}}^{i^{\mathrm{T}}} \tilde{\bar{\mathbf{u}}}^i \bar{\mathbf{G}}^i dV^i \tag{3.23}$$

where ρ and V^i are the mass density and the volume of the rigid body.

It can be easily verified that the integration in the Eq. (3.21) yields

$$\mathbf{m}^i_{RR} = \begin{bmatrix} m^i & 0 & 0 \\ 0 & m^i & 0 \\ 0 & 0 & m^i \end{bmatrix} \tag{3.24}$$

where m^i is the total mass of the body. Thus, the matrix $\mathbf{M}^i_{RR}$ is a diagonal matrix containing constant terms representing the mass of the body.

If the origin of the body reference is attached to the body centre of mass, the integral of Eq. (3.22) will vanish. In this case the matrix $\mathbf{m}^i_{R\theta}$ that represents the inertia coupling between the translation and rotation of body reference is a null matrix and, therefore, the mass matrix $\mathbf{M}^i$ of the rigid body can be written as follows:

$$\mathbf{M}^i = \begin{bmatrix} \mathbf{m}^i_{RR} & \mathbf{0} \\ \mathbf{0} & \mathbf{m}^i_{\theta\theta} \end{bmatrix} \tag{3.25}$$

Therefore, for simplicity and in order to eliminate the inertia coupling between the translation and rotation of the body reference, in this thesis the origin of the body reference frame is always positioned at the centre of mass of the bodies.

The matrix $\mathbf{m}^i_{\theta\theta}$ that is associated with the rotational coordinates of the body reference may be written as

$$\begin{aligned} \mathbf{m}^i_{\theta\theta} &= \int_{V^i} \rho^i \bar{\mathbf{G}}^{i^{\mathrm{T}}} \tilde{\bar{\mathbf{u}}}^{i^{\mathrm{T}}} \tilde{\bar{\mathbf{u}}}^i \bar{\mathbf{G}}^i dV^i \\ &= \bar{\mathbf{G}}^{i^{\mathrm{T}}} \int_{V^i} \rho^i \tilde{\bar{\mathbf{u}}}^{i^{\mathrm{T}}} \tilde{\bar{\mathbf{u}}}^i dV^i \bar{\mathbf{G}}^i \\ &= \bar{\mathbf{G}}^{i^{\mathrm{T}}} \mathbf{I}_{\theta\theta} \bar{\mathbf{G}}^i \end{aligned} \tag{3.26}$$

where $\mathbf{I}^i_{\theta\theta}$ is the inertia tensor of the rigid body defined as follows:

$$\mathbf{I}^i_{\theta\theta} = \int_{V^i} \rho^i \tilde{\bar{\mathbf{u}}}^{i^{\mathrm{T}}} \tilde{\bar{\mathbf{u}}}^i dV^i \tag{3.27}$$

For positioning the body reference frame at the body centre of mass, the inertia tensor is defined as in Eq. (3.28):

$$\mathbf{I}^i_{\theta\theta} = \begin{bmatrix} I_{11} & 0 & 0 \\ 0 & I_{22} & 0 \\ 0 & 0 & I_{33} \end{bmatrix} \tag{3.28}$$

where I_{11}, I_{22}, I_{33} are the moments of inertia of the rigid body with respect to the principal axes of the body reference.

3.2.4. Generalised Forces

Normally rigid bodies under motion are subjected to external forces. For the railway wagon system these forces include the gravity, the spring and the damper forces, the friction forces, the actuator forces, and the traction or the brake torques. The evaluation of these generalised applied forces associated with the generalised coordinates of the spatial rigid body system is an essential step in the formulation of the system dynamic equation.

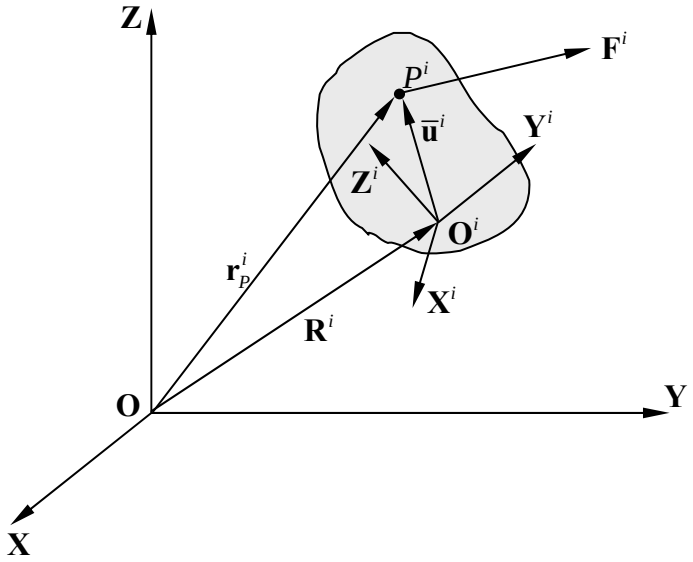

Figure 3.2. Rigid body subjected to external force

Fig. 3.2 shows a rigid body i subjected to an external force $\mathbf{F}^i$ that acts at an arbitrary point P^i. The virtual work of this external force vector is given by

$$\delta W_e^i = \mathbf{F}^{i^{\mathrm{T}}} \delta \mathbf{r}_P^i \tag{3.29}$$

where $\delta \mathbf{r}_P^i$ is the virtual displacement of the point P^i due to the application of the force $\mathbf{F}^i$. Using the first time-derivative of the vector position of point P^i defined in Eqs. (3.12) and.(3.13), the virtual displacement $\delta \mathbf{r}_P^i$ can be written as Eq. (3.30).

$$\delta \mathbf{r}_P^i = \delta \mathbf{R}^i - \mathbf{A}^i \tilde{\bar{\mathbf{u}}}_P^i \bar{\mathbf{G}}^i \delta \boldsymbol{\theta}^i \tag{3.30}$$

By substituting Eq. (3.30) into Eq. (3.29), we obtain

$$\delta W_e^i = \mathbf{F}^{i^{\mathrm{T}}} \delta \mathbf{R}^i - \mathbf{F}^{i^{\mathrm{T}}} \mathbf{A}^i \tilde{\bar{\mathbf{u}}}_P^i \bar{\mathbf{G}}^i \delta \boldsymbol{\theta}^i \tag{3.31}$$

We can rewrite Eq. (3.31) as

$$\delta W_e^i = \mathbf{F}_R^{i^{\mathrm{T}}} \delta \mathbf{R}^i + \mathbf{F}_\theta^{i^{\mathrm{T}}} \delta \boldsymbol{\theta}^i \tag{3.32}$$

where

$$\mathbf{F}_R^i = \mathbf{F}^i \tag{3.33}$$

$$\mathbf{F}_\theta^i = -\left(\mathbf{A}^i \tilde{\bar{\mathbf{u}}}_P^i \bar{\mathbf{G}}^i \right)^{\mathrm{T}} \mathbf{F}^i \tag{3.34}$$

Eq. (3.32) determines the virtual work as the summation of two components, namely, the work done by the direct force acting at the origin of the body reference and the work done by the moment acting on the body.

System of forces and moments

If a set of forces $\mathbf{F}_1^i, \mathbf{F}_2^i, \ldots \mathbf{F}_{n_f}^i$ and a set moments $\mathbf{M}_1^i, \mathbf{M}_2^i, \ldots \mathbf{M}_{n_m}^i$ act on the a rigid body i, then we will have vectors of generalised forces that can be expressed as

$$\mathbf{Q}_R^i = \mathbf{F}_1^i + \mathbf{F}_2^i + \cdots + \mathbf{F}_{n_f}^i = \sum_{j=1}^{n_f} \mathbf{F}_j^i \tag{3.35}$$

$$\begin{aligned}\mathbf{Q}_\theta^i &= \mathbf{G}^{iT}\left[\mathbf{M}_1^i + \mathbf{M}_2^i + \cdots + \mathbf{M}_{n_m}^i\right] - \left[\left(\mathbf{A}^i\tilde{\bar{\mathbf{u}}}_1^i\bar{\mathbf{G}}^i\right)^{\mathrm{T}}\mathbf{F}_1^i + \left(\mathbf{A}^i\tilde{\bar{\mathbf{u}}}_2^i\bar{\mathbf{G}}^i\right)^{\mathrm{T}}\mathbf{F}_2^i + \cdots + \left(\mathbf{A}^i\tilde{\bar{\mathbf{u}}}_{n_f}^i\bar{\mathbf{G}}^i\right)^{\mathrm{T}}\mathbf{F}_{n_f}^i\right] \\ &= \mathbf{G}^{iT}\sum_{j=1}^{n_m}\mathbf{M}_j^i - \sum_{j=1}^{n_f}\left[\left(\mathbf{A}^i\tilde{\bar{\mathbf{u}}}_j^i\bar{\mathbf{G}}^i\right)^{\mathrm{T}}\mathbf{F}_j^i\right]\end{aligned} \tag{3.36}$$

where $\mathbf{Q}_R^i$ and $\mathbf{Q}_\theta^i$ are the vectors of generalised forces associated with the generalised translational and rotational coordinates respectively.

Linear spring-damper system

As a wagon suspension system consists of springs and dampers, it becomes important to accommodate the generalised forces exerted by these elements in our formulation. Consider two bodies i and j connected by a spring-damper element at points P^i and P^j respectively as shown in Fig. 3.3.

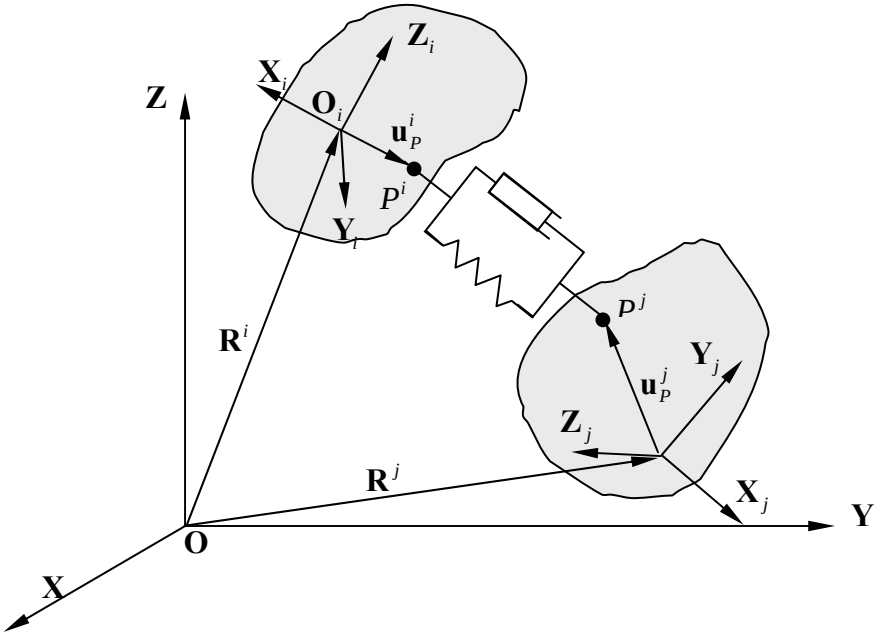

Figure 3.3. Linear spring and damper

Let k be the spring constant, c be the damping coefficient, and l_0 be the undeformed length of the spring. The magnitude of the spring-damper force along a line that connects points P^i and P^j can be written as

$$F_s = k(l - l_0) + c\dot{l} \tag{3.37}$$

where l is the current spring length. If $\mathbf{r}_P^{ij}$ is the position vector of point P^i with respect to point P^j which is defined by

$$\begin{aligned} \mathbf{r}_P^{ij} &= \mathbf{r}_P^i - \mathbf{r}_P^j \\ &= \mathbf{R}^i + \mathbf{A}^i \overline{\mathbf{u}}_P^i - \mathbf{R}^j - \mathbf{A}^j \overline{\mathbf{u}}_P^j \end{aligned} \tag{3.38}$$

The current spring length is the modulus of vector $\mathbf{r}_P^{ij}$, that is,

$$l = \left| \mathbf{r}_P^{ij} \right| = \sqrt{\mathbf{r}_P^{ij\mathrm{T}} \mathbf{r}_P^{ij}} \tag{3.39}$$

The unit vector $\hat{\mathbf{r}}_P^{ij}$ of the vector $\mathbf{r}_P^{ij}$ can, therefore, be written as

$$\hat{\mathbf{r}}_P^{ij} = \frac{\mathbf{r}_P^{ij}}{l} \tag{3.40}$$

Using this unit vector, we can express the vectors of the generalised spring-damper forces that act on body i as follows

$$\begin{aligned} \mathbf{Q}_R^i &= -F_s \hat{\mathbf{r}}_P^{ij} \\ \mathbf{Q}_\theta^i &= F_s \left(\mathbf{A}^i \tilde{\overline{\mathbf{u}}}_P^i \overline{\mathbf{G}}^i \right)^{\mathrm{T}} \hat{\mathbf{r}}_P^{ij} \end{aligned} \tag{3.41}$$

Similarly, the vectors of the generalised spring-damper forces acting on body j are represented as follows:

$$\mathbf{Q}_R^i = F_s \hat{\mathbf{r}}_P^{ij}$$
$$\mathbf{Q}_\theta^j = -F_s \left(\mathbf{A}^j \tilde{\bar{\mathbf{u}}}_P^j \bar{\mathbf{G}}^j \right)^{\mathrm{T}} \hat{\mathbf{r}}_P^{ij} \tag{3.42}$$

Torsional spring-damper system

Torsional spring-damper that is often used in the wagon suspension system can be represented schematically by the diagram shown in Fig. 3.4. It is obvious that the torsional spring damper generates/resists only torque with no capability for resisting linear forces acting at the body centre of mass.

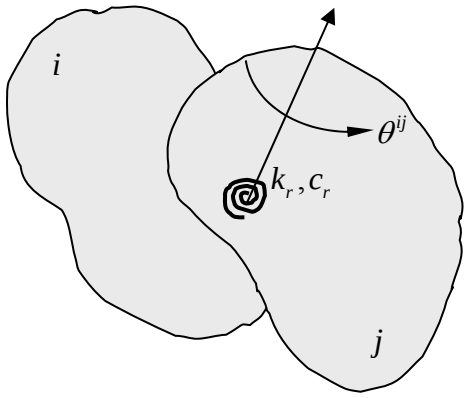

Figure 3.4. Torsional spring-damper element

The torque exerted by the element on the two bodies is caused by the relative rotation θ^{ij} between them. The magnitude of this torque is

$$T^{ij} = \left(k_r \theta^{ij} + c_r \dot{\theta}^{ij} \right) \tag{3.43}$$

where k_r and c_r are the rotational spring and damper coefficient respectively. If $\mathbf{h}^{ij}$ is the unit vector along the joint axis, then it can be easily verified that the vectors of the generalised force that act on the body i are represented as follows:

$$\mathbf{Q}_R^i = \mathbf{0}$$
$$\mathbf{Q}_\theta^i = -T^{ij}\mathbf{G}^{i^{\mathrm{T}}}\mathbf{h}^{ij} \tag{3.44}$$

and on the body j are represented as follows:

$$\mathbf{Q}_R^j = \mathbf{0}$$
$$\mathbf{Q}_\theta^j = T^{ij}\mathbf{G}^{j^{\mathrm{T}}}\mathbf{h}^{ij} \tag{3.45}$$

3.2.5. Contact between Two Rigid Bodies: Definition and Constraint

The dynamics of wagons running on track involves contact between wheel and rail. A formulation of the contact problem proposed by Shabana et al. (2001), which has been briefly discussed in Chapter 2, has preferable features to perform simulation of wagons under longitudinal braking or traction forces. The fixed inertial reference frame (IRF) is used and the rotation of the wheel with respect to its lateral axis (wheel pitch) is also calculated accurately. The formulation is explained in this section.

Definition of the contact point

Consider two rigid bodies i and j that are in contact at point P^k as shown in Fig. 3.5. $\mathbf{R}^i$ and $\mathbf{R}^j$ are the vectors that define the global position of the origin of the coordinate system of each body while $\bar{\mathbf{u}}^{ik}$ and $\bar{\mathbf{u}}^{jk}$ are the position vectors of the contact point in the local coordinate system of each body.

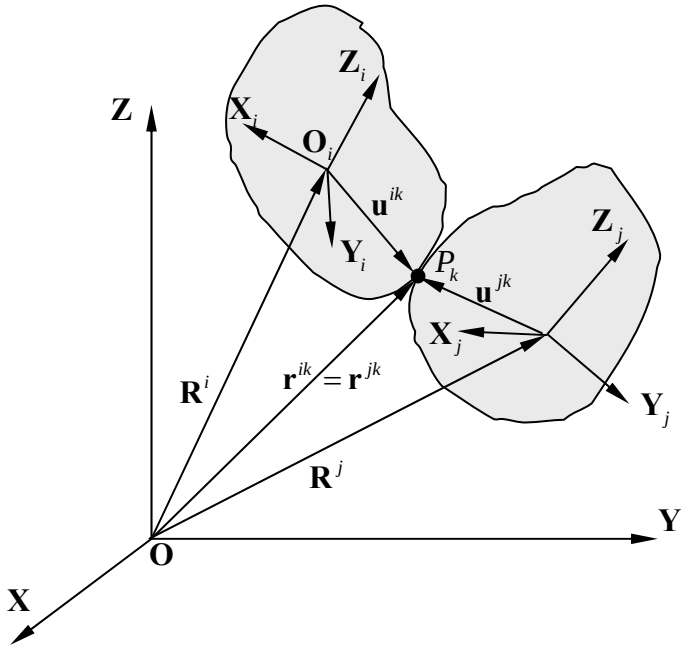

Figure 3.5. Two rigid bodies in contact

The global position vector of the contact point P^k on bodies i and j can be written, respectively, as

$$\mathbf{r}^{ik} = \mathbf{R}^i + \mathbf{A}^i \overline{\mathbf{u}}^{ik} \tag{3.46}$$

$$\mathbf{r}^{jk} = \mathbf{R}^j + \mathbf{A}^j \overline{\mathbf{u}}^{jk} \tag{3.47}$$

where $\mathbf{A}^i$ and $\mathbf{A}^j$ are the transformation matrices that define the orientation of bodies i and j respectively in the global reference frame.

A surface in space can be described by using parametric representation. As surfaces are two-dimensional, two parameters are required (Greenberg (1978), Kreyszig (1999)). In the formulation of two rigid bodies in contact, the contact surface of each body i and j are assumed to be defined by the two surface parameters as follows:

$$\mathbf{s}^{ik} = \begin{bmatrix} s_1^{ik} & s_2^{ik} \end{bmatrix}^{\mathrm{T}} \tag{3.48}$$

$$\mathbf{s}^{jk} = \begin{bmatrix} s_1^{jk} & s_2^{jk} \end{bmatrix}^{\mathrm{T}} \tag{3.49}$$

Therefore, for each single point of contact between two rigid bodies i and j, there exist four surface parameters. These surface parameters are independent variables that are treated in the system dynamics in the same manner as the system generalised coordinates. The difference between these surface parameters and the generalised coordinate is that there is no inertia or generalised forces associated with these surface parameters. Thus, the surface parameters are also referred as the non-generalised coordinates.

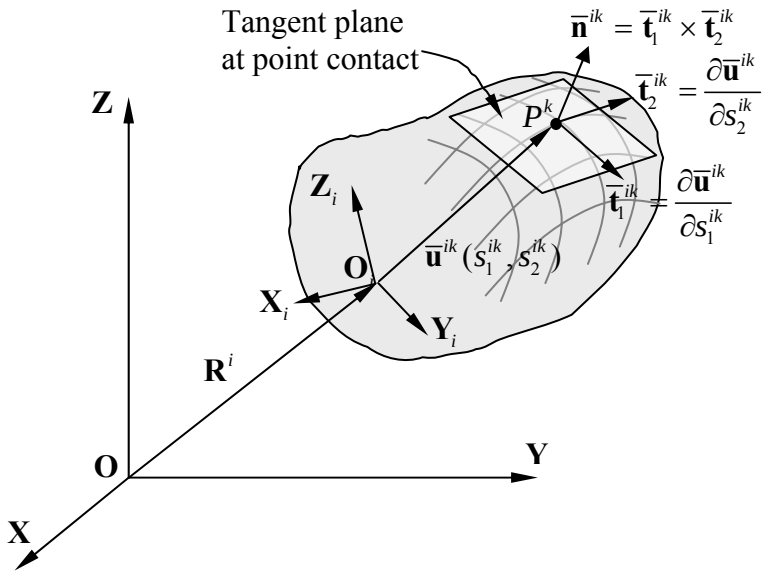

Figure 3.6. Tangent and normal vectors to the body surface at a contact point P^k

At the contact point, for each surface in contact a tangent plane is defined by two tangents vectors as shown in Fig. 3.6. These tangent vectors are linearly independent

and not necessarily orthogonal. The tangent vectors to the surfaces of bodies i and j are defined, respectively, in the body coordinate system as

$$\overline{\mathbf{t}}_l^{ik} = \frac{\partial \overline{\mathbf{u}}^{ik}}{\partial s_l^{ik}} \quad , \quad l = 1,2 \tag{3.50}$$

$$\overline{\mathbf{t}}_l^{jk} = \frac{\partial \overline{\mathbf{u}}^{jk}}{\partial s_l^{jk}} \quad , \quad l = 1,2 \tag{3.51}$$

Using these tangent vectors we can define the normal vectors to the surfaces in contact as

$$\overline{\mathbf{n}}^{ik} = \overline{\mathbf{t}}_1^{ik} \times \overline{\mathbf{t}}_2^{ik} \tag{3.52}$$

$$\overline{\mathbf{n}}^{jk} = \overline{\mathbf{t}}_1^{jk} \times \overline{\mathbf{t}}_2^{jk} \tag{3.53}$$

where $\overline{\mathbf{n}}^{ik}$ and $\overline{\mathbf{n}}^{jk}$ are, respectively, the normal vectors to the surface of body i and j at the point of contact defined in the body coordinate system.

Contact constraints

The non-conformal contact between two rigid bodies, should satisfy two conditions listed below (Litvin (1994), Shabana and Sany (2001)):

- The point of contact between the two bodies must occupy the same position in space.
- The two surfaces must have the same tangent contact plane at the contact point.

The first condition provides the following equation known as the contact point constraint equation that contains three scalar nonlinear algebraic equations.

$$\mathbf{r}^{ik} = \mathbf{r}^{jk} \tag{3.54}$$

or,

$$\mathbf{R}^i + \mathbf{A}^i \overline{\mathbf{u}}^{ik} = \mathbf{R}^j + \mathbf{A}^j \overline{\mathbf{u}}^{jk} \tag{3.55}$$

In the form of the generalised constraint equation, it is written as

$$\mathbf{C}(\mathbf{q}, \mathbf{s}) = \mathbf{R}^i + \mathbf{A}^i \overline{\mathbf{u}}^{ik} - \mathbf{R}^j - \mathbf{A}^j \overline{\mathbf{u}}^{jk} = 0 \tag{3.56}$$

The second condition implies that at the contact point there exists one common unit normal for the two surfaces. This means that the dot product between the normal vector to the surface of one body and the tangent vector to the surface of the other body should vanish. For the case of bodies i and j in contact at point P^k, this condition can be represented by the following equation:

$$\mathbf{n}^{jk\mathrm{T}} \mathbf{t}_l^{ik} = 0, \qquad l = 1, 2 \tag{3.57}$$

Defining the tangent vector and the normal vectors in the body coordinate systems, Eq. (3.57) can also be written as Eq. (3.58).

$$\overline{\mathbf{n}}^{jk\mathrm{T}} \mathbf{A}^{j\mathrm{T}} \mathbf{A}^i \overline{\mathbf{t}}_l^{ik\mathrm{T}} = 0, \qquad l = 1, 2 \tag{3.58}$$

This constraint equation represents the orientation constraint.

Thus, for each contact between two rigid bodies we have five non linear algebraic constraint equations. Since we have six degrees of freedom and four additional independent non-generalised surface parameters (i.e., a total of ten unknowns), the five constraint equations will not help solving all unknowns; we will have five degree of freedom left as unknowns with only one degree of freedom, that is the relative translation between the two bodies in the contact normal direction, eliminated.

Sub-Jacobian matrices of the contact constraint

Sub-Jacobian matrices of the contact constraint equations are defined as:

$$\mathbf{C}_{\mathbf{q}} = \left[\frac{\partial \mathbf{C}}{\partial \mathbf{q}} \right] \tag{3.59}$$

$$\mathbf{C}_{\mathbf{s}} = \left[\frac{\partial \mathbf{C}}{\partial \mathbf{s}} \right] \tag{3.60}$$

where $\mathbf{q}$ is the vector of generalised coordinates and $\mathbf{s}$ is the vector of surface parameters.

Substituting Eq. (3.56) into Eq. (3.59) and (3.60), we obtain the sub-Jacobian matrices for the contact constraint as follows (Berzeri (2000)):

$$\mathbf{C}_{\mathbf{q}} = \begin{bmatrix} \mathbf{I} & -\mathbf{A}^i \tilde{\bar{\mathbf{u}}}^{ik} \bar{\mathbf{G}}^i & -\mathbf{I} & \mathbf{A}^j \tilde{\bar{\mathbf{u}}}^{jk} \bar{\mathbf{G}}^j \end{bmatrix} \tag{3.61}$$

$$\mathbf{C}_{\mathbf{s}} = \begin{bmatrix} \mathbf{A}^i \bar{\mathbf{T}}^{ik} & -\mathbf{A}^j \bar{\mathbf{T}}^{jk} \end{bmatrix} \tag{3.62}$$

where $\bar{\mathbf{G}}^i$ is the matrix as defined in the Eq. (3.14) and $\bar{\mathbf{T}}^{ik}$ is the matrix defined as

$$\bar{\mathbf{T}}^{ik} = \begin{bmatrix} \bar{\mathbf{t}}_1^{ik} & \bar{\mathbf{t}}_2^{ik} \end{bmatrix} \tag{3.63}$$

A similar formulation is used to determine matrices $\bar{\mathbf{G}}^j$ and $\bar{\mathbf{T}}^{jk}$ for body j.

Substituting Eq. (3.58) into Eq. (3.59) and Eq. (3.60), the sub-Jacobian matrices of the orientation constraint can also be derived. These sub-Jacobian matrices of the orientation constraint can be written as follows (Berzeri (2000)):

$$\mathbf{C}_{l,\mathbf{q}} = \begin{bmatrix} \mathbf{0} & -\bar{\mathbf{n}}^{jk\mathrm{T}} \mathbf{A}^{j\mathbf{T}} \mathbf{A}^i \tilde{\bar{\mathbf{t}}}_l^{ik} \bar{\mathbf{G}}^i & \mathbf{0} & -\bar{\mathbf{t}}_l^{ik\mathbf{T}} \mathbf{A}^{i\mathrm{T}} \mathbf{A}^j \tilde{\bar{\mathbf{n}}}^{jk} \bar{\mathbf{G}}^j \end{bmatrix}, \quad l = 1,2 \tag{3.64}$$

$$\mathbf{C}_{l,\mathbf{s}} = \begin{bmatrix} \bar{\mathbf{n}}^{jk\mathrm{T}} \mathbf{A}^{j\mathbf{T}} \mathbf{A}^i \dfrac{\partial \bar{\mathbf{t}}_l^{ik}}{\partial \mathbf{s}^{ik}} & \bar{\mathbf{t}}_l^{ik\mathrm{T}} \mathbf{A}^{i\mathbf{T}} \mathbf{A}^j \dfrac{\partial \bar{\mathbf{n}}^{jk}}{\partial \mathbf{s}^{jk}} \end{bmatrix}, \quad l = 1,2 \tag{3.65}$$

Mathematical detail to determine these sub-Jacobian matrices can be seen in Appendix I.

3.2.6. Augmented System Dynamic Equations

The contact constraint equations can be written in general as

$$\mathbf{C}(\mathbf{q}, \mathbf{s}, t) = 0 \tag{3.66}$$

where $\mathbf{q}$ is the vector of the system generalised coordinates, $\mathbf{s}$ is the vector of the non-generalised surface parameters of all the contact surfaces in the multibody system and t is time.

Differentiating this equation with respect to time yields

$$\mathbf{C}_\mathbf{q}\dot{\mathbf{q}} + \mathbf{C}_\mathbf{s}\dot{\mathbf{s}} + \mathbf{C}_t = 0 \tag{3.67}$$

where

$$\mathbf{C}_t = \frac{\partial \mathbf{C}}{\partial t} \tag{3.68}$$

is the partial derivative of the vector of constraints with respect to time. For the contact constraint which is not an explicit function of time, $\mathbf{C}_t = \mathbf{0}$.

Differentiating Eq. (3.67) again with respect to time, we will have

$$\left(\mathbf{C}_\mathbf{q}\dot{\mathbf{q}} + \mathbf{C}_\mathbf{s}\dot{\mathbf{s}} + \mathbf{C}_t\right)_\mathbf{q}\dot{\mathbf{q}} + \left(\mathbf{C}_\mathbf{q}\dot{\mathbf{q}} + \mathbf{C}_\mathbf{s}\dot{\mathbf{s}} + \mathbf{C}_t\right)_\mathbf{s}\dot{\mathbf{s}} + \left(\mathbf{C}_\mathbf{q}\dot{\mathbf{q}} + \mathbf{C}_\mathbf{s}\dot{\mathbf{s}} + \mathbf{C}_t\right)_t = \mathbf{0} \tag{3.69}$$

Because the contact constraint is not an explicit function of time, any partial derivatives with respect to time will be zero. Thus, Eq. (3.69) can be simplified and rearranged as follows:

$$\mathbf{C}_\mathbf{q}\ddot{\mathbf{q}} + \mathbf{C}_\mathbf{s}\ddot{\mathbf{s}} + \left(\mathbf{C}_\mathbf{q}\dot{\mathbf{q}}\right)_\mathbf{q}\dot{\mathbf{q}} + \left(\mathbf{C}_\mathbf{q}\dot{\mathbf{q}}\right)_\mathbf{s}\dot{\mathbf{s}} + \left(\mathbf{C}_\mathbf{s}\dot{\mathbf{s}}\right)_\mathbf{q}\dot{\mathbf{q}} + \left(\mathbf{C}_\mathbf{s}\dot{\mathbf{s}}\right)_\mathbf{s}\dot{\mathbf{s}} = \mathbf{0} \tag{3.70}$$

or it can be simplified as

$$\mathbf{C}_\mathbf{q}\ddot{\mathbf{q}} + \mathbf{C}_\mathbf{s}\ddot{\mathbf{s}} = \mathbf{Q}_\mathbf{d} \tag{3.71}$$

where

$$\mathbf{Q}_{\mathbf{d}} = -\left(\mathbf{C}_{\mathbf{q}}\dot{\mathbf{q}}\right)_{\mathbf{q}}\dot{\mathbf{q}} - \left(\mathbf{C}_{\mathbf{q}}\dot{\mathbf{q}}\right)_{\mathbf{s}}\dot{\mathbf{s}} - \left(\mathbf{C}_{\mathbf{s}}\dot{\mathbf{s}}\right)_{\mathbf{q}}\dot{\mathbf{q}} - \left(\mathbf{C}_{\mathbf{s}}\dot{\mathbf{s}}\right)_{\mathbf{s}}\dot{\mathbf{s}} \tag{3.72}$$

is a vector that absorbs the quadratic terms in the first order time-derivatives of the generalised coordinates and the surface parameters, and $\mathbf{C}_{\mathbf{q}}$ and $\mathbf{C}_{\mathbf{s}}$ are the sub-Jacobians of the constraint equations.

From Eq. (3.65) we infer that the sub-Jacobian matrix of the orientation constraint contains second-order derivatives of the vector position of the contact points with respect to the surface parameter due to the fact that the tangent vector is the first partial derivative of the vector position of the contact points with respect to the surface parameter. Thus, from the last term in Eq. (3.72) we can clearly see that the vector $\mathbf{Q}_{\mathbf{d}}$ contains third-order derivatives of the vector position of the contact points with respect to the non-generalised surface parameters.

Using the Lagrange multiplier technique, the algebraic kinematic constraint equations can be augmented into the differential equations of motion. For the system of rigid bodies that involves contact constraint, the equation of motion is written as:

$$\left.\begin{aligned} \mathbf{M}\ddot{\mathbf{q}} + \mathbf{C}_{\mathbf{q}}^{\mathrm{T}}\boldsymbol{\lambda} &= \mathbf{Q}_e + \mathbf{Q}_v \\ \mathbf{C}_{\mathbf{s}}^{\mathrm{T}}\boldsymbol{\lambda} &= \mathbf{0} \end{aligned}\right\} \tag{3.73}$$

where $\mathbf{M}$ is the mass matrix of the system, $\boldsymbol{\lambda}$ is the vector of the Lagrange multiplier, $\mathbf{Q}_e$ is the vector of externally applied force, and $\mathbf{Q}_v$ is a quadratic velocity vector that arises from differentiating kinetic energy with respect to time and with respect to the generalised coordinates of the systems. For the body i this quadratic velocity vector is given by (Shabana (1989))

$$\mathbf{Q}_v = \begin{bmatrix} \mathbf{0}^{\mathrm{T}} & -2\bar{\boldsymbol{\omega}}^{i\mathrm{T}}\mathbf{I}_{\theta\theta}^{i}\dot{\bar{\mathbf{G}}}^{i} \end{bmatrix} \tag{3.74}$$

The vector of generalised applied force $\mathbf{Q}_e$ includes externally applied forces such as braking or traction forces, suspension forces, creep forces, and gravity forces but excludes the constraint forces which are automatically eliminated using the virtual work principle.

By combining Eq. (3.71) with Eq. (3.73), the augmented form of the system equation that contains generalised coordinates and non-generalised surface parameters can be finally written as (Shabana and Sany (2001)):

$$\begin{bmatrix} \mathbf{M} & \mathbf{0} & \mathbf{C}_{\mathbf{q}}^{\mathrm{T}} \\ \mathbf{0} & \mathbf{0} & \mathbf{C}_{\mathbf{s}}^{\mathrm{T}} \\ \mathbf{C}_{\mathbf{q}} & \mathbf{C}_{\mathbf{s}} & \mathbf{0} \end{bmatrix} \begin{bmatrix} \ddot{\mathbf{q}} \\ \ddot{\mathbf{s}} \\ \boldsymbol{\lambda} \end{bmatrix} = \begin{bmatrix} \mathbf{Q} \\ \mathbf{0} \\ \mathbf{Q}_d \end{bmatrix} \tag{3.75}$$

where

$$\mathbf{Q} = \mathbf{Q}_e + \mathbf{Q}_v \tag{3.76}$$

3.3. APPLICATION: WHEEL-RAIL CONTACT

As has been previously discussed, the main difficulty in the modelling of rail wagon track system dynamics is the formulation of the contact between the wheel and the rail. The complication of the problem arises due to the complex geometry of wheel and rail profiles and the non-linear creep forces generated by relative motion in the contact area. There are numerous references in the literature that have provided solutions to the wheel-rail contact problem (Matsudaira (1952), de Pater (1987), and Wickens (2003)). However, to make use of these solutions, detailed description of the kinematics of the wheelset and the rail are required. This includes the calculation of relative velocity between the wheel and the rail at the point of contact and the prediction of the location

and orientation of the contact point that are crucial in the formulation of the system equations of motion.

The contact problem formulation described in Section 3.2. is used to model the rolling contact dynamics between the wheel and the rail. This section discusses the determination of the wheel and the rail surfaces in the terms of surface parameters to be used in the formulation, the relation between surface parameters and the profiles of the wheel and the rail, contact parameters, normal contact force, contact area, and creep forces.

3.3.1. Parameterisation of the Wheel-Rail Contact Surfaces

It is very important to accurately predict the location and orientation of the point of contact between the wheel and the rail where the contact occurs. The first step in this task is to describe the location in space of all points on the surfaces of the wheel and the rail, where the contact may occur. This becomes difficult as the wheel and the rail surface profiles are usually complex in geometry and cannot be defined by simple analytical functions. However in general, the surface profiles of the wheel and the rail can be seen as being generated from two-dimensional curves as shown in Figs. 3.7 and 3.8 (for new wheels and rails with no localised damage) respectively.

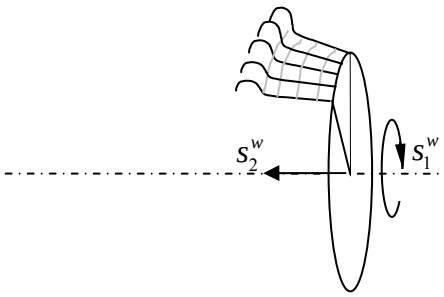

Figure 3.7. Wheel tread and flange surface

The wheel can be described as a surface obtained by rotating a two-dimensional curve that defines the wheel profile through 360 degrees about the wheel axis as shown in Fig. 3.7. The surface formed by such rotation can be defined by the following set of equations.

$$\left.\begin{aligned} x &= x_0 + r(s_2^w)\sin s_1^w \\ y &= y_0 + s_2^w \\ z &= z_0 - r(s_2^w)\cos s_1^w \end{aligned}\right\} \tag{3.77}$$

where s_1^w and s_2^w are the surface parameters of the wheel. In this case the parameter s_1^w represents the rotation about the wheel axis and the parameter s_2^w represents the translation in the lateral direction.

The surface of the rail can also be described by translating the two-dimensional curve that defines the rail profile in the longitudinal direction as shown in Fig. 3.8.

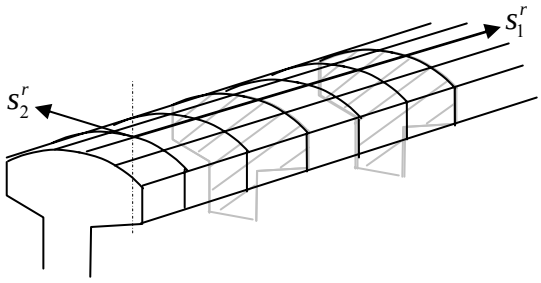

Figure 3.8. Rail head surface

In similar manner of describing the wheel profile, the rail surface profile can be defined by the following set of equations.

$$\left.\begin{aligned} x &= x_0 + s_1^r \\ y &= y_0 + s_2^r \\ z &= z_0 + f(s_2^r) \end{aligned}\right\} \tag{3.78}$$

where s_1^r is the surface parameter that represents the translation along the longitudinal axis and s_2^r is the surface parameter that represents the lateral translation.

3.3.2. Spline Representation of Wheel and Rail Profiles

From the Eq. (3.77) and Eq. (3.78) we know that to fully describe the 3D wheel and rail surface profiles, we require 2D functions of $r(s_2^w)$ and $f(s_2^r)$ that represent the wheel profile and the rail profile respectively. As it is difficult to write simple analytical expression, measured profiles are often given in the form of tables of data to describe the 2D profiles of wheel and rails.

In the kinematic and dynamic analyses of wheel-rail contact, second order time-derivatives of the contact constraint equations are required as shown in Eq. (3.72). This will lead to a term that contains third-order derivatives with respect to the non-generalised surface parameters (see Section 3.2.6). Thus, in order to accurately define the location of the contact points, an accurate description of derivatives of the position vectors of the contact point with respect to the surface parameter up to the third order is necessary. This also means that the interpolated profiles and their derivatives have to be continuous and smooth (no point of singularity) up to the third order differential. In this thesis the spline curve fitting method with smoothing process is used for this purpose. A spline function is basically a piecewise polynomial function (Boor (1978)) that can be easily differentiated or integrated.

To build a spline function, the data range is divided into a certain number of intervals and each interval is fitted with a polynomial function. These polynomial functions are constructed in such a way that, at the point of connection with the adjacent polynomial

functions there exists continuity of the defined functions and their first, second and third order derivatives. Putting all of these polynomial pieces together, one can form a smooth curve whose flexibility is strongly influenced by the number of intervals and distribution pattern of the data. To assure smoothness of the data profile up to the third derivatives, in this thesis fifth order polynomial functions have been used. The number of intervals and their distribution are also optimized. More details about spline curves can be found in Boor (1978) and hence are not repeated here.

3.3.3. Wheel-Rail Contact Parameters

In order to derive the equation of motion, the location of the contact points, the contact angle and radius of curvature at the contact points are required. All of these parameters are mainly affected by the profiles of the wheel tread and rail head as well as the lateral displacement and yaw of the wheelset. In many dynamic simulation packages, these parameters are calculated *prior* to the simulation and arranged in tables (known as "look-up" tables) as a function of wheelset lateral and yaw displacement. During the simulation, the data in these tables are interpolated based on the calculated lateral and yaw displacement of the wheelset at the current time step. For the tangent track simulations, where small yaw is expected, the effect of yaw is often ignored.

By using the contact constraint formulation as described in this section, all of these contact parameters are automatically calculated during the simulation process. Thus, prior kinematic calculation of contact parameters and table generation are not required. Although this approach could increase the computational time, any inaccuracy in interpolation of the tabulation method is eliminated.

The contact constraint formulation also allows calculation of the contact parameters independent of the dynamic simulation if required. This can be done by constraining all degrees of freedom and setting the lateral and yaw degrees of freedom as driving constraints. In this case the system of the wheelset and the rail should be regarded as kinematically driven systems, where the total number of constraint equations n_c is equal to the number of system coordinates n. The vector of the constraint equation of the kinematically driven system can then be written as:

$$\mathbf{C}(\mathbf{q},t) = \left[\mathbf{C}_1(\mathbf{q},t) \quad \mathbf{C}_2(\mathbf{q},t) \quad \mathbf{C}_n(\mathbf{q},t)\right]^{\mathrm{T}} = \mathbf{0} \tag{3.79}$$

The above equation contains n unknown coordinates with an equal number of equations. Therefore, the unknown coordinates

$$\mathbf{q} = \left[q_1 \quad q_2 \quad \ldots \quad q_n\right]^{\mathrm{T}}. \tag{3.80}$$

can be solved uniquely.

3.3.4. Normal Contact Force

The contact force that is developed normal to the common tangent plane of the contacting solids is known as the constraint force. Thus, like other constraints, the normal contact force can also be determined using the vector of the Lagrange multiplier $\boldsymbol{\lambda}$ (Eq. (3.75)). It can be shown that the vector of the Lagrange multiplier is equal to the negative of the reaction force vector.

$$\boldsymbol{\lambda} = -\mathbf{F}^k \tag{3.81}$$

The reaction force prevents only the penetration and the separation between the bodies in contact. Therefore the reaction force due to the contact point constraint is always referred in the normal direction and any relative motion between the bodies in the

direction of the tangent plane is not constrained. Thus, Eq. (3.75) can be used to determine the normal contact forces between the wheel and the rail; these forces are subsequently used to calculate the contact area and creep forces.

3.3.5. Contact Area

To calculate the creep forces, we require the shape and the size of the contact area. Using the Hertz's normal contact theory it can be proved that the contact area between the wheel and the rail is an ellipse (Johnson (1985)). To calculate the creep force, the size of the ellipse which is represented by its semi-axes has to be determined. The semi-axes are calculated using either a table of constants (Garg and Dukkipati (1984)) or direct method (de Pater et al. (1999)). In this thesis the direct method is used and described briefly in this section.

Consider a_e as the major (longitudinal) semi axis of the ellipse and b_e as the minor (lateral) semi-axis, then the geometric mean of a_e and b_e is defined as Eq. (3.82).

$$c = \sqrt{a_e b_e} \,. \tag{3.82}$$

Introducing ρ_x^r and ρ_y^r as the radius of curvature of the rail in the longitudinal and the lateral direction respectively, and ρ_x^w and ρ_y^w as the radius of curvature of the wheel in the longitudinal and the lateral direction as shown in Fig. 3.9, two constants A and B are defined as follows:

$$A = \frac{1}{2}\left(\frac{1}{\rho_x^r} + \frac{1}{\rho_x^w}\right), \quad B = \frac{1}{2}\left(\frac{1}{\rho_y^r} + \frac{1}{\rho_y^w}\right). \tag{3.83}$$

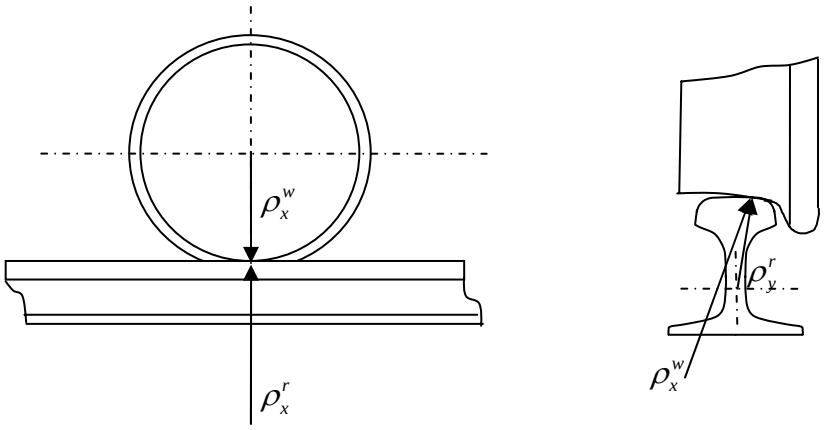

Figure 3.9. Principal Radius of Curvature of the Wheel and the Rail

Using these two constants, the effective radius of curvature is determined as

$$\rho = \frac{2}{(A+B)}. \tag{3.84}$$

Let the angle ($0 \le \alpha \le \frac{\pi}{2}$) be determined as

$$\alpha = \arccos\left(\frac{|A-B|}{A+B}\right) \tag{3.85}$$

According to Hertzian theory ((Johnson (1985), Kalker (1990)) we can derive equation for the quantity e^2 which determines the ratio between the semi-axes of the contact ellipse (mathematical detail can be found in de Pater et al. (1999)). The parameter e^2 is related to the ratio a_e / b_e of the ellipse semi-axes as follows:

$$a_e / b_e = \sqrt{1-e^2} \qquad \text{for } a_e \le b_e, \quad A \ge B \tag{3.86.a}$$

$$a_e / b_e = \frac{1}{\sqrt{1-e^2}} \qquad \text{for } a_e \ge b_e, \quad A \le B. \tag{3.86.b}$$

It is clear that a_e / b_e is independent of the value of the normal force at the contact point. The geometric mean c of the ellipse semi-axes as in Eq. (3.82) can be determined using the following relation:

$$c = \sqrt[3]{\frac{3N(1-\nu)\rho E}{4\pi G\sqrt{g}}} \tag{3.87}$$

where,

$$g = \sqrt{1-e^2}\ , \tag{3.88}$$

N is the normal force at the contact point,

G is the shear modulus and

ν is Poisson's ratio.

Thus, a_e and b_e can be determined by Eq. (3.82) and Eq. (3.86) depending on the value of the ratio A/B.

3.3.6. Creep Forces

The creep forces are calculated using Polach's method (Polach (1999)). Using this method the creep forces can be computed efficiently with significant saving in computational effort. As stated before, calculating the contact parameters as part of the process of dynamic simulation potentially could increase the computational time. However, Polach method's efficiency can help reduce any potential increase in computational time to a minimum. The effect of spin creepage is included in the calculation. The calculated values using this method are shown to be very close to the prediction of the exact theory.

Polach's method uses Hertz formulation for the calculation of the ellipsoidal contact area with semi-axes a_e, b_e and normal stress distribution. At an arbitrary point in the contact area, the maximum value of the tangential stress is defined by

$$\tau_{\max} = \mu\sigma \tag{3.89}$$

where μ is the coefficient of friction, which is assumed to be constant in the whole contact area, and σ is normal stress.

Fig. 3.10 shows the distribution of normal and tangential stress in the contact area according to the Polach's theory. The contact area is divided into two zones; the shaded area is the area of adhesion and the unshaded area is the area of slip.

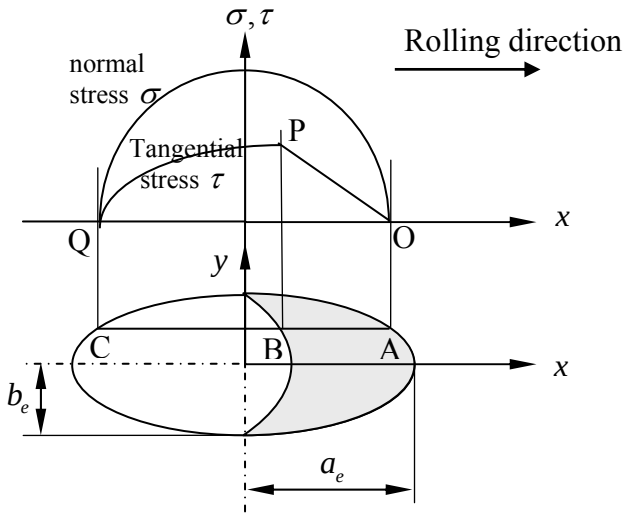

Figure 3.10. Distribution of normal and tangential stress according to Polach's theory

The formulation of the creep forces according to the Polach's theory assumes that, in the area of adhesion, the tangential stress is proportional to slip or creepage ξ and the distance from the leading edge. This means the larger the distance from the leading edge the larger the tangential stress as shown by the section OP of the tangential stress

curve in Fig. 3.10. The growth of the tangential stress in the area of adhesion is linear and the gradient of the tangential stress curve OP is formulated by Polach as

$$\varphi = \frac{2}{3}\frac{C\pi a_e^{\,2} b_e}{Q\mu}\xi \tag{3.90}$$

where Q is normal load and C is a proportionality constant, which is a value characterizing the contact elasticity of the body (tangential contact stiffness) that can be obtained from the Kalker's constant as

$$C = \frac{3}{8}\frac{G}{a_e}c_{jj} \tag{3.91}$$

where G is modulus of elasticity and c_{jj} is defined as

$$c_{jj} = \sqrt{\left(c_{11}\frac{\xi_x}{\xi_t}\right)^2 + \left(c_{22}\frac{\xi_y}{\xi_t}\right)^2} \tag{3.92}$$

where c_{11} and c_{22} are Kalker's constants and ξ_x and ξ_y are the components of the creepage in the x and y directions respectively and ξ is total the creepage given by

$$\xi_t = \sqrt{\xi_x^{\,2} + \xi_y^{\,2}}\,. \tag{3.93}$$

After substituting Eq. (3.91) into Eq. (3.90), the gradient of the tangential stress becomes

$$\varphi = \frac{1}{4}\frac{G\pi a_e b_e c_{jj}}{Q\mu}\nu \tag{3.94}$$

The tangential force (creep force) is then defined by

$$F = -\tau_0 \frac{4a_e b_e}{3}\left(\frac{\varphi}{1+\varphi^2} + \tan^{-1}\varphi\right) \tag{3.95}$$

where τ_0 is the maximum stress in the contact area.

From simple theory of friction,

$$\tau_0 = \mu\sigma_0 = \frac{3}{2}\frac{Q\mu}{\pi a_e b_e} \tag{3.96}$$

where σ_0 is maximum normal stress in the contact area.

By substituting Eq. (3.96) into Eq. (3.95) , we obtain

$$F = -\frac{2Q\mu}{\pi}\left(\frac{\varphi}{1+\varphi^2} + \tan^{-1}\varphi\right) \tag{3.97}$$

where the vector of the creep forces in the x and the y directions is calculated as

$$F_i = F\frac{\xi_i}{\xi_t} \quad , \quad (i = x, y) \tag{3.98}$$

Incorporation of spin

According to Polach's formulation, if spin is taken into account, then the creep force in the y direction becomes

$$F_{yc} = F_y + F_{ys} \tag{3.99}$$

where F_{ys} is the increase of creep force caused by the spin, that is

$$F_{ys} = -\frac{9}{16}a_e Q\mu K_m\left[1 + 6.3\left(1 - e^{-\frac{a}{b}}\right)\right]\frac{\xi_{sp}}{\xi_t} \tag{3.100}$$

where

$$K_m = |\varphi_s|\left(\frac{\delta^3}{3} - \frac{\delta^2}{2} + \frac{1}{6}\right) - \frac{1}{3}\sqrt{\left(1-\delta^2\right)^3} \tag{3.101}$$

$$\delta = \frac{\varphi_s^{\,2} - 1}{\varphi_s^{\,2} + 1} \tag{3.102}$$

$$\varphi_s = \frac{8}{3}\frac{Gb_e\sqrt{a_e b_e}}{Q\mu}\frac{c_{23}\xi_{yc}}{1 + 6.3\left(1 - e^{-\frac{a_e}{b_e}}\right)} \tag{3.103}$$

The total creepage is, therefore, defined as follows:

$$\xi_c = \sqrt{\xi_x^{\,2} + \xi_{yc}^{\,2}} \tag{3.104}$$

where

$$\xi_{yc} = \xi_y \quad for \quad \left|\xi_y + \xi_s a\right| \le \left|\xi_y\right| \tag{3.105a}$$

$$\xi_{yc} = \xi_y + \xi_s a \quad for \quad \left|\xi_y + \xi_s a\right| > \left|\xi_y\right| \tag{3.105b}$$

3.3.7. Flange Contact

The constraint contact formulation is strictly restricted to single point contact between two surfaces; for wheel-rail interaction, it is the contact point between the wheel tread surface and the rail head surface. However, another point of contact between the wheel flange and the gauge face of the railhead occurs when the wheel lateral displacement exceeds the clearance between the wheel flange and the gauge face of the railhead. To overcome the limitation of the constraint contact formulation in dealing with the flange contact in addition to the primary wheel thread – railhead top contact (two point contact), an additional lateral force term is introduced as shown in Eq. (3.106). The magnitude of the lateral force due to the flange contact is calculated as provided in the approximate formulation of Garg and Dukkipati (1984):

$$\begin{aligned} F_{flange} &= (y_w - y_f)\cdot k_{y\_rail}, \quad for \quad y_w > y_f \\ F_{flange} &= (y_w + y_f)\cdot k_{y\_rail}, \quad for \quad y_w < -y_f \end{aligned} \tag{3.106}$$

where y_w is the lateral displacement of the wheelset, y_f is the clearance, and k_{y_rail} is the lateral stiffness of the rail. It should be noted that the calculation of flange contact force approximately as above provide solution under two point contact. However, if the primary constraint of the wheel thread – rail top surface is lost, the algorithm will fail leading to abrupt termination of the simulation. In other words, the simulation could not proceed with the flange contact only and the constraint contact formulation will have to terminate indicating wheel-climb mechanism of derailment. Simulation in Chapter 9 of the thesis further illustrates this principle using numerical examples.

3.4. SOLUTION OF SYSTEM EQUATIONS

The dynamics of the multibody system is described by a set of differential and algebraic equations which are augmented in the total system equation of motion given by Eq. (3.75). To numerically solve this system equation, a technique proposed by Wehage (1980), which is called *Generalised Coordinate Partitioning Method*, is used in this thesis.

Because of the constraints, the components of the vectors of generalised coordinates $\mathbf{q}$ and the surface parameters $\mathbf{s}$ are not independent. Thus, we can write them in partitioned form as follows:

$$\mathbf{q} = \begin{bmatrix} \mathbf{q}_d^{\mathrm{T}} & \mathbf{q}_i^{\mathrm{T}} \end{bmatrix}^{\mathrm{T}} \tag{3.107}$$

and

$$\mathbf{s} = \begin{bmatrix} \mathbf{s}_d^{\mathrm{T}} & \mathbf{s}_i^{\mathrm{T}} \end{bmatrix}^{\mathrm{T}} \tag{3.108}$$

where $\mathbf{q}_d$ and $\mathbf{q}_i$ are, respectively, dependent and independent generalised coordinates, and $\mathbf{s}_d$ and $\mathbf{s}_i$ are, respectively, dependent and independent surface parameters. The

number of dependent generalised coordinates and the number of dependent surface parameters altogether is the same as the number of constraint equations.

For a virtual change in the system coordinates, the constraint equation of Eq. (3.66) forms

$$\mathbf{C}_{\mathbf{q}}\delta\mathbf{q}+\mathbf{C}_{\mathbf{s}}\delta\mathbf{s}=0 \tag{3.109}$$

Then applying the coordinate partitioning of Eq. (3.107) and Eq. (3.108), we can write

$$\mathbf{C}_{\mathbf{q}_d}\delta\mathbf{q}_d+\mathbf{C}_{\mathbf{q}_i}\delta\mathbf{q}_i+\mathbf{C}_{\mathbf{s}_d}\delta\mathbf{s}_d+\mathbf{C}_{\mathbf{s}_i}\delta\mathbf{s}_i=0 \tag{3.110}$$

In matrix form Eq. (3.110) can be rewritten as

$$\begin{bmatrix}\mathbf{C}_{\mathbf{q}_d} & \mathbf{C}_{\mathbf{s}_d}\end{bmatrix}\begin{bmatrix}\delta\mathbf{q}_d\\ \delta\mathbf{s}_d\end{bmatrix}+\begin{bmatrix}\mathbf{C}_{\mathbf{q}_i} & \mathbf{C}_{\mathbf{s}_i}\end{bmatrix}\begin{bmatrix}\delta\mathbf{q}_i\\ \delta\mathbf{s}_i\end{bmatrix}=0 \tag{3.111}$$

Because the total number of dependent generalised coordinates and the number of dependent surface parameters altogether is the same as the number of constraint equations n_c, and the constraint equations are assumed to be linearly independent, the matrix $\begin{bmatrix}\mathbf{C}_{\mathbf{q}_d} & \mathbf{C}_{\mathbf{s}_d}\end{bmatrix}$ is square of size $n_c \times n_c$ and is non-singular. Consequently $\begin{bmatrix}\mathbf{C}_{\mathbf{q}_i} & \mathbf{C}_{\mathbf{s}_i}\end{bmatrix}$ is a matrix of size $n_c \times (n-n_c)$. Eq. (3.111) therefore can be rewritten as

$$\begin{bmatrix}\delta\mathbf{q}_d\\ \delta\mathbf{s}_d\end{bmatrix}=\begin{bmatrix}\mathbf{C}_{\mathbf{q}_d} & \mathbf{C}_{\mathbf{s}_d}\end{bmatrix}^{-1}\begin{bmatrix}\mathbf{C}_{\mathbf{q}_i} & \mathbf{C}_{\mathbf{s}_i}\end{bmatrix}\begin{bmatrix}\delta\mathbf{q}_i\\ \delta\mathbf{s}_i\end{bmatrix} \tag{3.112}$$

or in further simplified form,

$$\begin{bmatrix}\delta\mathbf{q}_d\\ \delta\mathbf{s}_d\end{bmatrix}=\mathbf{C}_{di}\begin{bmatrix}\delta\mathbf{q}_i\\ \delta\mathbf{s}_i\end{bmatrix} \tag{3.113}$$

where

$$\mathbf{C}_{di}=\begin{bmatrix}\mathbf{C}_{\mathbf{q}_d} & \mathbf{C}_{\mathbf{s}_d}\end{bmatrix}^{-1}\begin{bmatrix}\mathbf{C}_{\mathbf{q}_i} & \mathbf{C}_{\mathbf{s}_i}\end{bmatrix} \tag{3.114}$$

Eq. (3.113) implies that the virtual change in the dependent coordinates can be written in terms of the virtual change of the independent coordinates.

In a similar manner, the first derivatives of the constraint equation with respect to time can also be written as

$$\begin{bmatrix}\mathbf{C}_{\mathbf{q}_d} & \mathbf{C}_{\mathbf{s}_d}\end{bmatrix}\begin{bmatrix}\dot{\mathbf{q}}_d \\ \dot{\mathbf{s}}_d\end{bmatrix}+\begin{bmatrix}\mathbf{C}_{\mathbf{q}_i} & \mathbf{C}_{\mathbf{s}_i}\end{bmatrix}\begin{bmatrix}\dot{\mathbf{q}}_i \\ \dot{\mathbf{s}}_i\end{bmatrix}+\mathbf{C}_t=0 \tag{3.115}$$

Using this equation, the dependent velocities can be written in terms of the independent velocities as

$$\begin{bmatrix}\dot{\mathbf{q}}_d \\ \dot{\mathbf{s}}_d\end{bmatrix}=\mathbf{C}_{di}\begin{bmatrix}\dot{\mathbf{q}}_i \\ \dot{\mathbf{s}}_i\end{bmatrix}+\begin{bmatrix}\mathbf{C}_{\mathbf{q}_d} & \mathbf{C}_{\mathbf{s}_d}\end{bmatrix}^{-1}\mathbf{C}_t \tag{3.116}$$

The independent and dependent sets of coordinates are identified by using Gaussian elimination (Strang (1980)). Having identified the independent and dependent sets of coordinates the following state vector may be defined.

$$\mathbf{y}=\begin{bmatrix}\mathbf{q}_i^{\mathrm{T}} & \mathbf{s}_i^{\mathrm{T}} & \dot{\mathbf{q}}_i^{\mathrm{T}} & \dot{\mathbf{s}}_i^{\mathrm{T}}\end{bmatrix}^{\mathrm{T}} \tag{3.117}$$

This allows us to define the associated independent state equation as

$$\dot{\mathbf{y}}=\begin{bmatrix}\dot{\mathbf{q}}_i^{\mathrm{T}} & \dot{\mathbf{s}}_i^{\mathrm{T}} & \ddot{\mathbf{q}}_i^{\mathrm{T}} & \ddot{\mathbf{s}}_i^{\mathrm{T}}\end{bmatrix}^{\mathrm{T}}=\mathbf{g}\left(\mathbf{q},\dot{\mathbf{q}},\mathbf{s},\dot{\mathbf{s}},t\right) \tag{3.118}$$

By providing a set of initial conditions, the state equations can be integrated forward in time using a direct numerical integration method such as the Runge-Kutta method. More details on the numerical method in multibody dynamics can be found in Eich-Sollner and Fuhrer (1998) and Shabana (2001). The solution of the state equation

defines the independent coordinates and velocities as well as the independent surface parameters and their first derivatives. Then the dependent coordinates and surface parameters are determined using the kinematic relation of the constraint equations, while the dependent velocities and the first derivatives of dependent surface parameters are determined using Eq. (3.116). The independent and dependent accelerations as well as the second time derivatives of the surface parameters are determined from the solution of Eq. (3.79).

3.4.1. Solution of the Non-linear Algebraic Constraint Equation

It has been described previously that the dependent coordinates are determined using the kinematic relation which is defined by constraint equations. For the contact constraint equations which are nonlinear, the system of algebraic equations is solved by using the iterative procedure of Newton-Raphson algorithm. The procedure is started by assuming a desired solution vector which is close enough to the exact solution. If the assumed solution is denoted as $\mathbf{q}_{d_k}$ and $\mathbf{s}_{d_k}$ for the dependent generalised coordinates and dependent surface parameters respectively, we can write the exact solution as $\mathbf{q}_{d_k} + \Delta\mathbf{q}_{d_k}$ and $\mathbf{s}_{d_k} + \Delta\mathbf{s}_{d_k}$. According to the Taylor's theorem (Riley et al. (2002)), the vector of constraint equations defined in Eq. (3.66) can then be written as Eq. (3.119).

$$\begin{aligned}\mathbf{C}(\mathbf{q}_{d_k} + \Delta\mathbf{q}_{d_k}, \mathbf{s}_{d_k} + \Delta\mathbf{s}_{d_k}, t) = \mathbf{C}(\mathbf{q}_{d_k}, \mathbf{s}_{d_k}, t) + \begin{bmatrix} \mathbf{C}_{\mathbf{q}_{dk}} & \mathbf{C}_{\mathbf{s}_{dk}} \end{bmatrix} \begin{bmatrix} \Delta\mathbf{q}_{d_k} \\ \Delta\mathbf{s}_{d_k} \end{bmatrix} \\ + \frac{1}{2} \begin{bmatrix} (\mathbf{C}_{\mathbf{q}_{dk}} \Delta\mathbf{q}_{d_k})_{\mathbf{q}_{dk}} & (\mathbf{C}_{\mathbf{s}_{dk}} \Delta\mathbf{s}_{d_k})_{\mathbf{s}_{dk}} \end{bmatrix} \begin{bmatrix} \Delta\mathbf{q}_{d_k} \\ \Delta\mathbf{s}_{d_k} \end{bmatrix} + \ldots\end{aligned} \tag{3.119}$$

where vectors $\Delta\mathbf{q}_{d_k}$ and $\Delta\mathbf{s}_{d_k}$ are called vectors of Newton differences.

Because we assume that the vectors $\mathbf{q}_{d_k}+\Delta\mathbf{q}_{d_k}$ and $\mathbf{s}_{d_k}+\Delta\mathbf{s}_{d_k}$ are the exact solution, $\mathbf{C}(\mathbf{q}_{d_k}+\Delta\mathbf{q}_{d_k},\mathbf{s}_{d_k}+\Delta\mathbf{s}_{d_k},t)=0$, and Eq. (3.119) reduces to

$$\begin{aligned}&\mathbf{C}(\mathbf{q}_{d_k},\mathbf{s}_{d_k},t)+\begin{bmatrix}\mathbf{C}_{\mathbf{q}_{d_k}} & \mathbf{C}_{\mathbf{s}_{d_k}}\end{bmatrix}\begin{bmatrix}\Delta\mathbf{q}_{d_k}\\ \Delta\mathbf{s}_{d_k}\end{bmatrix}\\ &+\frac{1}{2}\begin{bmatrix}(\mathbf{C}_{\mathbf{q}_{d_k}}\Delta\mathbf{q}_{d_k})_{\mathbf{q}_{d_k}} & (\mathbf{C}_{\mathbf{s}_{d_k}}\Delta\mathbf{s}_{d_k})_{\mathbf{s}_{d_k}}\end{bmatrix}\begin{bmatrix}\Delta\mathbf{q}_{d_k}\\ \Delta\mathbf{s}_{d_k}\end{bmatrix}+\ldots=0\end{aligned} \tag{3.120}$$

The higher order term in Eq. (3.120) can be neglected if $\Delta\mathbf{q}_{d_k}$ and $\Delta\mathbf{s}_{d_k}$ are small. In this case we can write the first order approximation of Eq. (3.120) as

$$\mathbf{C}(\mathbf{q}_{d_k},\mathbf{s}_{d_k},t)+\begin{bmatrix}\mathbf{C}_{\mathbf{q}_{d_k}} & \mathbf{C}_{\mathbf{s}_{d_k}}\end{bmatrix}\begin{bmatrix}\Delta\mathbf{q}_{d_k}\\ \Delta\mathbf{s}_{d_k}\end{bmatrix}\approx 0 \tag{3.121}$$

which yields

$$\mathbf{C}(\mathbf{q}_{d_k},\mathbf{s}_{d_k},t)=-\begin{bmatrix}\mathbf{C}_{\mathbf{q}_{d_k}} & \mathbf{C}_{\mathbf{s}_{d_k}}\end{bmatrix}\begin{bmatrix}\Delta\mathbf{q}_{d_k}\\ \Delta\mathbf{s}_{d_k}\end{bmatrix} \tag{3.122}$$

Since the dependent and independent coordinates have been partitioned and the constraint equations are assumed to be linearly independent, the Jacobian matrix $\begin{bmatrix}\mathbf{C}_{\mathbf{q}_{d_k}} & \mathbf{C}_{\mathbf{s}_{d_k}}\end{bmatrix}$ will be a square non-singular matrix. Thus, we can solve Eq. (3.122) for the vectors of Newton differences $\Delta\mathbf{q}_{d_k}$ and $\Delta\mathbf{s}_{d_k}$ which can be used to iteratively update the vectors of system coordinates as

$$\left.\begin{aligned}\mathbf{q}_{d_{k+1}} &= \mathbf{q}_{d_k} + \Delta\mathbf{q}_{d_k} \\ \mathbf{s}_{d_{k+1}} &= \mathbf{s}_{d_k} + \Delta\mathbf{s}_{d_k}\end{aligned}\right\} \tag{3.123}$$

where k is the iteration number. This updated vector of system coordinates is then used to reconstruct Eq. (3.121) and solve the system of equations for the new vector of Newton-differences $\Delta\mathbf{q}_{d_{k+1}}$ and $\Delta\mathbf{s}_{d_{k+1}}$ which can be used again to update the vectors of system coordinates $\mathbf{q}_{d_{k+2}}$ and $\mathbf{s}_{d_{k+2}}$. This process is repeated until the norm of the Newton-differences vector or the norm of the constraint equations vector becomes less than a specified tolerance, that is,

$$\left\| \begin{bmatrix} \Delta\mathbf{q}_{d_k}^{\mathrm{T}} & \Delta\mathbf{s}_{d_k}^{\mathrm{T}} \end{bmatrix}^{\mathrm{T}} \right\| < \varepsilon_1 \quad \text{or} \quad \left\| \mathbf{C}(\mathbf{q}_{d_k}, \mathbf{s}_{d_k}, t) \right\| < \varepsilon_2 \tag{3.124}$$

where ε_1 and ε_2 are specified tolerances and k is the iteration number.

3.5. ALGORITHM FOR RAILWAY BOGIE DYNAMIC ANALYSIS

In the preceding sections, detailed formulation of the multi-body system dynamics equations has been presented with a view to building the railway bogie dynamics model. The equations of motion which involve the independent coordinates are solved using direct integration with respect to time. The dependent coordinates and the dependent surface parameters are calculated by solving the algebraic constraint equation using the Newton-Rhapson algorithm. The application of the formulation to the modelling of railway bogie dynamics is presented in a flowchart shown in Fig. 3.11. The referenced sections for each step are also given in the flow chart.

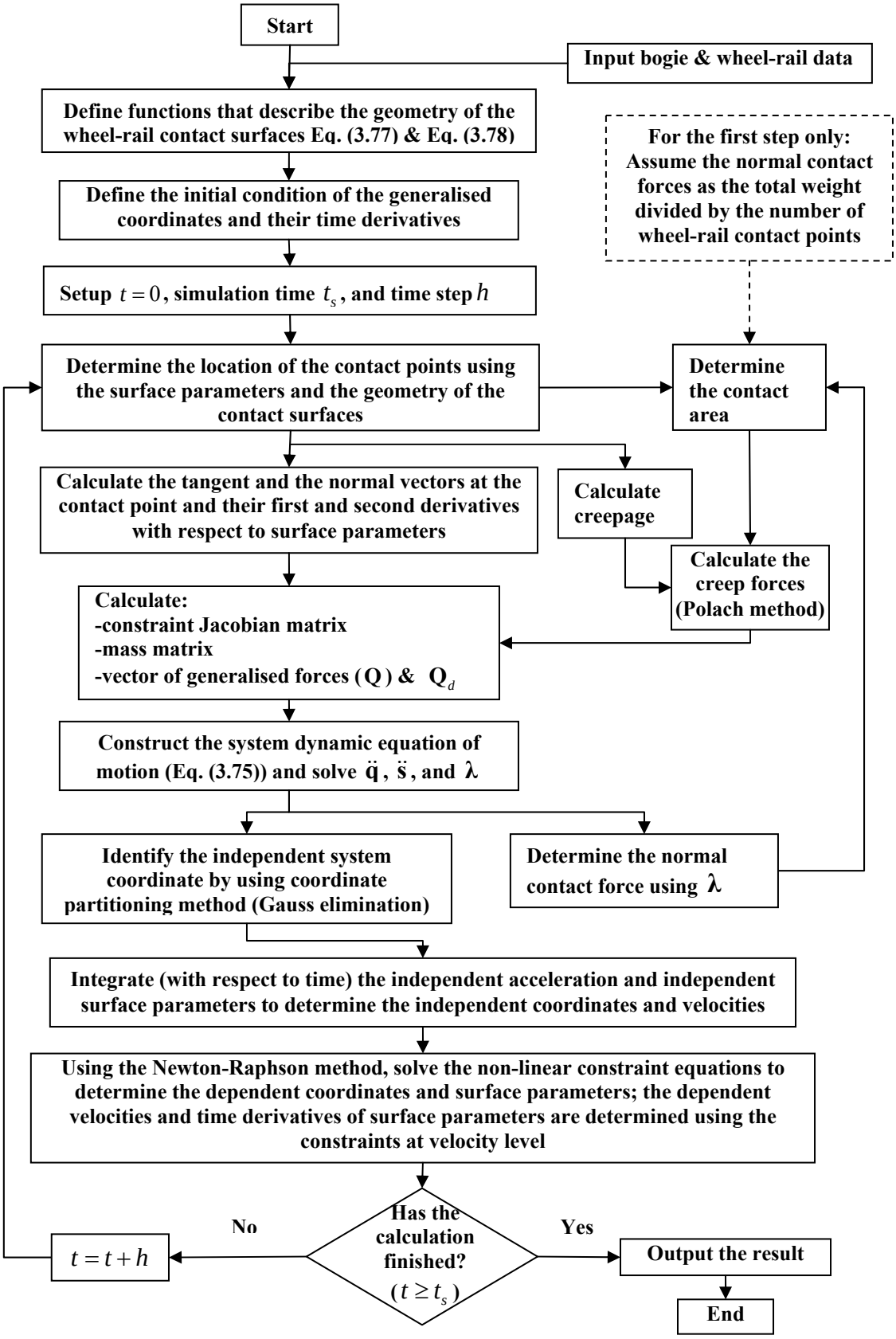

Figure 3.11. Flow chart of railway bogie dynamic analysis

4. DYNAMICS OF A WHEELSET WITHIN A BOGIE FRAME

4.1. INTRODUCTION

Using the inertial reference frame (IRF) modelling platform described in Chapter 3, a computer program for the simulation of the dynamics of wheelsets within a bogie frame is developed and reported in this chapter. The program is named the Rail Bogie Dynamics (RBD) program for convenience. The RBD program is currently developed in MATLAB environment. The limited size of the problem solved as part of this thesis has never posed problems related to computational time; if that becomes a serious issue, the algorithm based on the formulation provided in Chapter 3 could be programmed in alternate languages such as FORTRAN or C++.

First the RBD program has been used to examine the dynamics of railway wheelsets as these are the basic units that provide guidance for the wagon on the track. The wheelset is assembled with the suspension system to provide stability whilst they are at rest and in motion. The assemblages are known as bogies. The bogies of locomotives usually have three wheelsets each, whilst the bogies of the wagons and passenger cars have two wheelsets each. Some utility wagons containing single wheelset bogies are also used in the industry.

Irrespective of the design of the bogie system, the stability of wagons in motion is largely dictated by the dynamics of the wheelset within the bogie frame (Wickens (2003)). Therefore a very simple form of a bogie system containing a single wheelset within a bogie frame is considered for the examination of its dynamics using the RBD program. First the dynamics of this assembly has been investigated under the steady-

state (constant speed) condition using the RBD program and the results validated against a commercial software package VAMPIRE (Evans (1999)). Second, the RBD program has been used to simulate the effect of longitudinal braking and traction torques to the dynamics of the simple bogie. This chapter reports the process and results of these analyses.

4.2. DESCRIPTION OF MODELLED SYSTEM

In order to understand the railway wagon dynamics, it is common to investigate the motion of a single wheelset running on the track. However, in actual condition, the wheelset is attached to a bogie frame that restricts its motion. Therefore, in this investigation the wheelset is connected to a mass, which represents the sprung mass of the bogie frame or the wagon body. The connection is formed by a set of linear springs and dampers in the longitudinal, the lateral, and the vertical directions as shown in Fig. 4.1. The lateral distance between the right and the left suspension was 0.7 m. The characteristics of the springs and dampers are presented in Table 4.1. The characteristics of the springs and dampers have been optimized in such a way that the bogie is stable up to 25 m/s (90 km/h). As a reference, the critical speed of wagons containing three-pieces bogies running on the rigid track calculated by Sun (2002) is in the range between 79 km/h – 159 km/h, depending on the wheel profile and wheel radius being used. The inertia properties of the wheelset and the bogie frame used in the simulation are given in Table 4.2. The mass and moment of inertia of the bogie frame is chosen so that the axle load represents the axle load of the common normal operation of four axle wagons.

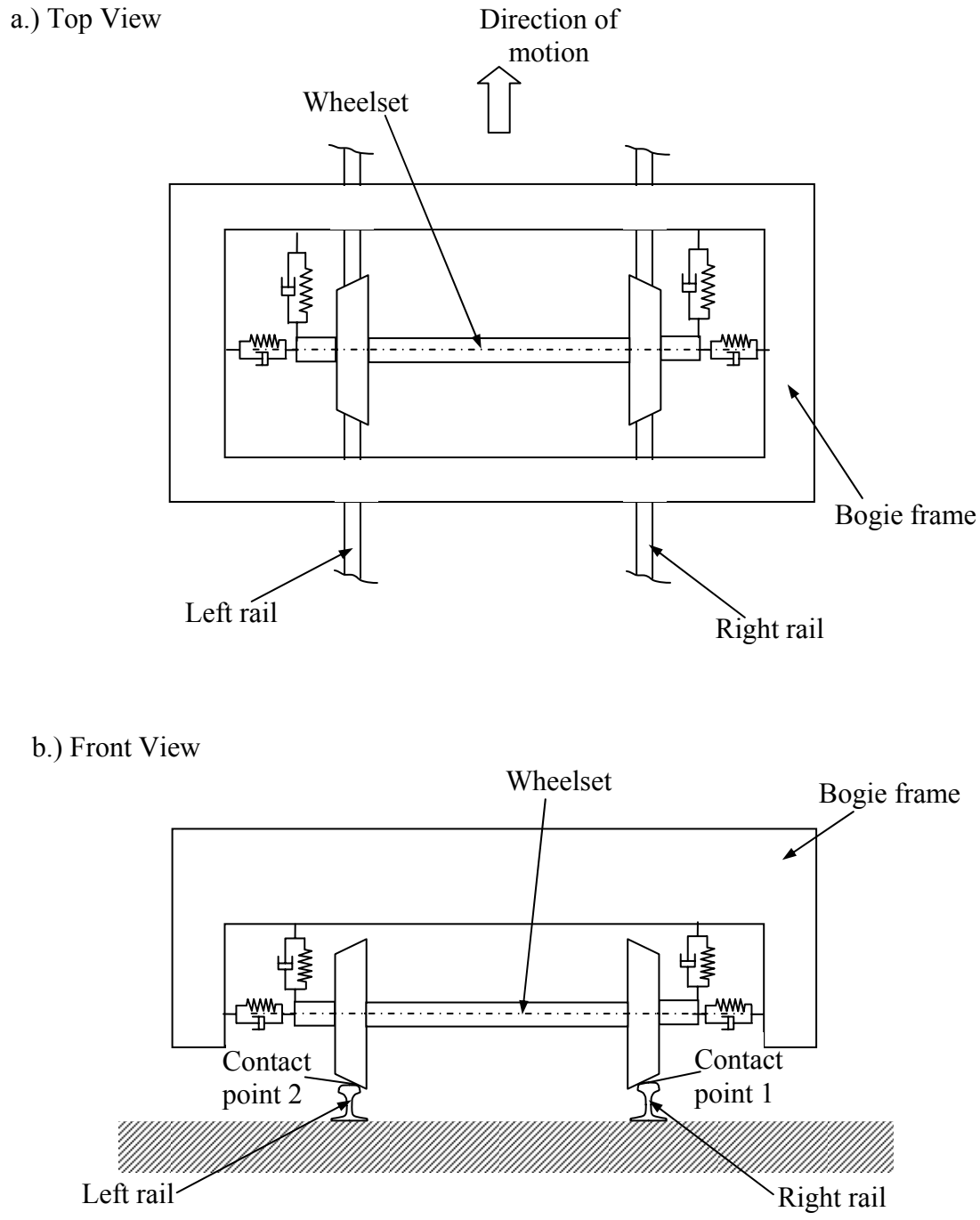

Figure 4.1. A wheelset within a bogie frame

Because the bogie frame is supported only by two vertical springs (on the left and the right), an unbalanced moment with respect to the lateral axis will act on the bogie frame. In anticipation of this, a constraint is added so that the pitch degree of freedom

of the bogie frame is eliminated. Therefore the bogie frame is represented with five degrees of freedom only. The springs and dampers are attached to the wheelset at the points on the rotation axis of the axle (lateral axis of wheelset body reference frame). By using such an arrangement the points of connection do not rotate about the axle so the additional revolute joint is not needed.

Table 4.1. Spring and damper characteristics

	Spring Stiffness , K (N/m)	Damping Coefficient, C (N.s/m)
Longitudinal	20×10^4	10×10^3
Lateral	8×10^4	6×10^3
Vertical	5×10^4	4×10^3

Table 4.2. Inertia properties of the wheelset and the sprung mass

	Wheelset	Sprung Mass
Mass (kg)	1200	10000
Mass moment of inertia I_{xx} ($\mathrm{kg \cdot m^2}$)	720	20000
Mass moment of inertia I_{yy} ($\mathrm{kg \cdot m^2}$)	112	15000
Mass moment of inertia I_{zz} ($\mathrm{kg \cdot m^2}$)	720	20000

For generalisation, the left and the right rails are considered as separate bodies constrained to the ground. Thus, the total number of bodies in the system is four (the right rail, the left rail, wheelset and bogie frame). With this assumption it is possible to

simulate different lateral and vertical irregularities for each rail and also track gauge widening at the curve where the outer and inner rails each have a different curve radius. In spite of these opportunities, this thesis has neither considered the rail geometry irregularity nor other defects due to its primary focus on the effect of longitudinal forces to wheelset / bogie dynamics.

All the bodies involved are assumed as rigid with the body reference frames attached to their respective centres of mass. The motion of each body's local coordinate system with respect to the global system is described in the multibody formulation using three translational coordinates and four Euler parameters. For the system containing four rigid bodies, the vector of generalised coordinates is written as

$$\mathbf{q} = \begin{bmatrix} \mathbf{q}^{rr} & \mathbf{q}^{rl} & \mathbf{q}^{ws} & \mathbf{q}^{bf} \end{bmatrix}^{\mathrm{T}} \tag{4.1}$$

where $\mathbf{q}^{rr}, \mathbf{q}^{rl}, \mathbf{q}^{ws}, \mathbf{q}^{bf}$ are vectors of generalised coordinates of the right rail, the left rail, the wheelset and the bogie frame respectively. As the vector of the generalised coordinates of each body has seven components (three translational coordinates and four Euler parameters) the total vector coordinates will have a total of 28 components.

The vector of the non-generalised surface parameters is written as

$$\mathbf{s} = \begin{bmatrix} \mathbf{s}_1^{rr} & \mathbf{s}_2^{rl} & \mathbf{s}_1^{ws} & \mathbf{s}_2^{ws} \end{bmatrix}^{\mathrm{T}} \tag{4.2}$$

where each superscript represents a body as described in Eq. (4.1) and the subscript represents the number of each contact point (contact point 1 is located at the right wheel-rail patch and contact point 2 is located at the left wheel-rail patch; see Fig. 4.1). Because each contact surface is represent by two surface parameters, vectors of non-

generalised surface parameters in Eq. (4.2) will have eight components. Thus, the vectors of the generalised and the non-generalised coordinates will have 36 components in total.

Inducing four Euler parameter constraints (one for each body), ten contact constraints, twelve ground constraints, and one constraint of the bogie frame pitching, there will be a total of 27 constraint equations and hence there will be nine (36-27=9) unrestrained degrees of freedom. The 27 constraint equations also imply that the size of the sub-Jacobian matrix $\mathbf{C}_\mathbf{q}$ is 27×28 and the size of the sub-Jacobian matrix $\mathbf{C}_\mathbf{s}$ is 27×8. Hence, the total dimension of the augmented matrix of the mass matrices and sub-Jacobian matrices in Eq. (3.75) is 63×63. For the constant speed simulation a velocity constraint in the longitudinal direction is added, which increases the dimension of the augmented matrix to 64×64 and reduces the unrestrained degrees of freedom to eight.

4.3. WHEEL AND RAIL PROFILES

The wheel and the rail profile used in the simulation are shown in Fig. 4.2. AS 60 kg/m plain carbon rail and LW2 wheel profile in new condition are considered. Both profiles are taken from Queensland Rail (QR) data. The method of formulation of the wheel rail contact in the RBD program demands the derivatives of the spline representation of the wheel and the rail profile up to the third order. Therefore, fifth- order splines have been selected. For this purpose spline curves that represents the wheel and the rail profile are generated from the measured data points by using Spline2 V6.0 software developed by Delft University of Technology (Thijse (2002)).

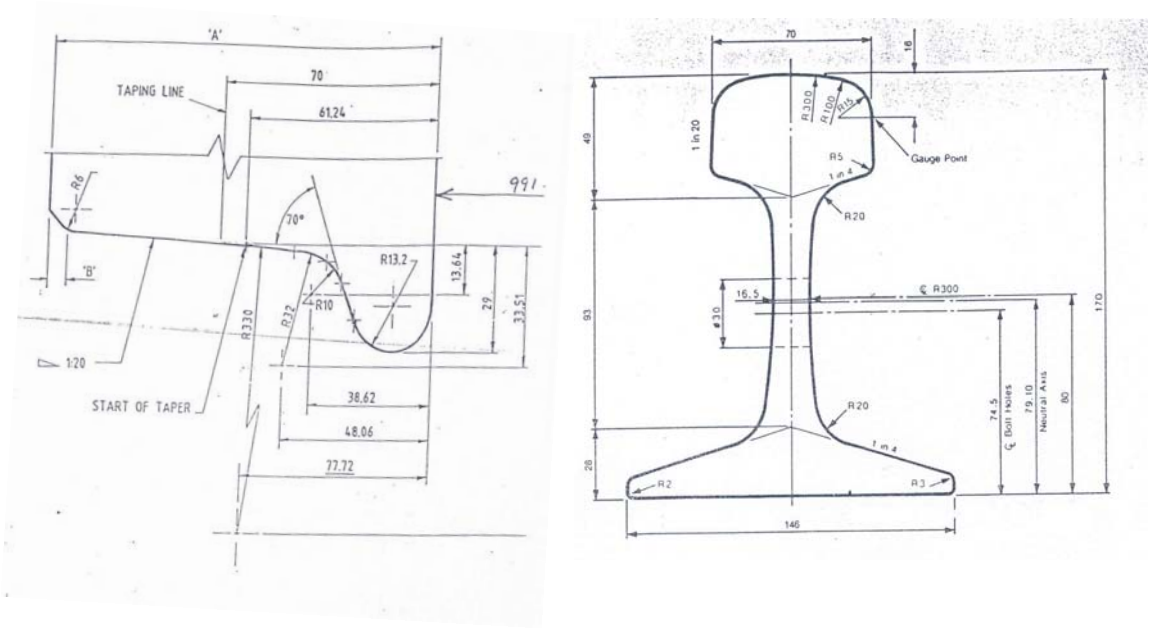

(a) wheel profile (b) rail profile

Figure 4.2. Technical drawing of the wheel and the rail profile

Fig. 4.3 shows the spline representation of the wheel profile which is generated using a fifth-order polynomial. The spline curve covered the profile of the wheel tread up to the flange tip.

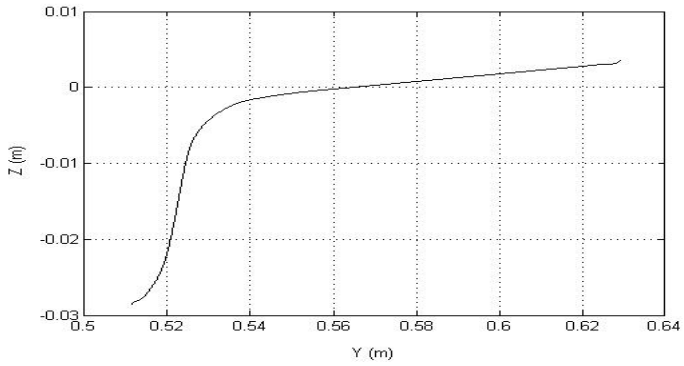

Figure 4.3. Spline curve of the wheel profile

Fig. 4.4 shows the 1st , 2nd , and 3rd derivatives of the wheel profile. From the figures we can see that the smooth (i.e. no point of singularity) and continuous curves are obtained until the third derivatives. Such continuous and smooth curves are required for

improving the accuracy and also to avoid numerical instability during the solution phase of the simulation.

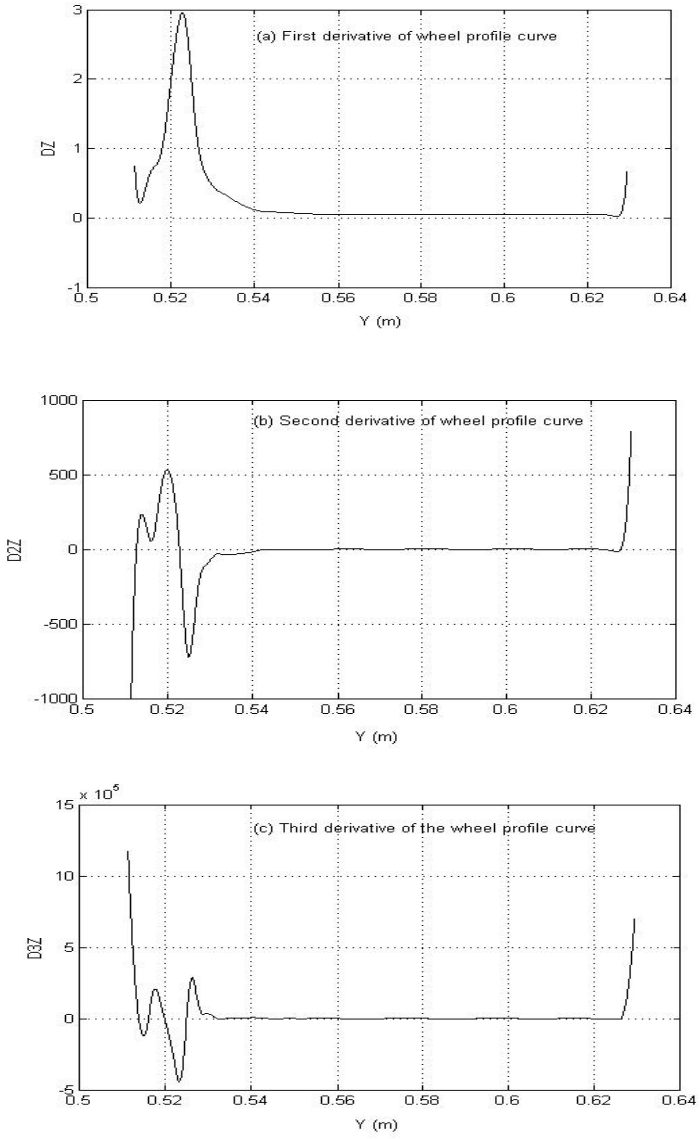

Figure 4.4. Derivatives of the wheel profile curve

Rails are normally fitted to the track containing concrete sleepers with 1 in 20 inclination (Esveld (2001)). Fig. 4.5 shows the spline representation of the rail profile with 1 in 20 inclination and Fig. 4.6 shows its first three derivatives; all function are seen to be continuous and smooth. Similar to the wheel profile spline, the rail profile spline was also generated using a fifth-order polynomial.

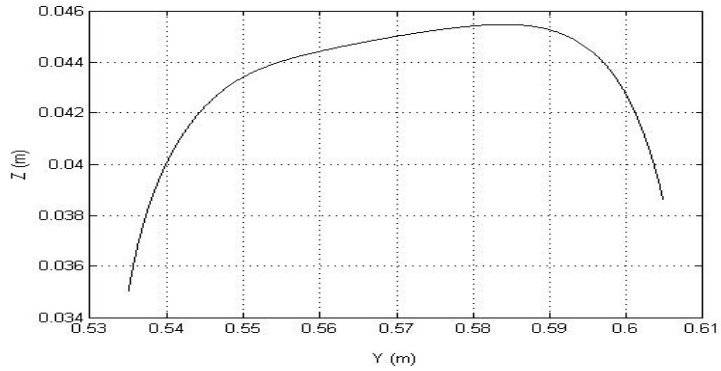

Figure 4.5. Spline curve of the rail profile

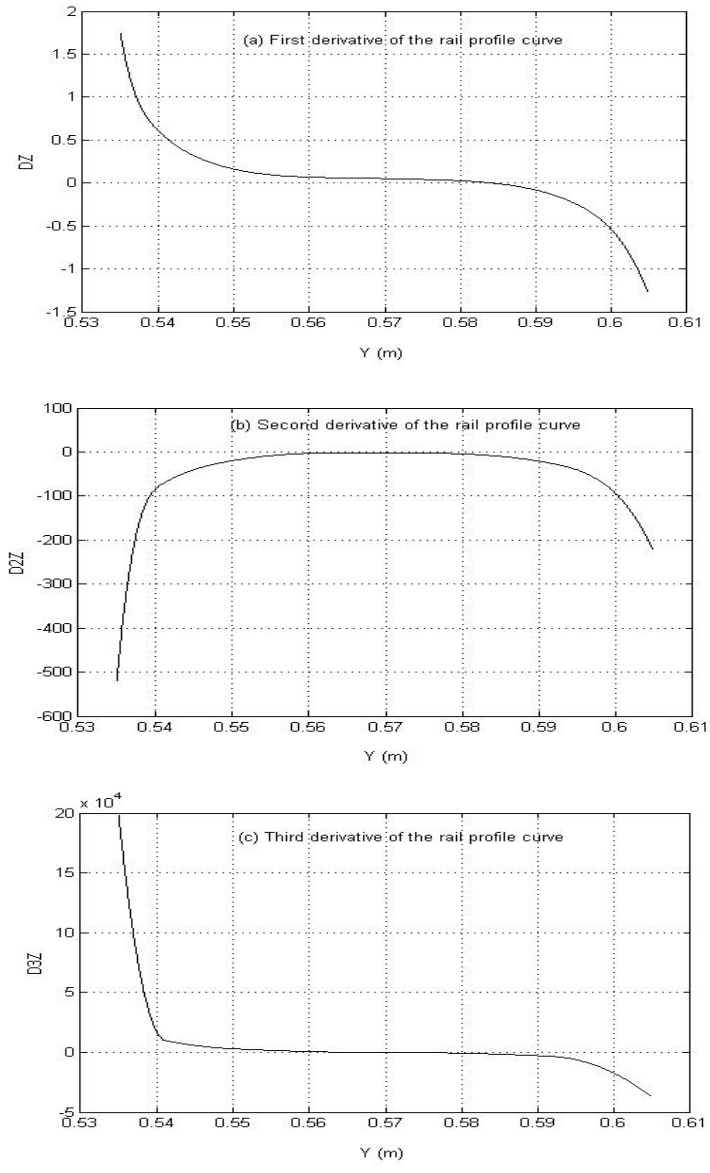

Figure 4.6. Derivatives of the wheel profile curve

Placing the wheelset on the centre of narrow gauge track (1067mm) and applying the law of contact between rigid bodies, the contact point between wheels and rails could be found as shown in Fig. 4.7. The nominal distance between the left and the right contact points was 1140 mm.

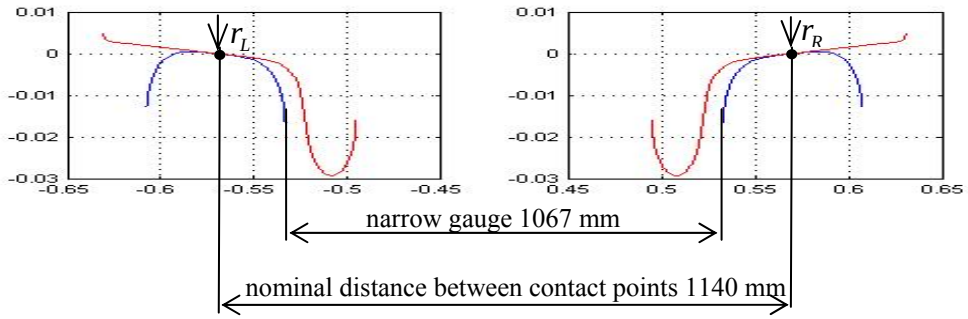

Figure 4.7. Wheelset on narrow gauge track

In the centre position the rolling radius of the right wheel and the left rail are equal ($r_R = r_L = r_w =$ *nominal radius*). Shifting the wheelset to the left and/or to the right causes differences between the rolling radius of the right and the left wheels. The rolling radius difference between the right and the left wheels is the important parameter that defines the wheelset dynamics. This parameter is plotted in Fig. 4.8. The figure reveals that the change of rolling radius difference was linear until flange contact occurred at approximately 9.5 mm lateral shifting of the wheelset.

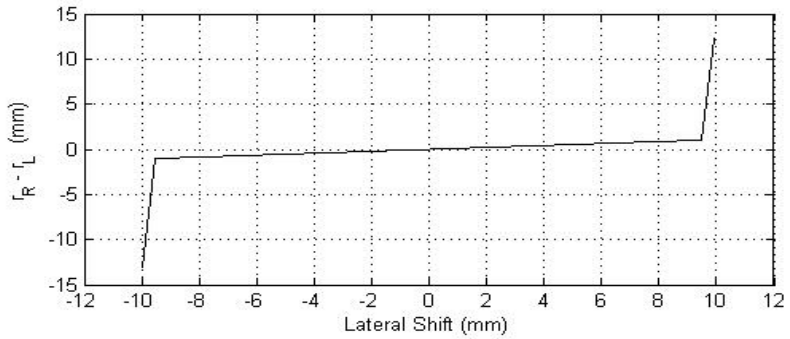

Figure 4.8. Rolling radius difference

4.4. SIMULATION AT CONSTANT SPEED

The results of the simulation using the RBD program are compared with that of VAMPIRE which is used by many railway wagon manufacturers and operators to investigate the dynamics of railway wagons in the design and operational phases (AEA Technology Rail (2004)). VAMPIRE uses the TFR coordinate system that moves at a pre-defined speed along the track and does not explicitly account for the wheelset pitch (AEA Technology Rail (2003)). These are the major difference between VAMPIRE and the RBD program. The other difference is that VAMPIRE calculates all the contact parameters (angle and radius) separately prior to the simulation and interpolates them during simulation, whilst the RBD program calculates these parameters using the contact law algorithm (see Section 3.2.5) in every time step of the simulation.

The cases that were simulated included the system of a wheelset and a bogie frame travelling on a tangent track with specified constant forward velocities. At a specified distance of travel a lateral disturbance in the form of track lateral displacement was provided to the wheelset to initiate lateral oscillation. The coefficient of friction between the wheel and the rail was assumed to be 0.3 in all cases of simulation. To gain a comprehensive view on the results, simulations were carried out with various velocities, starting from the low speed where the wheelset motion remained stable to the high speed where the wheelset motion became unstable. Some important results of the simulation at three selected velocities of 15 m/s, 25 m/s, and 30 m/s are presented in this chapter.

Fig. 4.9 shows the lateral displacement against the travel distance of the wheelset and bogie frame at 15 m/s. The result presented in this figure is obtained using the RBD program. From the figure it can be seen that the wheelset and the bogie frame have had

damped lateral oscillations. The decrement of the wheelset oscillation shows a high damping ratio. The oscillations have a 13.25 m wavelength; for the speed of 15 m/s, this wavelength is associated with a frequency of 1.13 Hz. The oscillation of the bogie frame follows the wheelset oscillation with the same wavelength but with almost 180^{o} phase lag due to the existence of the spring and damper system.

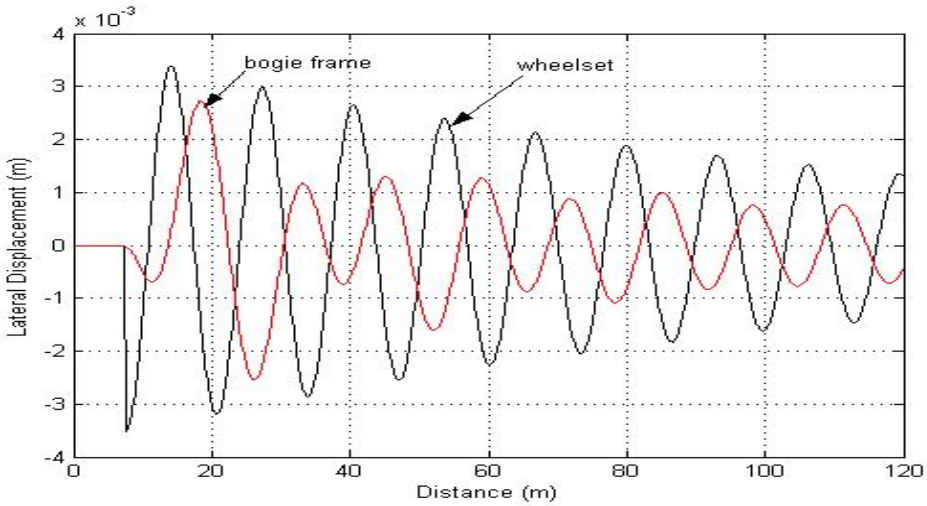

Figure 4.9. Lateral displacements - RBD Program at V=15 m/s

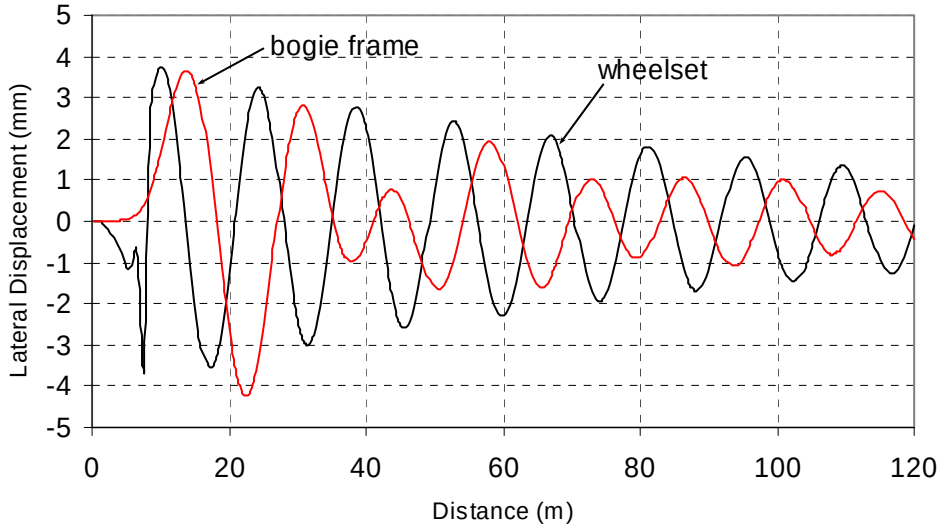

Figure 4.10. Lateral displacement - VAMPIRE at V=15m/s

Fig. 4.10 exhibits the lateral displacement of the wheelset and bogie frame simulated by VAMPIRE for the speed of 15 m/s. This figure shows, in general, the same trend and magnitudes as that provided by the RBD program presented in Fig. 4.9. The oscillation of the bogie frame shows a similar lag of about 180^{o} phase difference compared to the wheelset oscillation. The wheelset and the bogie motions are also damped well. However the wavelength of the oscillation calculated by VAMPIRE is 14 m which is slightly larger than that calculated by the RBD program (13.25 m). For the speed of 15 m/s this wavelength is associated with a frequency of 1.07 Hz (RBD predicted frequency is 1.13 Hz). These results correspond to an error margin of 5.6 %, which is considered negligible given both programs use entirely different formulations. With the nominal radius of 0.425 m and nominal lateral distance between left and right contact points of 1140 mm (Fig. 4.7), by using the simple Klinger formulation in Eq. (2.1) of Chapter 2, the wavelength of 13.25 m resulted from the simulation using RBD program is associated with 0.054 effective conicity, while the wavelength of 14 m calculated by VAMPIRE is associated with the effective conicity of 0.049 (an error margin in conicity of 10.2 % that is considered acceptable).

Fig. 4.11 exhibits the longitudinal and lateral creep forces at the right wheel-rail contact point calculated by the RBD program while Fig. 4.12 exhibits the same information calculated by VAMPIRE, both for the velocity of 15 m/s. From Figs. 4.11 and 4.12 we can clearly see that the values of the longitudinal creep forces obtained from both simulations agree very well. The RBD program and VAMPIRE calculate the longitudinal creep force that oscillates around zero with the maximum amplitude of about 0.2 kN. However, the value of the lateral creep forces calculated by the RBD program is approximately 8.4% larger than the value calculated by VAMPIRE. The

RBD program uses Polach's formulation to calculate the creep forces while VAMPIRE uses look-up tables generated from Kalker exact theory. A small variation in creep forces is thus considered acceptable.

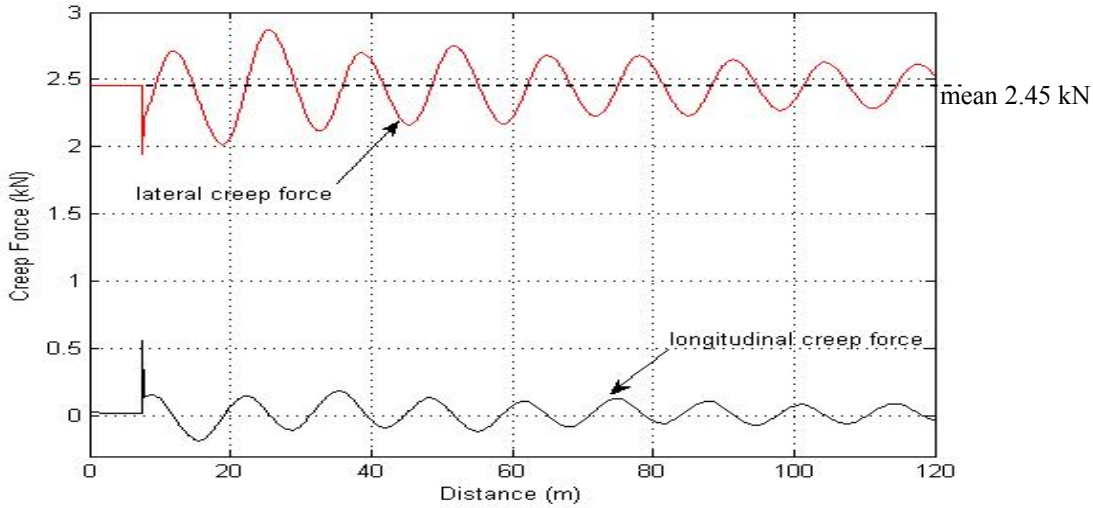

Figure 4.11. Creep forces at the right W/R contact point -RBD Program at V=15 m/s

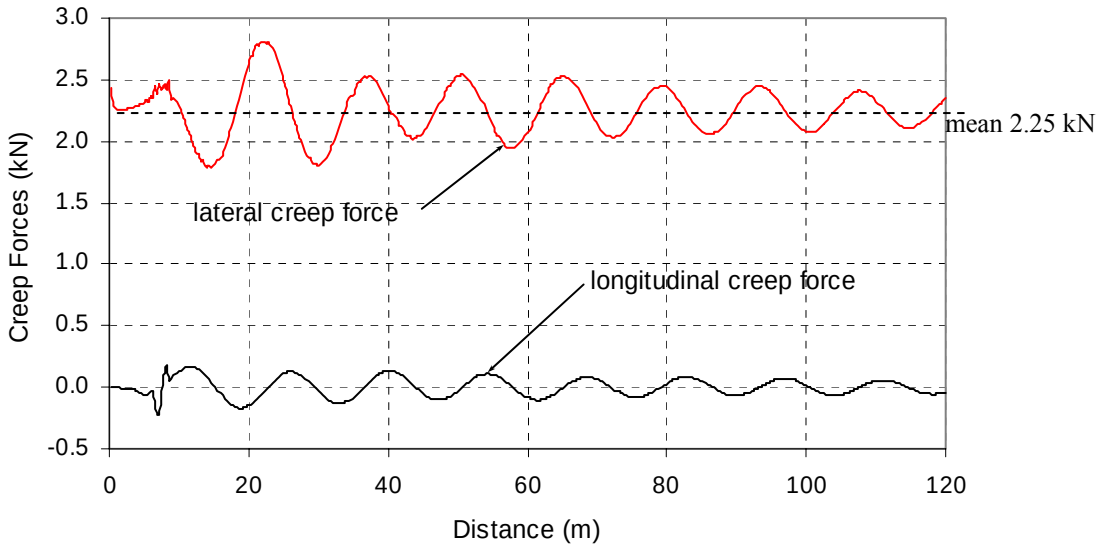

Figure 4.12. Creep forces at the W/R right contact point - VAMPIRE at V=15m/s

Fig. 4.13 and Fig. 4.14 show the lateral displacements calculated for the speed of 25 m/s by using the RBD program and VAMPIRE respectively. Both figures agree very

well and the system is still found to be stable. Compared to the simulation for the 15 m/s, however, the oscillations exhibit lower damping. The wavelengths do not change as they only depend on the wheel and the rail profile used. As a consequence, the associated oscillation frequencies become larger due to higher speed. For the simulation using the RBD program the oscillation frequency now becomes 1.89 Hz and for the simulation using VAMPIRE it now becomes 1.79 Hz (an error margin of only 5 %).

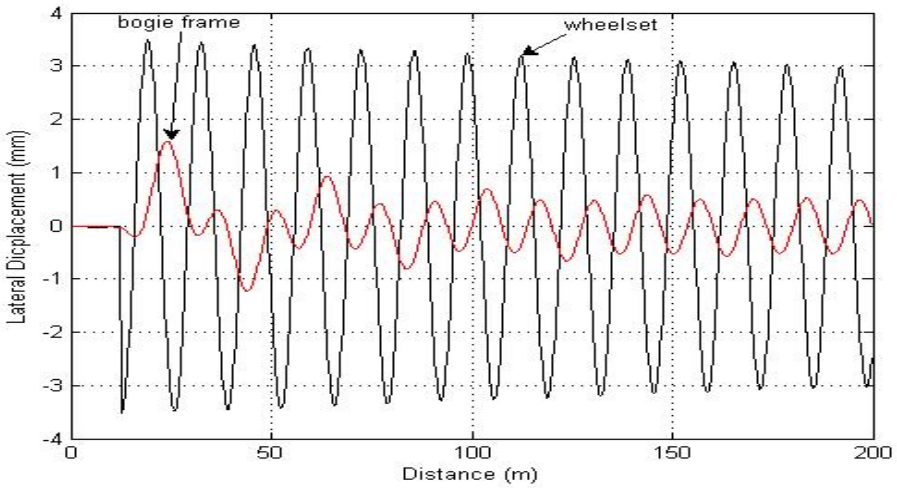

Figure 4.13. Lateral displacements - RBD Program at V=25 m/s

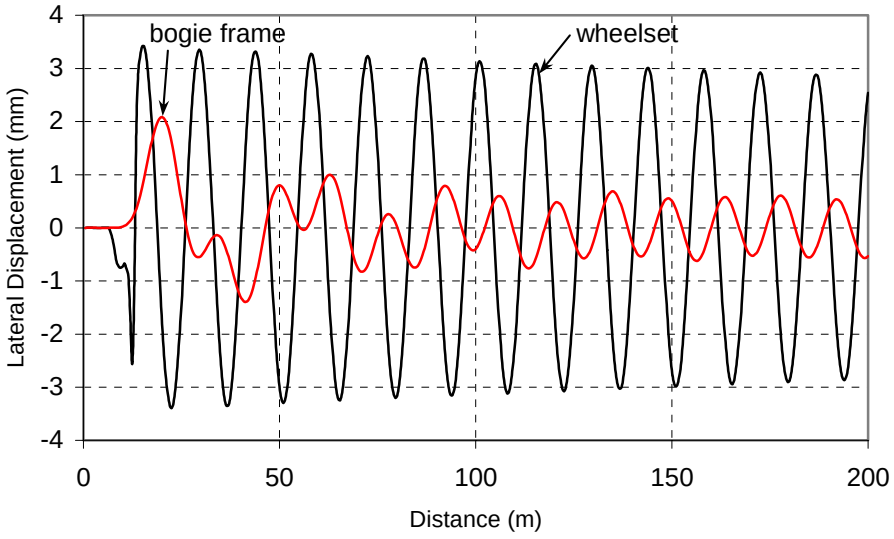

Figure 4.14. Lateral displacement - VAMPIRE at V=25m/s

The creep forces resulted from the simulation for 25 m/s using the RBD program and VAMPIRE are shown by Fig. 4.15 and Fig. 4.16 respectively. There are relatively no significant differences in values in comparison to the creep forces calculated in the simulation for the velocity of 15 m/s. In general, the results calculated by both programs present very good agreement.

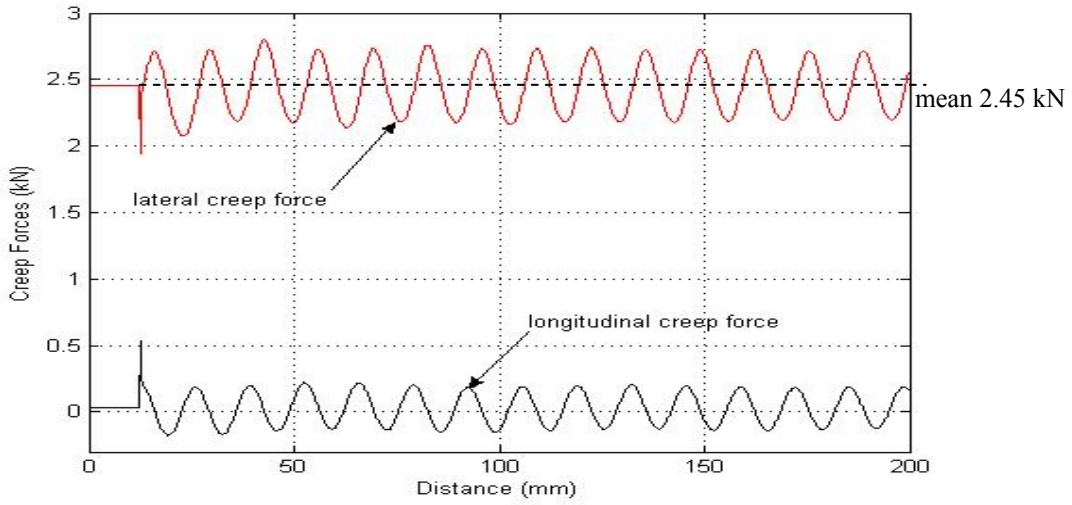

Figure 4.15. Creep forces at the right W/R contact point - RBD program at V=25 m/s

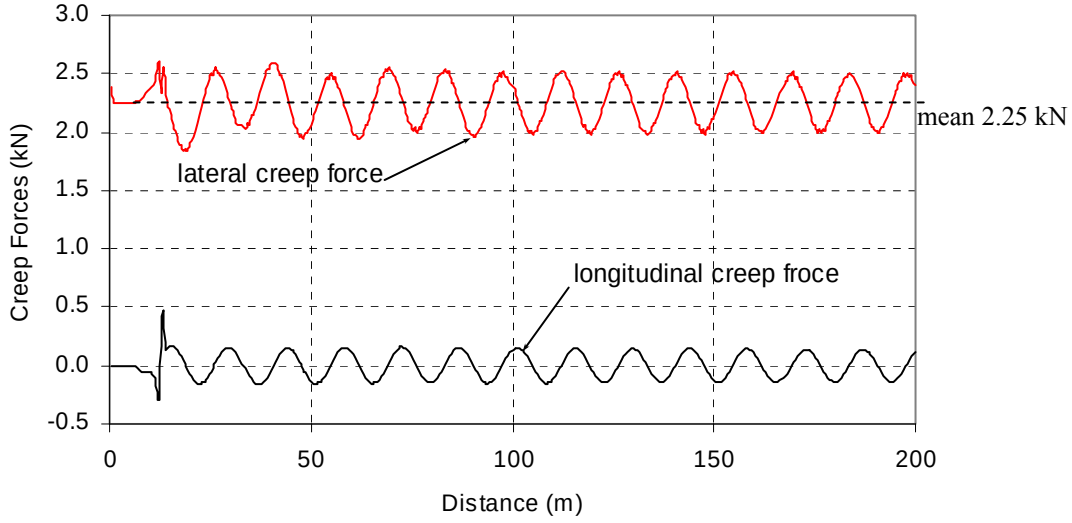

Figure 4.16. Creep forces at the right W/R contact point - VAMPIRE at V=25 m/s

For the velocity of 30 m/s, the simulation using both the RBD program and VAMPIRE show that the system becomes unstable as exhibited in Fig. 4.17 and Fig. 4.18. Further refined simulations using the RBD program and VAMPIRE have shown that the system actually just begins to exhibit unstable response at a velocity of approximately 27 m/s.

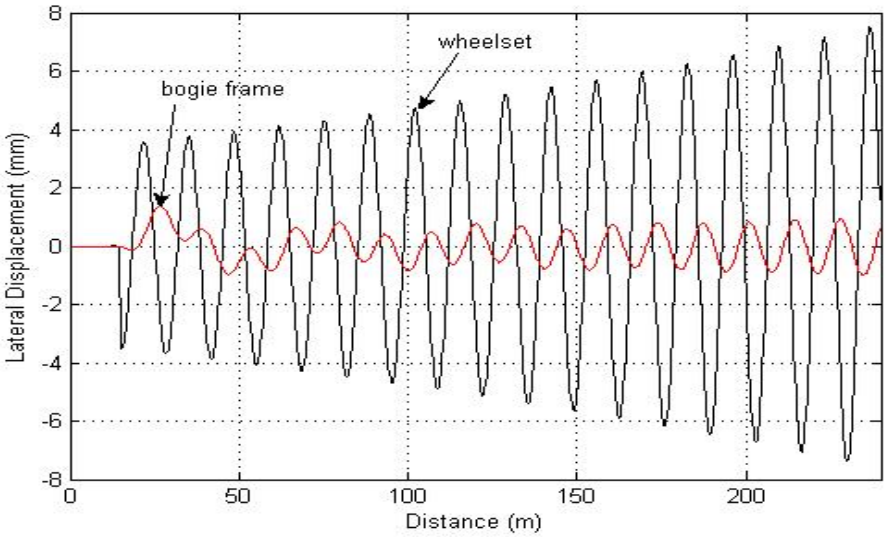

Figure 4.17. Lateral displacements calculated by RBD program at V=30 m/s

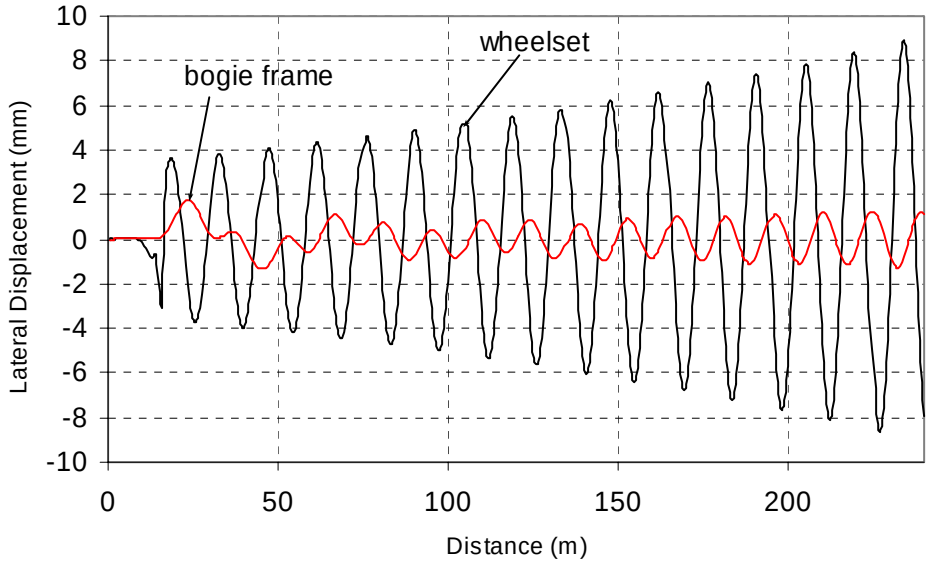

Figure 4.18. Lateral displacements calculated by VAMPIRE at V=30 m/s

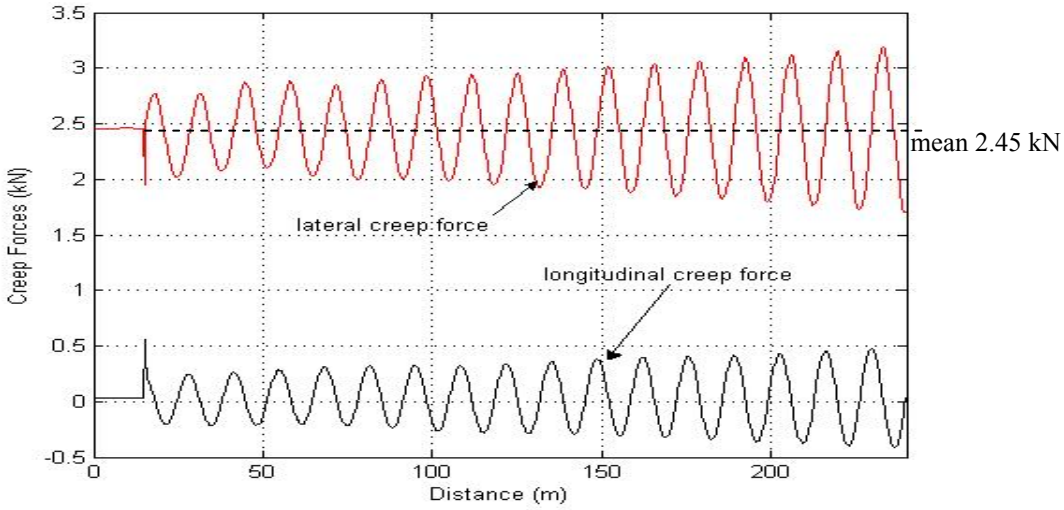

Figure 4.19. Creep forces at the right W/R contact point - RBD Program at V=30 m/s

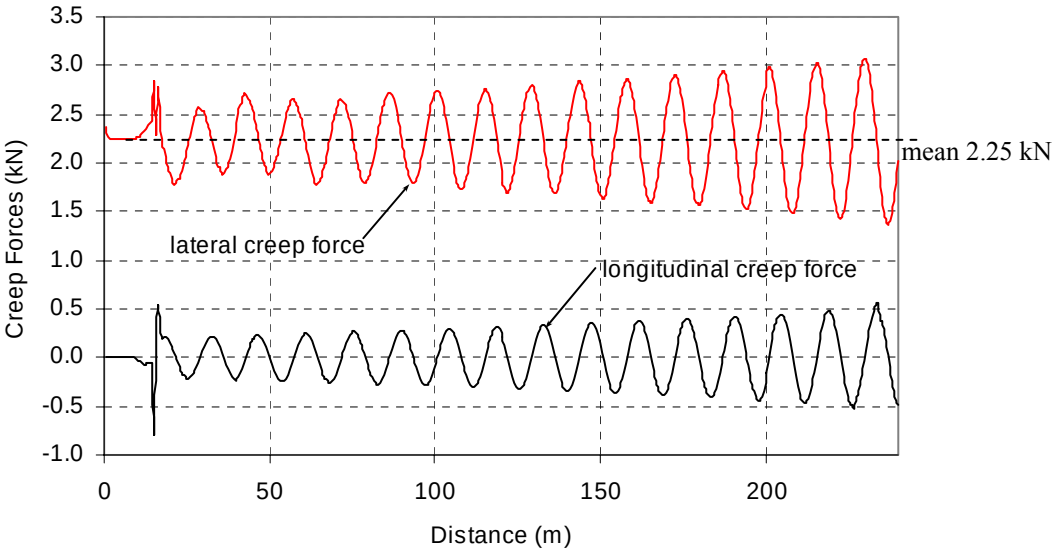

Figure 4.20. Creep forces at the right W/R contact point - VAMPIRE at V=30 m/s

The creep forces at the velocity of 30 m/s calculated by the RBD program is presented in Fig. 4.19 while Fig. 4.20 presents the calculated creep forces using VAMPIRE for the same velocity. Like the simulation at the lower speeds, both results show very good agreement. Compared to the creep forces calculated at the speeds where the wheelset

motion is stable, the creep forces calculated at the speed of 30 m/s show a different trend where they increase following the unstable motion of the wheelset.

In conclusion, the results obtained from the constant velocity simulation using the RBD program compare very well with the results provided by VAMPIRE. The insignificant differences on the calculated wavelengths, frequencies and the lateral creep forces indicate that the RBD program, although formulated using a fundamentally different coordinate system, is capable of reproducing the results of the VAMPIRE simulation. From the constant velocity simulation results presented in this section, we could conclude that the IRF system formulation presented in Chapter 3 and the RBD program developed based on the formulation are appropriate for general analysis of the dynamics of wheelsets contained within a bogie frame.

4.5. SPEED PROFILE - EFFECT OF LONGITUDINAL FORCES

In the modelling using the track-following reference (TFR) platform, the speed of wagons is an input that is also used to define the velocity of the reference frame. To do the simulation under variable speed with this method of modelling, a speed profile has to be predefined. However, in real-life conditions, speed change is caused by the application of longitudinal forces either due to braking or traction. In other words, the speed profile is a dependent variable that is affected by the independent action of longitudinal forces. Therefore, to closely simulate the real-life conditions, these longitudinal forces must be input into the simulation models and the speed profile must be output from the simulation model. Unfortunately simulation models based on the TFR formulation (for example VAMPIRE) can not perform the task in this manner.

The RBD program is capable of performing this task that reflects the real-life situation adequately as described in Chapter 3.

To illustrate the capability of the RBD program in producing the speed profile as an output of the simulation, the system of wheelset and bogie frame considered in Section 4.4 was subjected to traction and braking torque sequences provided in Fig. 4.21. The simulation commenced with the initial speed of 10 m/s.

The application of the traction and the braking torque modified the velocity of the system in the longitudinal direction. This is shown in the output of the simulation in Fig. 4.22 (a). The figure shows that the longitudinal velocity of the bogie increases from 10 m/s to 25 m/s in about 15 seconds, which means an acceleration of about 1 m/s^2. With the total mass of the wheelset and bogie frame of 11200 kg, a simple calculation can determine that the 5000 N.m traction torque applied to the wheel that has a radius of 0.425 m will accelerate the system at the rate of 1.05 m/s^2. The acceleration obtained from the simulation is approximately 5% smaller than this value due to the frictional loss at the wheel rail contact patch that occurs in the form of longitudinal creepage or slip. A similar mechanism also occurs during the application of braking torque.

Fig. 4.22 (b) shows the wheelset angular velocity as a function of time, which follows the same trend of the longitudinal velocity. At the maximum longitudinal velocity, the wheelset angular velocity had a value of about 58 rad/s.

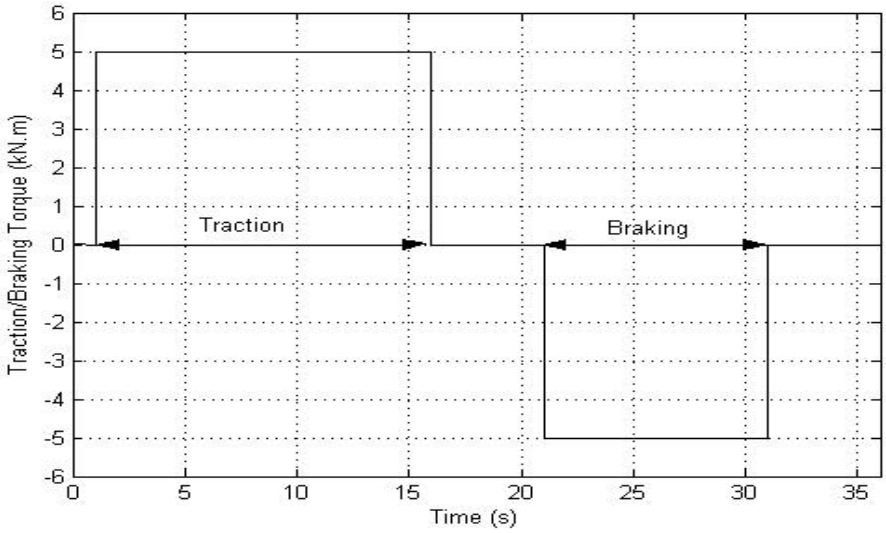

Figure 4.21. Traction/Braking Torque Profile

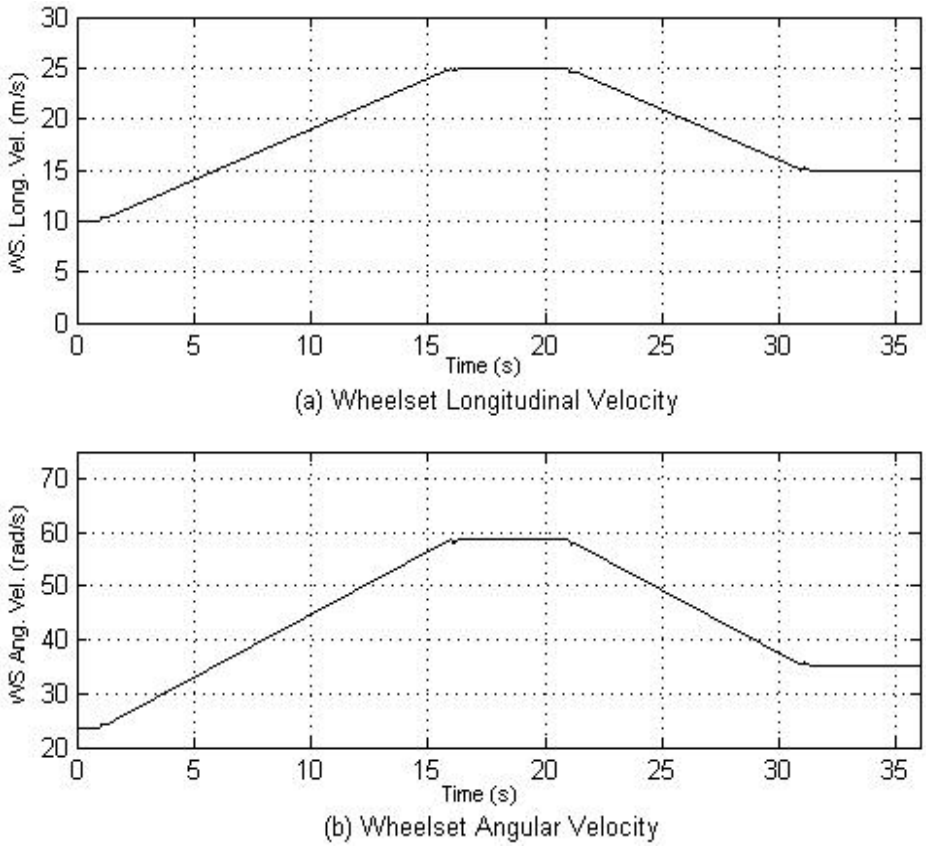

Figure 4.22. Speed Profile

One of the capabilities of the RBD program is the inclusion of the large displacement in the longitudinal direction due to the speed of the vehicle as well as the rotation of the wheelset. This capability is exhibited in the output of the simulation shown in Fig. 4.23. The travel distance of the wheelset as a function of time is presented in Fig. 4.23 (a), while Fig. 4.23 (b) shows the wheelset rotation angle. Both figures show similar trends.

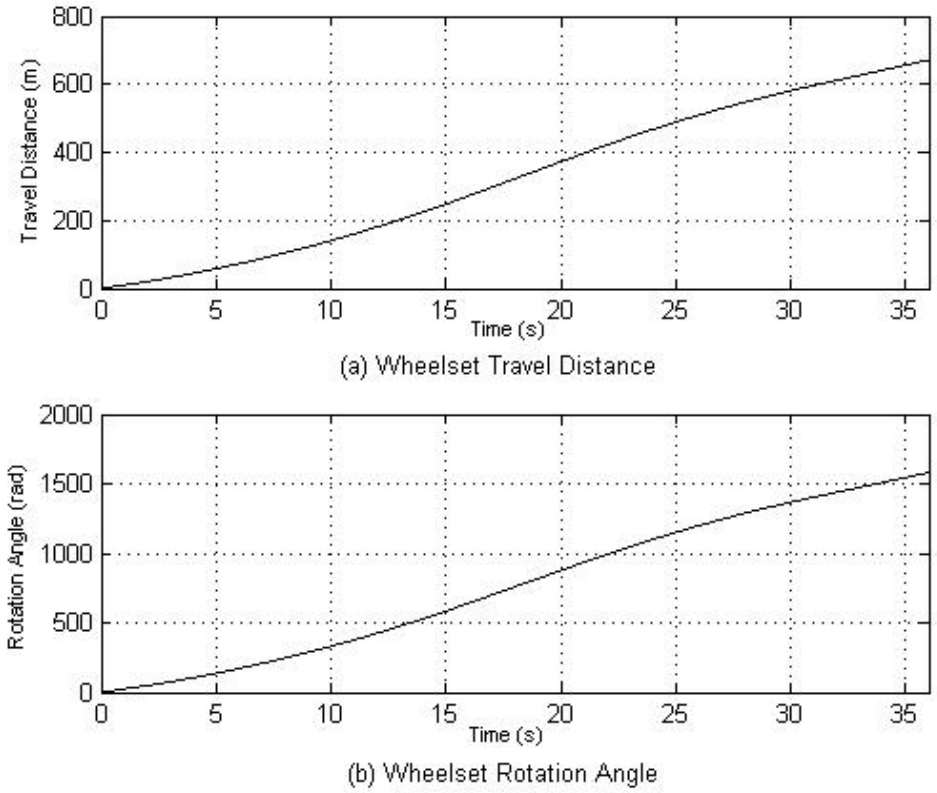

Figure 4.23. Travel distance and wheelset rotation

There are advantages of knowing the total wheelset rotation angle. For example, we can calculate how many rotations are made by the wheelset during travelling a certain distance where the brake or tractive forces are applied. Multiplying the number of rotations with the nominal circumference of the wheel and by comparing the result with the actual travel distance, we can calculate the average slip percentage between the

wheel and the rail along the travelling distance. To illustrate this in the present simulation, during the braking ($21 \le t < 31$) the wheelset has made 74.72 rotations (469.52 rad). Without slip this amount of rotation of the wheelset of 0.425 m radius corresponds to 199.55 m of travelling distance. However due to slip the actual distance travelled was 199.65 m that is 0.10 m more. In other words 0.1 m slip travel has occurred during the 199.65 m nominal simulation.

Such outputs of the RBD program shown in this section must be validated. Unfortunately, no tools are found for the purpose. Therefore a laboratory test presenting the bogie under braking condition was performed as part of this thesis. The construction and the results of the testing as well as their comparison with the simulation using the RBD program are reported in Chapter 6 of this thesis.

4.6. LATERAL DYNAMICS UNDER VARIABLE SPEED

The RBD program, similar to other wagon dynamics programs, can predict lateral dynamics of the bogie system due to lateral disturbance. To show this capability, a lateral disturbance was given to the wheelset while it oscillated under the brake or traction force. Fig. 4.24 shows the result of such simulation under braking condition.

As shown in the Fig. 4.24, the simulation started at the speed of 32 m/s. From the simulation at constant speed discussed in Section 4.4, we know that at this speed the oscillation of the wheelset is unstable. The brake force was applied at t = 2.5 sec, as can be seen in Fig. 4.24 (a), where the velocity begin to decrease at that time. Fig. 4.24 (b) shows the associated lateral displacement of the wheelset.

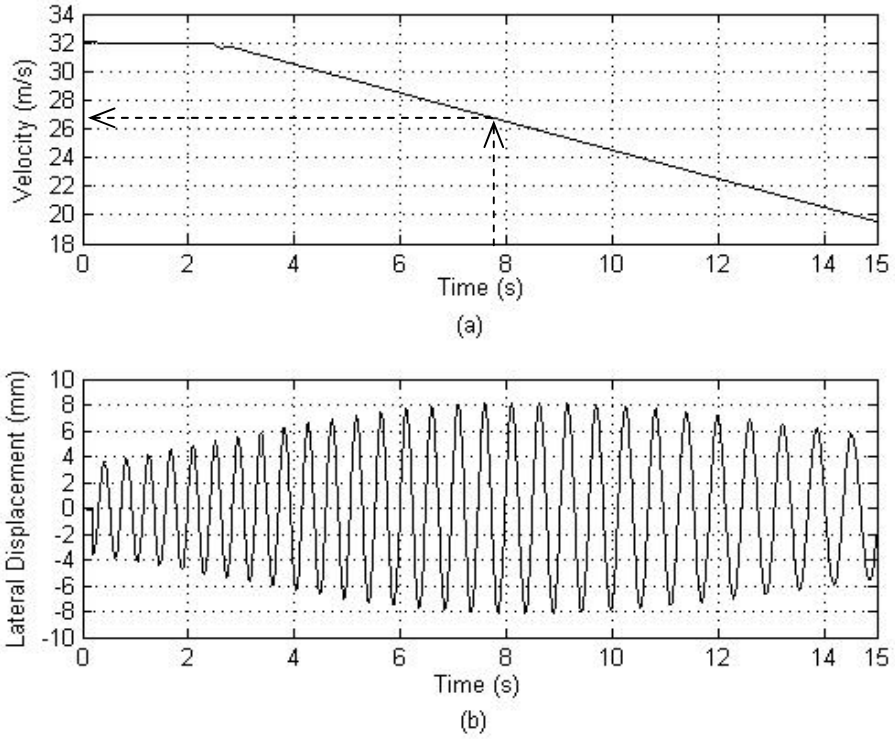

Figure 4.24. Speed profile and wheelset lateral displacement under braking calculated by the RBD program

From these figures it can be seen that the wheelset oscillation remains unstable until the velocity decreases to around 27 m/s; below this speed the oscillation of the wheelset is decayed. Fig. 4.24 (b) also reveals that the frequency of oscillation decreases with the reduction in the velocity. It can be explained that the oscillation wavelength remains constant as it depends only on the wheel and the rail profile. In other words, lower speed provides lower oscillation frequency and higher speed provides higher oscillation frequency.

Utilising the output speed profile of the RBD program shown in Fig. 4.24 (a) as an input, the simulation under variable speed was carried out in VAMPIRE for comparison (as previously explained, in VAMPIRE the speed profile is required as an input). The result of the lateral displacement calculated by VAMPIRE is shown in Fig.

4.25, the value of which closely relates to the lateral displacement calculated by the RBD program.

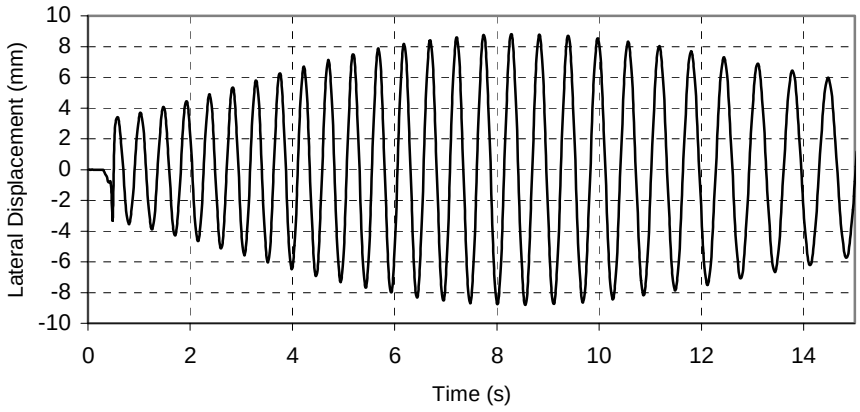

Figure 4.25. Wheelset lateral displacement during braking calculated by VAMPIRE

A similar type of simulation was performed under traction force. The lateral disturbance was given to the wheelset and while it was oscillating the traction force was applied. The result of such simulation is presented in Fig. 4.26. The simulation started at the speed of 20 m/s. At t = 2.5 sec the traction force provided positive torque to the wheelset that increased the speed (Fig. 4.26 (a)). The oscillation of the wheelset was stable until the speed of around 27 m/s (Fig. 4.24 (b)). At speeds higher than this (for example 28 m/s) the oscillation became unstable.

Similar to the simulation under braking condition the output speed profile calculated by the RBD program shown in Fig. 4.26 (a) was used as an input to do the equivalent simulation in VAMPIRE. The associated lateral displacement calculated by VAMPIRE is exhibited in Fig. 4.27.

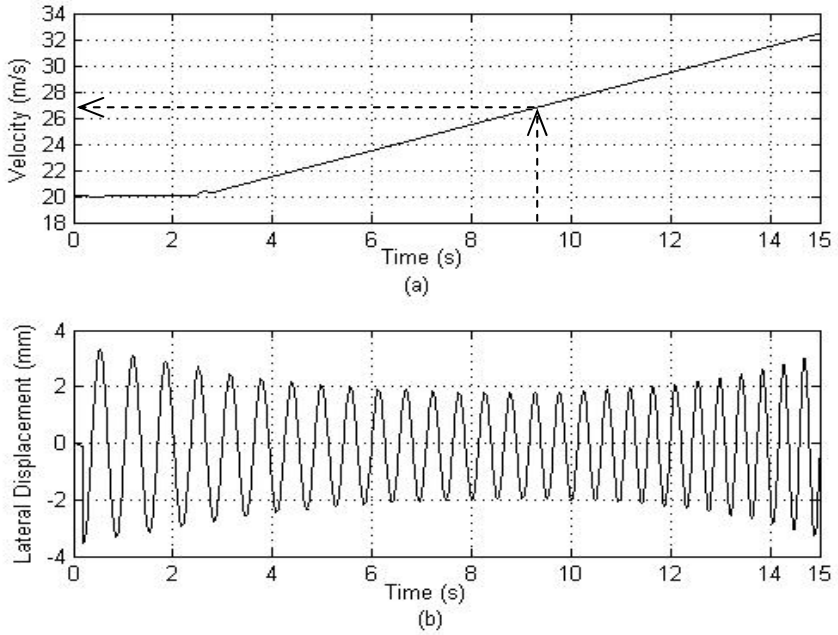

Figure 4.26. Speed profile and wheelset lateral displacement during traction calculated by the RBD program

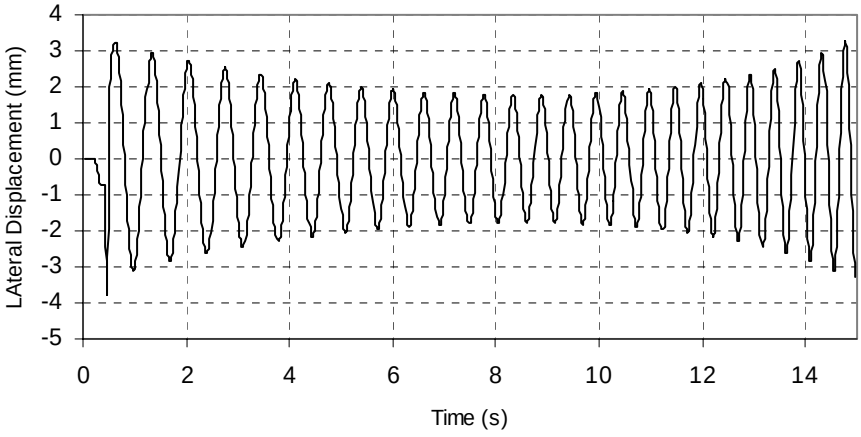

Figure 4.27. Wheelset lateral displacement during traction calculated by VAMPIRE

The above two simulations under variable speed (traction and braking) show that the RBD program can naturally model the effect of the longitudinal force on the longitudinal and the lateral dynamics of the wheelset, whilst VAMPIRE requires pre-

calculated speed profile as an input. The critical speed can also be predicted effectively using the RBD program.

4.7. WHEELSET DYNAMICS UNDER HEAVY BRAKING

When the applied brake force is greater than the available adhesion between the wheel and the rail, skidding occurs. In such condition the wheelset is "locked", i.e. does not rotate, while the body is still in motion. The RBD program has the capability to model such conditions as reported in this section.

A large brake torque (25 kN.m) was applied to the wheelset. Constant friction coefficient between the wheel and the rail is set to be 0.3. With this friction coefficient, and the total mass of the system of 11200 kg, the maximum longitudinal force that can be generated will be around 16.48 kN at each rail. At the nominal wheel radius of 0.425 m, the maximum brake torque that may be applied to the wheelset without causing slip will be around 14 kN.m only.

The simulation started at the speed of 25 m/s as shown in Fig. 4.28 (a) where the motion of the wheelset was still in the stable range. Brake torque was applied at t = 2 sec. From Fig. 4.28 (b) it can be seen that the wheelset rotation has quickly decreased to zero in about 1 sec while the speed was still more than 20 m/s. This means that the wheel has stopped rotating while it still moves forward at high velocity (skid). Fig. 4.28 (c) shows the lateral displacement of the wheelset, indicating very clearly that at the time the skid happens, the motion of the wheelset becomes unstable with very low frequency of oscillation.

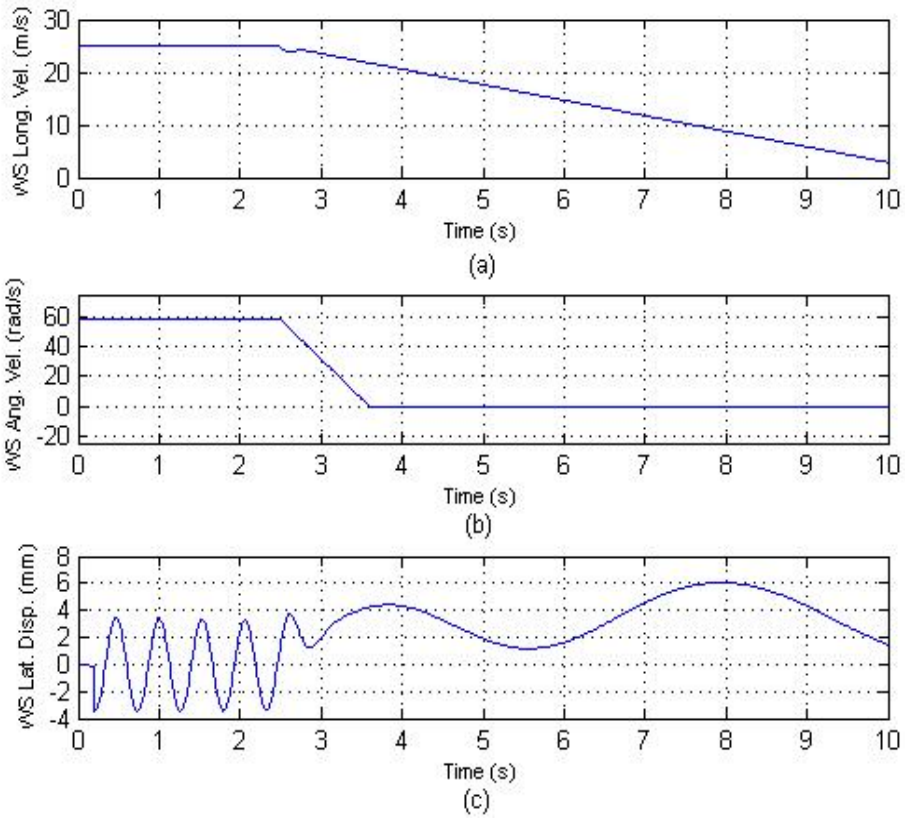

Figure 4.28. Skid at wheel-rail friction coefficient $\mu_r = 0.3$

Fig. 4.29 shows the similar type of simulation with the same brake torque but lower friction coefficient ($\mu = 0.1$) between the wheel and the rail. The situation is more dangerous compared to higher friction coefficient. The reduction in the wheel angular velocity to zero in less than a half second occurred as shown in Fig. 4.29 (b). The wheelset lateral motion is badly unstable, where it has continuously increased without oscillation, as shown in Fig. 4.29 (c).

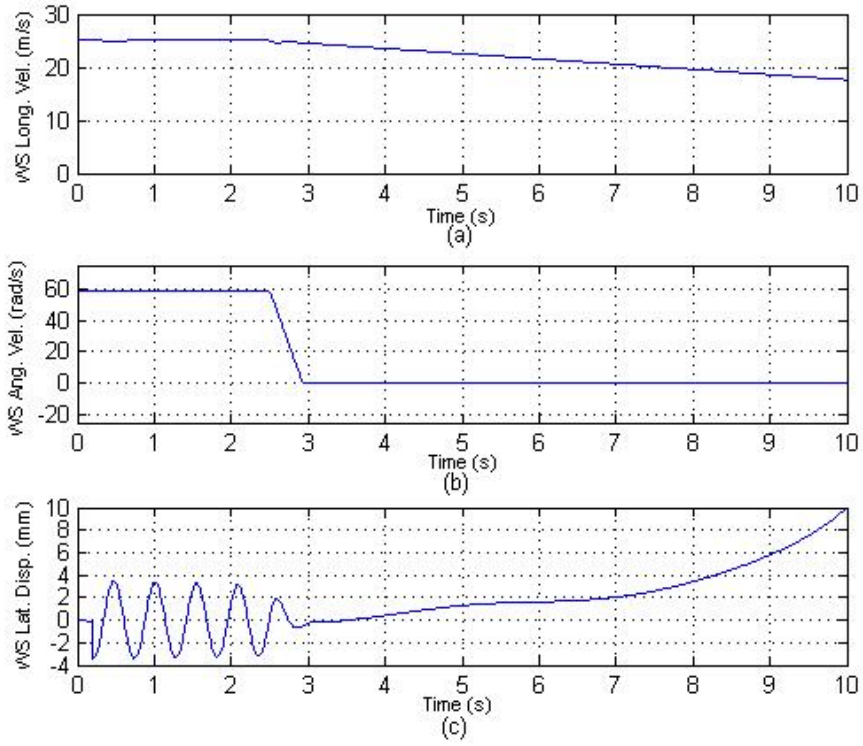

Figure 4.29. Skid at wheel rail friction coefficient $\mu = 0.1$

Both examples of simulation of the skid condition shows the capability of the RBD program to simulate extreme conditions of braking which can not be performed using the software developed using a track-following reference (TFR) platform.

4.8. SUMMARY AND CONCLUSION

This chapter has described the capability of the RBD program in predicting the dynamics of a wheelset within a bogie frame both under constant speed and under variable speed due to traction and braking. Novel features of the RBD program to evaluate the speed profile as a function of input braking / traction torques as well as precisely determining wheelset angular velocity have been demonstrated through examples in this chapter. The results have been validated wherever possible with the

simulations using VAMPIRE that illustrated very good agreement. From the results we can draw the following conclusions:

- Under constant speed the wheelset remained laterally stable up to 27 m/s. The insignificant difference between the results of RBD and VAMPIRE might have resulted from the different methods used in the calculation of the contact parameters and creep forces as well as the method of numerical integration used.

- The RBD program can calculate the longitudinal dynamics of the bogie due to the application of traction and braking where the speed profile is an output of the simulation in a natural manner.

- The application of very large braking torques can lead to wheelset skid and tends to destabilise wheelset lateral oscillation. Simulation results showed that skid at the low wheel-rail friction coefficient is more dangerous than at the higher friction coefficient.

- Part of the results of the RBD program, namely the speed profile and skid as a function of the application of brake torque, could only be validated using carefully designed experiments as other commercial dynamics packages do not explicitly account for these factors.

5. DYNAMICS OF SIMPLIFIED TWO-AXLE BOGIES

5.1. INTRODUCTION

This chapter reports the modelling of simplified two-axle bogies using the Rail Bogie Dynamic (RBD) Program. As most of the wagons and passenger cars use this type of bogie, the examination of its dynamics has become a subject of interest to railway engineers and researchers for many years. Thus this type of bogie was considered in evaluating the capability of the RBD program.

First, the bogie dynamics under constant speed are reported and the results are validated against VAMPIRE. Second, the RBD program has been used to simulate the effect of the longitudinal braking and traction forces to the speed profile and the associated lateral, vertical and pitch dynamics of the bogie. The results of the simulation under the variable speed profile have also been validated using VAMPIRE; for this purpose the output speed profile calculated by the RBD program has been used as input for the VAMPIRE simulation. The capability of the RBD program to simulate severe bogie dynamics with the associated wheel skid is also demonstrated in this chapter. To the best knowledge of the author, no wagon dynamics commercial programs possess the capability of skid analysis.

5.2. DESCRIPTION OF MODELLED SYSTEM

The system of a simplified two-axle bogie containing one bogie frame and two wheelsets is shown in Fig.5.1. The distance between axles was 1.675 mm (distance between axles of most of QR three-piece bogie)

a.) Top View

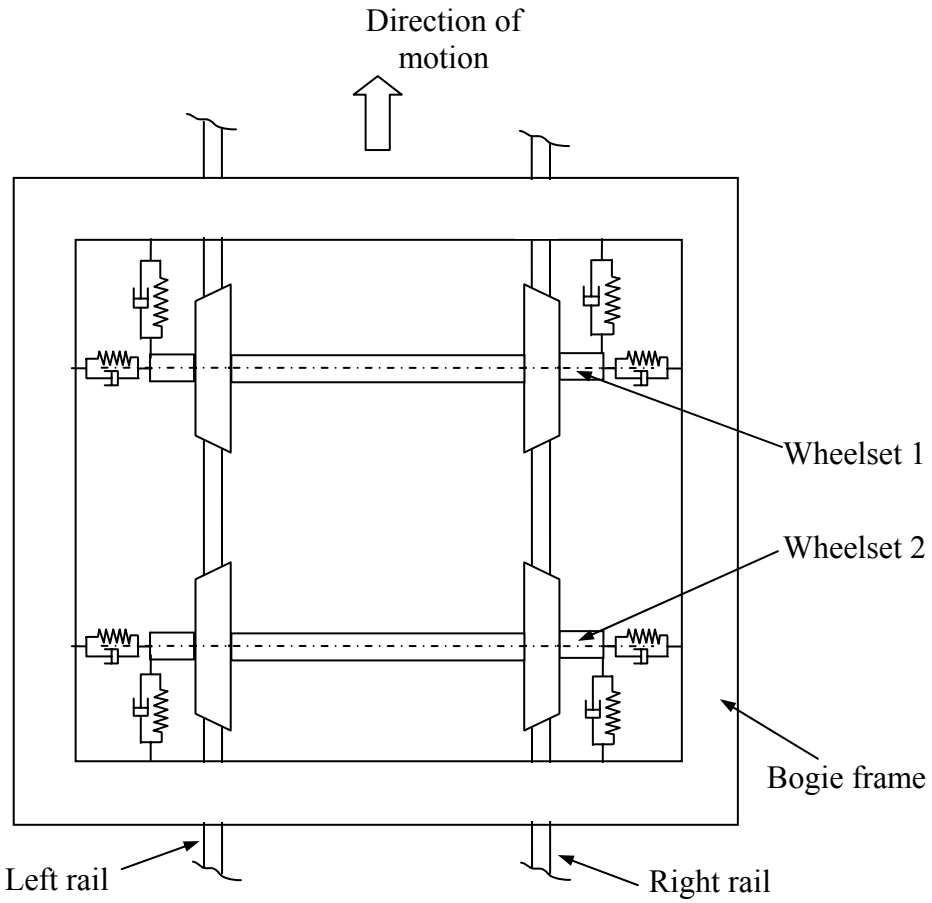

b.) Front View

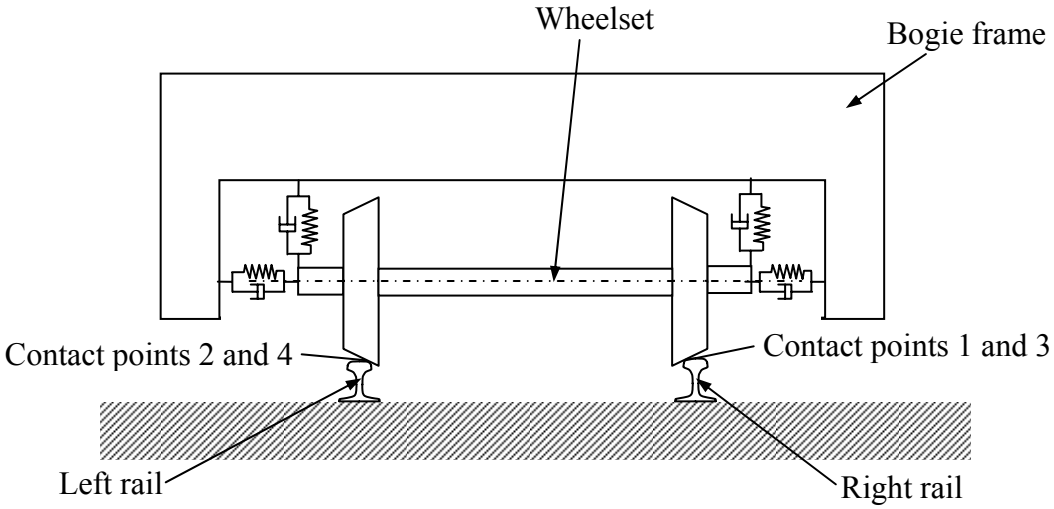

Figure 5.1. Simplified two-axle bogie

Each wheelset is connected to the bogie frame by a set of linear springs and dampers. The total number of bodies involved was five; the bogie frame, the leading wheelset (wheelset 1), the trailing wheelset (wheelset 2), the left rail and the right rail. All the bodies were assumed as rigid with the body reference frames attached to their respective centres of mass. The coordinate system is described using the same convention as defined in Section 2.1. Adopting the formulation in Chapter 3, the motion of each body's local coordinate system with respect to the global system is described in the multibody formulation using three translational coordinates and four Euler parameters. The vector of generalised coordinates of the modelled system that contains five bodies can now be written as:

$$\mathbf{q} = \begin{bmatrix} \mathbf{q}^{rr} & \mathbf{q}^{rl} & \mathbf{q}^{ws1} & \mathbf{q}^{ws2} & \mathbf{q}^{bf} \end{bmatrix}^{\mathrm{T}} \tag{5.1}$$

where $\mathbf{q}^{rr}, \mathbf{q}^{rl}, \mathbf{q}^{ws1}, \mathbf{q}^{ws2}, \mathbf{q}^{bf}$ are vectors of generalised coordinates of the right rail, the left rail, the leading wheelset (ws1), the trailing wheelset (ws2) and the bogie frame respectively. Because each body has three translational coordinates and four Euler parameters, the total vector coordinates in Eq.5.1 will have 35 components.

There are four contact points involved in the system. Thus, the vector of non-generalised surface parameters is written as

$$\mathbf{s} = \begin{bmatrix} \mathbf{s}_1^{rr} & \mathbf{s}_2^{rl} & \mathbf{s}_3^{rr} & \mathbf{s}_4^{rl} & \mathbf{s}_1^{ws1} & \mathbf{s}_2^{ws1} & \mathbf{s}_3^{ws2} & \mathbf{s}_4^{ws2} \end{bmatrix}^{\mathrm{T}} \tag{5.2}$$

where each superscript represents a body as described in Eq.(5.1) and the subscript represents the number of contact points:

- contact point 1 is located at the *right* wheel-rail patch of the *leading* wheelset
- contact point 2 is located at the *left* wheel-rail patch of the *leading* wheelset

- contact point 3 is located at the *right* wheel-rail patch of the *trailing* wheelset
- contact point 4 is located at the *left* wheel-rail patch of the *trailing* wheelset

Because each contact surface is represented by two surface parameters, vectors of non-generalised surface parameters in Eq.(5.2) will have sixteen components. Thus, in total, the vector of generalised and non-generalised coordinates will have 51 components.

Through the introduction of five Euler parameter constraints (one for each body), 20 contact constraints, and twelve ground constraints, there have been a total of 37 constraint equations associated with fourteen (51-37=14) unrestrained degrees of freedom. As there are 37 constraint equations, 35 generalised coordinates, and 16 non-generalised surface parameters, the size of sub-Jacobian matrix $\mathbf{C}_\mathbf{q}$ is 37×35 and the size of sub-Jacobian matrix $\mathbf{C}_\mathbf{s}$ is 37×16. Hence, for the system of the simplified two-axle bogie, the total dimension of the augmented matrix of the mass matrices and sub-Jacobian matrices in Eq.(3.75) was 88×88. For the constant speed simulation a velocity constraint in the longitudinal direction was added, which increased the dimension of the augmented matrix to 89×89 and reduced the unrestrained degrees of freedom to thirteen.

The characteristics of the springs and dampers of the bogie shown in Fig.5.1 are presented in Table 5.1. The inertia properties of the wheelsets and the lumped spring mass used in the simulation are given in Table.5.2. The inertia properties of the sprung mass were chosen so that the axle load represents the heavy haul wagon operation (approximately 300 kN). The spring stiffness and damping coefficient of the suspension was optimised so that the bogie remained stable (no wheelset hunting) at least up to 25

m/s (90 km/h). The wheel and the rail profiles used were the same as those presented in Section 4.3 of the previous chapter.

Table 5.1. Spring and damper characteristics

	Spring Stiffness , K (N/m)	Damping Coefficient, C (N.s/m)
Longitudinal	9.5×10^6	8×10^4
Lateral	6.0×10^6	4×10^4
Vertical	3.5×10^6	2.5×10^4

Table 5.2. Inertia properties of the wheelsets and the sprung mass

	Wheelset	Sprung Mass
Mass (kg)	1200	60,000
Mass moment of inertia I_{xx} ($\mathrm{kg \cdot m^2}$)	720	80,000
Mass moment of inertia I_{yy} ($\mathrm{kg \cdot m^2}$)	112	60,000
Mass moment of inertia I_{zz} ($\mathrm{kg \cdot m^2}$)	720	20,000

5.3. SIMULATION AT CONSTANT SPEED

5.3.1. Response to Lateral Track Irregularities

Response of the model to lateral disturbance has been studied. Instead of simply using the initial value of lateral displacement, a sinusoidal track irregularity as shown in Fig 5.2 was input to initiate the lateral oscillation.

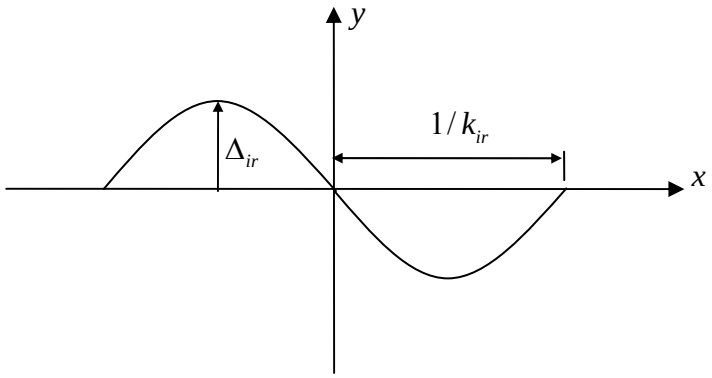

Figure 5.2. Parameters representing sinusoidal track irregularity

The analytical representation of the sinusoidal irregularity is expressed as shown in Eq. (5.3).

$$y(x) = \Delta_{ir} \sin \pi k_{ir} x \qquad (5.3)$$

where Δ_{ir} is the amplitude and k_{ir} is a parameter that defines the sine wavelength. For the lateral irregularity, a value in the range of $\Delta_{ir} = (0.0203 \sim 0.0305)\, m$ and $k_{ir} = (0.0426 \sim 0.0656)\ m^{-1}$ suggested by Garg and Dukkipati (1984) has been used in the simulation. Specific values adopted were $\Delta_{ir} = 0.025\ m$ and $k_{ir} = 0.045\ m^{-1}$, which corresponded to an amplitude of 0.025 m and wavelength of 44.44 m. The irregularity was assumed to occur at the fifth metre of travel as plotted in Fig 5.3. Some important results of the constant speed simulation at two selected speeds of 15 m/s (54 km/h) and 25 m/s (90 km/h) are presented in this section.

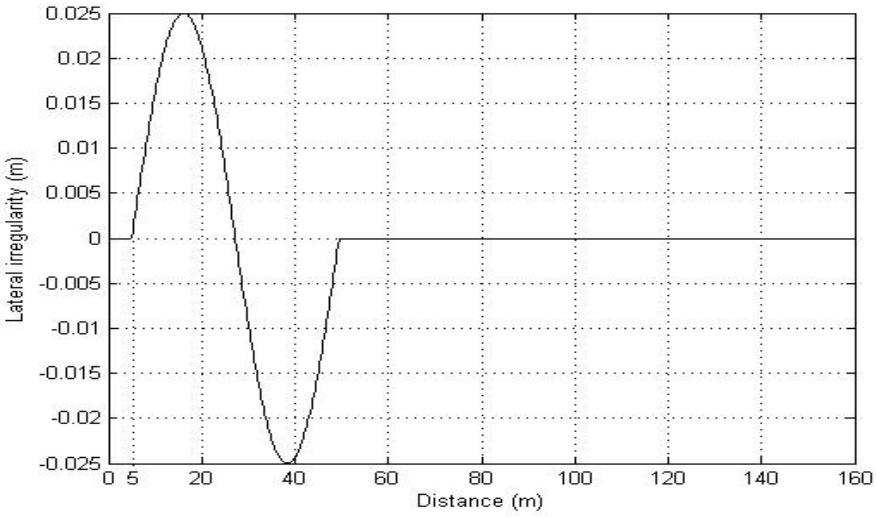

Figure 5.3. Input Lateral Track Irregularity

Response at 15 m/s (54 km/h)

Fig 5.4 shows the lateral displacement of the trailing and the leading wheelsets, relative to the centre of the track, against travel distance at 15 m/s (54 km/h) obtained by the RBD program. As expected, when running on the track containing lateral irregularity (from 5 m to 50 m travel distance) the wheelsets were subjected to a lateral displacement of 9.5 mm (exhibited by the leading wheelset at the travelling distance of 17 m). After passing the irregularity section the amplitude of the lateral oscillations decreased very quickly suggesting that at this speed the bogie was stable with very high level of damping. Fig.5.4 also reveals that the oscillation of the trailing wheelset was lagging in phase and had relatively lower amplitude. The marginal phase difference in time series between the leading and the trailing wheelsets corresponds to the speed of travel and the distance between the axles.

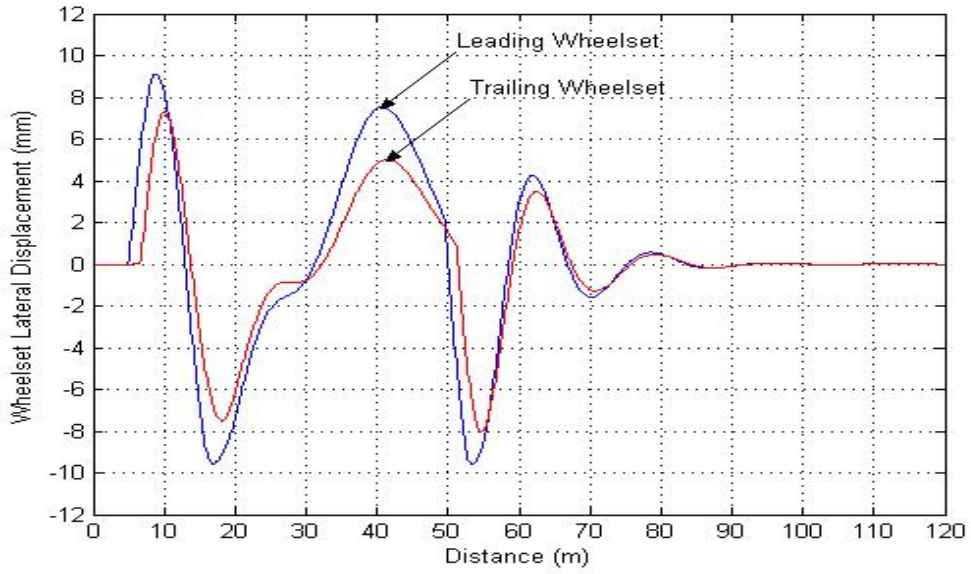

Figure 5.4. Wheelset lateral displacement - RBD program at V = 15 m/s

Figure 5.5. Wheelset lateral displacement - VAMPIRE at V = 15m/s

For comparison, the same system was also modelled using VAMPIRE software. The lateral displacement of the wheelsets calculated by VAMPIRE for the speed of 15 m/s

(54 km/h) are shown in Fig.5.5. This figure shows, in general, the same trend and magnitude as that provided by the RBD program presented in Fig 5.4. The maximum lateral displacement of the bogie due to the passage across the track section containing the sinusoidal irregularity was 10 mm, (0.5 mm larger than that calculated by the RBD program) occurring at the travel distance of 17 m (same as that predicted by the RBD program).

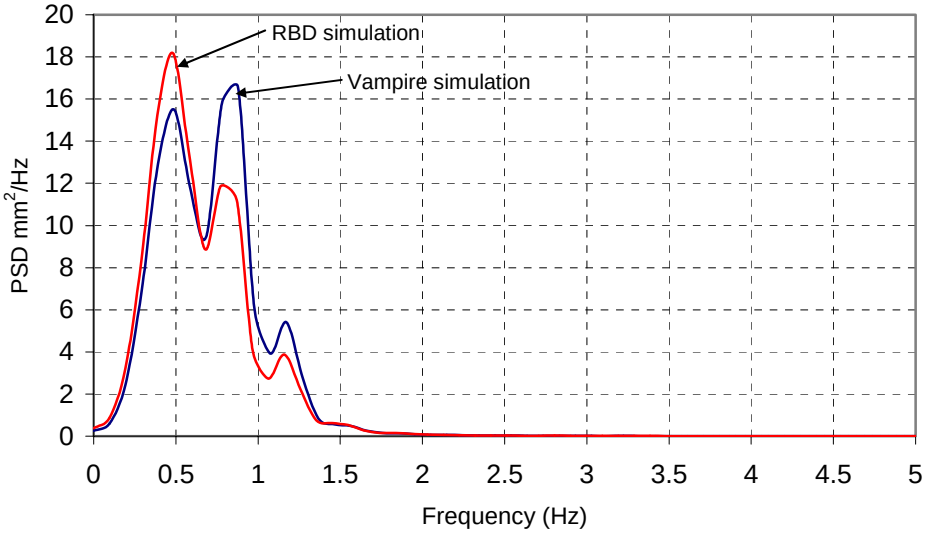

Figure 5.6. Frequency spectrum of the leading wheelset lateral oscillation at 15 m/s

Fig.5.6 shows the frequency spectrum of the oscillation of the leading wheelset calculated by the RBD program and VAMPIRE at a speed of 15 m/s. Both spectrums identify two high peaks. For the first peak, the RBD program obtained a frequency of 0.488 Hz and VAMPIRE obtained 0.483 Hz (1.04 % error); while for the second peak the RBD program calculated 0.774 Hz and VAMPIRE calculated 0.879 Hz (11.95 % error). The differences are considered insignificant. The peak at the lower frequency was related to the forced excitation due to the lateral irregularity, while the peak at the

higher frequency was related to the kinematic oscillation of the wheelsets due to their conicity.

The phase difference between the leading and the trailing wheelsets induces bogie frame yaw. The yaw of the bogie frame calculated by the RBD program (red line) and VAMPIRE (blue line) are presented in Fig.5.7. It can be seen that both of these results agree very well.

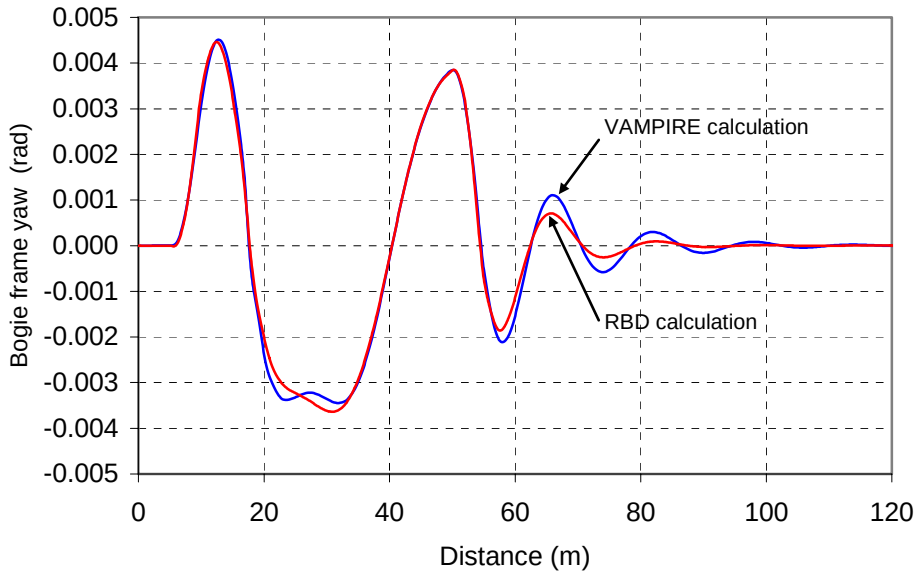

Figure 5.7. Bogie frame yaw at 15 m/s

Response at 25 m/s (72 km/h)

Fig 5.8 shows the lateral displacement of the trailing and the leading wheelsets obtained by the RBD program at a constant speed of 25 m/s while Fig 5.9 shows the same information calculated by VAMPIRE. Comparing both figures, it can be seen that in general the trend and magnitude of the wheelset lateral displacement calculated by the RBD program agree very well with that of the VAMPIRE simulation.

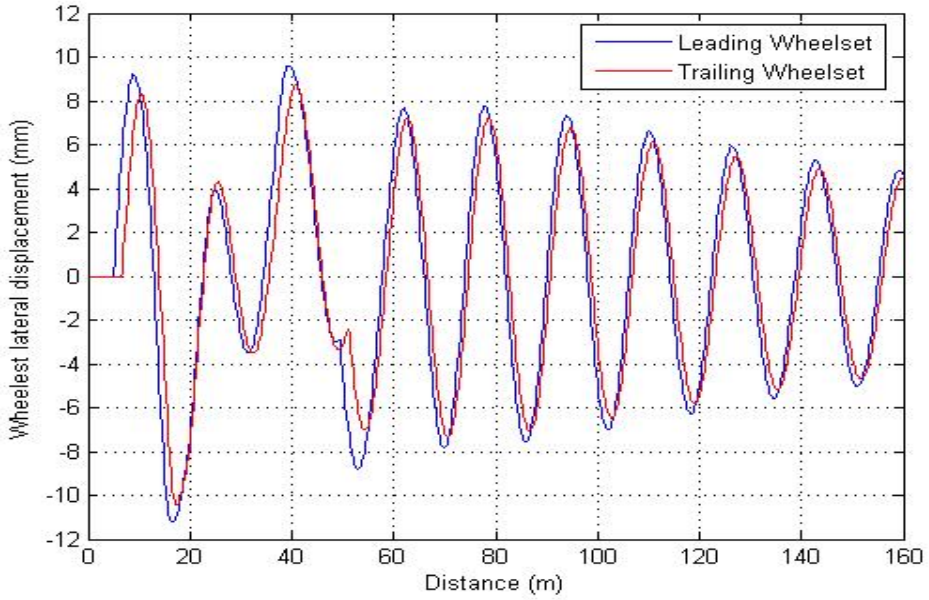

Figure 5.8. Wheelset lateral displacement calculation by RBD program at 25 m/s

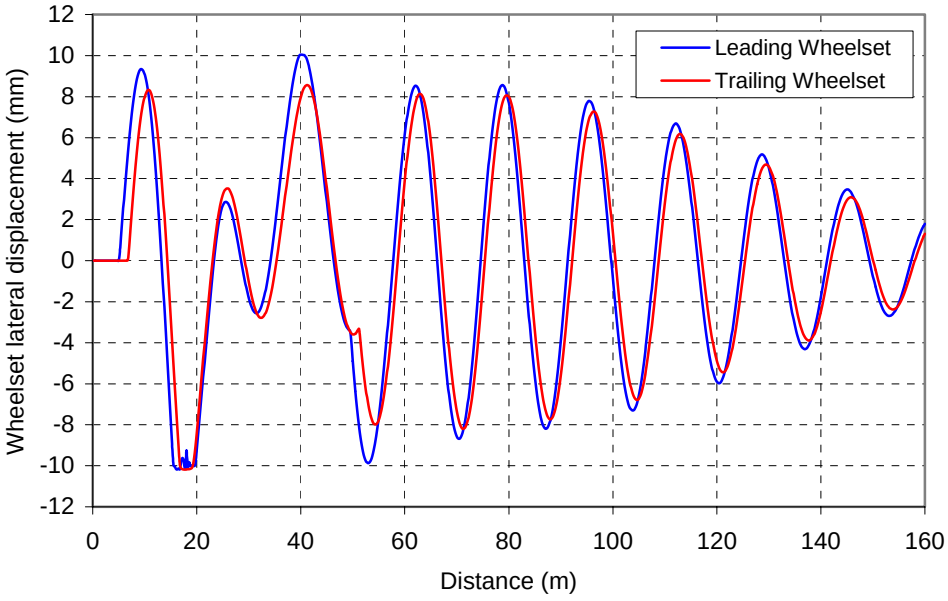

Figure 5.9. Wheelset lateral displacement calculation by VAMPIRE at 25 m/s

Fig.5.10 presents the frequency spectrum of the lateral oscillation of the leading wheelset at 25 m/s. Both the frequency spectrum of the lateral oscillation calculated by VAMPIRE and the RBD program exhibit similar trends where only one dominant peak

appears on the spectrum. This peak is related to the frequency of the kinematics oscillation due to the conicity of the wheelset. The RBD program predicted 89.01 mm^2/Hz peak at the frequency of 1.45 Hz while VAMPIRE predicted 106.44 mm^2/Hz peak at the frequency of 1.46 Hz. The difference in peak values calculated by VAMPIRE and the RBD program is insignificant.

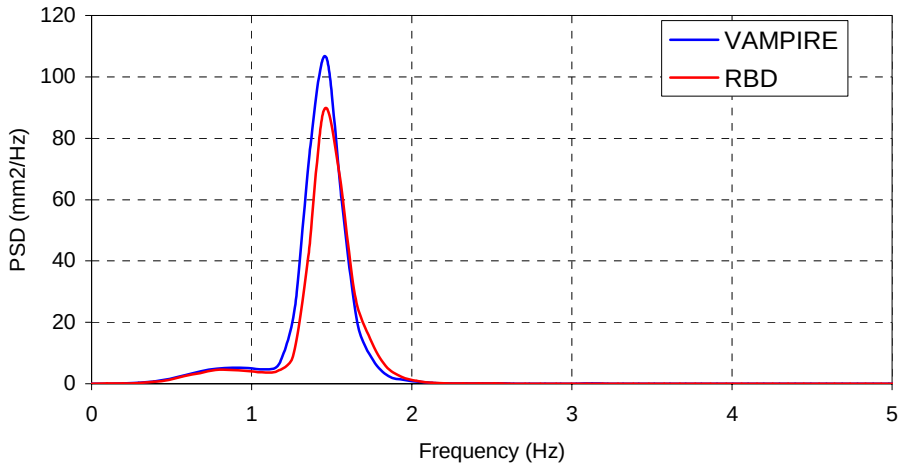

Figure 5.10. Frequency spectrum of the leading wheelset lateral oscillation at 25 m/s

The yaw of the bogie frame obtained from both simulations at 25 m/s are shown in Fig.5.11. As expected the yaw oscillation of the bogie frame follows the trend of the wheelset lateral oscillation, because the bogie frame yaw oscillation was initiated by the phase difference between the leading and the trailing wheelset lateral oscillations.

Simulations at the constant speeds of 15 m/s and 25 m/s reveal that the RBD program results are as good as, if not better than that of the VAMPIRE. Some inevitable differences have resulted due to the difference in the adopted methods of calculation of the contact parameters and creep forces as well as the method of numerical integration used. As has been explained previously, the creep forces were calculated using the

Polach formulation and the British Table Book derived from the Kalker Non-Linear formulation respectively by the RBD program and VAMPIRE.

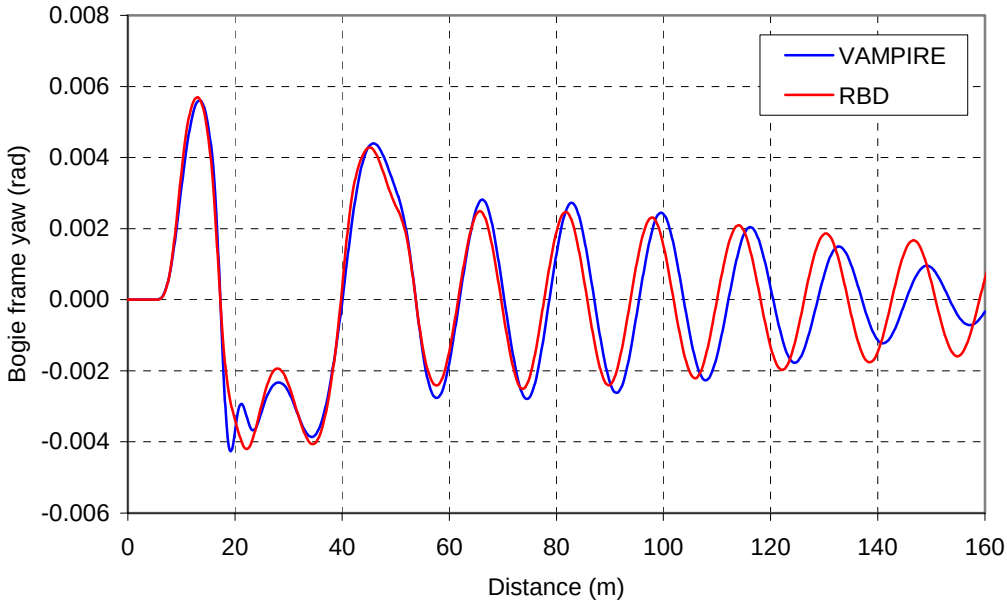

Figure 5.11. Bogie frame yaw 25 m/s

5.3.2. Response to Track Vertical Irregularity

With a view to examining the capability of the RBD program to predict dynamic response in the vertical direction we have considered vertical irregularity in the track profile as an input. A vertical disturbance in the form of a sinusoidal vertical irregularity was input. The analytical representation of the sinusoidal irregularity as expressed in Eq.(5.3) was used with the vertical irregularity parameters $\Delta_{ir} = (0.0254 \sim 0.0381)\ m$ and $k_{ir} = (0.0656 \sim 0.0820)\ m^{-1}$ (Garg and Dukkipati (1984)). For the simulation reported in this section the values of $\Delta_{ir} = 0.03\ m$ and $k_{ir} = 0.07\ m^{-1}$ were used. With the chosen parameter $k_{ir} = 0.07$, the corresponding wavelength of the irregularity was 28.57 m. The vertical irregularity was assumed to be

located at the fifth metre of travel as shown in Fig 5.12. Simulations were carried out at two constant speeds of 15 m/s (54 km/h) and 25 m/s (90 km/h).

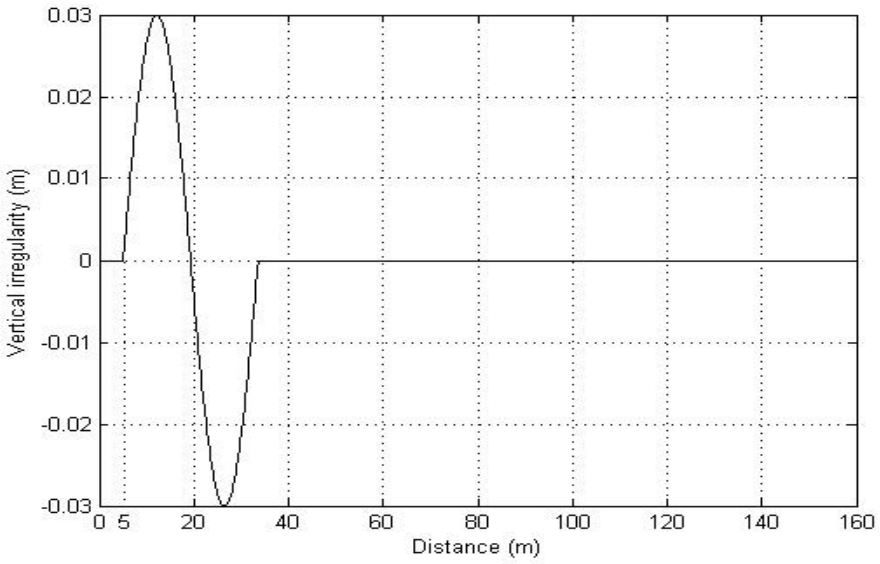

Figure 5.12. Input Track Vertical Irregularity

The dynamic response of the bogie frame in the vertical direction calculated by the RBD program at 15 m/s and 25 m/s due to the input of the track vertical irregularity is exhibited in Fig.5.13, while the corresponding response calculated using VAMPIRE is shown in Fig.5.14. It can be seen that the results calculated by the RBD program and VAMPIRE agree very well both at the low speed of 15 m/s and the high speed of 25 m/s. The amplitude and wavelength obtained from the RBD program were found to have almost exactly the same value as that obtained from VAMPIRE. The associated frequency spectrums of the bogie frame vertical oscillation calculated by the RBD program and VAMPIRE are shown in Fig.5.15 (a) and (b) respectively.

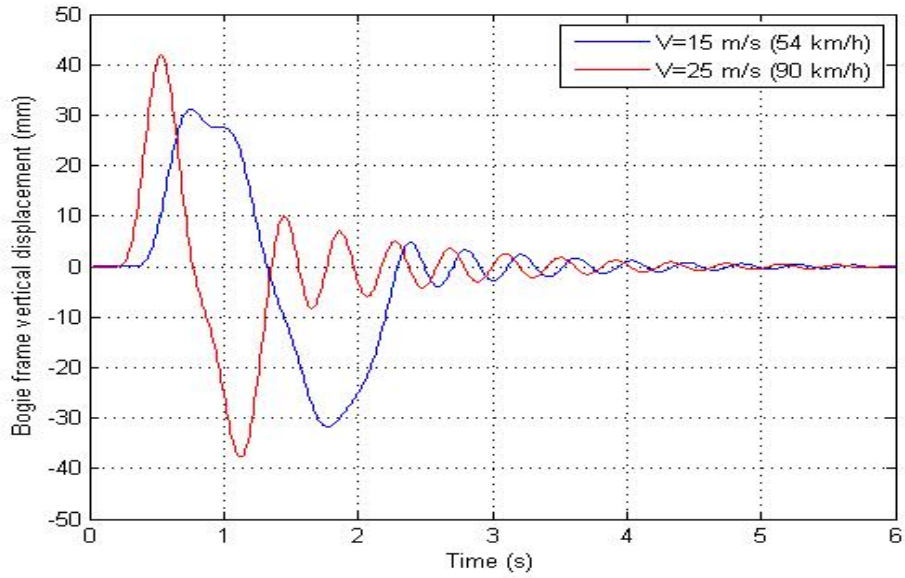

Figure 5.13. Bogie frame vertical displacement calculated by RBD program

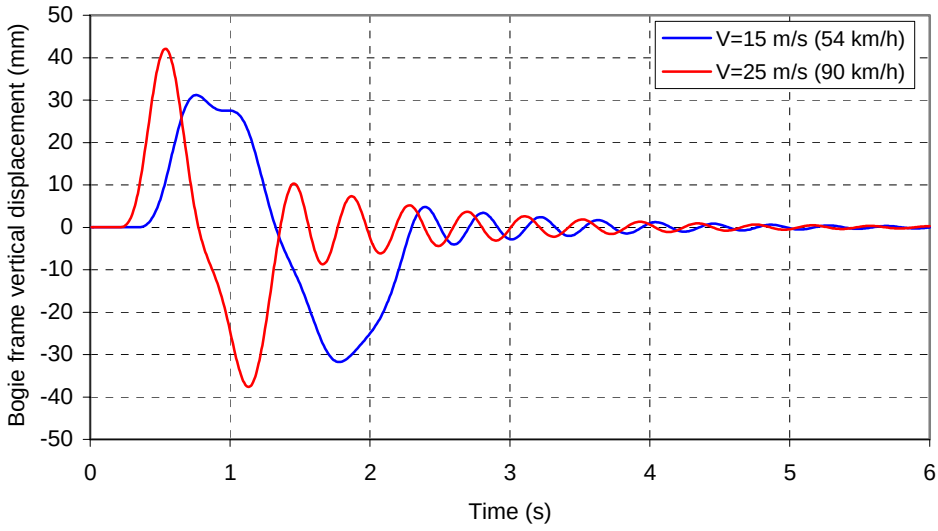

Figure 5.14. Bogie frame vertical displacement calculated by VAMPIRE

Two peaks are found in the frequency spectrum shown in Fig.5.15 (a) and (b). The peak at the low frequency is related to the forced excitation due to the track irregularity. The frequency of this peak normally changes with the change in speed. At the speed of 15 m/s the first peak has been found to occur at 0.48 Hz and 0.49 Hz respectively as per

predictions of the RBD program and VAMPIRE. At the speed of 25 m/s the first peak frequency has been determined as 0.77 Hz and 0.78 Hz respectively by RBD program and VAMPIRE. The second peak at the higher frequency is related to the natural frequency (2.31 Hz as calculated by the RBD program and 2.34 Hz as calculated by VAMPIRE) of the system in the vertical direction. The frequency of this second peak, therefore, has not changed with the changes of the speed of the bogie.

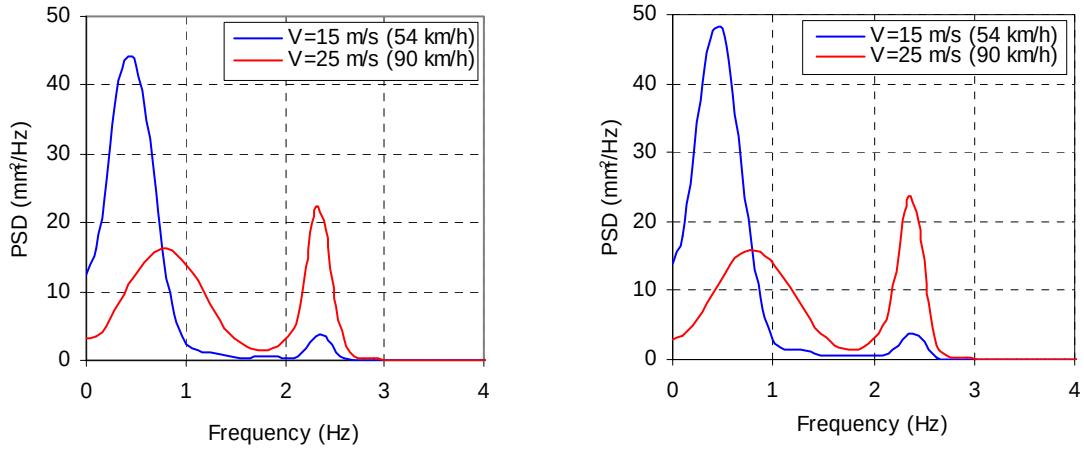

(a) RBD Program (b) VAMPIRE

Figure 5.15. Frequency spectrum of bogie frame vertical oscillation

Fig.5.16 presents the axle load time series due to the same sine wave vertical irregularity calculated by the RBD program at the speed of 15 m/s (Fig.5.16.a) and 25 m/s (Fig.5.16.b). It also agrees very well with the similar information calculated by VAMPIRE shown in Fig 5.17 (a) and (b). The different phase of the axle load oscillation between the leading and the trailing wheelset shows that the given vertical irregularity also generated bogie pitch because both wheelsets did not contact the track irregularity at the same time; the delay was due to the distance between axles and the running speed.

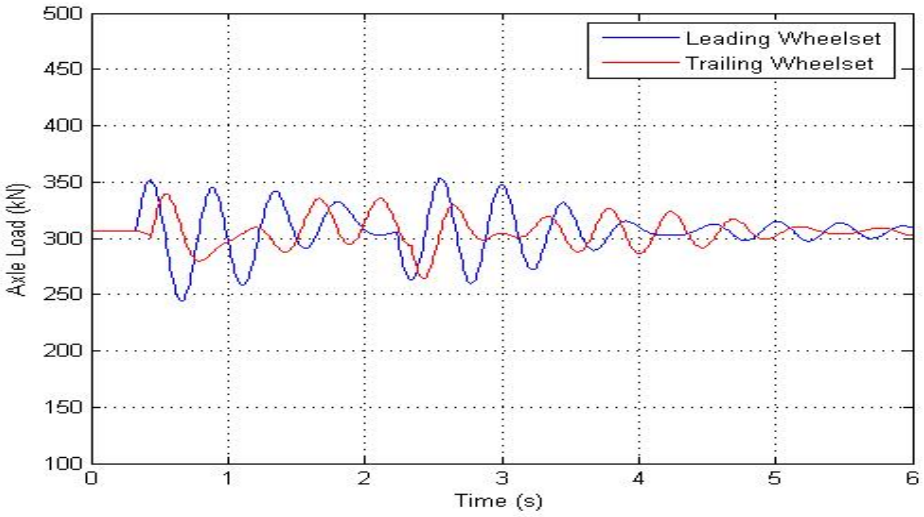

(a.) V = 15 m/s (54 km/h)

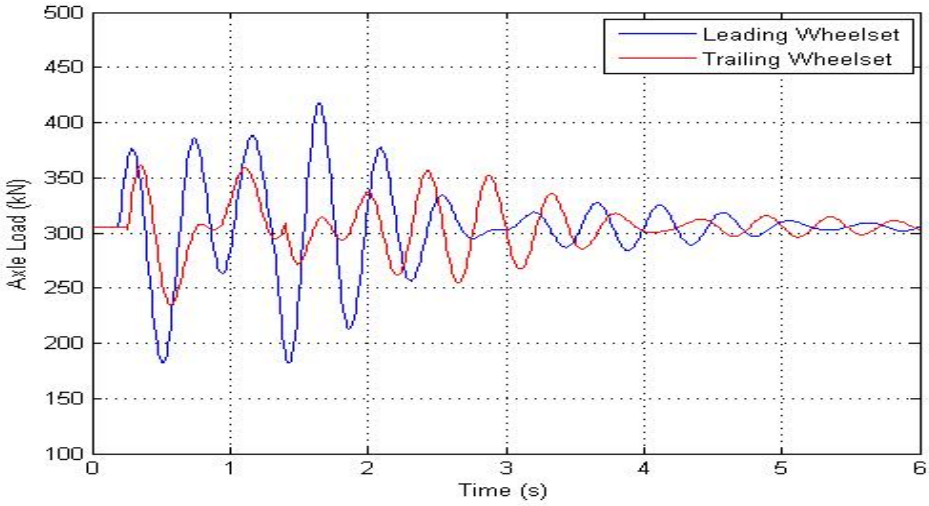

(b.) V=25 m/s (90 km/h)

Figure 5.16. Axle load due to vertical irregularity calculated by RBD program

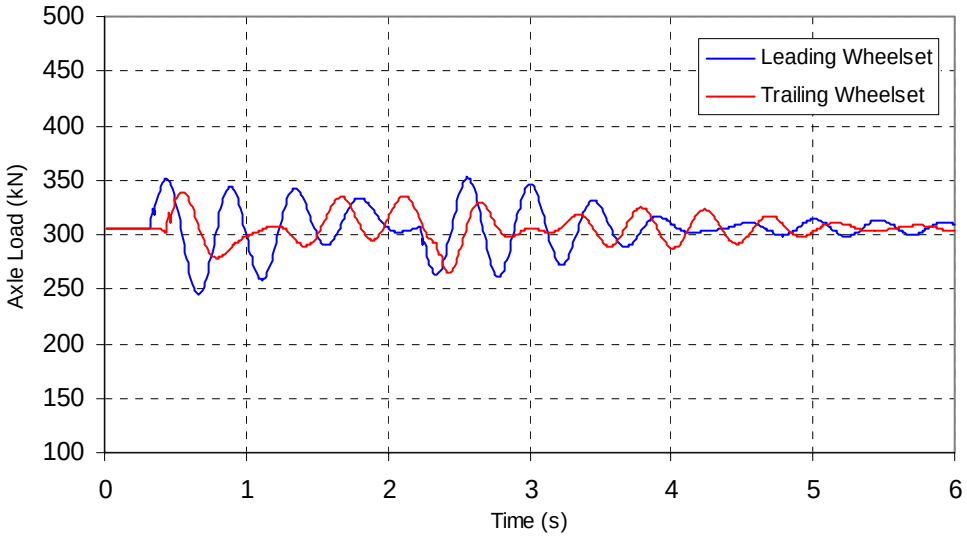

(a.) V=15 m/s (54 km/h)

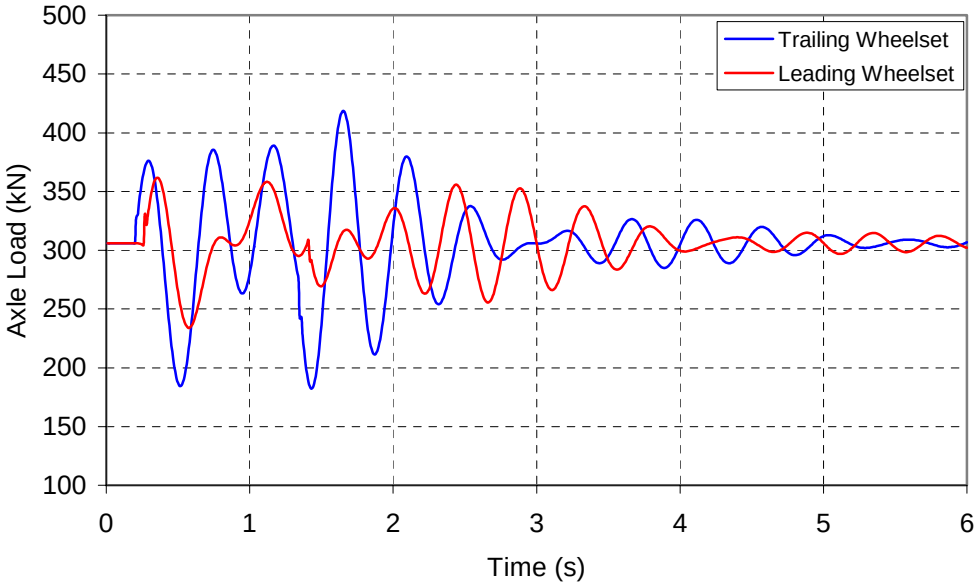

(b.)V=25 m/s (90 km/h)

Figure 5.17. Axle load due to vertical irregularity calculated by VAMPIRE

5.3.3. Response to Track Cross Level Irregularity

Response of the system to cross-level irregularity was also studied. Cross-level irregularity is defined as the height difference between the right and the left rail (see Section 2.4). It is assumed to be positive if the left rail is higher than the right rail when the observer is facing the running direction of the bogie. A typical form of the cross level irregularity, which is called a "plateau" is shown in Fig.5.18.

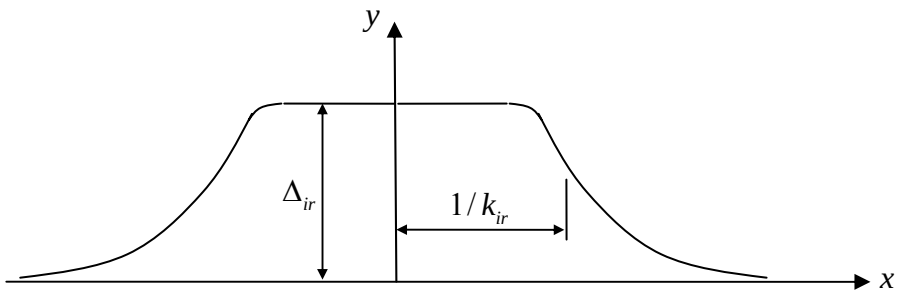

Figure 5.18. Cross level plateau irregularity and its parameters

The analytical representation of the plateau can be expressed as:

$$y(x) = \left(\frac{{\Delta_{ir}}^2}{1 + (k_{ir} x)^8} \right)^{1/2} \qquad (5.4)$$

where x is the longitudinal travel and y is the height difference between the right and the left rails. For the simulation reported in this section the values of $\Delta_{ir} = 0.02\ m$ and $k_{ir} = 0.07\ m^{-1}$ have been used based on the range of values given by Garg and Dukkipati (1984), which gives the plateau irregularity as shown in Fig.5.19.

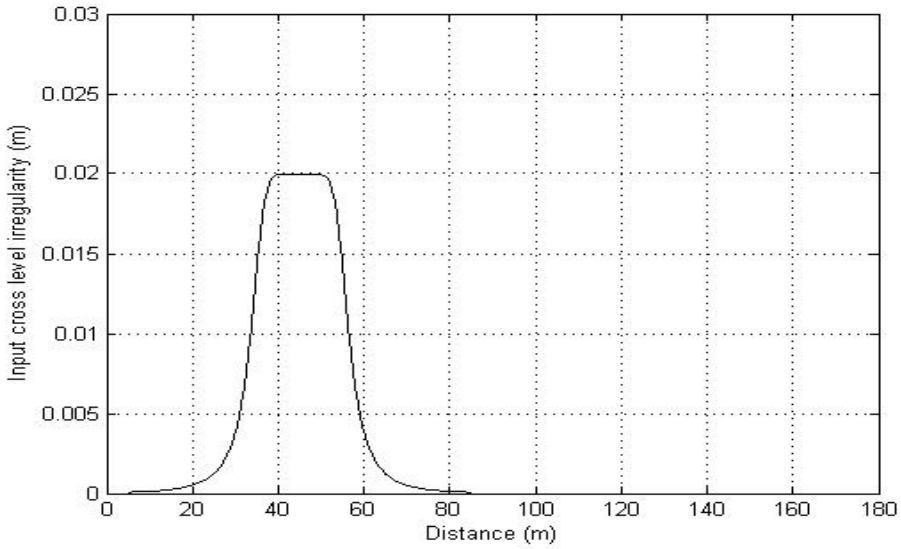

Figure 5.19. Input cross level irregularity

The input of cross-level irregularity caused the rolling motion of the bogie as revealed in Fig.5.20 calculated by the RBD program at the speed of 15 m/s (54 km/h) and 25 m/s (90 km/h). In general, this result agrees very well with that of VAMPIRE shown in Fig.5.21.

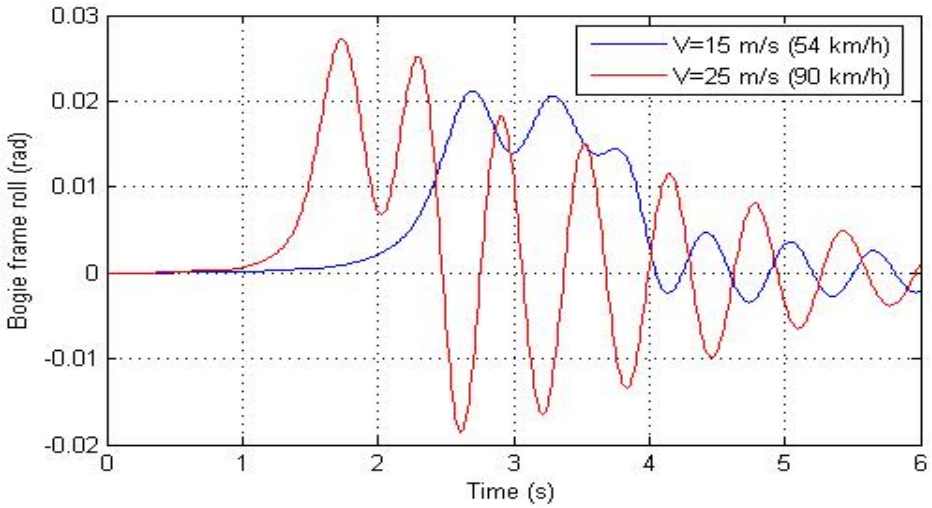

Figure 5.20. Bogie frame roll calculated by RBD program

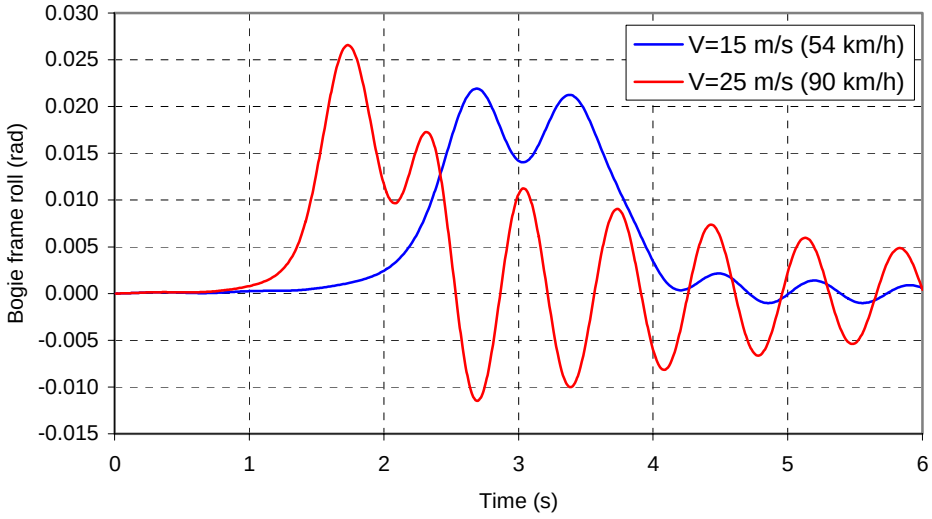

Figure 5.21. Bogie frame roll calculated by VAMPIRE

The maximum roll occurred at the track section containing the irregularity. At 15 m/s and 25 m/s, the RBD program calculated maximum rolling of 0.021 radian and 0.028 radian respectively; and VAMPIRE gave 0.022 radian and 0.027 radian respectively.

The calculated wheel load time series from the RBD program at the right and the left wheel of the leading wheelset due to this cross-level irregularity is exhibited in Figure 5.22 and the result calculated by VAMPIRE is presented in Fig 5.23. At the speed of 15 m/s the RBD program recorded 188 kN maximum value while VAMPIRE obtained 169 kN (approximately 11 % error margin). At the speed of 25 m/s the RBD program calculated 243 kN while VAMPIRE gave 224 kN (approximately 8 % error margin). The opposite phase of the wheel load between the left and the right rail shows that the bogie was subjected to rolling motion.

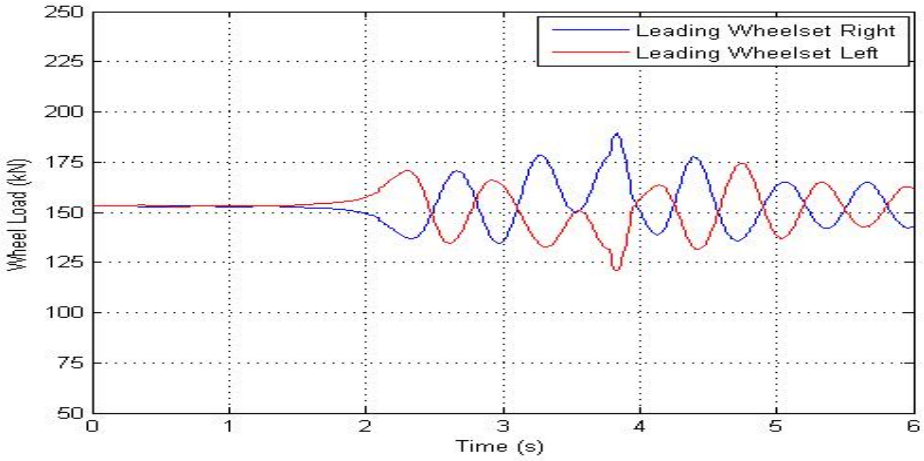

(a.) V=15 m/s (54 km/h)

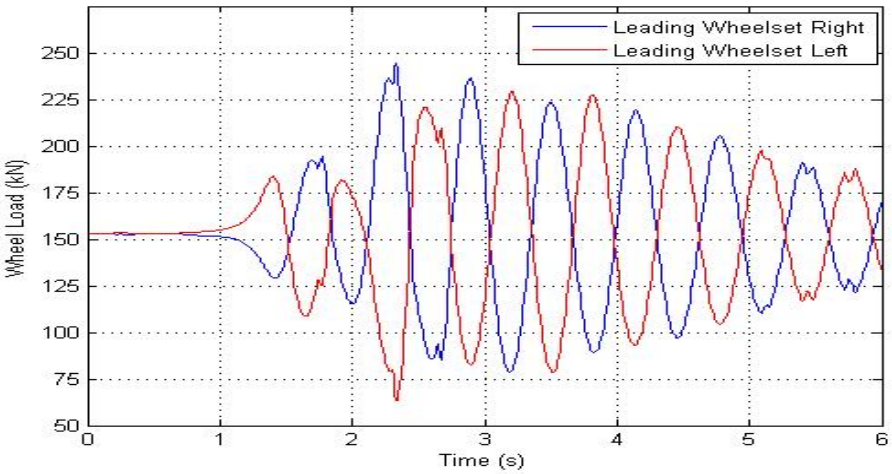

(b.) V=25 km/h (90 km/h)

Figure 5.22. Wheel load due to cross level irregularity calculated by RBD program

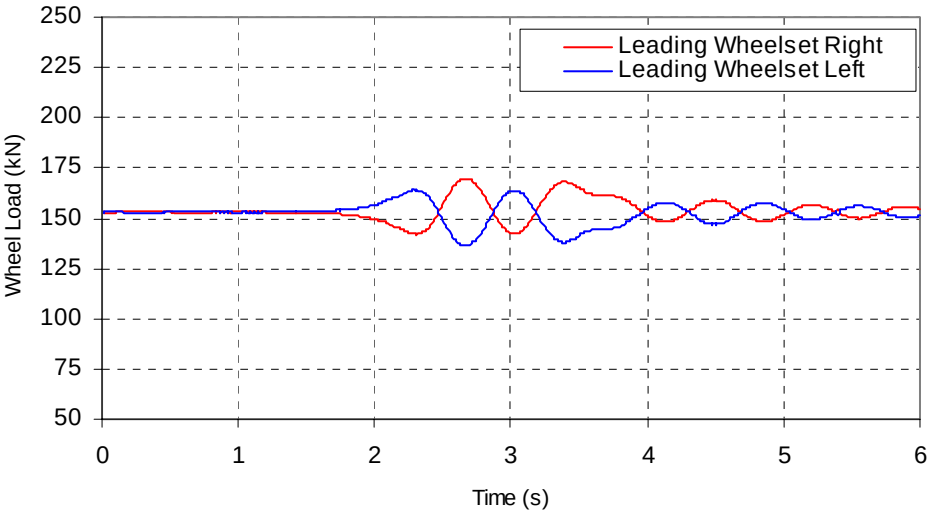

(a.) V=15 m/s (54 km/h)

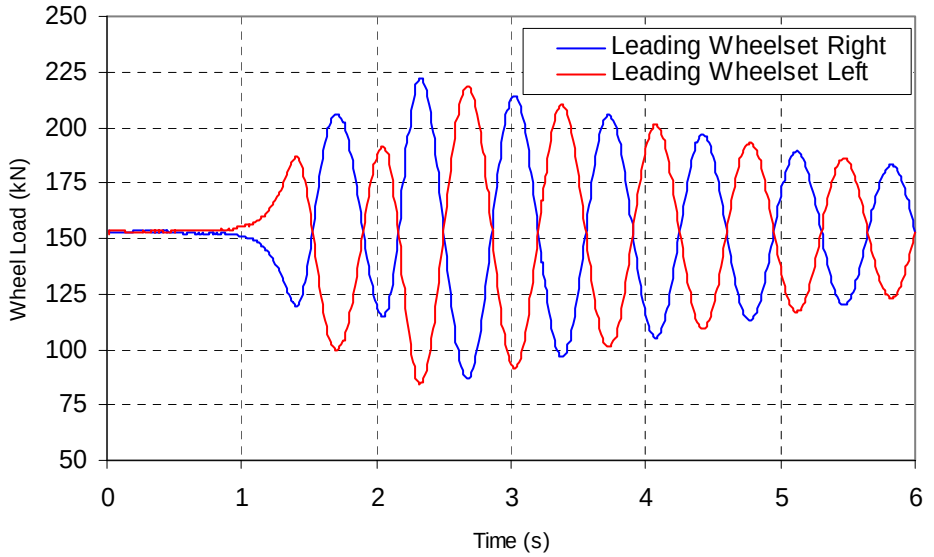

(b.) V=25 m/s (90 km/h)

Figure 5.23. Wheel load due to cross level irregularity calculated by VAMPIRE

5. 4. APPLICATION OF LONGITUDINAL FORCE

5.4.1. Speed Profile

The simulation reported in this section is intended to examine the capability of the RBD program to calculate the speed profile due to the application of the longitudinal force. For this purpose, a sequence of traction and braking torques was applied to both wheelsets of the bogie system. To the best of the knowledge of the author, none of the commercial wagon dynamics programs available in the market has the potential to predict what the RBD program has provided. Therefore the results of the RBD program (the output speed profile) in this section could not be validated using VAMPIRE.

The sequence of traction and braking torque applied to each wheelset is presented graphically in Fig. 5.24; a positive sign of torque represents traction and a negative sign represents braking. The initial speed of the bogie was set as 0.01 m/s to avoid numerical instability caused by floating point arithmetic in the calculation of the creepage (see Section 2.6).

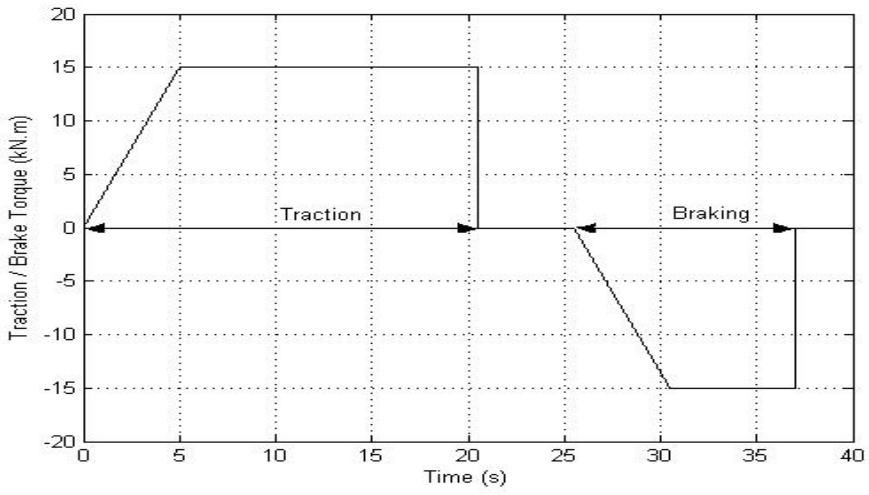

Figure 5.24. Traction/Braking torque profile

The traction torque was assumed to linearly increase from zero to 15 kN.m within 5 seconds, then remained constant until the bogie reached 20 m/s and then the traction torque was assumed to be released to zero. After maintaining a constant speed of 20 m/s for 5 seconds the brake torque was applied. Similar to traction torque, the brake torque was assumed to be gradually increased in 5 seconds from zero to 15 kN.m and was held at this value until the speed reduced to 10 m/s and then the brake was assumed to be released to zero.

The output acceleration and speed profile due to the traction/brake torque profile calculated by the RBD program is displayed in Fig. 5.25 and Fig.5.26 respectively. From t=0 sec to t=5 sec the longitudinal acceleration increased linearly from zero to a maximum value of 1.109 m/s^2 due to the gradual increment of the applied traction torque. During this time period the speed increment remained non-linear. After t=5 sec the acceleration was held constant until the bogie attained 20 m/s (approximately at t=20.5 sec). As the traction was reduced to zero, the acceleration reduced to zero between t=20.5 sec and t=25.5 sec. A similar trend was also observed during the braking process, where the speed reduction was not linear for the first five seconds of the braking process and then under the constant maximum braking torque the speed decreased linearly with a constant deceleration of about 1.109 m/s^2.

Fig.5.27 shows the output angular velocity of the leading and the trailing wheelsets and Fig 5.28 shows the total travel distance during the process which shows the bogie had travelled 496 m when the simulation ended. Fig.5.28 also reveals that the linear increment of travel distance happened at the constant speed section; i.e. between t=20.5 sec and t=25.5 sec and between t=37 and to t=40 sec.

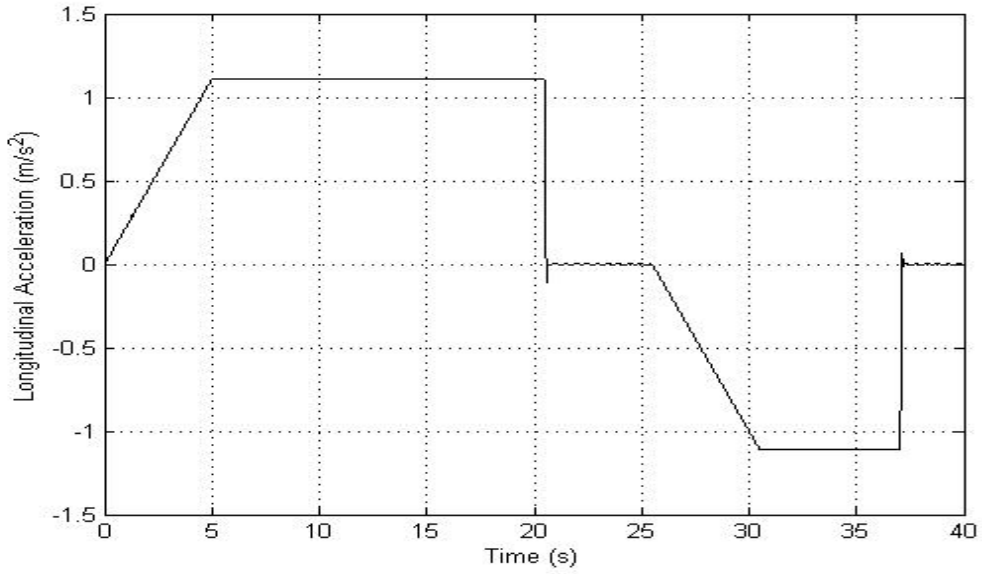

Figure 5.25. Output longitudinal acceleration

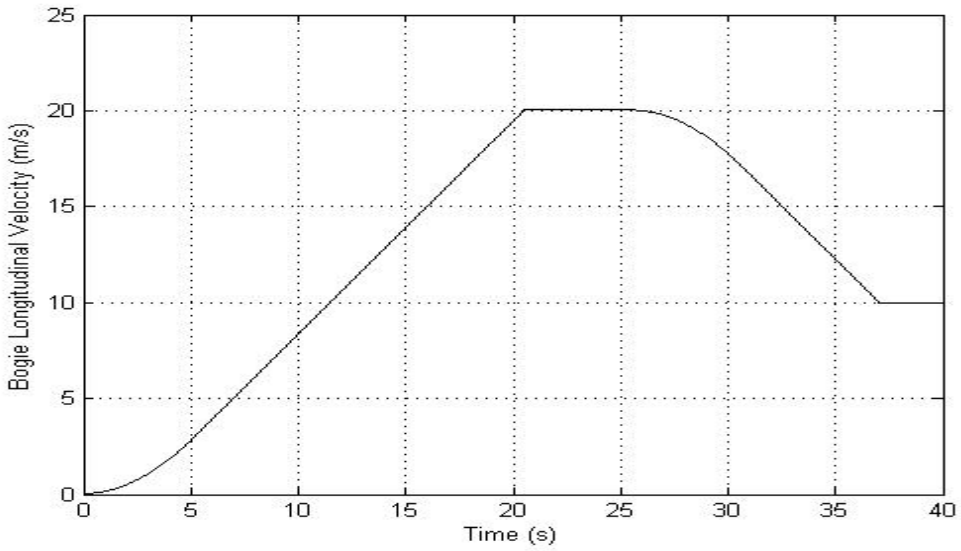

Figure 5.26. Output speed profile

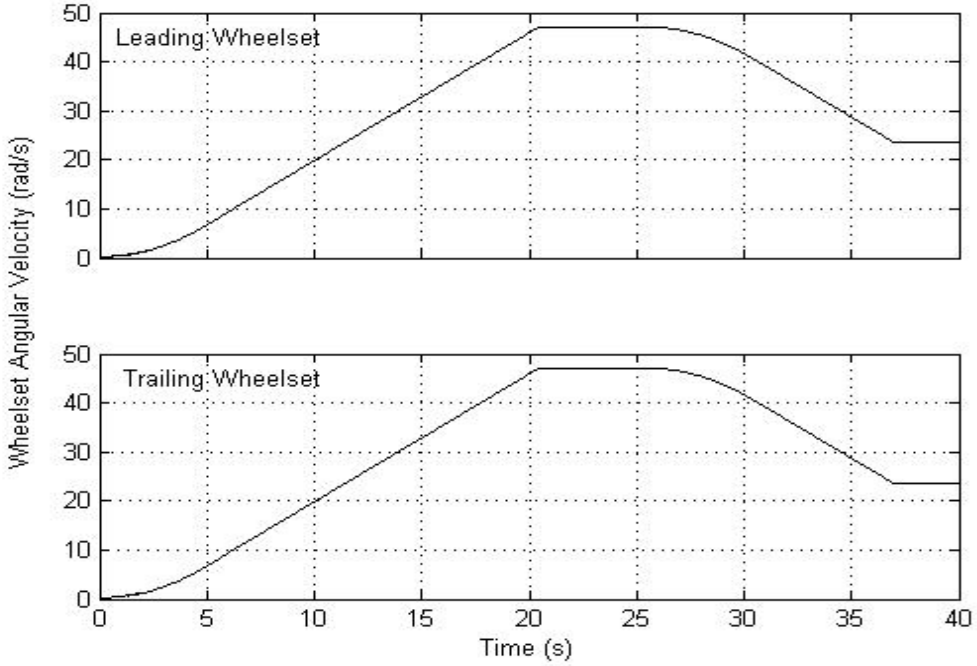

Figure 5.27. Output wheelset angular velocity (rad/s)

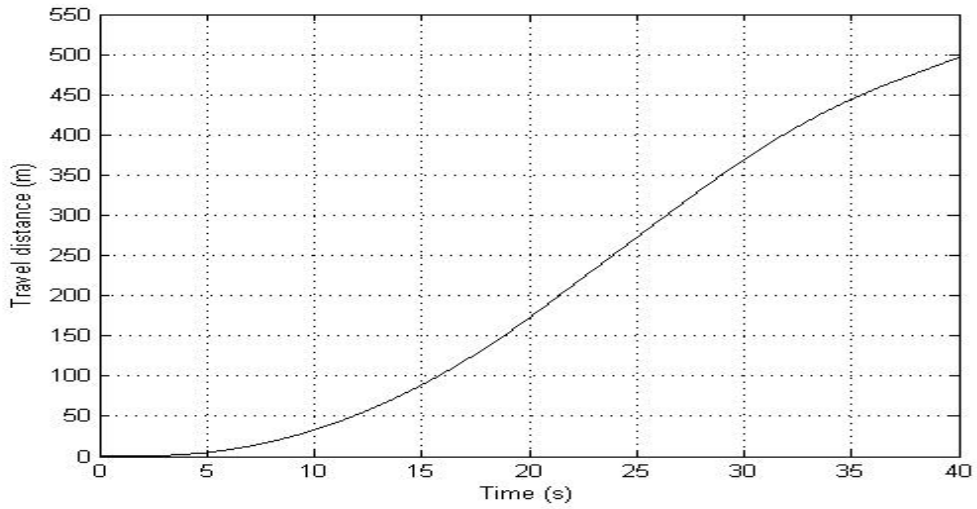

Figure 5.28. Travel distance

The speed profile and the wheelset angular velocity (as well as travel distance and wheelset rotation) calculated by the RBD program as the function of brake torque must be validated using an independent method. For this purpose, a full scale lab test was carried out. Chapter 6, 7 and 8 report this experiment and results including comparison with the simulation data set.

5.4.2. Bogie Pitch due to Longitudinal Force Application

As the longitudinal force due to traction or braking acts at a line below the centre of mass of the bogie frame, there exists a pitch moment acting on the bogie frame. Thus, during the application of the longitudinal force, pitch motion of the bogie frame is normally expected. Fig.5.29. shows the bogie frame pitch displacements during the application of the traction/braking profile of Fig.5.24. As expected, Fig.5.29 reveals that during traction, the pitch displacement attained negative values. The sudden reduction of the traction torque from 15 kN.m to zero (at t=20.5 sec) caused the bogie frame to experience a pitch oscillation when it ran at constant speed (between t=20.5 sec and t=25.5 sec). Then, during braking (t=25.5 sec and t=37 sec) the pitch displacement attained positive values. When the braking was suddenly released, the bogie frame experienced a pitch oscillation. These results show that the RBD program can truly model the longitudinal dynamics of the bogie due to application of traction and braking torques in a natural way.

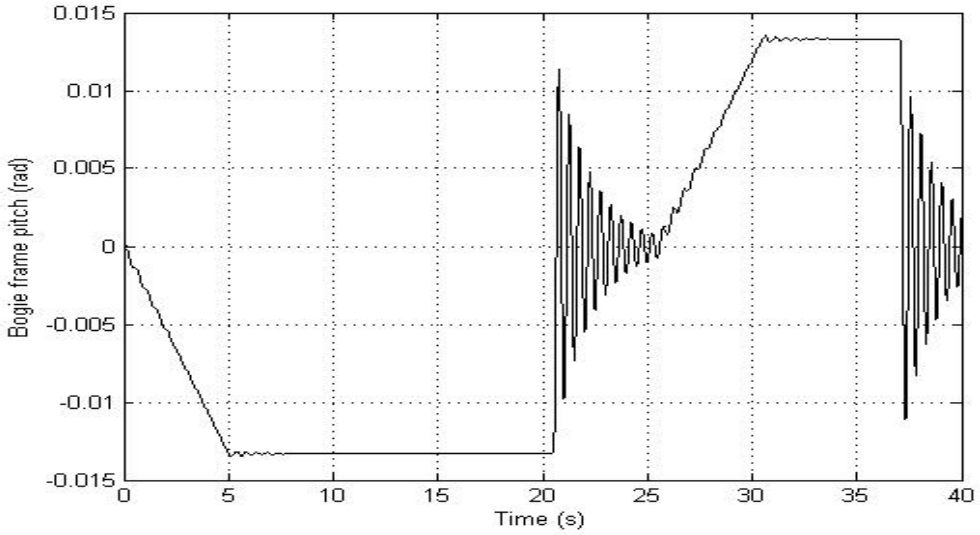

Figure 5.29. Bogie frame pitch calculated by RBD program

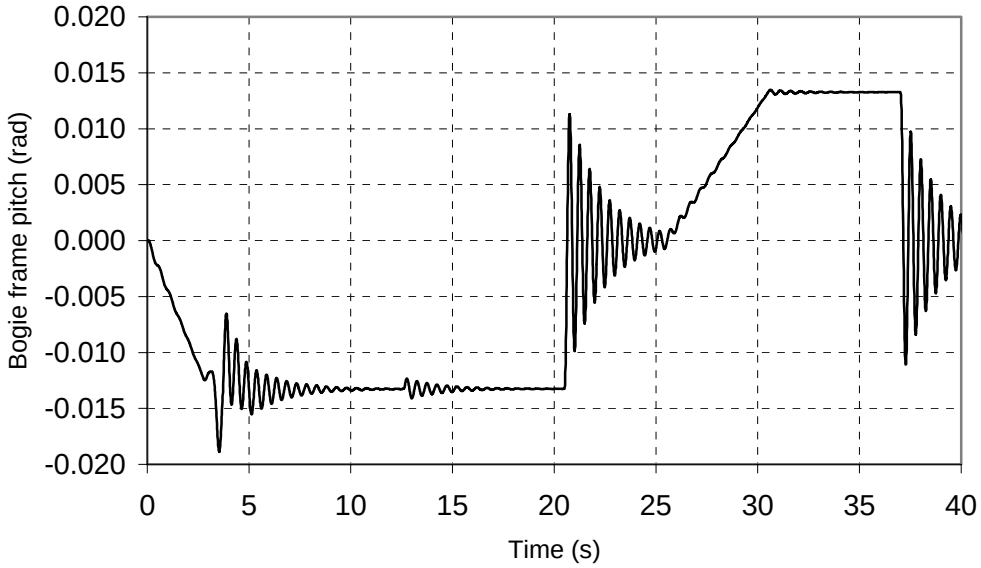

Figure 5.30. Bogie frame pitch calculated by VAMPIRE

The output speed profile in Fig.5.26 as well as the brake/traction torque profile of Fig.5.24 was then used as input for simulation in VAMPIRE. The bogie frame pitch displacement calculated by VAMPIRE is presented in Fig.5.30 which shows good

agreement with the prediction by the RBD program shown in Fig.5.29. Only small differences were found especially in the very low speed region (between 4 sec to 10 sec time period where the speed ranged between 3 m/s and 8 m/s). The pitch vibration predicted by VAMPIRE at low speed is not of practical significance and hence not further explored.

5.4.3. Bogie Lateral Dynamics under Variable Speed

The RBD program has the capability to calculate longitudinal dynamics due to traction and braking whilst calculating the response in the lateral and the vertical directions due to track irregularity. This section reports some examples of such simulation to investigate the lateral dynamics during traction and braking using the RBD program. The output speed profile calculated by the RBD program was then used as an input into VAMPIRE simulation and the results compared.

Lateral dynamics under traction

Two cases of traction application were investigated. First the traction torque was applied and increased gradually from zero to 15 kN.m in five seconds (normal application) as shown in Fig.5.31.(a) and then was held constant until the bogie attained 20 m/s (72 km/h). Fig.5.31.(b) shows the output speed profile (from the RBD program) due the input traction torque. While the bogie was under traction, the relevant section of the track was assumed to contain the sinusoidal lateral track irregularity as shown in Fig.5.32.

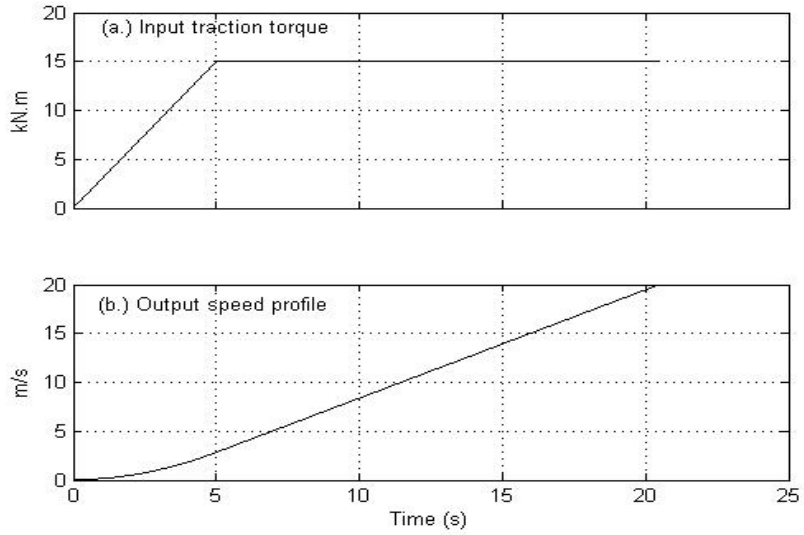

Figure 5.31. Input traction torque (normal application) and output speed profile calculated by RBD program

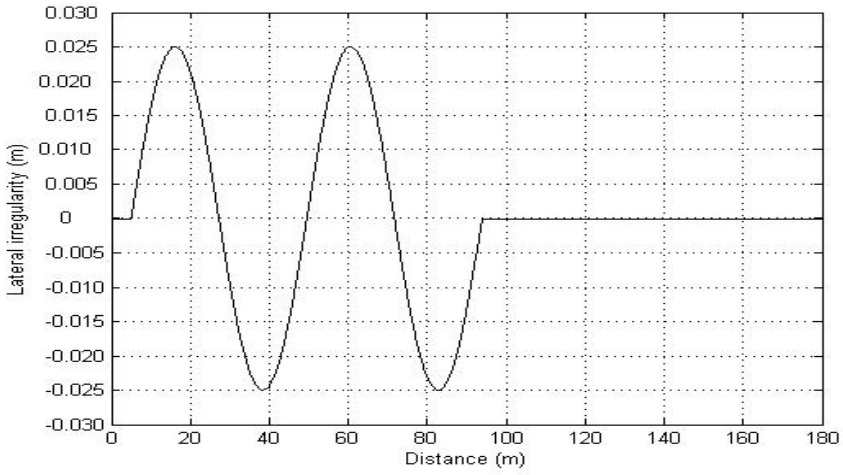

Figure 5.32. Input lateral track irregularity

Fig.5.33 shows the wheelset lateral displacement calculated by the RBD program during the traction application during movement over the track with irregularity. The figure reveals that the wheelsets experienced stable oscillation with maximum amplitude of approximately 9 mm. The frequency of oscillation increased with the

increase in speed as depicted by the shorter time period of the oscillation waves at the higher speed.

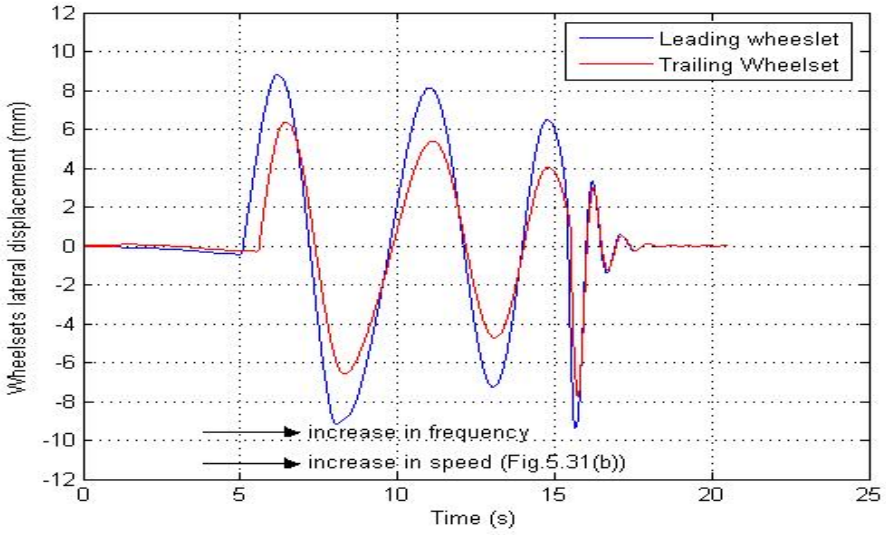

Figure 5.33. Wheelset lateral displacement during normal traction calculated by the RBD program

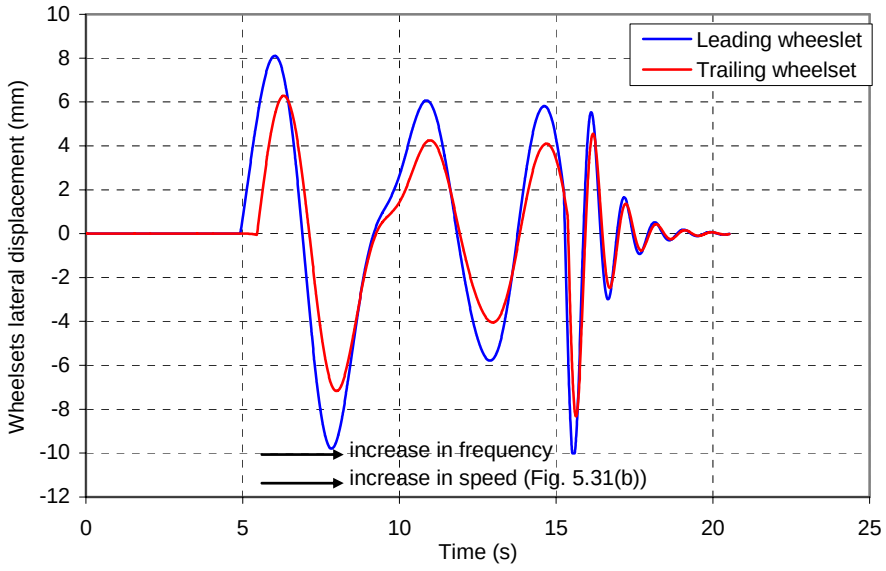

Figure 5.34. Wheelset lateral displacement during normal traction calculated by VAMPIRE

By inputting the traction torque as well as the speed profile calculated by the RBD program, an equivalent simulation was conducted by VAMPIRE. The wheelset lateral displacement calculated by VAMPIRE is exhibited in Fig.5.34. The result given by VAMPIRE agrees very well with the results of the RBD program shown in Fig.5.33. It should be remembered that VAMPIRE can calculate *only* if the speed profile was accurately input whereas the RBD program can determine the lateral dynamics in a natural way with the input of brake torque and track irregularity.

Quick application of traction torque was considered in the second case where the traction torque was increased from zero to 15 kN.m within one second before it was held constant until the bogie reached 20 m/s (72 km/h). The traction torque and the output speed profile are shown in Fig.5.35(a) and 5.35(b) respectively. As expected, compared to the normal traction application in Fig.5.31, the bogie attained the speed of 20 m/s quicker (in 18.2 seconds compared to 20.5 sec of normal traction).

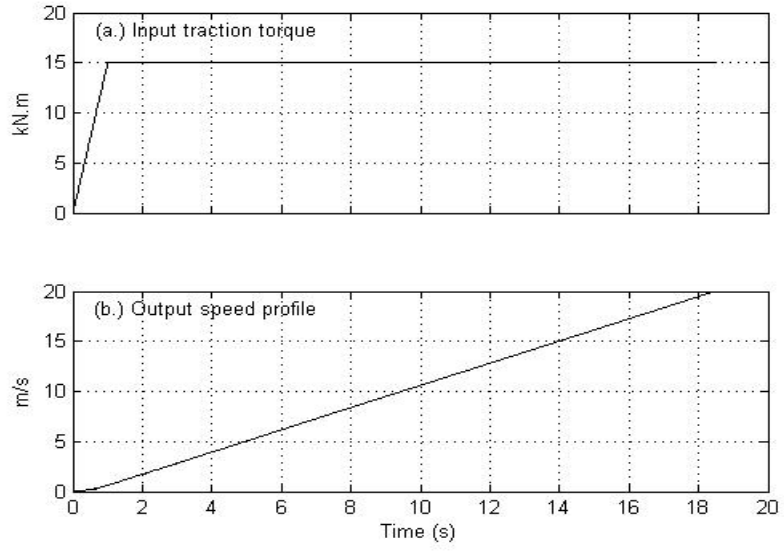

Figure 5.35. Input traction torque (quick application) and output speed profile calculated by RBD program

Lateral track irregularity shown in Fig 5.32 was also used in this second case. The lateral response of the bogie in the lateral direction calculated by the RBD program, in terms of wheelset lateral displacement, is shown in Fig.5.36. This result does not seem to be much different to the one just presented in Fig.5.33 from the simulation under normal application of traction. The wheelset oscillation remained stable with the frequency increased due to the increase in speed.

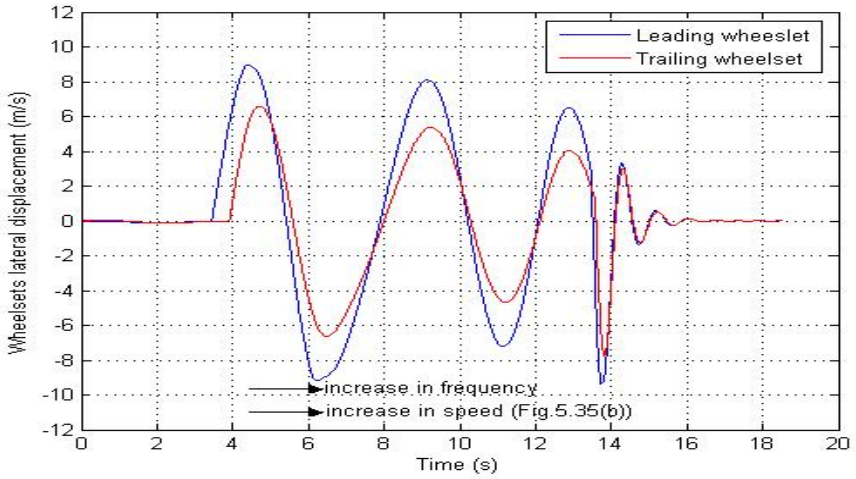

Figure 5.36. Wheelset lateral displacement during quick traction calculated - RBD program

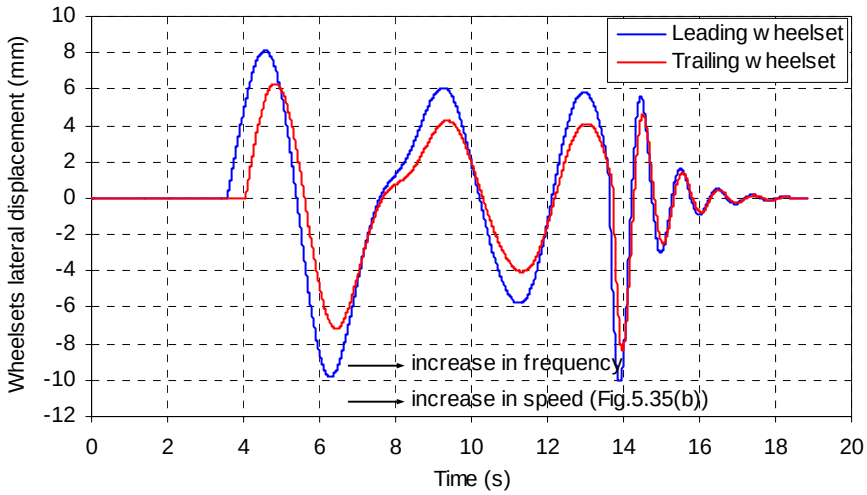

Figure 5.37. Wheelset lateral displacement during quick traction - VAMPIRE

The simulation using VAMPIRE also provided similar results as shown in Fig.5.37. These results show that as long as the speed of the bogie remains below its hunting speed level, its lateral response remains the same irrespective of the type of traction application (quick/normal).

Lateral dynamics under braking

Two cases of braking application were investigated. The simulation started at the constant speed 20 m/s (72 km/h). The braking was input as a negative pitch torque applied to the wheelset. First the normal application of braking torque was applied (brake torque increased gradually from zero to 15 kN.m in five seconds; from t=1 sec to t=6 sec) and then was held constant until the bogie stopped ("stop" here is assumed to be 0.01 m/s as absolute zero speed to avoid numerical instability) shown in Fig.5.38(a). Fig.5.38(b) shows the output speed profile. While braked, the bogie was running on the track that contained the sinusoidal lateral track irregularity as shown in Fig.5.32.

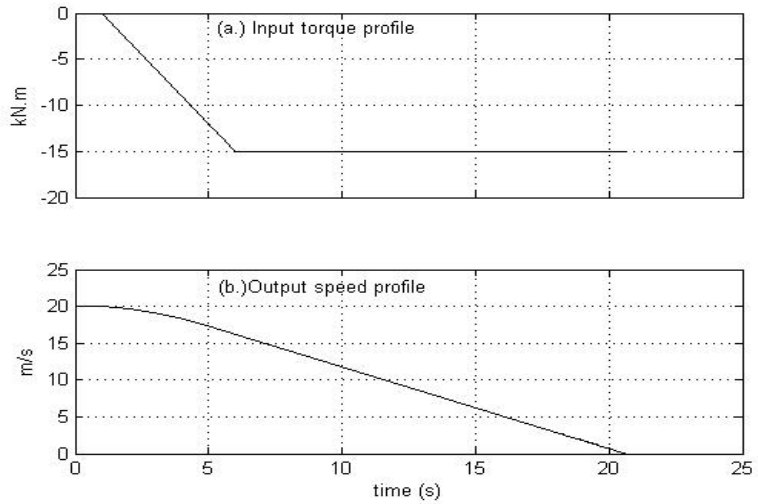

Figure 5.38. Input braking torque (normal application) and output speed profile

Fig.5.39 shows the wheelset lateral displacement during normal braking application during movement over the track with irregularity. This figure shows that the wheelsets

experienced stable oscillation with maximum amplitude of approximately 10.5 mm. The frequency of oscillation has decreased with the decrease in speed (shown by the longer time period of the oscillation waves at the higher speed). By inputting the braking torque as well as the speed profile calculated by the RBD program, an equivalent simulation was then conducted in VAMPIRE. The wheelset lateral displacement calculated by VAMPIRE is exhibited in Fig.5.40 which shows good agreement with that of the result calculated by the RBD program presented in Fig.5.39.

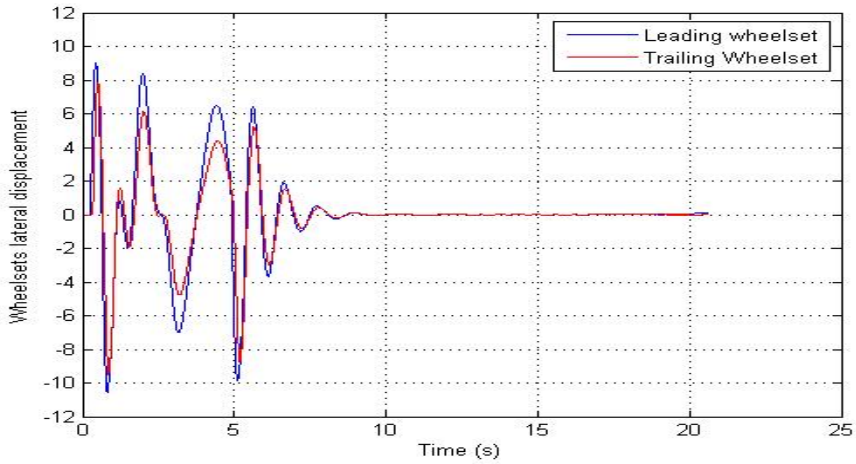

Figure 5.39. Wheelset lateral displacement during normal braking - RBD program

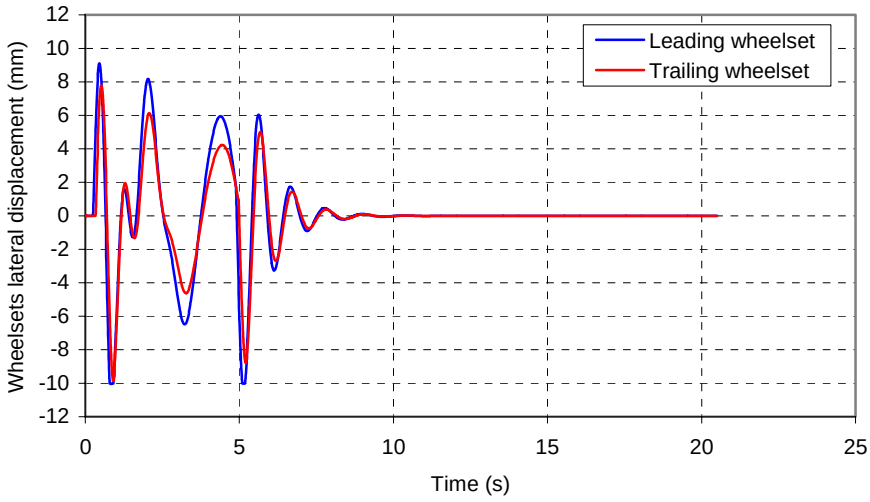

Figure 5.40. Wheelset lateral displacement during normal braking – VAMPIRE

The second case was concerned with quick braking application, where the braking torque was increased very quickly from zero to 15 kN.m within one second before it was held constant until the bogie stopped. As previously explained, “stop” here is assumed to be 0.01 m/s. The initial speed was 20 m/s (72 km/h). The braking torque and the output speed profiles are exhibited in Fig.5.41(a) and 5.41(b) respectively.

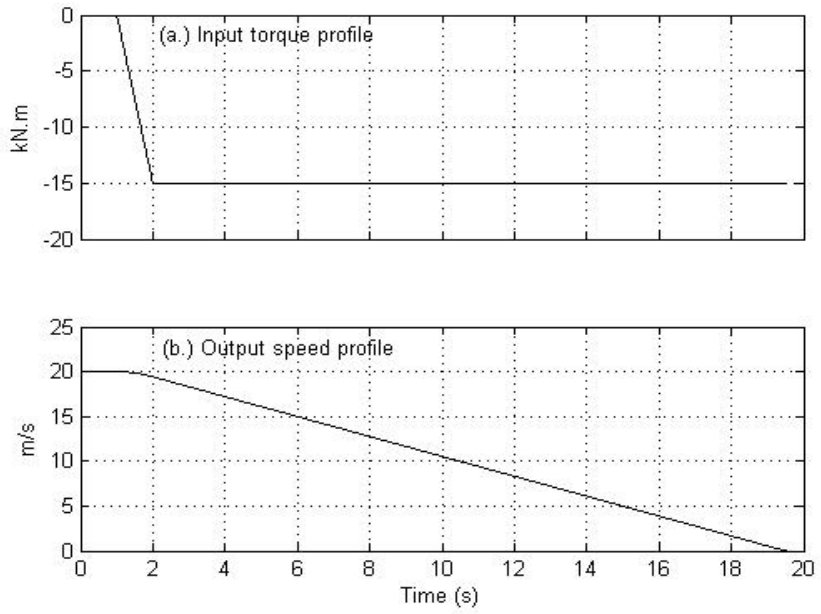

Figure 5.41. Input braking torque (quick application) and output speed profile

During the quick braking application the bogie was running on the same lateral track irregularity shown in Fig 5.32. The response of the bogie in the lateral direction calculated by the RBD program, which is represented by the wheelset lateral displacement, is shown in Fig.5.42. This result does not seem to be much different to the one presented in Fig.5.39 from the simulation under normal braking. The wheelset oscillation remained stable with the frequency decreased due to the decrease in speed. The simulation using VAMPIRE also provided similar result as shown in Fig.5.43.

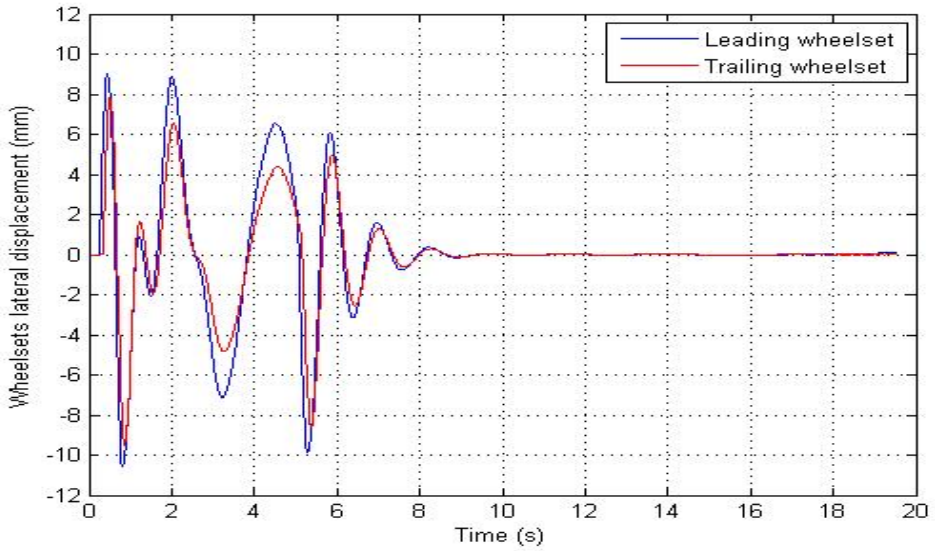

Figure 5.42. Wheelset lateral displacement under quick braking - RBD program

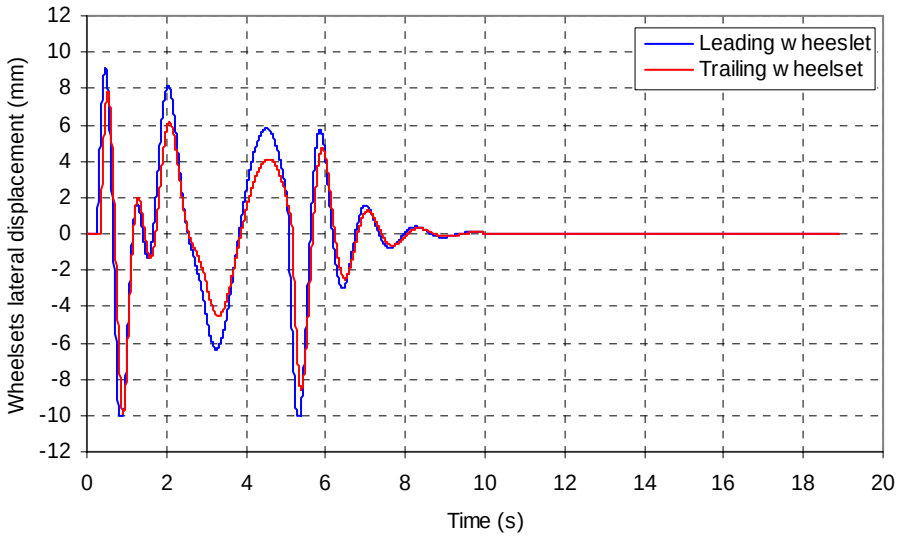

Figure 5.43. Wheelset lateral displacement under quick braking - VAMPIRE

5.5. BOGIE DYNAMICS UNDER HEAVY BRAKING

Two cases of heavy braking application were studied and reported in this section. Obviously these results containing wheel skid can not be compared with the simulations using VAMPIRE or other commercial package programs as they do not

explicitly include wheelset pitch in their formulation. The only option for validating these skid results is to carry out careful laboratory experiments capable of precisely measuring wheelset pitch and longitudinal position even under very low speed (due to restrictions in track lengths and increased levels of safety requirement). A full scale lab test satisfying all technical and safety needs was carried out for this purpose. Chapter 6, 7 and 8 report this experiment and results including comparison with the simulation data set.

Case #1 of heavy braking simulation deals with the application of a large brake torque to the leading wheelset while the trailing wheelset was left unbraked. The initial speed was set as V=25 m/s. Previous constant speed simulations (see Section 5.3) have shown that at this speed the bogie remained stable. At t=4 seconds a constant 60 kN.m brake torque was applied to the leading wheelset. The brake torque was specifically chosen large enough to initiate skidding.

The large brake torque application to the leading wheelset that exceeded the adhesion capacity between the wheel and the rail surface caused skidding of the leading wheelset as shown in Fig.5.44. Fig. 5.44(b) shows that the angular velocity of the leading wheelset has decreased rapidly to zero while the forward speed and the angular velocity of the trailing wheelset has remained much greater than zero (Fig.5.44 (a) and (c)).

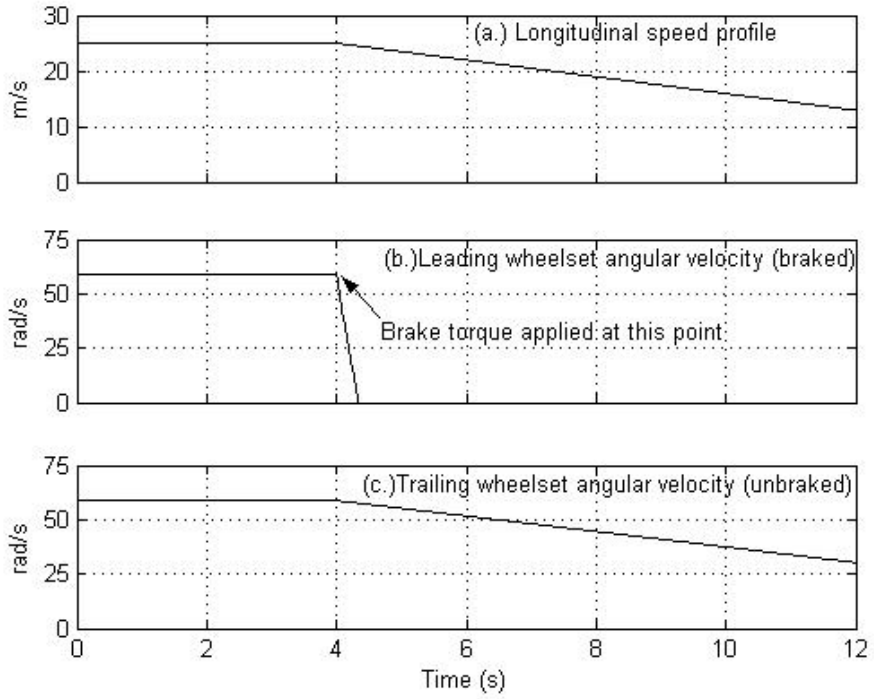

Figure 5.44. Skid on leading wheelset

Prior to the application of braking, the bogie was exposed to the sinusoid lateral irregularity of Fig 5.3. Fig.5.45 revealed that from just after passing this track section containing the lateral irregularity up until the application of brake (t=2 sec to t=4 sec) the bogie remained stable as shown by the reduction of lateral displacement. However it was found that after the application of the brake, which caused the wheelset to skid, the wheelset lateral oscillation became unstable exhibiting hunting motion. The amplitude of the lateral oscillation of the trailing wheelset which was left unbraked remained smaller than the oscillation of the braked leading wheelset.

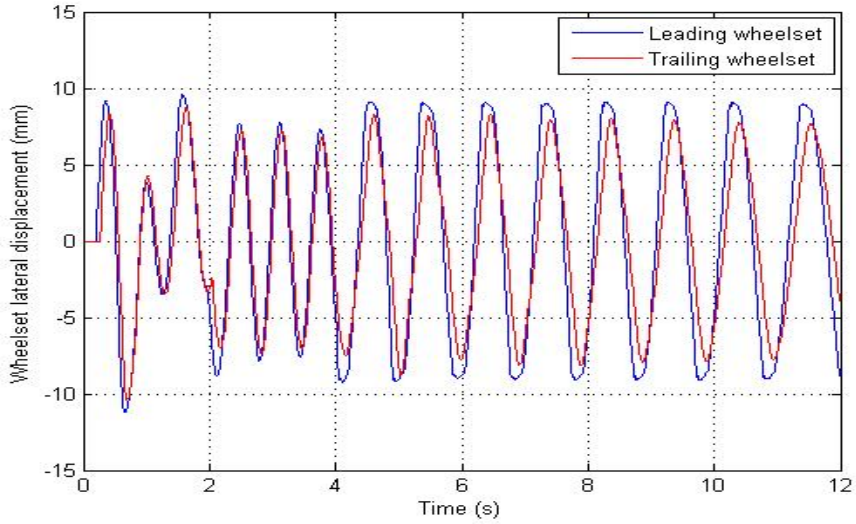

Figure 5.45. Lateral displacement; skid on leading wheelset

Case #2 of heavy braking was related to the application of 60 kN.m braking torques applied to both wheelsets. It caused skidding of both wheelsets as shown in Fig.5.46. This figure shows that the angular velocity of both wheelsets has rapidly decreased to zero while the speed remains non-zero. Prior to the application of braking, the bogie was exposed to the sinusoidal lateral irregularity to initiate the lateral oscillation. The lateral displacement time history is shown in Fig.5.47. Just after passing the track section that contains the lateral irregularity and up until the application of brake (t=2 sec to t=4 sec) the bogie has remained stable as shown by the reduction of lateral displacement. However after the application of the brake, which caused skidding on both wheelsets, the lateral movement of the wheelset became unstable with irregular form of oscillation. Even at low speed (less than 12 m/s), large oscillation wavelengths have been predicted.

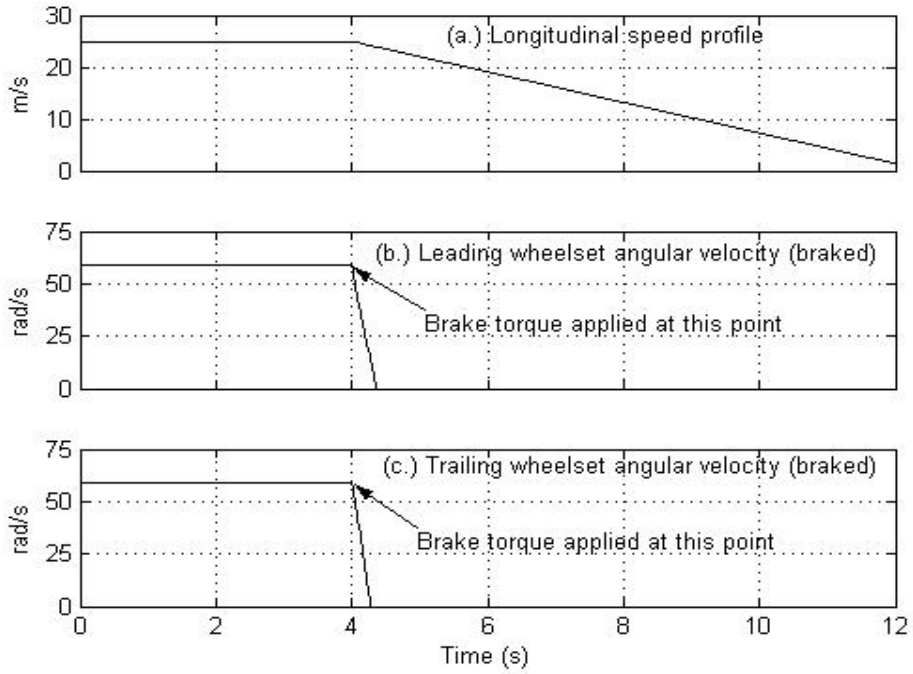

Figure 5.46. Skid on both wheelsets

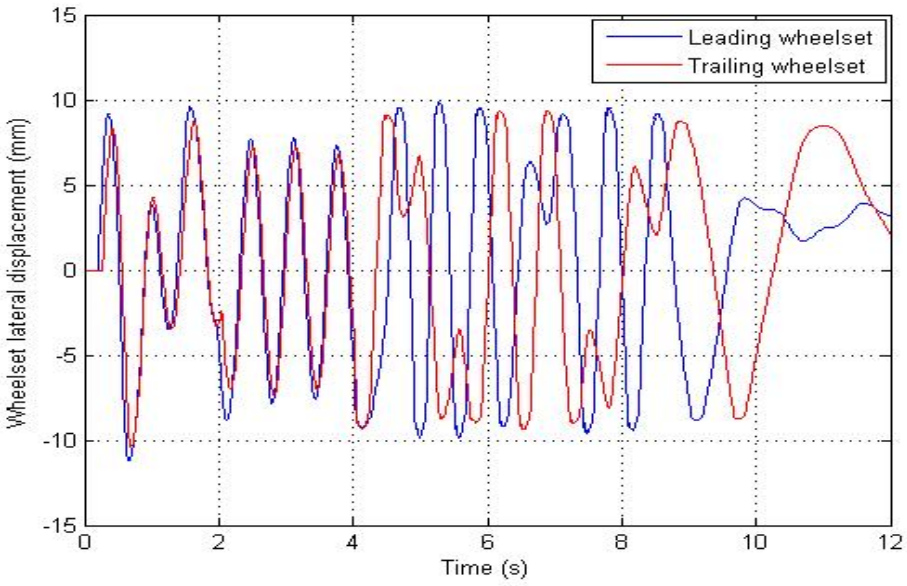

Figure 5.47. Lateral displacement, skid on both wheelsets

5.6. SUMMARY AND CONCLUSION

This chapter has described the capability of the RBD program in predicting the dynamics of the simplified two-axle bogies both under constant speed and under variable speed due to traction and brake. Novel features of the RBD program are the ability to evaluate the speed profile as a function of input braking / traction torques as well as explicitly determine wheelset angular velocity. These features have been demonstrated through examples in this chapter. The results have been validated whenever possible with the simulations using VAMPIRE that illustrated very good agreement. From the results we can draw the following conclusions:

- Under constant speed it was found that the bogie remained laterally stable up to 25 m/s. The insignificant difference between the results of RBD and VAMPIRE might have resulted from the different methods used in the calculation of the contact parameters and creep forces as well as the method of numerical integration used.

- The natural frequency of the bogie suspension in the vertical direction can be clearly detected by determining the frequency peaks which do not change with the change of the speed.

- The RBD program calculates the longitudinal dynamics of the bogie due to the application of traction and brake where the speed profile is an output of the simulation in a natural manner. The RBD program has the capability to effectively calculate the lateral and vertical dynamics simultaneously during the application of traction and braking.

- From the study of the lateral dynamics under variable speed it was found that, the lateral response of the bogie remains the same irrespective of the type of traction or braking application (quick/normal).

- The application of very large braking torques can lead to wheelset skid and tends to destabilize wheelset lateral oscillation. Simulation results showed that skidding on one wheelset or on both wheelsets of bogies affect the lateral oscillation differently.

- Part of the results of the RBD program, namely the speed profile and skid as a function of the application of brake torque, could only be validated using carefully designed experiments as other commercial dynamics packages do not explicitly account for these factors.

6. EXPERIMENTAL VALIDATION OF THE EFFECT OF BRAKING TORQUE TO BOGIE DYNAMICS: PART A. DESIGN OF EXPERIMENTAL PROGRAM

6.1. INTRODUCTION

As has been described earlier in this thesis, the RBD program calculates the longitudinal dynamics of bogies including speed profile and the corresponding wheelset pitch due to the application of braking/traction torque. This capability could only be validated using careful experimentation. A full-scale laboratory test was, therefore, designed and commissioned for this purpose at the heavy testing laboratory (HTL) of the Central Queensland University (CQU). This chapter describes the design of the experimental program. Analysis of the dataset and validation of the simulated response of the bogie dynamics are reported in the subsequent chapters.

6.2. EXPERIMENTAL DESIGN

6.2.1. The Concept

The primary objective of the test was to examine the dynamics of bogies subjected to brake torque. A bogie running on a tangent track was considered for this purpose. A three-piece bogie (QR30) provided by Queensland Rail (QR) was used. Due to space limitation in the laboratory a 24m long track could only be constructed, thus restricting the maximum speed of the bogie to 4 m/s (14.4 km/h). The bogie was braked using its own brake system. Traction was not specifically considered as a test parameter. Only the rear wheelset was braked and the front one was left un-braked to allow comparison of the dynamic characteristics of the braked and the un-braked wheelsets. The brake

force was controlled using a pneumatic circuit that maintained the brake pressure and brake application time (time needed to reach maximum pressure) to the required levels. A set of measurement equipment and devices was installed on the bogie in order to gather data of the applied brake force, the longitudinal, the vertical and the lateral dynamics (travel distance, velocity and acceleration), as well as the wheelset rotation (pitch).

Andrews (1986) reported a similar experiment carried out in the early 1960's by British Railway Electrical Laboratory in Willesden, with a particular focus on traction effects to locomotive bogie dynamics. A single bogie powered with a traction motor and loaded appropriately to simulate the static axle load was used in their test. A sketch and photo of the test setup are shown in Fig. 6.1 and Fig. 6.2 respectively. Their test did not pay any attention to braking as adhesion and traction torque induced slip were the major study parameters. The test described in this thesis was primarily developed for examining the effect of brake torque to bogie dynamics. To the best knowledge of the author, no other similar experiment was found in the literature.

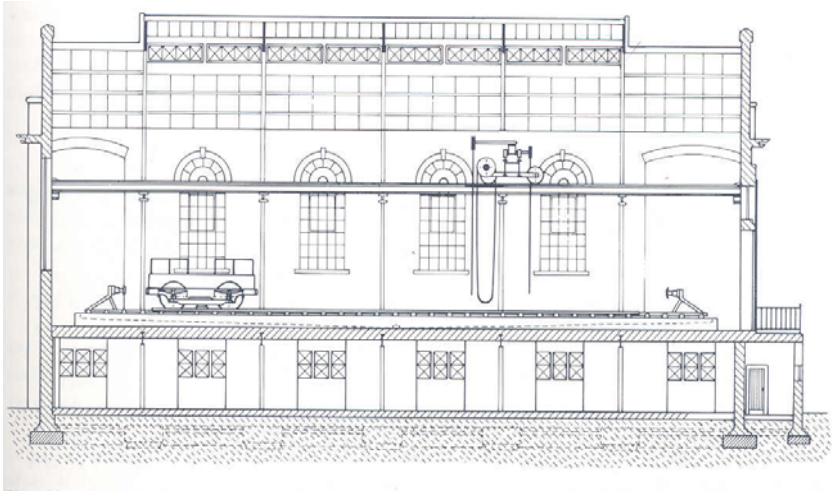

Figure 6.1. Sketch of traction test at British Railway Electrical Laboratory (Andrews (1986))

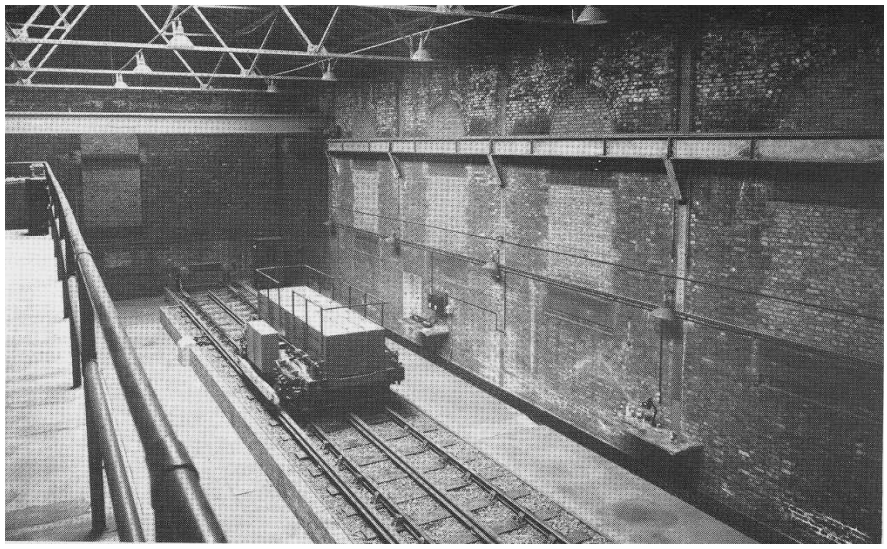

Figure 6.2. Photo of traction test at British Railway Electrical Laboratory (Andrews (1986))

6.2.2. Track Section and Estimated Speed Profile

The 24m long track was divided into zones of acceleration, steady-state rolling (coasting) and deceleration, followed by a safety zone as shown in Fig. 6.3. Choice of maximum length of these zones was constrained from the safety perspective. The estimated speed profile shown graphically in Fig. 6.3 has been used as a base to define the range of the traction force (pulling force) and brake force required for safe operation of the bogie.

The acceleration a_a and deceleration a_b were assumed to be maintained at 1 m/s^2 to avoid excessive slip. Assuming linear change in speed in the acceleration and braking zones, the relation between the maximum speed and the distance travelled in each zone is written as shown in Eq. (6.1) and (6.2):

$$a_a = \frac{1}{2}\frac{v^2}{s_a} = 1 \cdot m/s^2, \tag{6.1}$$

$$a_b = \frac{1}{2}\frac{v^2}{s_b} = 1 \cdot m/s^2, \tag{6.2}$$

Substituting longitudinal distance travelled $s_a = s_b = 8m$ into the above equations, $v = 4 \cdot m/s$ was obtained as the maximum permissible safe speed.

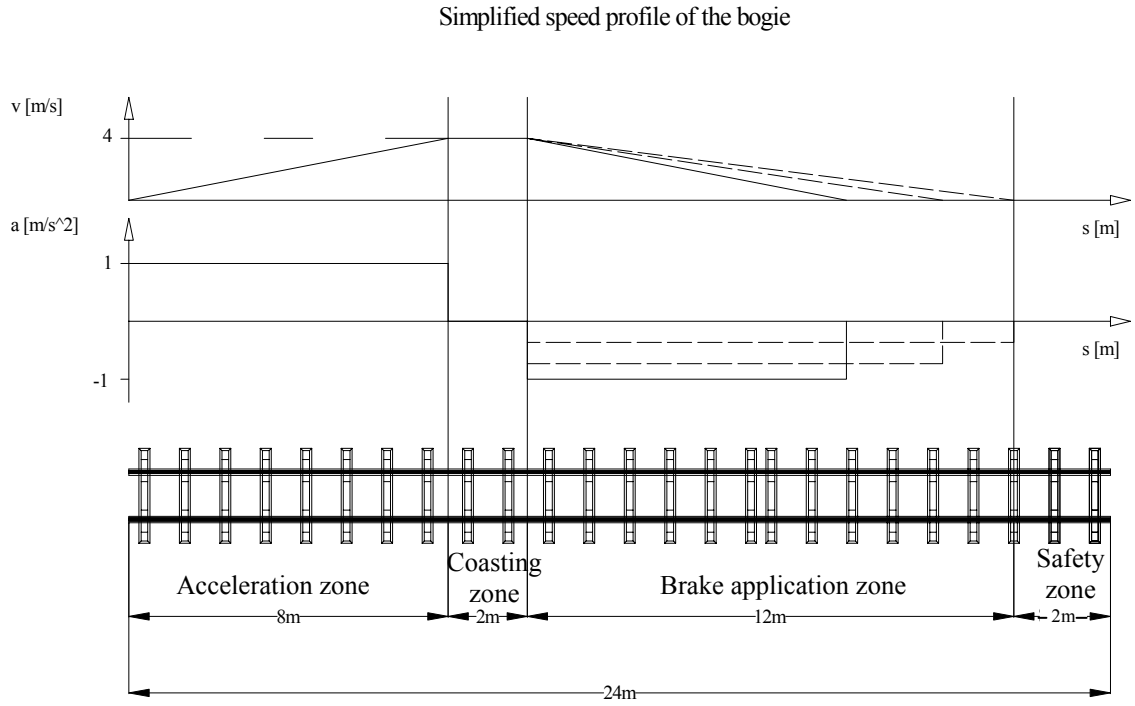

Figure 6.3. Track section and estimated speed profile

However, as a constant braking rate of 1 m/s^2 was most likely not achievable using the available brake equipment (lower acceleration was also considered), the braking section was chosen longer than ideally necessary. Effect of potential lower deceleration rate to stopping distance is shown by the dashed lines in the speed profile curve of Fig. 6.3

6.2.3. Specification of Equipment

Braking force

A reliable and accurate measurement of brake force applied to the wheelset was needed. In the QR30 bogie, the brake torque is transmitted through tangential friction force due to the contact of the brake shoes onto the wheel tread. Force on the brake shoes is provided by a cross-beam that is on one side connected to the brake shoes and on the other side attached though pistons to the actuators (brake cylinders) as shown in Fig. 6.4. The movement of the brake beam is guided by slots provided in the side frame.

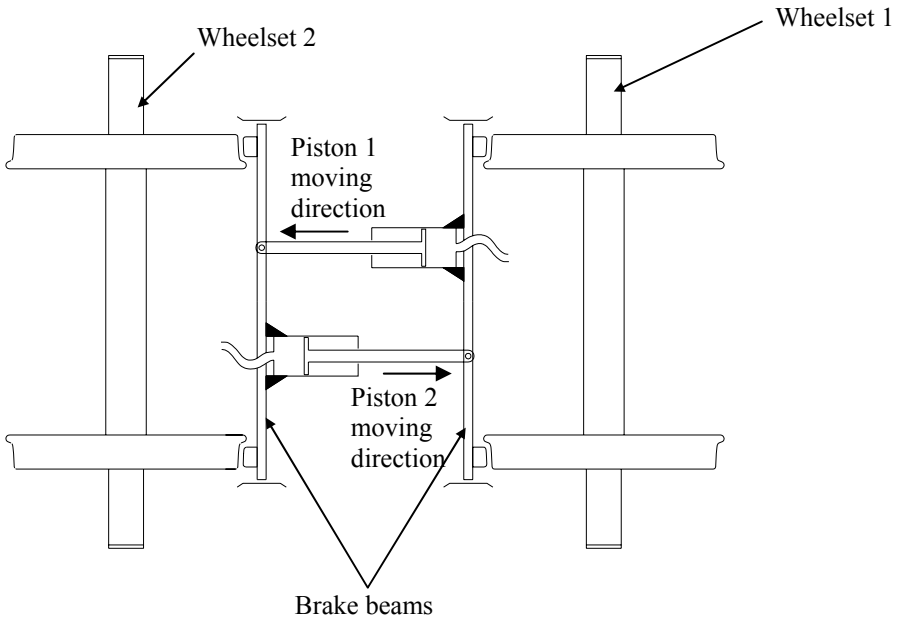

Figure 6.4. Schematic diagram of QR30 brake system

Fig. 6.5 shows the forces applied to the system; due to symmetry only half of the system is shown. It is, therefore, very important to measure the forces exerted by the

actuators F_{CT1} and F_{CT2} as well as the tangential force F_T produced due to friction between the shoes and the wheels as accurately as possible. By knowing the magnitude of the tangential force produced, the actual torque applied to the wheels can easily be calculated from the geometric data of the wheelset.

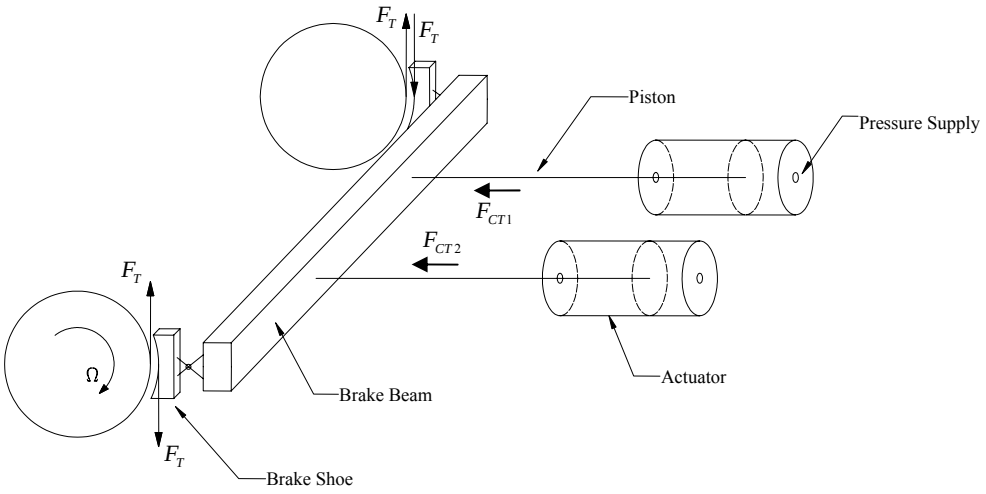

Figure 6.5. Forces acting on brake system of QR30 bogie

According to the QR30 bogie specification, total brake shoe normal force that can be generated by the bogie brake system is 0.164 kN for each kPa of air pressure supplied to the brake cylinders. The brake cylinder can receive a maximum of 350 kPa air pressure that could produce a total of 57.4 kN. However, due to the requirement of low load, during the test the pressure supplied to the brake cylinder was required to be maintained low, say below 200 kPa, to keep the force lower than 32.8 kN. This magnitude of the force is the sum of the normal forces applied to each of the four shoes. Therefore, the force acting on each wheel would be less than 8.2 kN. Due to symmetry, the same magnitude force would act on the brake cylinder rod (see the diagram of the

brake force distribution in Fig. 6.6). The calculation of the applied brake tangential force to the wheelset requires knowledge of the friction coefficient between the brake shoes and the wheels. Assuming the friction coefficient in the range of 0.2 to 0.4, the tangential force would be in the range of 1.64 kN to 3.28 kN.

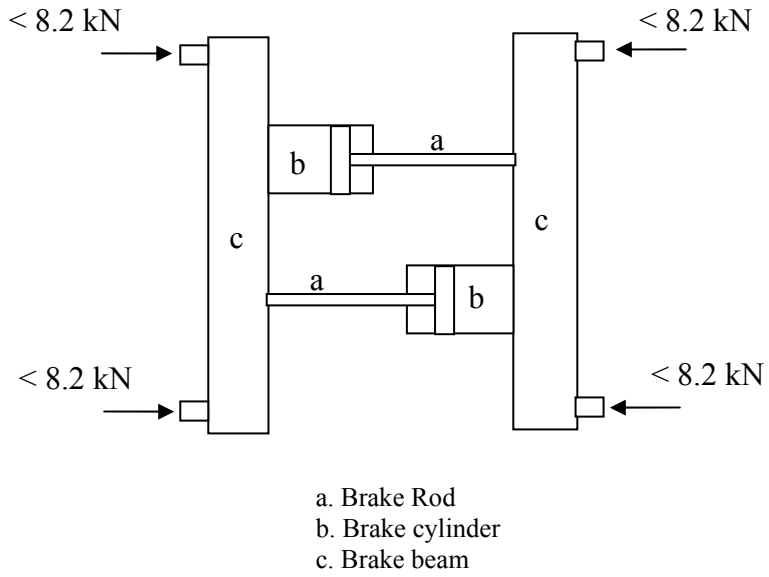

Figure 6.6. Distribution of brake normal force

Longitudinal dynamics of the bogie

In general the bogie dynamics in the longitudinal direction can be defined in terms of the following quantities:

- *Longitudinal acceleration*

- *Longitudinal velocity*

- *Longitudinal travel distance*

- *Wheelset rotation and angular velocity relative to its lateral axis*

As the purpose of the experiment was to investigate the longitudinal dynamics of the bogie under braking condition, the above quantities have to be measured accurately during the test. The brake torque application to the wheel creates longitudinal slip or creepage in the wheel rail contact patch, the definition of which has been described in Section 2.3. The creepage generates the longitudinal contact force that decelerates the bogie. Therefore the measurement equipment should detect this longitudinal slip to validate the creepage-creep force relationship used in the model.

Based on the creepage formulation presented in Section 2.3.1 of Chapter 2, longitudinal slip could be written as in Eq. (6.3):

$$\xi_x = \frac{v_c - v}{v} \tag{6.3}$$

where v_c and v are the circumferential velocity at the wheel-rail point of contact and the longitudinal velocity of the wheel respectively. Predicting the values of longitudinal slip $\xi_x = 0.02$ during the braking, while the circumferential and longitudinal velocities $v_c \approx v = 4 \cdot m/s$, the relative velocity to be measured can be calculated as in Eq. (6.4).

$$\left|v_c - v\right| \approx 0.02 \cdot 4 \cdot m/s = 0.08 \cdot m/s . \tag{6.4}$$

However, when the speed reduces to zero, relative velocities that are much lower than 0.08m/s could occur. Therefore, to increase the accuracy of the measurements, the relevant specification of the speed was set as 0.1 m/s and the relative velocity to be measured becomes

$$\left|v_c - v_x\right| \approx 0.02 \cdot 0.1 \cdot m/s = 0.002 \cdot m/s \tag{6.5}$$

The value of relative velocity in Eq. (6.5) was then used as a reference value to choose the resolution of the devices for the measurement of the wheel rotation and the longitudinal movement. Including the resolution specifications/tolerances of the sensors in operation, the measured slip or creepage could be written as Eq. (6.6):

$$\xi_{\exp} = \frac{\left(v_c \pm d\Omega_{Sensor} \cdot r_w\right) - \left(v \pm dv_{Sensor}\right)}{\left(v \pm dv_{Sensor}\right)} \tag{6.6}$$

where $d\Omega_{sensor}$ is the resolution tolerance of the sensor measuring the wheelset rotation, dv_{sensor} is the resolution tolerance of the sensor measuring longitudinal movement and r_w is the nominal radius of the wheel.

The error of slip detection in relation to the analytical values of slip is defined as shown in Eq. (6.7).

$$e_\xi = \frac{\left|\xi_{\exp} - \xi_{analytical}\right|}{\xi_{analytical}} \cdot 100\% . \tag{6.7}$$

Typical measurement equipment for longitudinal or rotational speed detection is based on resistive, inductive (analogue) or incremental (digital) principles. High accuracies demand exact inductive conditions in the case of analogue equipment like tachometers and precise adjustable resistors in the case of potentiometers. For the incremental devices, precise and small switching events are required. Table 6.1 exhibits a comparative study of the measurement devices for measuring longitudinal motion of the bogie and the angular measurement of wheelset rotation. As can be seen from Table

6.1, inductive devices are used for the measurement of velocities and resistance and optical devices are used for the measurement of position signal. As time (clock) is independently recorded during data acquisition, the calculation of velocities from position data is also possible. Thus, resistance and optical based devices could also be used for measuring the angular and the longitudinal velocities.

Table 6.1. Comparison of measurement devices for longitudinal and angular motion

Device	Signal	Longitudinal		Angular	
		Position	Velocity	Position	Velocity
Inductive	Voltage		Tachometer (Gear)		Tachometer
Resistance	Voltage	Potentiometer		Potentiometer	
Optical/Magnetic	TTL (Transistor-Transistor Logic)	Encoder (absolute or incremental)		Encoder (absolute or incremental)	

General motion of wheelsets

Besides the longitudinal dynamics of the bogie there is also an interest to examine the braking torque's influence to the lateral dynamics and furthermore to yaw and roll motions of the wheelset. To decide on the quantities to be measured for the purpose, it is important to understand how the wheelsets move relative to the track and relative to the bogie frame to which they are connected. Fig. 6.7 shows the end view of a wheelset linked to the side frame. Vertical and lateral motions are restricted by bump-stops and influenced by dry friction between the surfaces in contact. If the axle boxes are

assumed to be in permanent vertical contact with the pedestals on the side frames, the wheelsets will have two of their six degrees of freedom (vertical and roll) follow the corresponding degrees of freedom of the side frames. Permanent vertical contact between axle boxes and side frames can be assumed due to expected low vertical accelerations.

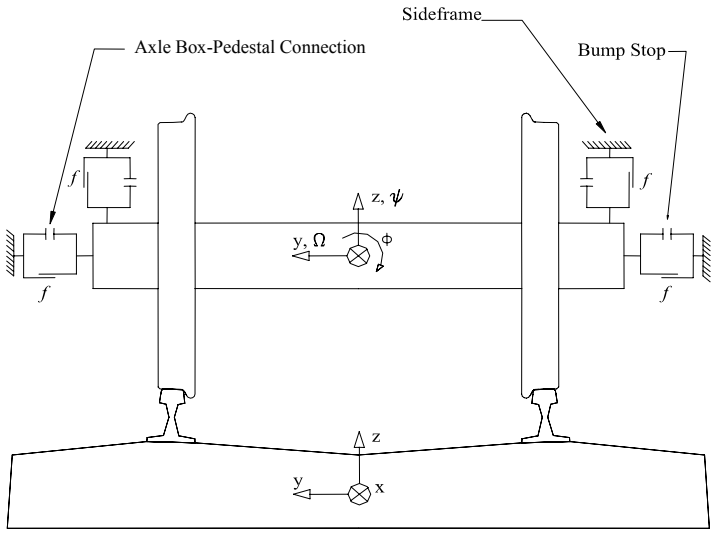

Figure 6.7.Wheelset connection to side frame

As the primary interest of the experiment is the movement of the wheelsets on the rail and *not* the displacements in relation to the bogie's side frame, the accelerations with respect to the three directions of space are required on each axle box. Placing accelerometers here and assuming permanent vertical connection between the side frame and the axle box allowed the detection of vertical running behaviour and pitch of the side frames of the bogie and the bogie itself. By obtaining acceleration data of the axle boxes in all three directions, yaw and lateral motions as well as roll of the wheelsets can be calculated as long as the set-up is held symmetric to the bogie frame.

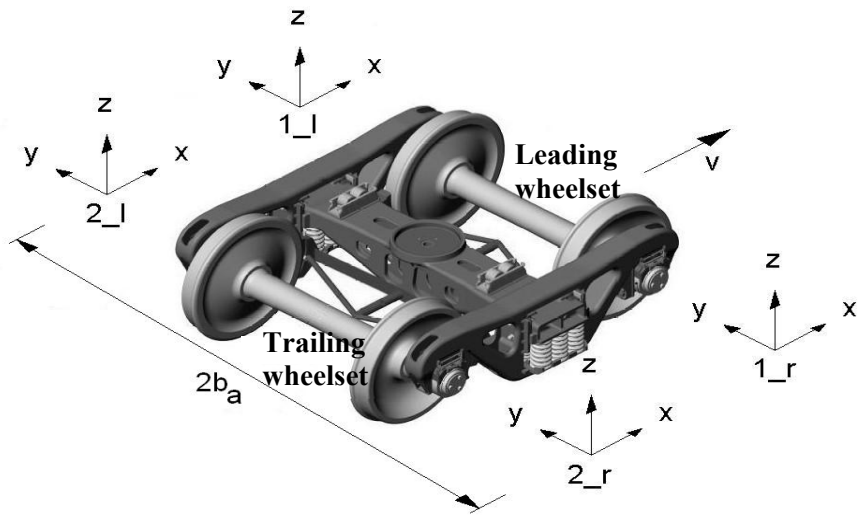

Figure 6.8. Axial acceleration to be measured on the bogie

The accelerometer directions are presented in Fig. 6.8[1]. The four Cartesian coordinate systems shown in Fig. 6.8 represent the directions of the accelerometers fitted at each axle end. If the angular displacements of the wheelset are assumed to be small, the roll and yaw accelerations can be calculated as follow (approximation):

$$\ddot{\phi} = \frac{1}{b_a}\left(\ddot{z}_{1,l} - \ddot{z}_{1,r} \right), \text{ roll,} \tag{6.5}$$

$$\ddot{\psi} = \frac{1}{b_a}\left(\ddot{x}_{1,r} - \ddot{x}_{1,l} \right), \text{ yaw.} \tag{6.6}$$

The variable b_a denotes half of the lateral distance between the accelerometer positions on the axle boxes. Lateral motion of the wheelset would ideally cause identical signals on both of the lateral accelerometers on one axle; thus only one accelerometer is necessary in the lateral direction. Therefore, only five accelerometers per wheelset (a total of 10 accelerometers) were used in the experiment.

[1] Picture taken from Standard Car Truck manual, modified

6.3. EQUIPMENT, INSTALLATION, AND DATA ACQUISITION

Based on the specification described in Section 6.2, a set of measurement equipment was chosen. Other factors such as the cost and the delivery time were also considered when selecting the equipment supplier. This section presents briefly the chosen measurement devices and their installation on the bogie.

6.3.1. Brake Force Measurement – Strain Gauge

As introduced in Section 6.2 the brake force was applied to one wheelset only; the trailing wheelset was braked while the non-braked leading wheelset was used as a reference. Originally the brake beam was supported and guided by slots in a slider housing provided in each side frame, which adversely affected the measurement of the tangential force. Therefore, the brake beam of the braked wheelset was cut as shown in Fig. 6.9 and hangers were then used to replace the function of the slots to support and guide the movement of the brake beam. The tangential brake force was measured from the strain in the hanger.

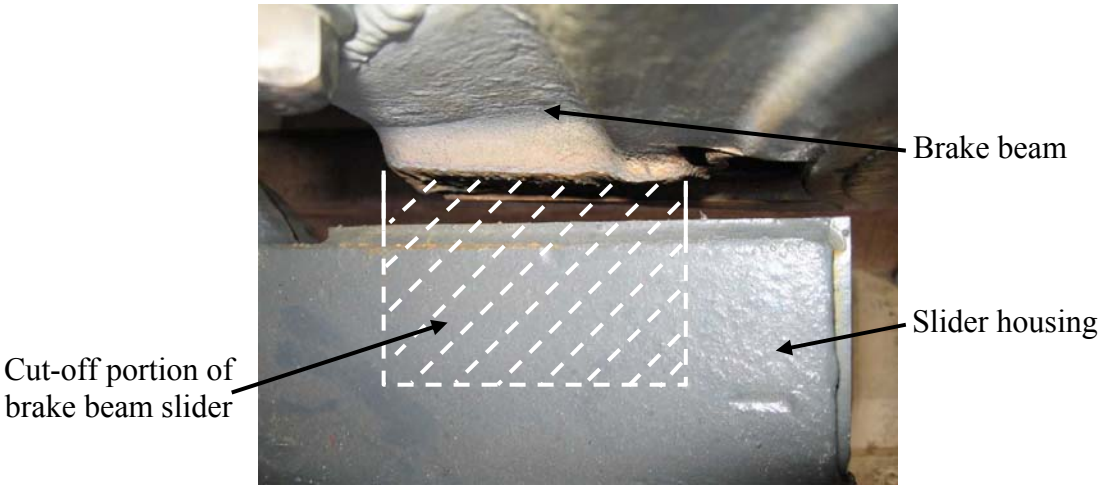

Figure 6.9. Modification (cutting) of the brake beam slider

Fig. 6.10 (a) shows part of the hanger fitted with a strain gauge and Fig.6.10 (b) shows its installation on the bogie. The design of hanger installation assembly allowed accurate positioning of the brake beam relative to wheelset both vertically and laterally.

(a) part of the hanger with strain gauge (b) installation on the bogie

Figure 6.10. Tangential brake force measurement

In the non-braked leading wheelset, the movement of the brake beam was restricted by a plate welded onto the slot providing a thread to allow adjustment of the longitudinal clearance using a bolt (Fig. 6.11). The force exerted by the brake actuator was measured by fitting a strain gauge on the brake rod as shown in Fig. 6.12.

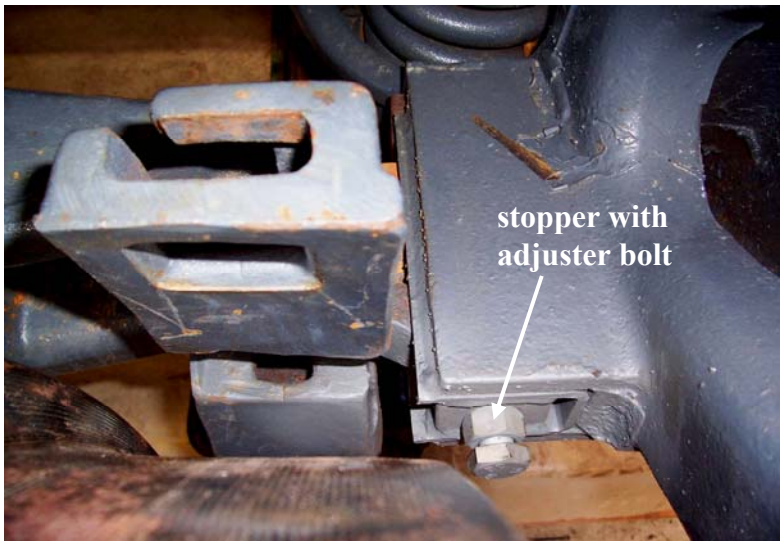

Figure 6.11. Brake beam stopper of the non-braked wheelset

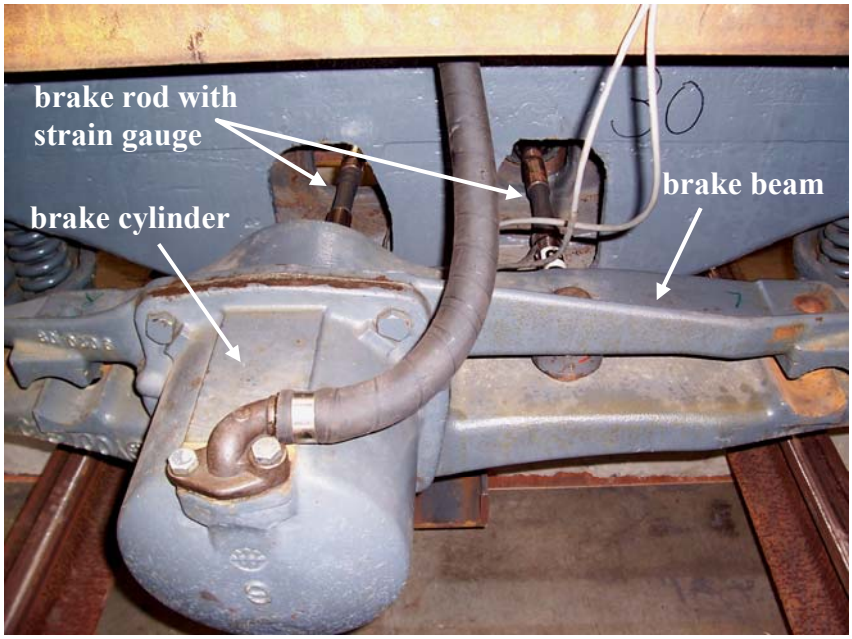

Figure 6.12. Brake cylinder and brake rod with strain gauge

6.3.2. Longitudinal Movement Measurement – Magnetic Linear Encoder

A magnetic linear encoder was used as a sensor to measure the longitudinal motion of the bogie. The specification of the sensor is provided in Table 6.2. The sensor is

capable of accurately detecting incremental motion reading on a longitudinally installed magnetic tape. The picture of the sensor and the magnetic tape are shown in Fig. 6.13.

Table 6.2. Specification of linear encoder

Manufacturer	Kuebler
Type	LIMES, K8.L2.122.2211.0005 and K8.B2.10.010.0250
Physical Principle	Detection of inductive currents due to polarity changes on the tape
Characteristic Output	TTL-Signal, 50000 lines per m, 0.02 (single) – 0.005(quadruple) acquisition
Range	0-14m/s

Figure 6.13. LIMES magnetic linear encoder

Based on the specification of the linear encoder, which requires high precision, a special support and guidance system was designed. The system provided longitudinal support for the magnetic tape which also guided a carriage with the sensor located on it ensuring safe signal reception. The sketch of the longitudinal travel distance measurement using LIMES linear encoder is presented in Fig. 6.14. A longitudinally rigid and laterally and vertically free to move link system was installed between the

bogie frame and the carriage. The LIMES linear encoder was fitted to the carriage. The mounting system of the sensor allowed for adjustment of the gap between the sensor and the magnetic tape (1 mm gap was required in addition to the adjustment of the lateral position of the sensor above the tape). The carriage and the guide beam containing magnetic tape are exhibited in Fig. 6.15.

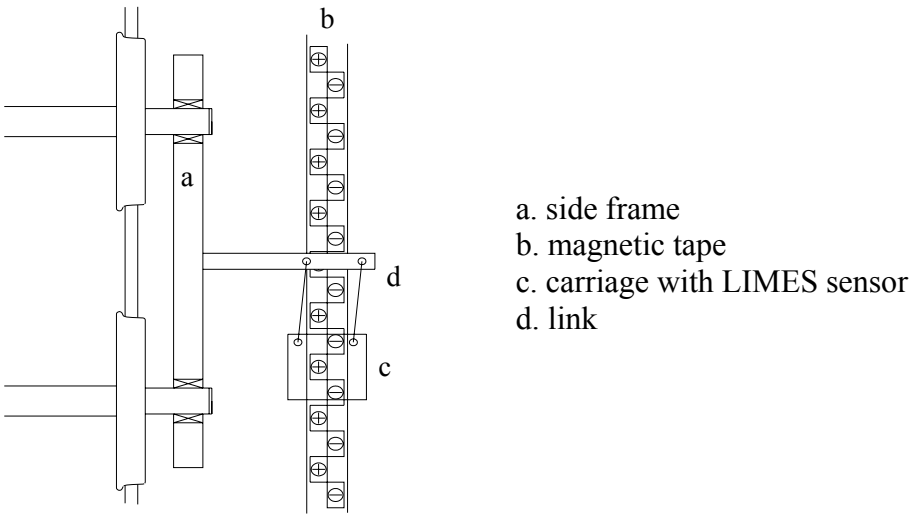

Figure 6.14.Sketch of longitudinal travel distance measurement

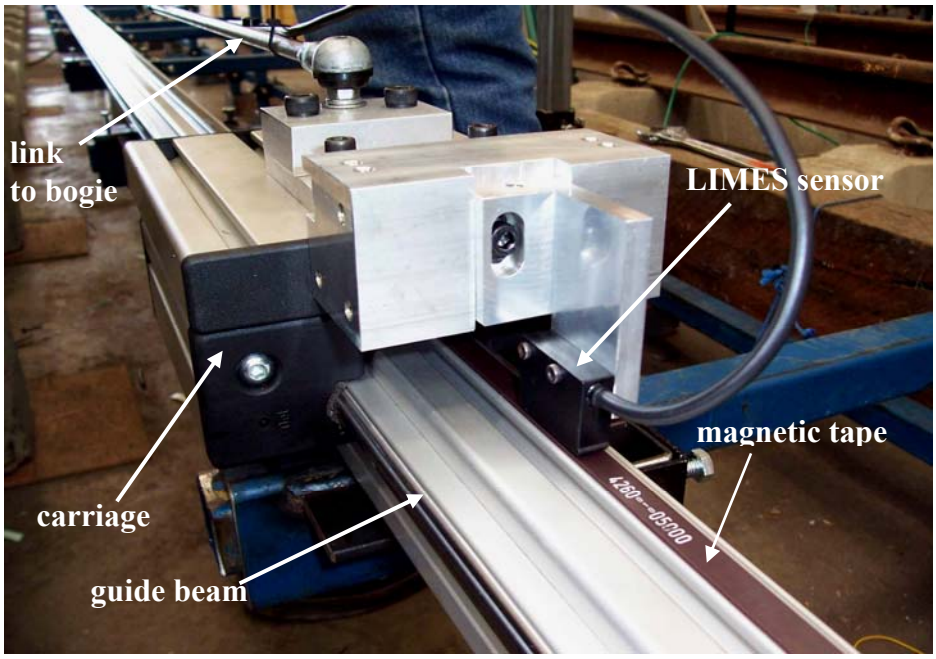

Figure 6.15.The carriage and guide beam for linear encoder

6.3.3. Wheel Rotation Measurement – Shaft Encoder

42mm Hollow Shaft Encoders of 10.000 pulses per revolution were chosen to measure the rotation of both wheelsets. The specification of the shaft encoder is presented in the Table 6.3 and its photo is shown in Fig. 6.16.

Table 6.3. Specification of shaft encoder

Manufacturer	Hengstler,
Type	RI176TD/10000AH.4A42TF
Physical Principle	Opto-electronic
Characteristic Output	TTL-Signal, 10000 lines per revolution, 0.036°
Range	0-1800 rpm

Figure 6.16. Hollow shaft encoder

Fig. 6.17 shows the installation of the shaft encoder to the axle end of one of the wheelsets. To achieve this installation the axle boxes were required to be cut open to provide access to the fitting of the encoder adaptor. In addition, a rigid link was also attached for the installation of the accelerometer box (also shown in Fig. 6.17).

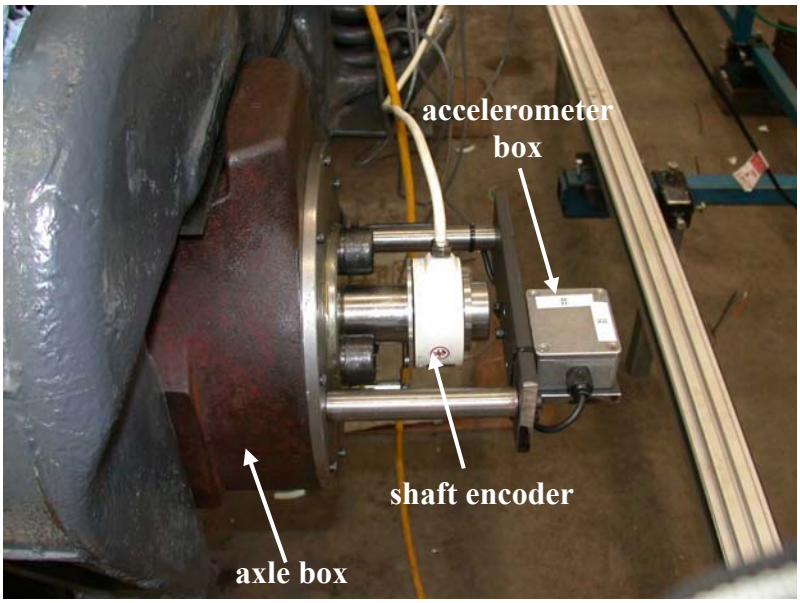

Figure 6.17. Shaft encoder and accelerometer installation through modification of axle box

6.3.4. Accelerometer Measurements

The specification of the accelerometers used for measuring the wheelset motion is presented in Table 6.4. The accelerometers are compactly installed in a small rigid box as shown in Fig. 6.18 (a). A cut-off frequency was chosen and an appropriate filtering device was implemented to facilitate its use for any other application beyond the current test. The accelerometer signal was filtered by a second order Butterworth filter (Fig. 6.18 (b)), cutting off the signal at the frequency of 20 Hz. The accelerometer installation on the bogie is exhibited in Fig.6.17.

Table 6.4. Accelerometer specification

Manufacturer	Analog Devices
Type	ADXL210
Physical Principle	Piezoelectric device
Characteristic Output	Voltage, 100 mV/g
Range	+/- 10g

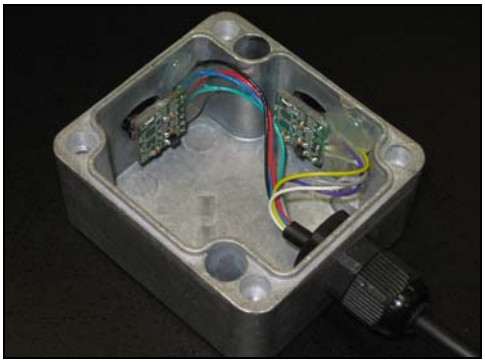

(a.) Accelerometer

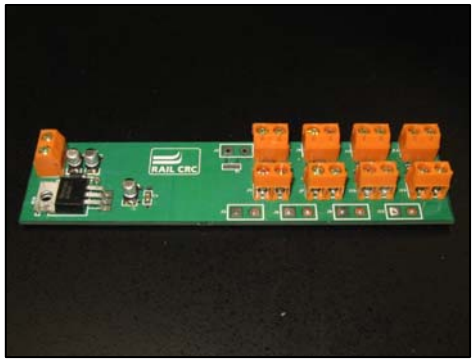

(b.) Butterworth filter

Figure 6.18. Accelerometer and CRC Butterworth filter

6.3.5. Wheel-Rail Profile Measurement – MiniProf

Real data of the wheel and the rail profile were measured using MiniProf (a special tool designed to measure wheel and rail profile). The equipment was provided by Queensland Rail (QR). The data of the wheel and the rail profile coordinates provided by the MiniProf was required as the input for the computer simulations (to be discussed in Chapter 8). Figs. 6.19 and 6.20 show the MiniProf tool used to measure the wheel profile and the rail profile respectively.

Figure 6.19. MiniProf tool for measuring the wheel profile

Figure 6.20. Measurement of the rail profile using MiniProf

6.3.6. Track Construction

The test track was carefully constructed to achieve the satisfactory *straightness of the track* along the length of 24 m. It was done by the professionals from the Queensland Rail. Two photos of track welding and grinding activities during the track construction are shown in Fig. 6.21 and Fig. 6.22.

Figure 6.21. Track welding

Figure 6.22. Track grinding

6.3.7. Rail Friction Coefficient Measurement - Tribometer

The friction coefficient of the rail surfaces was determined using a portable hand-pushed tribometer (product of Salient System) shown in Fig. 6.23. The tribometer measures the coefficient of friction at points along the rail head from the top of the running surface to the lower edge of the gauge face. As the experiment was only for a bogie running on the tangent track where the gauge face contact was an unlikely event, only the friction coefficient of the top of rail head was measured. The measurement was conducted by pushing the device at walking speeds to collect readings, while a proprietary algorithm reviewed the data for accuracy. The tribometer was provided by QR.

(a) arrangement on the rails

(b) close up of the sensor wheel and the reader

Figure 6.23. Portable Tribometer

6.3.8. Data Acquisition and Data Analysis

A total 18 channels of data signals were obtained and processed during the experiment. Three of them were digital signals (from two shaft encoders and one linear encoder), and the other 15 channels were analogue signals. These different types of the streams were synchronised with time (computer clock) during the experiment. For this purpose a data acquisition program was developed in Lab View software platform. The program

was then installed into the data acquisition (DAQ) computer mounted on the bogie (Fig. 6.24). The output of the DAQ program was provided in two binary files (one for the analogue data stream and the other for the digital data stream), which were then converted and merged into one data text file. To analyse the result, a program in Matlab platform was coded. The program read the data text file and plotted the data as required.

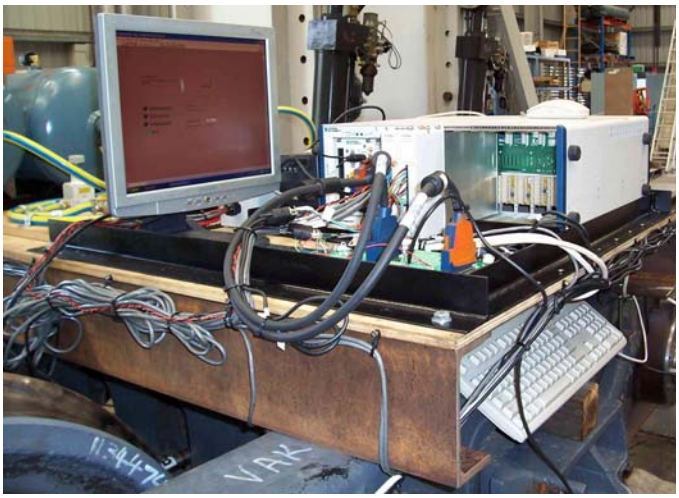

Figure 6.24. DAQ computer mounted on the bogie

6.3.9. Brake Controller

Fig. 6.25 shows the pneumatic system installed on the bogie for the control of the application of the brake force. Experimental conditions did not allow a person to sit on the bogie to control the brakes. Also no external control radio link or other network interaction was available. The pressure supplied to the brake actuators was set up using the pressure regulator while the application time was adjusted using a flow restriction valve.

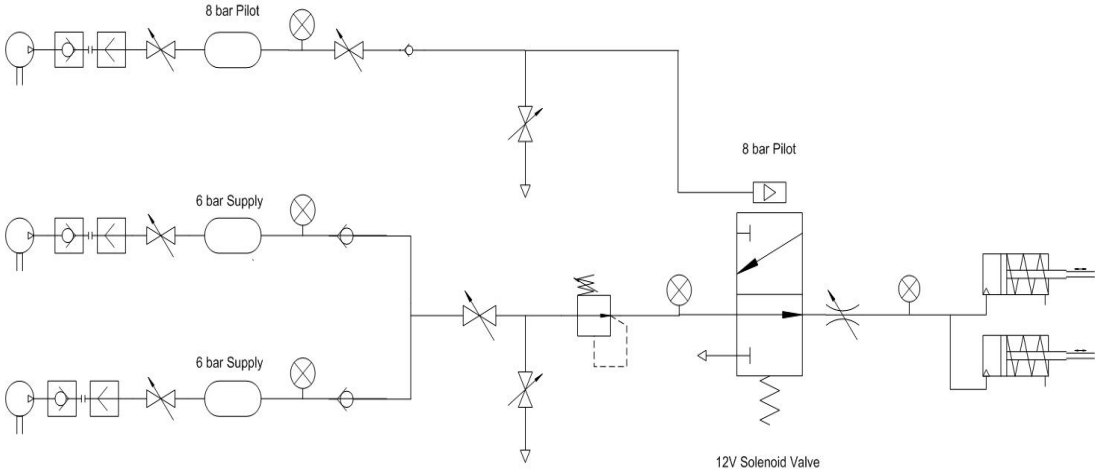

Figure 6.25. Diagram of pneumatic system used for brake controller

To control the event of braking, a solenoid valve was used. The solenoid valve opened the air pressure line to the brake actuators when the electric circuit was de-energised; this provided a fail-safe operation. De-energising of the electric circuit at a certain position along the track was controlled automatically by the DAQ computer system mounted on the bogie. The operator of the experiment was required to just input the distance at which the brake was required to be applied; the DAQ computer system recorded this value and then compared it to the data received from the measurement of the longitudinal movement of the bogie provided by the LIMES system. This process was performed in real time during the test execution.

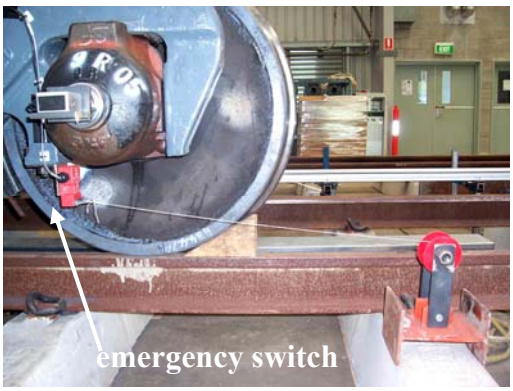

Figure 6.26. Brake emergency switch using string

To deal with any un-anticipated failure in the DAQ computer, a switch was designed and installed so that it could be simply disengaged (cut-off the electric circuit) by pulling a plug connected to a string (Fig 6.26). The length of the string was carefully worked out and the emergency brake was positioned accordingly on the track.

6.3.10. Complete Test Setup

Fig. 6.27 shows the fully instrumented bogie with its data acquisition system ready for commissioning.

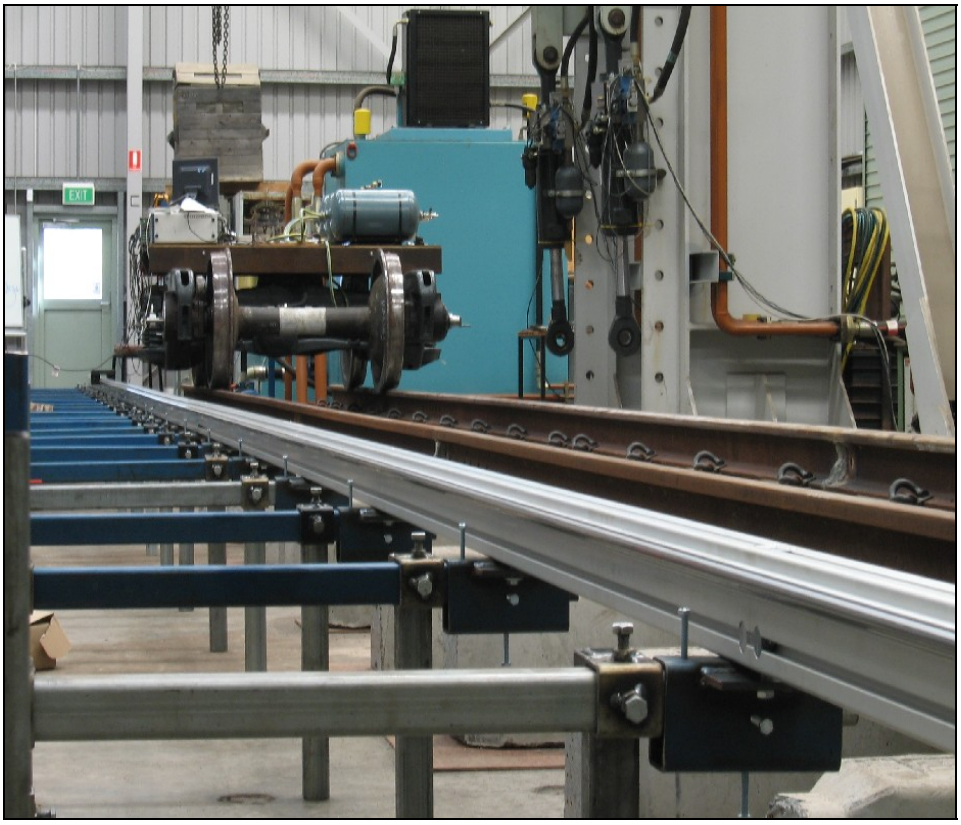

Figure 6.27. Instrumented Bogie with DAQ ready for commissioning

Prior to each test trial, the DAQ was supplied with the information on the required brake pressure and the start time and rate of application of brake pressure. A road truck was used to provide the traction.

6.4. SUMMARY

An experimental program was designed to validate the RBD program, in particular the calculated speed profile due to the application of braking torque and the corresponding wheelset pitch. The experimental program design may be summarised as follows:

- Due to the space constraint within the lab, the track length was limited to 24 m.
- Due to the limitation of the test track length, the experiment could only be performed at low speed (i.e. below 4 m/s).
- The test track was carefully divided into four zones namely acceleration zone (8m), coasting zone (2m), braking zone (12m) and safety buffer zone (2m).
- The primary objective of the experiment was to investigate the influence of braking torques to the bogie longitudinal dynamics. In relation to this, to avoid complexity and reduce cost, no traction motor was installed on the bogie. Instead, a small road truck was used to accelerate the bogie. This economical option, although adversely affecting the repeatability issues, was sufficient (discussed in Chapter 7) to achieve very close repeatable experiments.
- A fully controlled and measured brake force was applied to the trailing (rear) wheelset of the bogie.
- Measurement devices were carefully chosen to meet the requirement of high precision data. The mounting details for each of the devices were carefully designed so that the data could be gathered accurately.

- Different types of data streams (analogue and digital) from 18 channels were processed and synchronized by a data acquisition program built in Lab View software platform. The DAQ system computer was mounted on the bogie.

- A fail safe braking system was designed and installed to prevent any unexpected failure in brake circuit and /or DAQ program.

7. EXPERIMENTAL VALIDATION OF THE EFFECT OF BRAKING TORQUE TO BOGIE DYNAMICS: PART B. EXPERIMENTAL RESULTS

7.1. INTRODUCTION

This chapter reports some important results of the experiment presented in Chapter 6. Three cases of the bogie brake dynamics experiments were selected as listed in Table 7.1. For each case brake application time was set as 0.8 sec.

Table 7.1. Cases of the experiment

Case	Brake Pressure (kPa)
Case #1	130 kPa
Case #2	150 kPa
Case #3	180 kPa

Of the three cases examined, Case #2 (150 kPa pressure) was considered to be just on the verge of the onset of skid; any increase in pressure above this level was expected to most certainly induce skid (based on simple analytical calculation). Brake pressures of Case #1 and Case #3, could therefore be regarded as cases of mild (no possible skid) and heavy (high possibly skid) braking respectively.

This chapter describes the primary and derived data obtained from each case of the experimental program.

The primary data included:

1. Brake normal forces (kN); measured by the strain gauge on the brake rod
2. Tangential brake forces (kN); measured by the strain gauge on the brake beam hanger
3. Accelerations (m/s^2) in the longitudinal, the lateral and the vertical directions; measured by the accelerometers
4. Linear distance travelled (m); measured by the LIMES linear encoder
5. Angular revolution (rad); measured by the HENGSTLER shaft encoders

The derived data included:

1. Brake torque; calculated from the tangential brake force
2. Longitudinal speed profile (m/s); first derivative of the LIMES data
3. Angular velocity (rad/s); first derivative of the HENGSTLER data
4. Longitudinal acceleration (m/s^2); second derivative of the LIMES data
5. Slip

Where possible the derived data were compared to the measured primary data.

7.2. EXPERIMENT CASE #1 (P=130 KPA)

Four trials were executed where the brake cylinder pressure was set up to achieve 130 kPa within 0.8 second.

7.2.1. Primary Data

Brake cylinder forces – normal and tangential

The brake cylinder forces in the normal and in the tangential direction to the wheel tread at the point of application were measured using the strain gauged brake rods and brake beam hangers respectively. Fig. 7.1 presents the brake cylinder pressure and forces measured in the brake rods of each cylinder for trial 1 to trial 4. As can be seen in the figure, the pressure in the brake cylinder increased gradually from zero to 130 kPa in 0.8 second. The forces in the brake rods also increased gradually from zero to maximum during the corresponding period without any time lag. Both rods measured approximately the same magnitude of brake shoe normal forces. Using the specification of the new bogie (0.164 kN total normal force per kPa, see Section 6.2), the force in the rods was calculated as 5.33 kN, which was approximately 18% higher than the measurement. As the bogie was a refurbished old one, it was expected that lower efficiency of the cylinder would exist; the 18% reduction was, therefore, acceptable.

Fig. 7.2 shows the tangential brake force measured from the brake beam hanger for trials 1 to 4. Tangential brake force can be calculated as a function of the brake shoe normal force: $F_T = F_B \mu_b$, where μ_b is the friction coefficient between brake shoe and wheel tread and F_T and F_B are tangential and normal brake shoe force respectively (see Section 2.5). As both the normal and the tangential brake shoe forces were measured, the friction coefficient between the brake shoe and the wheel tread (μ_s) was able to be calculated; the calculated values varied between 0.27 and 0.33.

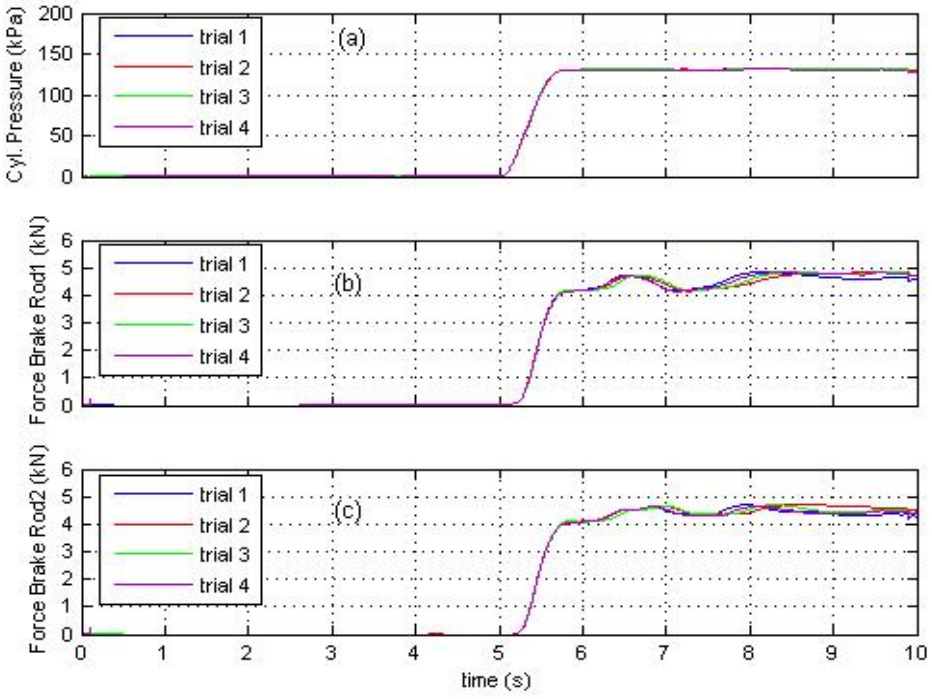

Figure 7.1. Brake cylinder pressure and normal forces in the brake rods, Case #1

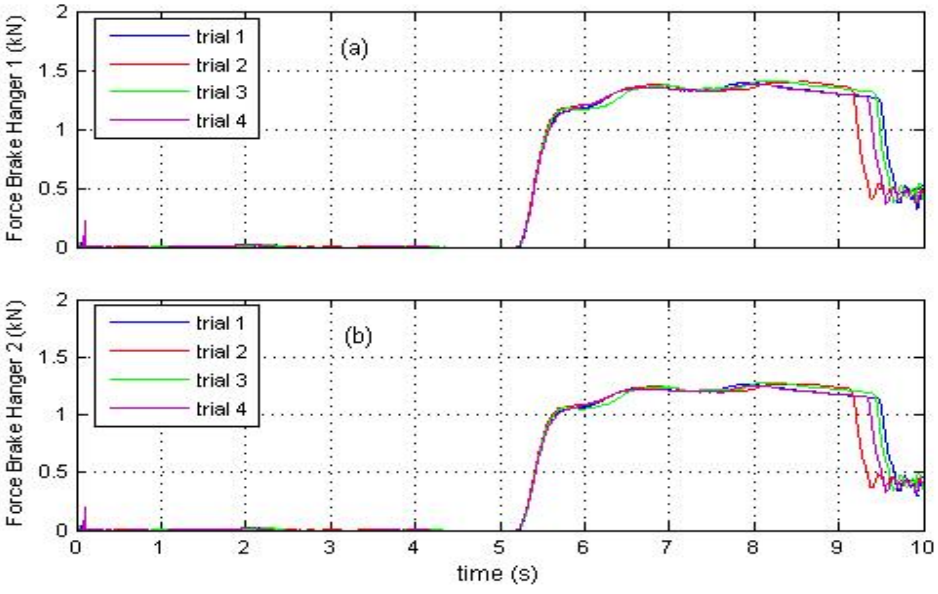

Figure 7.2. Tangential brake force in the brake beam hangers, Case #1

Acceleration – longitudinal, lateral and vertical

During the experiment, the longitudinal, the lateral and the vertical accelerations were measured using the accelerometers fitted to the axle boxes (see Section 6.2 and Section 6.3). Fig. 7.3 shows the average of the measured longitudinal acceleration obtained from four accelerometers which show very good consistency amongst the four trials although each trial was conducted *without* any assurance of repeatability. The maximum longitudinal acceleration recorded varied from 2.4 m/s^2 to 2.8 m/s^2, which is considered not very significant (16% variation). In the coasting zone each trial has provided very consistent acceleration (a deceleration of approximately 0.1 m/s^2). In the braking zone (the zone of interest of this test program) where the controlled brake was applied, the deceleration obtained from each trial remained relatively the same (approximately 0.75 m/s^2). Therefore the cost-effective means of accelerating the bogie was considered technically sound and satisfactory for the purpose of the investigation.

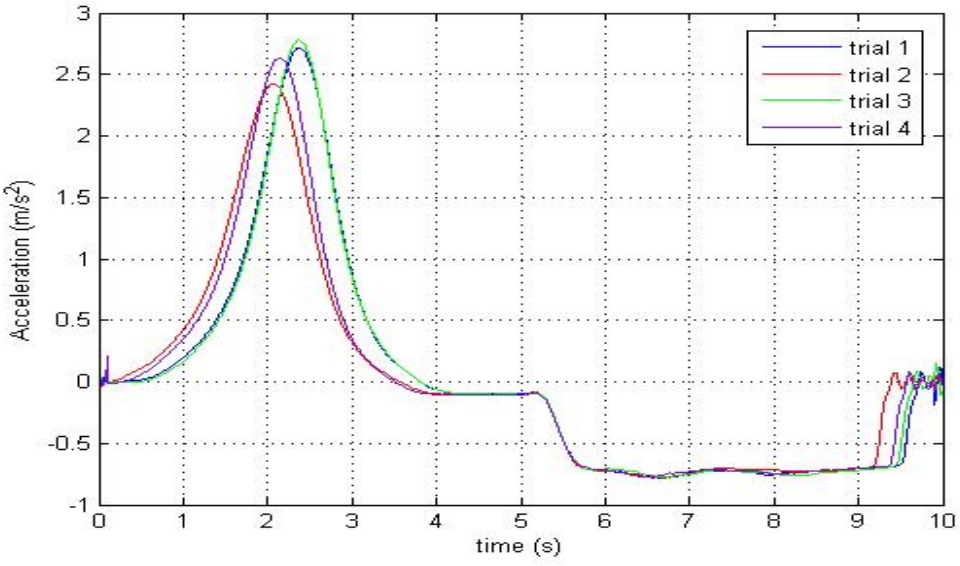

Figure 7.3. Longitudinal accelerations measured by accelerometers, Case #1

Fig.7.4 and Fig.7.5 show, respectively, the lateral (average of two measurements) and the vertical (average of four measurements) accelerations measured using the accelerometers. The magnitude of these accelerations was very small both in absolute term and relative to the longitudinal acceleration (Fig.7.3). The low magnitude could be regarded as an indication of the good control exercised in each trial especially the precision of the applied pull without any lateral shift; it also reflected on the smoothness of the track, in particular the top surface of the rail. The lateral and the vertical accelerations remained negligibly small for *all three cases* of the experiment reported in this chapter; thus these are not presented for other cases. All cases of the experiment can, therefore, be regarded as pure longitudinal dynamics investigation.

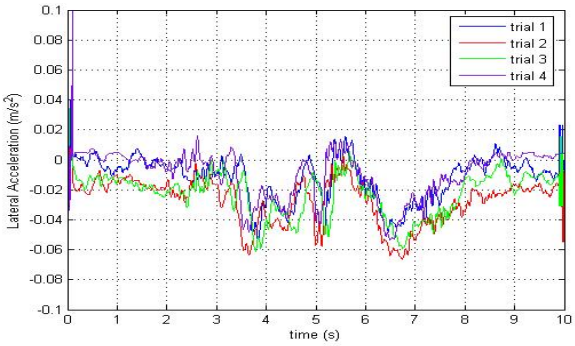

Figure 7.4. Lateral accelerations measured by accelerometers, Case #1

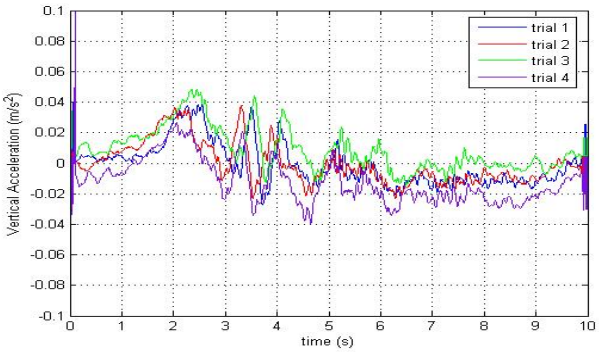

Figure 7.5. Vertical accelerations measured by accelerometers, Case #1

Linear distance travelled and angular revolution of wheelsets

The linear distance travelled of the bogie along the test track is shown in Fig.7.6.c, while the angular revolution of the leading and the trailing wheelsets are respectively presented in Fig.7.6.a and b. This figure depicts that the longest travel distance was approximately 16 m. During this travel, the wheelsets rotated approximately 40 rad, or just more than six full rotations.

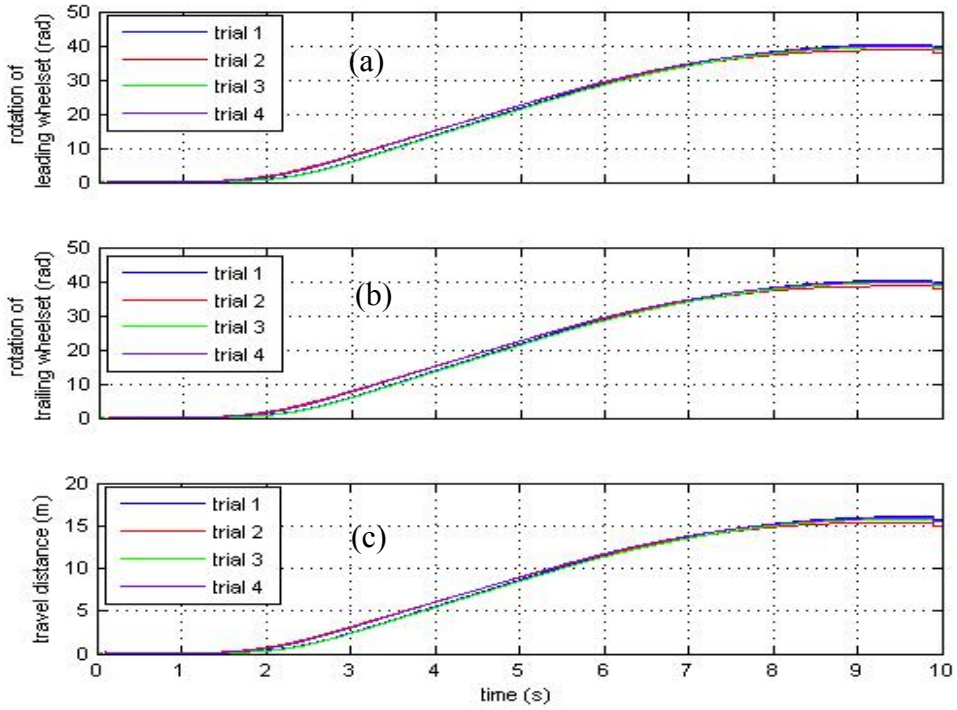

Figure 7.6. Travel distance and rotation of wheelsets, Case #1

7.2.2. Derived Data

Brake torque

Brake torque applied to the trailing wheelset was calculated using Eq.(7.1):

$$T_B = \left(F_{T1} + F_{T2}\right) r_w \qquad (7.1)$$

where T_B denotes the brake torque, F_{T1} and F_{T2} are the tangential force measured in hangers 1 and 2 respectively and r_w is the nominal radius of the wheels (0.398 m, measured before the test). The calculated brake torque time series is shown in the Fig. 7.7.

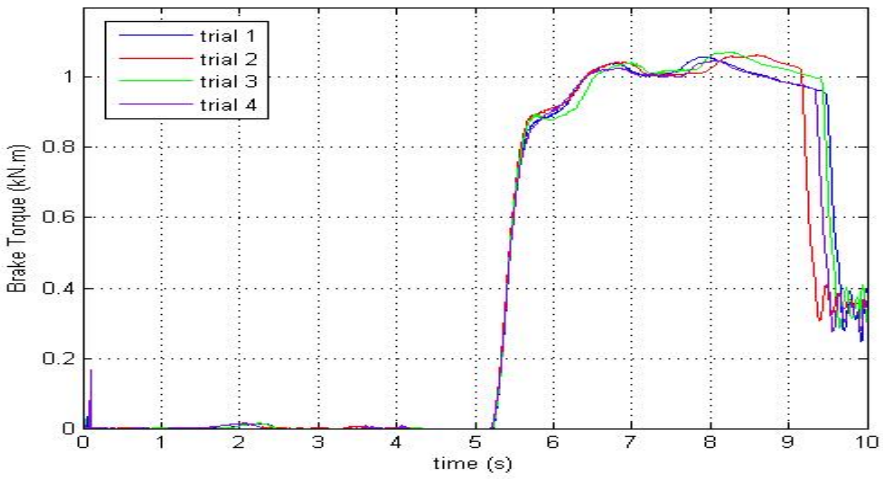

Figure 7.7. Brake torques applied to the trailing wheelset, Case #1

Speed profile and angular velocity of the wheelset

Fig. 7.8 shows the bogie speed profile and the angular velocities of the wheelsets. The bogie speed profile is the first derivative of the dataset obtained by the LIMES linear encoder with respect to time whilst the angular velocities of the wheelsets were obtained from the first derivatives of the HENGSTLER shaft encoder datasets. From Fig. 7.8, we can see that no skid happened at the braked trailing wheelset for all four trials as its angular velocity was reduced to zero at the same rate as the bogie speed and the angular velocity of the non braked leading wheelset. The maximum speed obtained was 3.14 m/s (trial 1), which was lower than the 4 m/s maximum speed for which the experiment was designed (Chapter 6). With the nominal wheel radius of 0.398 mm

(measured), the maximum angular velocity of 7.89 rad/s was calculated. The measured maximum angular velocity was 7.90 rad/s, showing the precision of the measurement system.

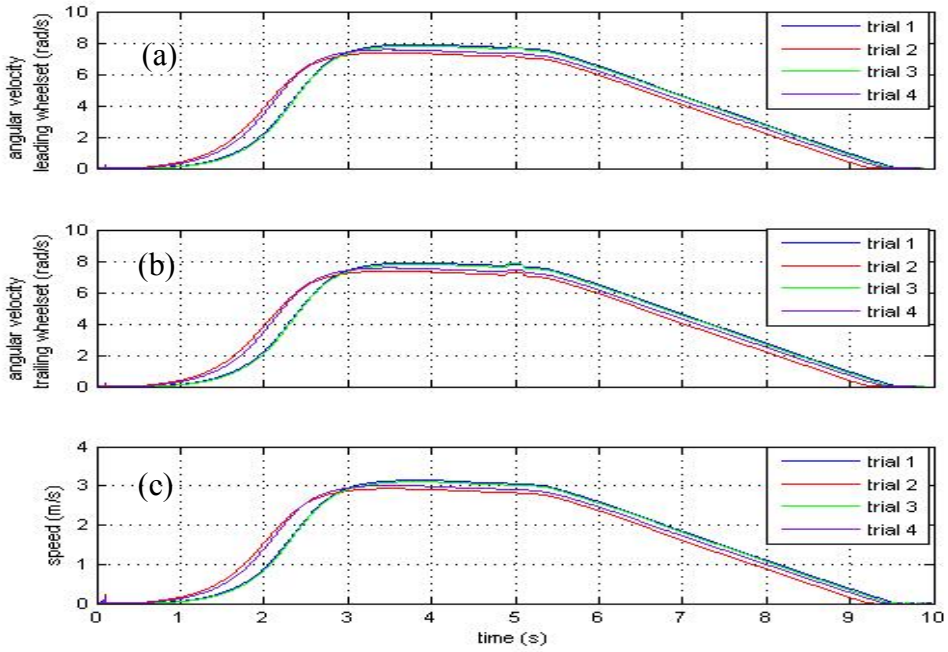

Figure 7.8. Speed profile and wheelsets angular velocity, Case 1

Longitudinal accelerations

Fig. 7.9 exhibits the bogie longitudinal acceleration calculated through the second order numerical differentiation of the linear distance data obtained from the LIMES linear encoder. It provides a very good agreement with the direct measurement of longitudinal acceleration using accelerometers (Fig. 7.3)

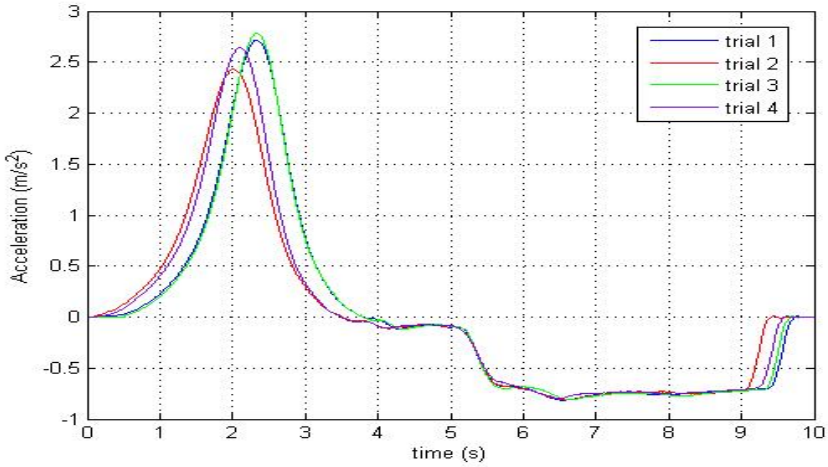

Figure 7.9. Accelerations calculated using Linear Encoder dataset, Case #1

Slip

Due to the application of the brake, slip (or creepage) occurred in the contact patch of the trailing wheelset (where brake was applied). The slip was measured as the difference between the longitudinal velocity (Fig. 7.8 (c)) and the circumferential velocity of the braked wheelset (Fig. 7.8. (b)). The occurrence of slip generated longitudinal retarding force that stopped the bogie. Fig 7.10 shows the difference between the longitudinal velocity and the circumferential velocity of the braked wheelset in the braking zone (from t=5s to t=10s). This figure *represents* the slip that occurred during the brake application.

With a view to obtaining slip through another data set (namely the velocity difference of the braked and unbraked wheelsets), the reference longitudinal velocity was set equal to the circumferential velocity of the unbraked leading wheelset. The slip calculated using this method is shown in Fig. 7.11. Both Fig. 7.10 and 7.11 show very good agreement. This finding has practical significance as it appears possible to

measure slip in the field without using the LIMES linear encoder system and purely through measurement of angular revolutions of the braked and unbraked wheelsets.

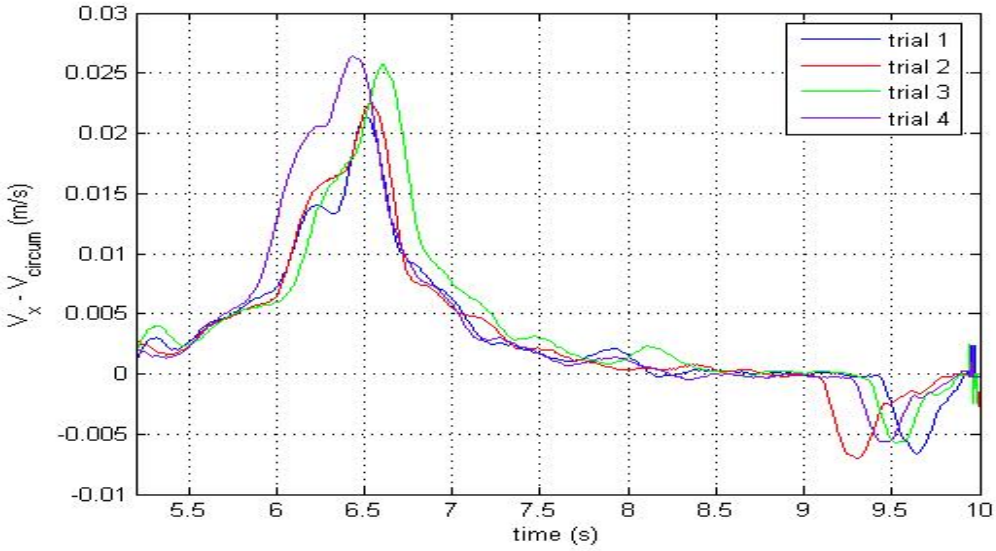

Figure 7.10 Difference between the longitudinal velocity (calculate from LIMES) and the circumferential velocity of the braked wheelset, Case #1

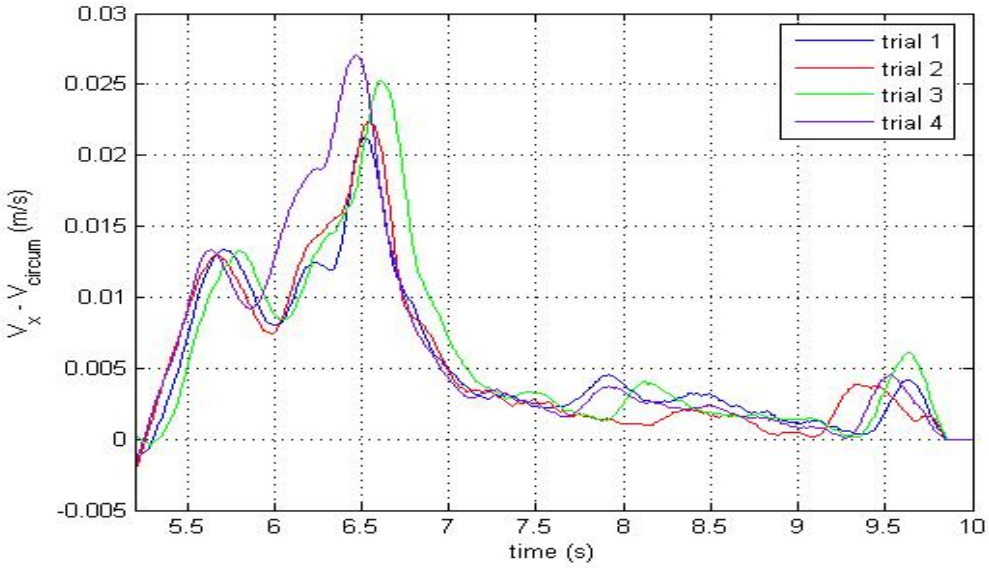

Figure 7.11. Difference between the longitudinal velocity (calculated from angular revolution of unbraked wheelset) and the circumferential velocity of the braked wheelset, Case #1

7.3. EXPERIMENT CASE #2 (P=150 KPA)

For the experiment Case #2, the brake pressure was increased to 150 kPa whilst maintaining the brake application time at 0.8 second. The brake force produced by 150 kPa cylinder pressure brought the braked trailing wheelset just into the skid limit. It was, therefore, difficult to predict whether skid would happen or not, as small changes to the system parameters, such as the friction coefficients and the dynamic wheel loads would have significant influence. Both the friction coefficient and the dynamic wheel load could easily change due to minor changes in the environmental and operational parameters.

7.3.1. Primary Data

Brake cylinder forces – normal and tangential

Fig 7.12 presents the brake cylinder pressure and forces measured in the brake rods of each cylinder for trials 1 to 4 during the execution of test Case #2. The figure shows that, when the brake was applied, the pressure in the brake cylinder increased from zero to 150 kPa in 0.8 second. The corresponding increase in the brake rod forces occurred without any time lag. Both rods measured approximately the same magnitude of brake shoe normal forces. The measured forces were approximately 19% lower than the force specified for new bogies (0.164 kN per kPa or 6.15 kN for 150 kPa) due to efficiency loss of the refurbished brake cylinder.

Fig. 7.13 shows the tangential brake force measured in the brake beam hanger for trials 1 to 4 of Case #2. As both the normal and the tangential brake shoe forces were measured, the friction coefficient between the brake shoe and the wheel tread (μ_s) was

able to be calculated, and the calculated values for Case #2 were found to vary between 0.23 and 0.30 (which compared favourably with Case #1 values of 0.27 - 0.33).

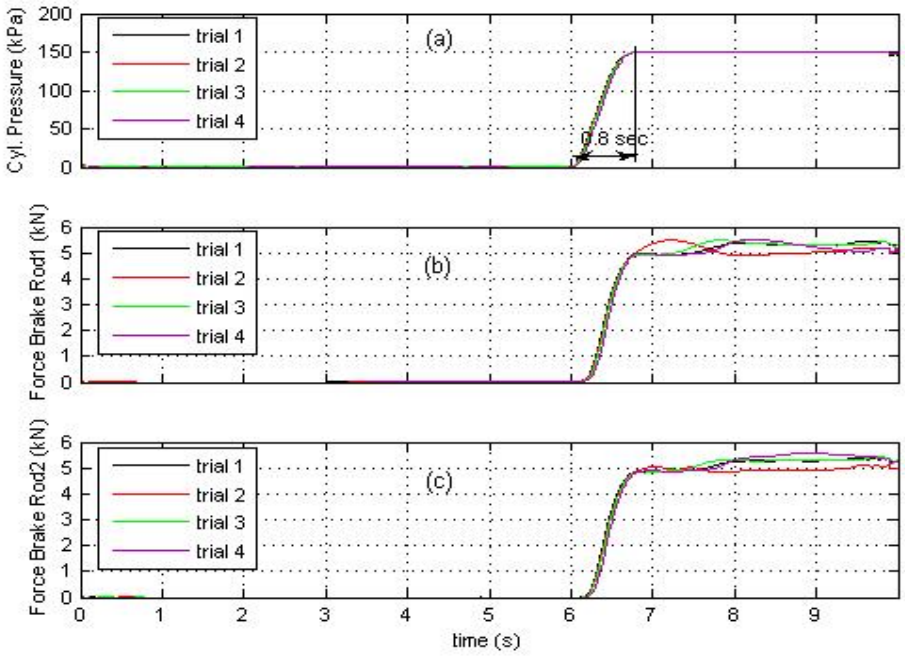

Figure 7.12. Brake cylinder pressure and forces in the brake rods, Case #2

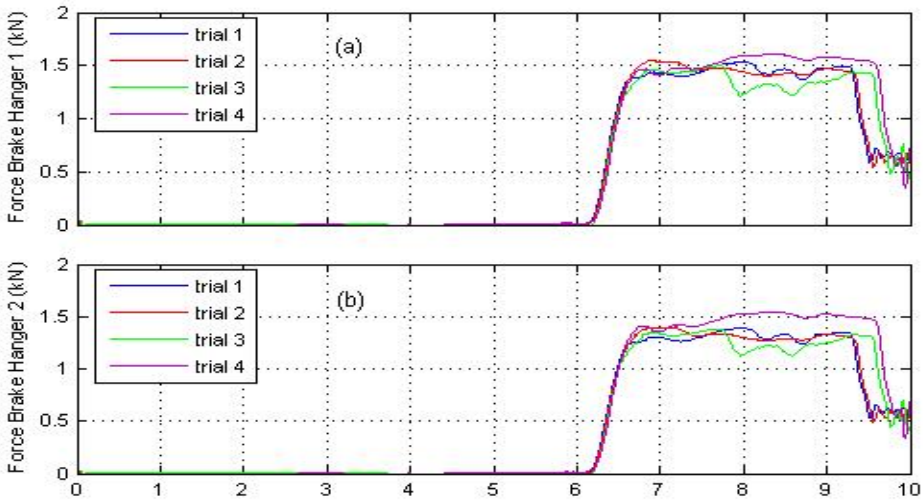

Figure 7.13. Tangential brake force in the brake beam hangers, Case #2

Accelerations

Fig. 7.14 shows the average of the measured longitudinal accelerations obtained from four accelerometers. The maximum longitudinal acceleration recorded varied from 1.8 m/s^2 to 2.4 m/s^2. Similar to the experiment Case #1, in the coasting zone each trial has provided a deceleration of approximately 0.1 m/s^2 due to rolling resistance. In the braking zone (the zone of interest of this test program) where the controlled brake was applied, the maximum deceleration obtained was 0.8 m/s^2 (trial 4).

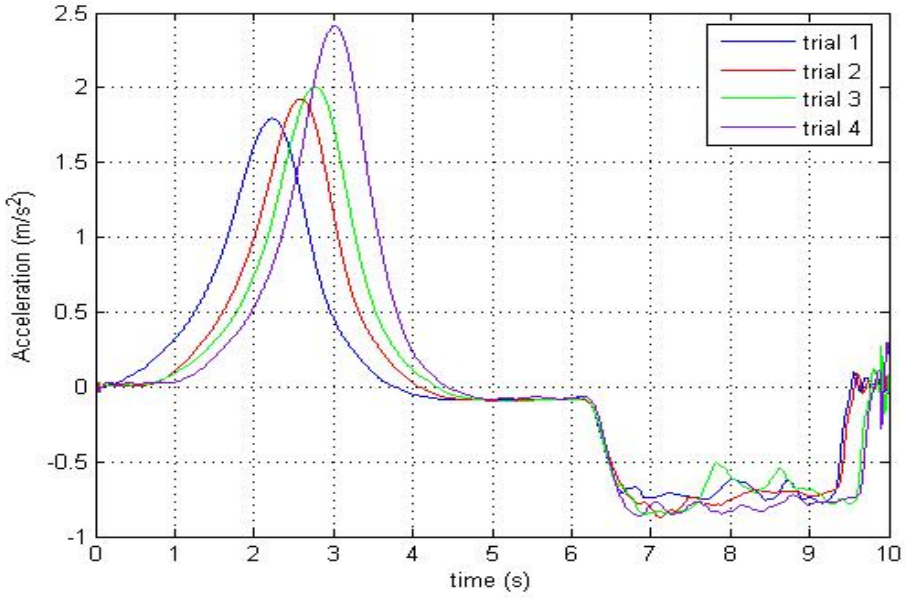

Figure 7.14. Accelerations measured by accelerometers, Case #2

Linear distance travelled and angular revolution of wheelsets

The travel distance of the bogie and rotation of the wheelsets during the experiment Case #2 is shown in Fig. 7.15. Fig. 7.15 (c) shows that the longest distance travelled has been 14.43 m. This distance related to the wheelset angular revolution of 36.25 rad, which was less than six full rotations of the wheelsets (see Fig. 7.15. (a) and (b)). The longest travel distance happened during the execution of the trial 4 when the highest

speed during the experiment Case #2 was achieved. When the skid occurred (trials 1 and 3), the angular revolution of the braked trailing wheelset was smaller than that of the unbraked leading wheelset.

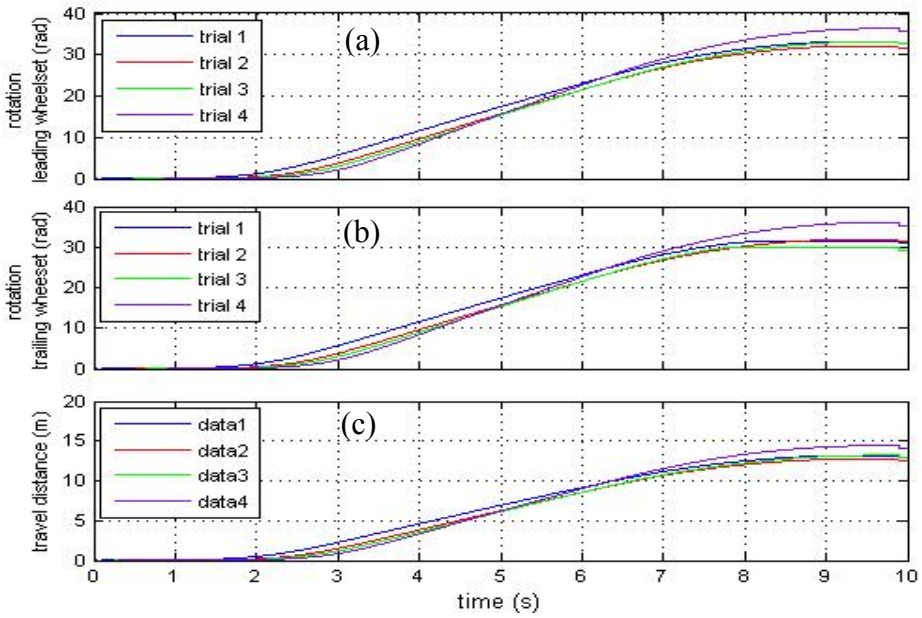

Figure 7.15. Travel distance and rotation of wheelsets, Case #2

7.3.2. Derived Data

7.3.2.1 Brake torque

Fig. 7.16 exhibits the brake torque applied to the trailing wheelset, calculated using Eq. 7.1. When severe skid happened (later discussion on Fig.7.17) the brake torque dropped drastically to 0.95 kN.m as shown in trial 3, whilst in the condition without skid the brake torque was as high as 1.25 kN.m. This result revealed that skid could adversely affect the braking performance of the bogie.

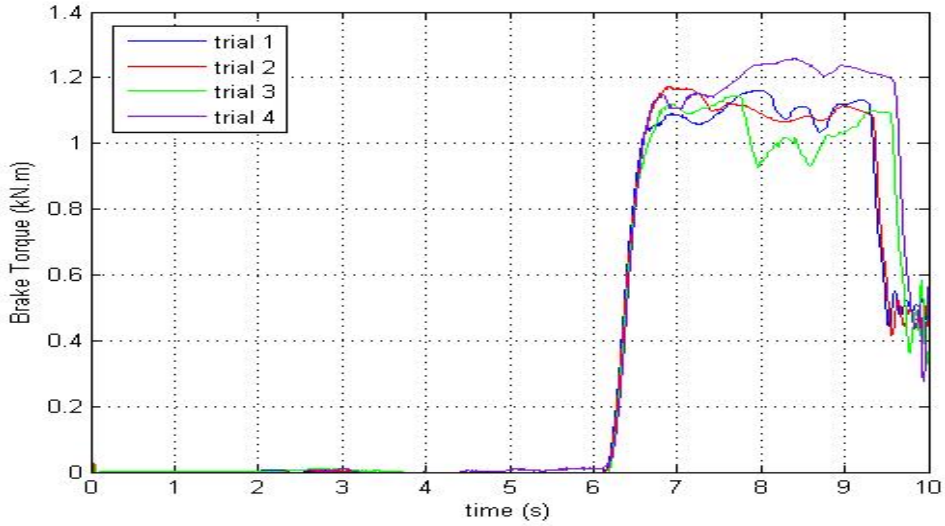

Figure 7.16. Brake torque applied to the trailing wheelset, Case #2

Speed profile and wheelsets angular velocity

The speed profile and the wheelset angular velocities of the bogie during the execution of the experiment Case #2 is presented in Fig. 7.17. The maximum speed obtained was 2.87 m/s (10.15 km/h), which occurred during trial 4. Fig. 7.17 (a) and (b) show that this speed is related to the wheelset angular velocity of 7.24 rad/s. Among the four trials of the experiment Case #2, wheelset skid occurred during trials 1 and 3 whilst in the other two trials wheelset skid did not occur. These results show that with the brake cylinder pressure of 150 kPa the braked wheelset was just on the verge of the onset of skid where the possibility to have skid is the same as the possibility of having no skid.

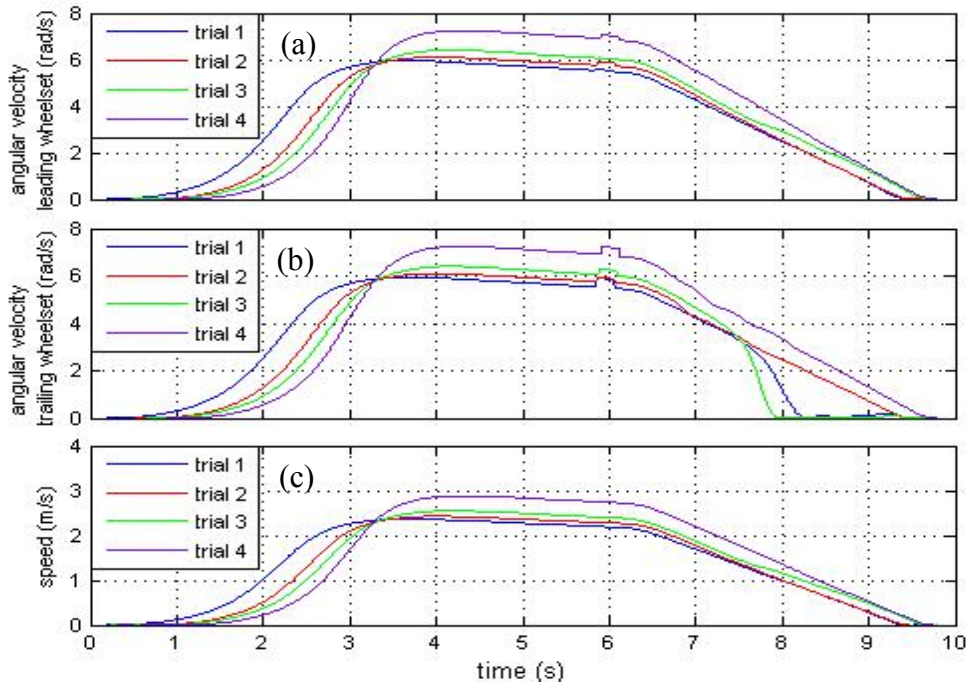

Figure 7.17. Speed profile and wheelsets angular velocity, Case #2

Longitudinal acceleration

Fig. 7.18 exhibits the bogie longitudinal acceleration time series obtained from the experiment Case #2 (calculated through the second order numerical differentiation of the linear distance data obtained from the LIMES linear encoder). Similar to the experiment Case #1, it provides a very good agreement with the direct measurement of longitudinal acceleration using accelerometers (Fig. 7.14). This shows that the onboard measurements are accurate enough and the wayside LIMES system provides an additional assurance on the accuracy of the onboard system measurements.

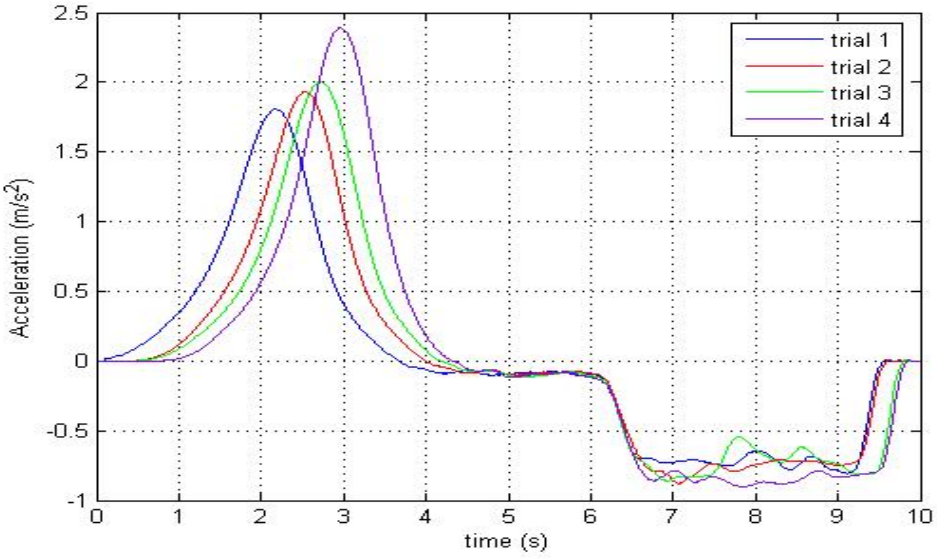

Figure 7.18. Accelerations calculated using Linear Encoder dataset, Case #2

Slip

Fig. 7.19 shows the difference between the longitudinal velocity and the circumferential velocity of the braked wheelset occurred during the application of the braking in Case #2. This figure represents the slip which occurred during the brake application. The longitudinal velocity used to obtain the curves in Fig. 7.19 was taken from the first derivative of the LIMES linear encoder dataset. For comparison, the slip was also calculated using the HENGSTLER shaft encoder of the unbraked wheelset as reference (Fig. 7.20). Both Fig. 7.19 and Fig. 7.20 show very good agreement. It can be clearly seen in Fig. 7.19 and Fig. 7.20 that, in trial 1, one hundred percent slip (skid) started to happen at t = 8.2 second as the circumferential velocity of the braked trailing wheelset becomes zero at this point of time. For trial 3, one hundred percent slip occurred earlier at t = 7.9 seconds.

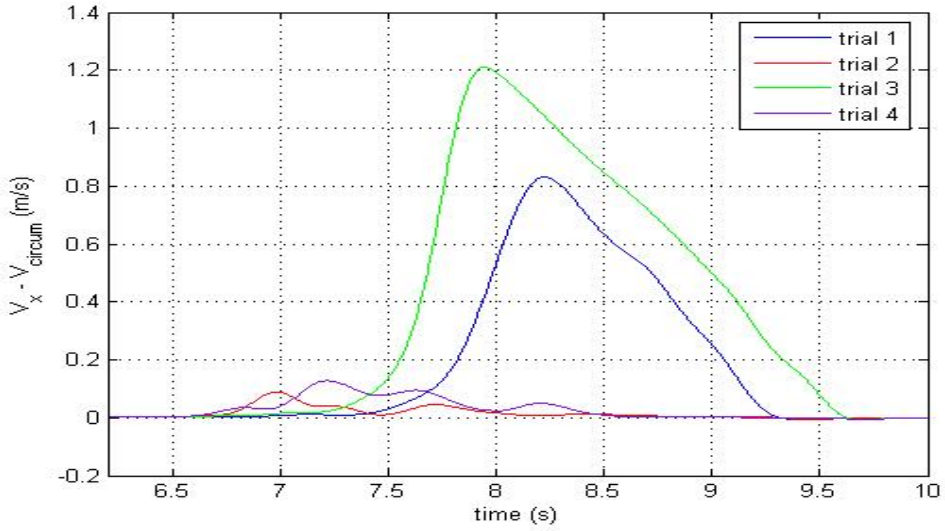

Figure 7.19. Difference between the longitudinal velocity (calculated from LIMES) and the circumferential velocity of the braked wheelset, Case #2

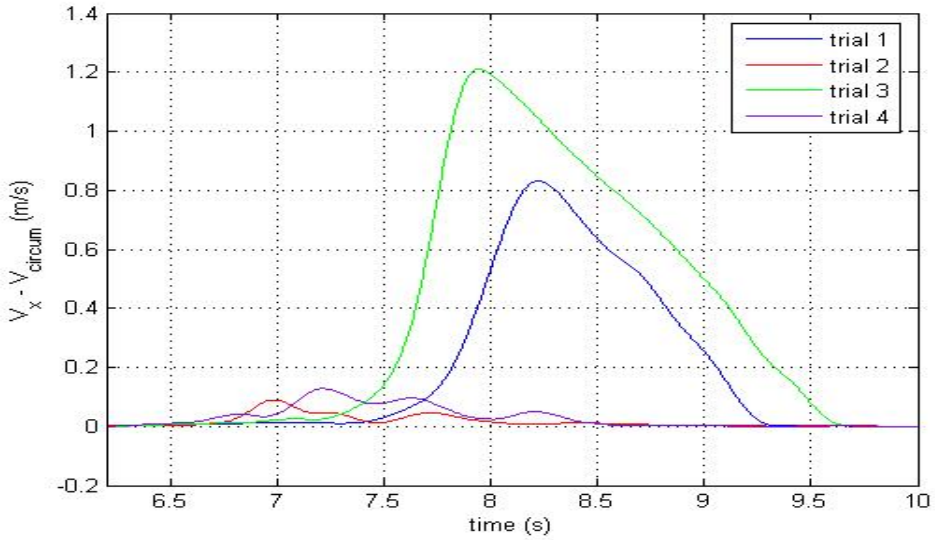

Figure 7.20. Difference between the longitudinal velocity (calculated from angular revolution of unbraked wheelset) and the circumferential velocity of the braked wheelset, Case #2

7.4. EXPERIMENT CASE #3 (P=180 KPA)

The purpose of the experiment Case #3 was to study the severe skid during the heavy braking. In the experiment Case #3 the brake pressure was increased to 180 kPa, much above the skid limit pressure. The brake application was maintained at 0.8 second. All trials exhibited skid of the braked wheelset. Results are presented below.

7.4.1. Primary data

Brake cylinder force – normal and tangential

Fig. 7.21 shows the brake cylinder pressure and forces measured in the brake rods of each cylinder for trials 1 to 4 during the execution of test Case #3. As can be seen in the figure, when the brake was applied the pressure in the brake cylinder increased from zero to 180 kPa in 0.8 second with the corresponding increase in the forces of the brake rods without any time lag. Both rods measured approximately the same magnitude of brake shoe normal forces. Similar to Case #1 and Case #2, the measured forces are slightly (approximately 15%) lower than that of the force specified for the new bogie (7.38 kN for 180 kPa) due to efficiency loss of the refurbished brake cylinder.

Fig. 7.22 shows the tangential brake force measured in the brake beam hanger for trials 1 to 4. As both the normal and the tangential brake shoe force were measured, the friction coefficient between brake shoe and wheel tread (μ_s) was able to be calculated. The calculated values for Case #3 varied between 0.21 and 0.28 (which compared favourably with Case #1 values of 0.27-0.33 and Case #2 values of 0.23-0.30)). It appears that with the increase in brake normal force, the friction coefficient reduces.

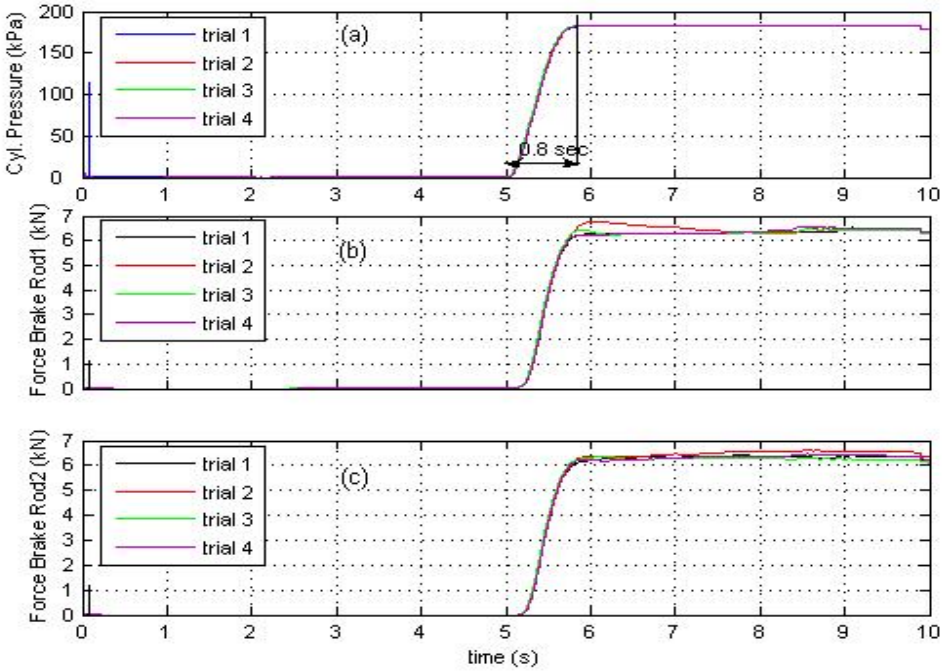

Figure 7.21. Brake cylinder pressure and forces in the brake rods, Case #3

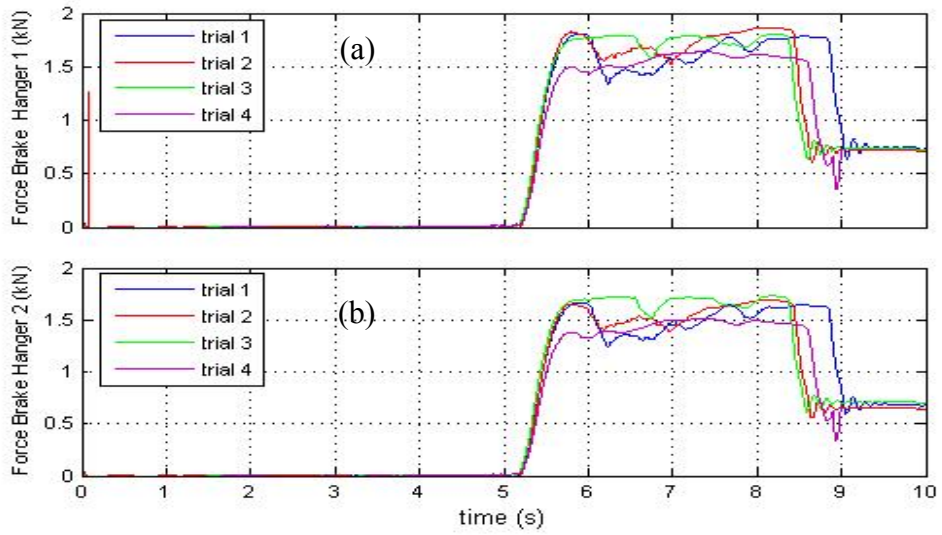

Figure 7.22. Tangential brake force in the brake beam hangers, Case #3

Accelerations

Fig. 7.23 shows the measured longitudinal acceleration of Case #3 (average value of four accelerometers). The maximum longitudinal acceleration recorded varied from 2.2 m/s^2 to 2.5 m/s^2. Similar to the experiments in Case #1 and Case #2, in the coasting zone each trial has provided a deceleration of approximately 0.1 m/s^2 due to rolling resistance. In the braking zone (the zone of interest of this test program) where the controlled brake was applied, the maximum deceleration recorded was 1.1 m/s^2 (trials 2 and 4). However, at the time of the severe skid (later discussion on Fig.7.26), the deceleration fell to 0.5 m/s^2 (trials 1 and 2).

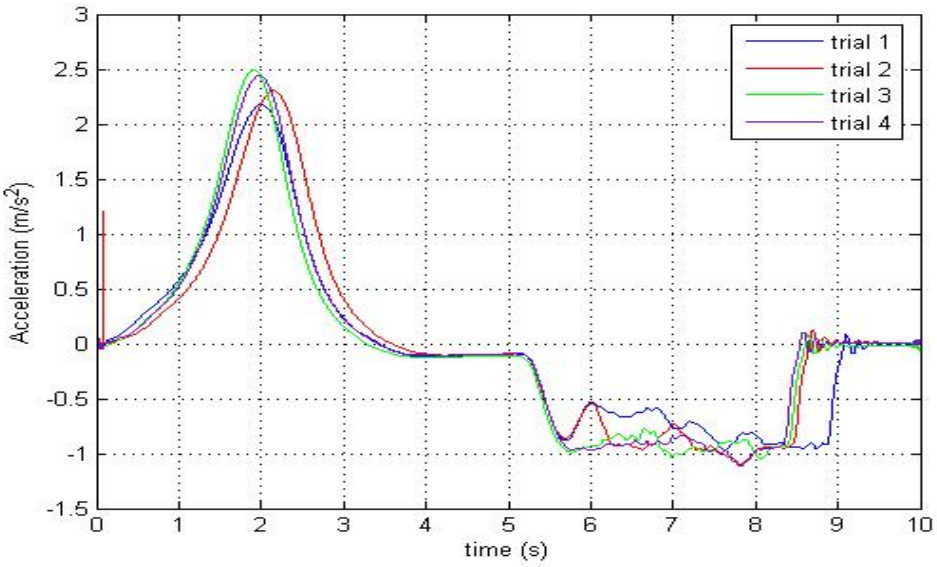

Figure 7.23. Acceleration measured by accelerometers, Case #3

Linear distance travelled and angular revolutions of wheelsets

Fig. 7.24 shows the angular revolution and the travel distance of the bogie obtained during Case #3. The maximum travel distance recorded was 16 m (Fig. 7.24 (c) – trial 1). Figs. 7.24 (a) and (b) reveal that for all trials the angular revolution of the braked

trailing wheelset was smaller than that of the unbraked leading wheelset due to skid (see Fig.7.26).

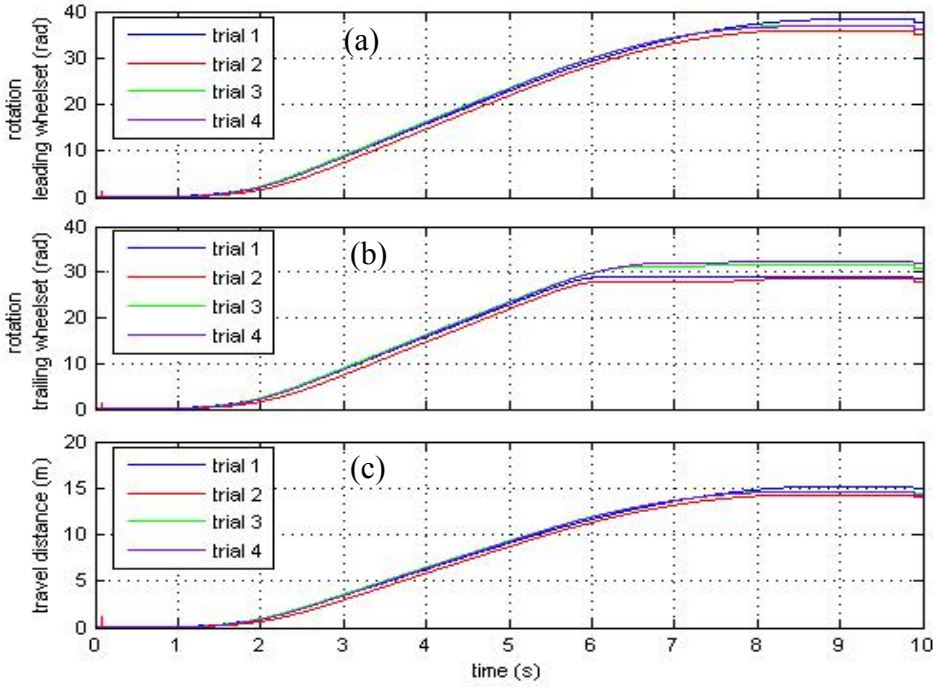

Figure 7.24. Travel distance and wheelsets rotation, Case #3

7.4.2. Derived Data

Brake torque

Fig. 7.25 shows the brake torque applied to the trailing wheelset during the experiment Case #3, calculated using Eq. 7.1. As expected, due to the skid of the trailing wheelset, the brake torque was found to drop drastically. As the most severe skid happened during trials 1 and 2 (see later discussion of Fig. 7.26), the most sudden decrease of the brake torque also occurred during these two trials. This result, again, shows that skid has significant negative effect on the braking performance.

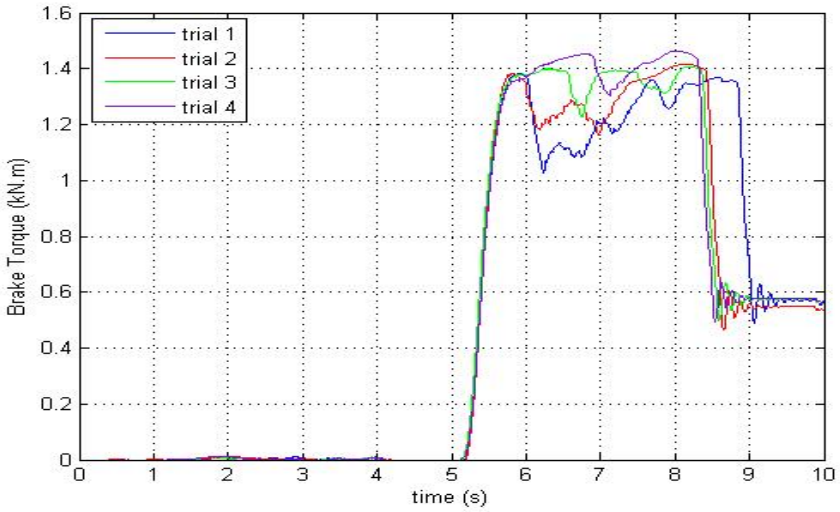

Figure 7.25. Brake torques applied to trailing wheelset, Case #3

Speed profile

Fig. 7.26 shows the speed profile and wheelset angular velocity during the experiment Case #3. As exhibited by Fig. 7.26, the rate of speed decrease was lower if the severe skid happened.

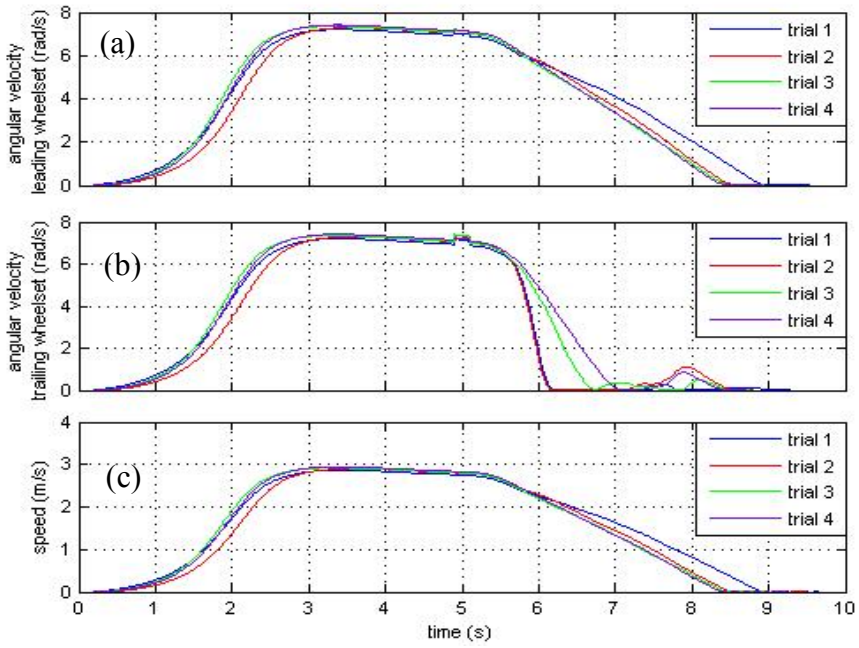

Figure 7.26. Speed profile and wheelsets angular velocity, Case #3

Longitudinal acceleration

Fig. 7.27 exhibits the bogie longitudinal acceleration time series obtained during the experiment Case #3, calculated through second order numerical differentiation of the linear distance data obtained from the LIMES linear encoder. Similar to the experiments in Case #1 and Case #2, it provides a very good agreement with the direct measurement of longitudinal acceleration using accelerometers (Fig. 7.23)

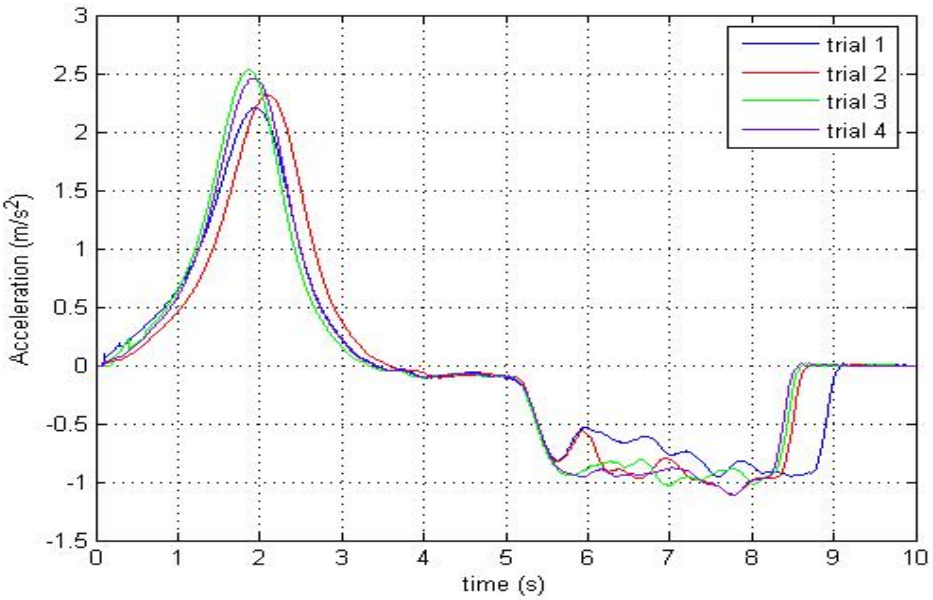

Figure 7.27. Longitudinal acceleration calculated from LIMES, Case 4

Slip

The slip that occurred during the brake application of Case #3 is shown in Fig. 7.28 and Fig. 7.29. The longitudinal velocity was used to obtain the curves in Fig. 7.28 whilst the angular revolution of the unbraked wheelset was used to obtain the curves in Fig. 7.29. Both Fig. 7.28 and Fig. 7.29 show very good agreement. Both figures show one hundred percent slip during all four trials of Case #3. For trials 1 and 2 the skid was detected at around 2.2 m/s, and for trials 3 and 4 it was detected at lower speeds of 1.65 m/s and 1.35 m/s respectively.

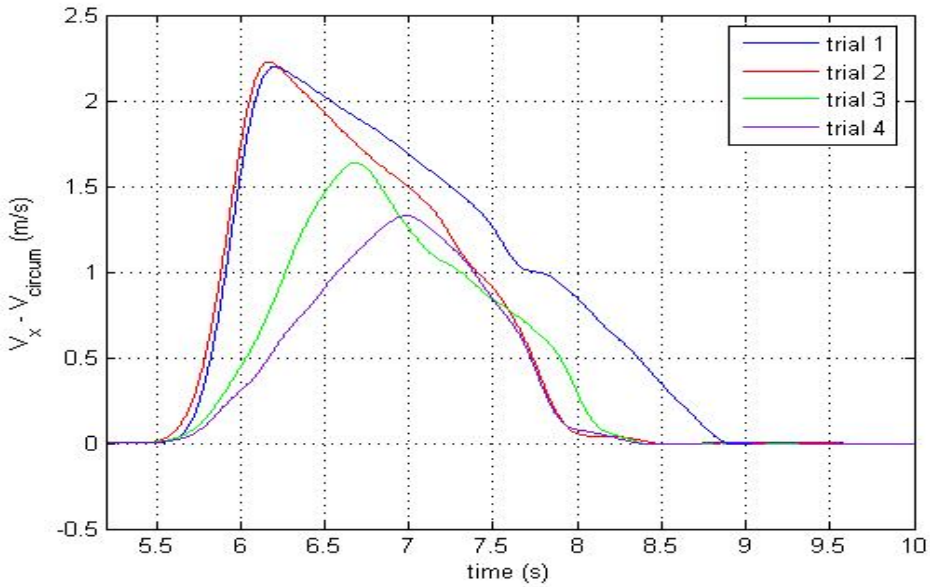

Figure 7.28. Difference between the longitudinal velocity (calculated from LIMES) and the circumferential velocity of the braked wheelset, Case #3

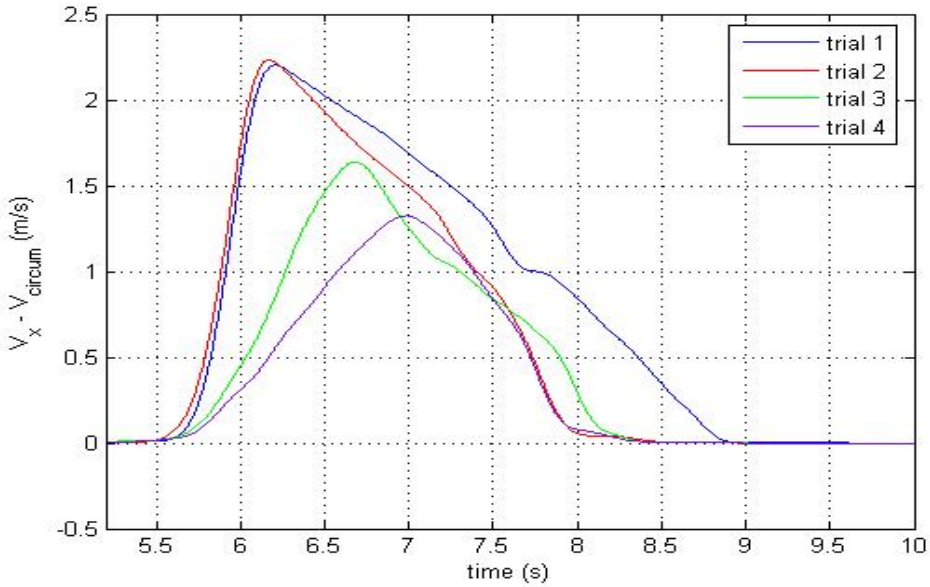

Figure 7.29.Difference between the longitudinal velocity (calculated from angular revolution of unbraked wheelset) and the circumferential velocity of the braked wheelset, Case #3

Friction coefficient between the wheel and the rail

When skid occurs the following equation is fulfilled:

$$T_B = (\mu_{r1} N_{w1} r_{w1}) + (\mu_{r2} N_{w2} r_{w2}) \quad (7.2)$$

where T_B is the brake torque applied to the wheelset (see Eq. (7.1)), μ_{r1} and μ_{r2} are the friction coefficients at the right and the left wheel-rail contact patches respectively, N_{w1} and N_{w2} are the normal loads on the right and the left wheel-rail contact patches respectively and r_{w1} and r_{w2} are the rolling radius of the right and the left wheels respectively. Assuming $\mu_{r1} \approx \mu_{r2} = \mu_r$ and rolling radius of the wheels $r_{w1} \approx r_{w2} = r_w$, Eq. (7.2) can be written as

$$T_B = \mu_r r_w (N_{w1} + N_{w2}) \quad (7.3)$$

During the experiments T_B was obtained by measuring the tangential brake force whilst the nominal wheel radius r_w=0.398m, measured prior to the test execution and N_{w1} and N_{w2} were the right and the left wheel load (sum of the components due to static load and bogie pitching dynamics) of the braked wheelset respectively ($N_{w1} \approx N_{w2} \approx 8.85kN$). Therefore, when skid happened, the friction coefficient between wheel and rail, μ_r, was calculated using Eq. (7.3).

The calculated friction coefficient between the wheel and the rail during the occurrence of skid in this experiment program was found to vary between 0.15 and 0.20. The low coefficient is believed to be typical of "rough" running surfaces; as the running surfaces were not polished to any precision and patches of corrosion products were visible to the naked eye, especially on the railhead, the low friction was considered acceptable.

The friction coefficient calculated from the skid measurements was much lower than the value obtained from the tribometer measurement (0.50 - 0.55 for dry rail and 0.43 - 0.46 if soapy water was applied to the rail surface; see Appendix II). As tribometer measurements could not be regarded as an accurate reflection of the actual case (due to speed /wheel profile /wheel material, for example), the measured tribometer values were disregarded. Field practice also agrees with this decision as tribometer values are only used to determine *relative* changes to the friction coefficients rather than for the *absolute* measure. The friction coefficient calculated from Eq. (7.3) was therefore incorporated in the simulation of the experimental cases reported in Chapter 8.

7.5. SUMMARY AND CONCLUSION

The results of the experimental program described in Chapter 6 have been presented in this chapter. All measurement devices (both onboard and wayside) worked well giving accurate results resulting in good inter-dependent comparisons. All the data gathered from the measurements were found to be consistent. Three cases of experiments were selected for the purpose of reporting. The only variable between the three cases was the brake pressure (130kPa, 150kPa and 180kPa) with the brake application time being kept constant (0.8 sec) for all cases.

From the results of the experiments some important conclusions can be drawn as listed below:

- The piston forces exerted by the brake cylinder (force measured in brake rod) were found to be approximately 15% to 20% lower than the value calculated from the bogie specification at its new condition indicating reduction of the efficiency of the refurbished bogie brake system compared to the new one.

- At the brake pressure of 130 kPa there was no skid detected, showing that at this pressure the bogie was braked below its skid limit.

- At the brake pressure of 150 kPa the braked trailing wheelset was brought into the skid limit region. Within this region the possibility of encountering skid was the same as the possibility of not encountering skid. This uncertainty is due to small changes in the system parameters, such as the friction coefficients and the dynamic wheel loads, would have significant influence.

- The acceleration signatures obtained from direct measurement using the accelerometers agree very well with the acceleration signatures calculated from the second order numerical difference of the LIMES linear encoder data set.

- At the brake pressure of 180 kPa, wheelset skid was detected for all the four trials, showing that at this pressure the bogie was braked above its skid limit.

- Both slip calculation using LIMES linear encoder and using non-braked wheelset shaft encoder as reference to calculate longitudinal velocity showed very good agreement. This finding leads to potential field measurement of slip without the LIMES linear encoder.

- From the measurement of the normal and tangential brake shoe forces, friction coefficients between the brake shoe and the wheel tread were calculated for all cases. It appeared that with the increase in brake shoe forces (or brake cylinder pressure), the coefficient of friction between the brake shoe and the wheel tread reduces. For the 130kPa, 150kPa and 180kPa cylinder pressures, the average friction coefficients determined were 0.30, 0.27 and 0.25 respectively.

- From the six skid trials reported in this chapter, the friction coefficient between the wheel tread and railhead was determined and was found to vary between 0.15 – 0.20. This range is much smaller than the coefficients determined from the tribometer readings (0.50 – 0.55). As the tribometer is considered more relevant for understanding relative changes in friction coefficient, the absolute values of friction coefficient obtained from the tribometer measurements were disregarded. More reliable determination of friction coefficient between the wheel tread and railhead is therefore considered to be the one obtained through the skid trials (0.15 – 0.20).

- The results of the experiment were found to be ***consistent and reliable***; thus they can be used to validate the RBD program built by the author. The validation is reported in Chapter 8.

8. EXPERIMENTAL VALIDATION OF THE EFFECT OF BRAKING TORQUE TO BOGIE DYNAMICS: PART C. COMPARISON WITH THE SIMULATION

8.1. INTRODUCTION

This chapter reports the comparison between the experimental results and the results of the simulations using the RBD program developed as part of this thesis. The parameters considered were the longitudinal acceleration / deceleration, speed profile, angular velocity and slip. The input was the applied brake torque to the trailing wheelset. The wheel-rail friction coefficient used in the simulation was set as 0.18, which was the average value (of 0.15-0.20) obtained from the skid level forces measured from the experiments described in Chapter 7. This value of the friction coefficient was found to be the most representative capable of providing the best result of the simulation as indicated by a series of sensitivity studies..

8.2. MODELLING OF THE BOGIE USED IN THE EXPERIMENT

8.2.1. Bogie Properties

The bogie used in the experiment was modelled as a system containing two wheelsets and one mass (the bolster and the side frames were regarded as one sprung mass), the arrangement of which was the same as that of the model presented in Chapter 5. The mass properties and the dimensions of the bogie are presented in Table 8.1 and Table 8.2 respectively. The dimension and the mass of the bogie were the actual values measured from the bogie used in the experiment; the mass moments of inertia were calculated assuming even distribution of the body mass.

Table 8.1. Inertia properties of the bogie components used in the experiment

	Wheelset	Sprung Mass
Mass (kg)	1050	1480
Mass moment of inertia I_{xx} ($\mathrm{kg \cdot m^2}$)	450	2,000
Mass moment of inertia I_{yy} ($\mathrm{kg \cdot m^2}$)	90	1,500
Mass moment of inertia I_{zz} ($\mathrm{kg \cdot m^2}$)	450	2,500

Table 8.2. Dimensions of bogie used in the experiment

	Measured value (m)
Wheel base	1.675
Lateral distance between primary suspension	0.8
Nominal wheel radius	0.398

8.2.2. Wheel and Rail Profile

Prior to the execution of the experiment, the wheel and the rail profile were measured using the MiniProf tool (see Section 6.3). The rail profile was measured at every 1 m interval and the profile of each wheel was measured at four points (90 degree interval). Samples of measured profiles can be seen in Appendix III. For the purpose of the simulation the measured profile data were averaged. Fig. 8.1 shows the measured wheel profile (average) used in the experiment compared to the LW2 profile and Fig. 8.2 shows the measured rail profile (average) used in the experiment compared to the AS

60kg/m rail profile (LW2 profile and AS 60 kg/m rail profile were used for simulations reported in Chapters 4 and 5).

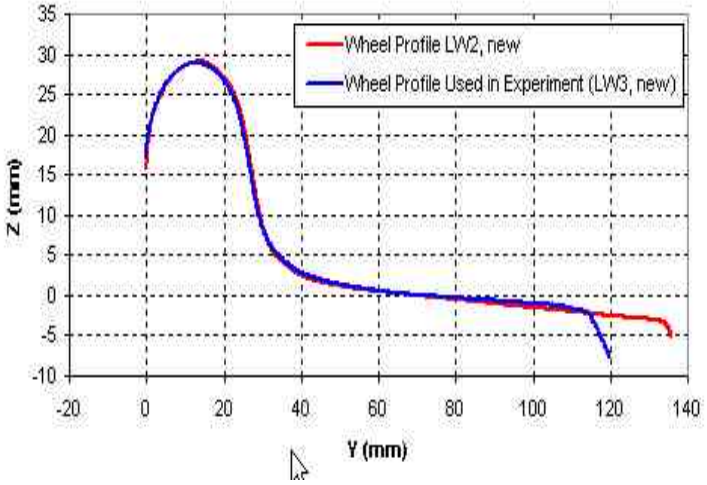

Figure 8.1. Wheel profile used in experiment (LW3) compared to LW2 profile

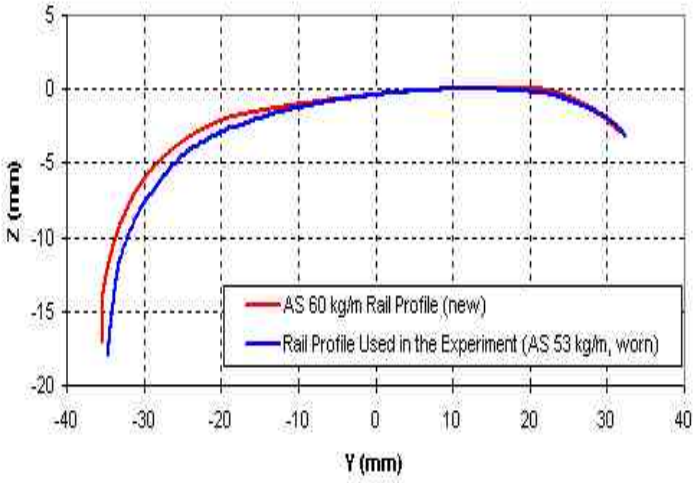

Figure 8.2. Rail profile used in experiment compare to UIC-60 profile

8.3. COMPARISON OF THE RESULTS

The simulation used the measured forces/torques from the experiments as the input. Because the experiments only measured the applied forces/torques of braking, thus the simulation was performed for the braking phase only. The initial speed input for the

simulation was the nominal speed obtained during the coasting (steady state) phase before the brake was applied. To represent the actual condition of the test, a constant torque (65 kN.m) that represented the rolling resistance was required to be added to the input brake torque.

8.3.1. Simulation of Case #1 (Brake Pressure = 130 kPa)

Input brake torque

The input brake torque for the simulation of Case #1 is shown in Fig. 8.3. It is the average value of the brake torques gathered from the four trials of the experiments presented previously in Section 7.2.

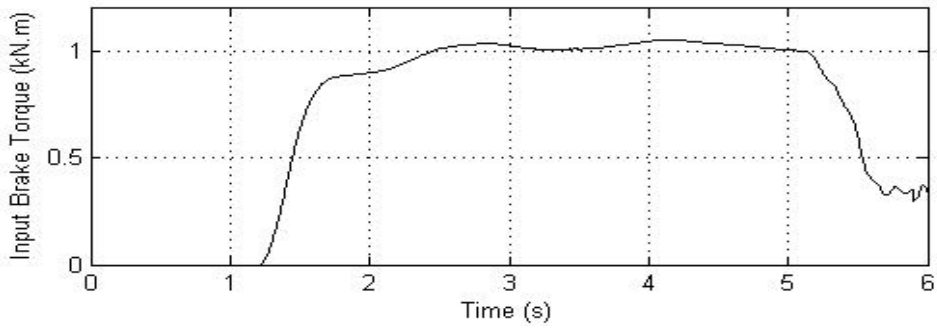

Figure 8.3. Input brake torque for simulation of Case #1

Output deceleration

Fig. 8.4 presents the calculated acceleration profile from the RBD simulation compared to the experimental results of Case #1. This figure reveals that the output acceleration profile of the simulation agrees very well with the measured experimental values, vindicating the accuracy of the formulation and the programming of the RBD program.

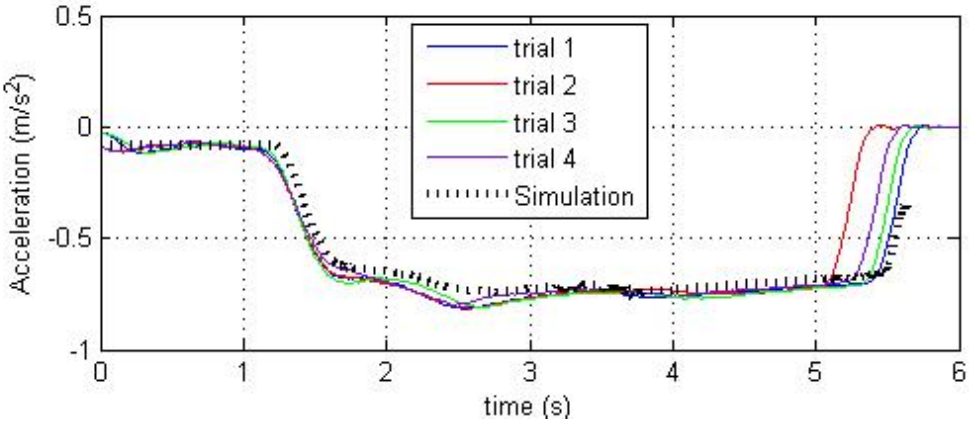

Figure 8.4. Simulation output of Case #1: deceleration

Output speed profile and angular velocity

The output speed profile and the angular velocity of both wheelsets for Case #1 is exhibited in Fig. 8.5.

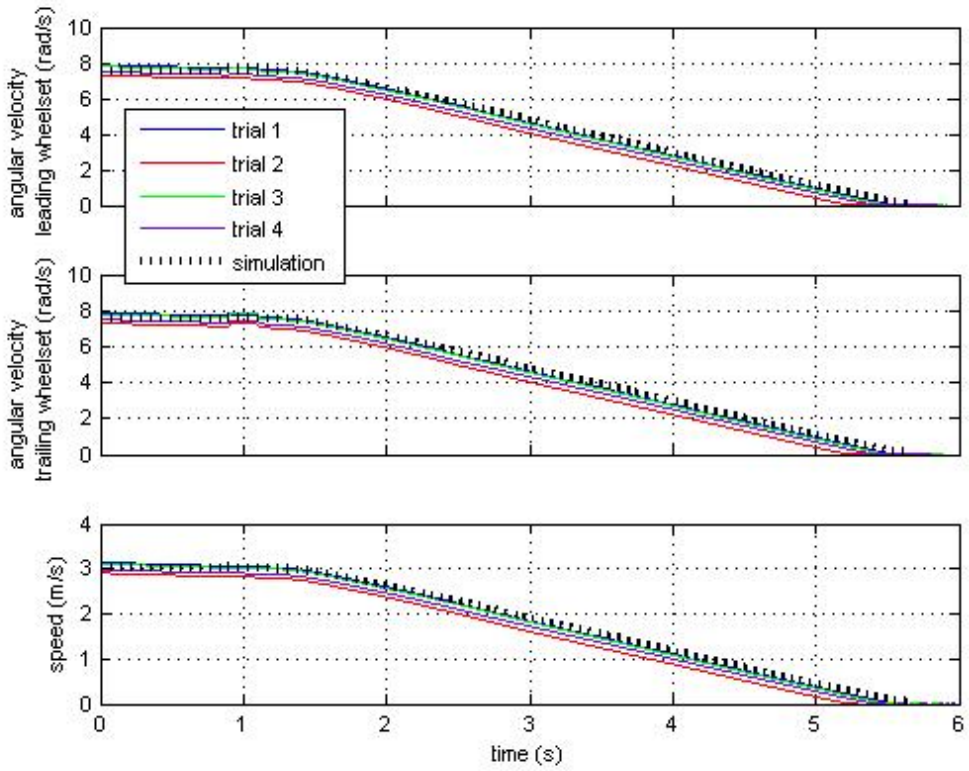

Figure 8.5. Simulation output of Case #1: speed profile and angular velocity

The input nominal initial speed for the simulation was set as 3 m/s. From Fig. 8.5, it can be seen that the RBD program calculates the speed profile and the angular velocity very well in comparison to the experimental results.

Output slip

Fig. 8.6 shows the comparison between the slip calculated by the RBD program and the experimental result for the Case #1. The maximum slip calculated by the RBD program was smaller than the experiment results. However the RBD program predicted the time of occurrence of the maximum slip comparable with the experimental results (around t=2.5s).

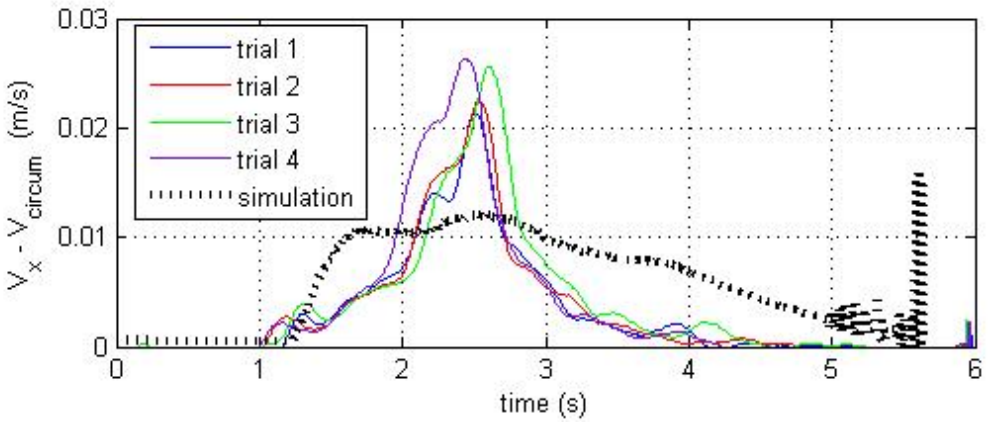

Figure 8.6. Simulation output of Case #1: slip

The areas under the slip curves that represents the energy dissipated due to braking are comparable to each other. Fig. 8.6 shows that the RBD program calculated instantaneous peak of the slip differed to the experimental prediction. In spite of this disagreement at micro-level, the RBD program in general calculates the global behaviour such as the acceleration (Fig. 8.4) and the speed profile (Fig. 8.5) correctly. It seems that the creepage-creep relationship used in the RBD program (the standard

Polach method) was able to generally model the overall dynamics but not the wheel-rail contact detail accurately especially for low values of slip. Future research opportunities exist to improve the creepage-creep force relationship during braking. Another issue that requires consideration is the maximum magnitude of slip for this case, which is very small (≈ 0.025 m/s in Fig. 8.6) and can be regarded as micro-slip. Creepage-creep force relationship due to the slip of such small magnitudes will be more likely affected significantly by the surface condition (tribological properties), which are considered beyond the scope of this thesis.

8.3.2. Simulation of Case #2 (Brake Pressure = 150 kPa)

Input brake torque

The input brake torque for the simulation of Case #2 is shown in Fig. 8.7. It is the average value of the brake torques gathered from the four trials of the experiments presented previously in Section 7.3.

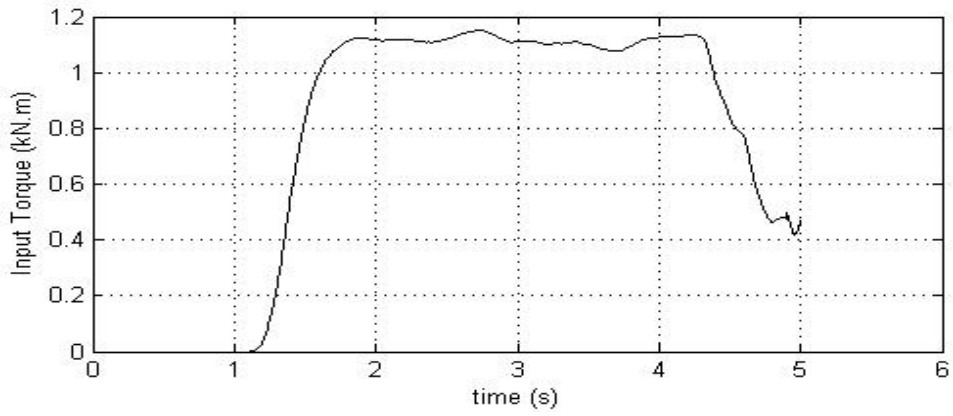

Figure 8.7. Input brake torque for simulation of Case #2

Output deceleration

Fig. 8.8 presents the calculated deceleration from the RBD simulation. The experimental results of Case #2 are also shown in the figure. The output of the simulation agrees very well with the experimental results, once again re-assuring the accuracy of the formulation and programming of the RBD program.

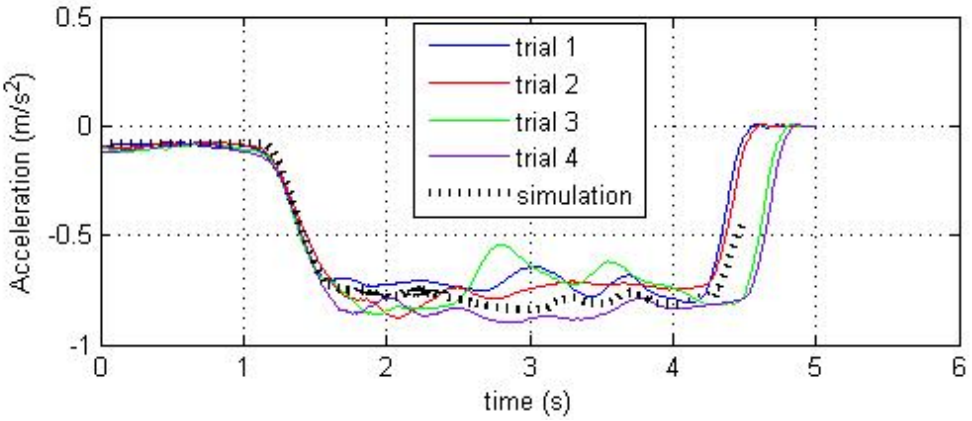

Figure 8.8. Simulation output of Case #2: deceleration

Output speed profile and angular velocity

The output speed profile and the wheelset angular velocity of the simulation are presented together with the experimental results of Case #2 in Fig. 8.9.

The nominal initial speed was set as 2.5 m/s. From Fig. 8.9, it can be seen that the RBD program predicted no skid condition has agreed well with the experimental results of trials 2 and 4. Without having detailed creepage formulation allowing for tribological surface parameters, it was not possible to predict skid that happened in trials 1 and 3 of the experiment. In other words, from the parameters considered in the simulation, for the wheel and rail profile and the friction coefficient used, and the initial speed specified, prediction is that the bogie will experience no wheelset skid. The trials that

exhibited skid in the experiment could be regarded as some special cases where some parameter has slightly varied unfavourably.

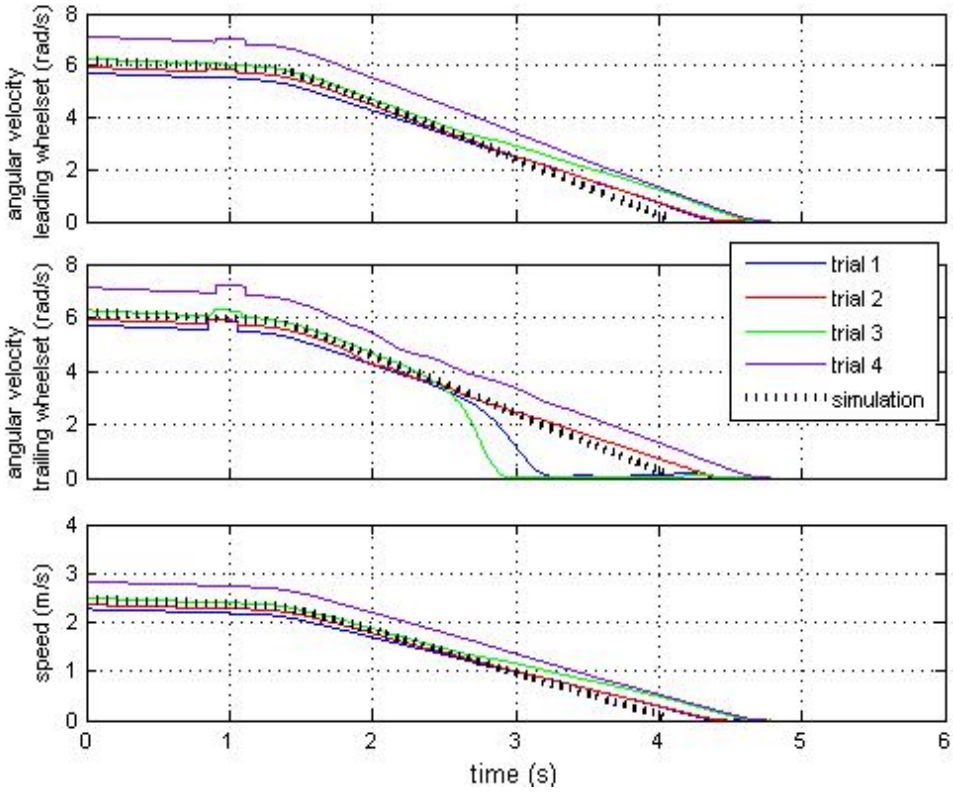

Figure 8.9. Simulation output of Case #2: speed profile and angular velocity

Output slip

Fig. 8.10 shows the slip calculated by the RBD program and the experimental result for Case #2. The maximum slip calculated by the RBD program, which predicted no skid, was smaller than the experiment results of trials 1 and 3 where the skid occurred. However compared to the experimental trials 2 and 4 where no skid occurred, the slip calculated by the RBD program was marginally larger. It should be noted that the vertical axis of the graph shown in Fig. 8.10 represents 50 times larger slip compared to the vertical axis of the graph in Fig. 8.6 (Case#1).

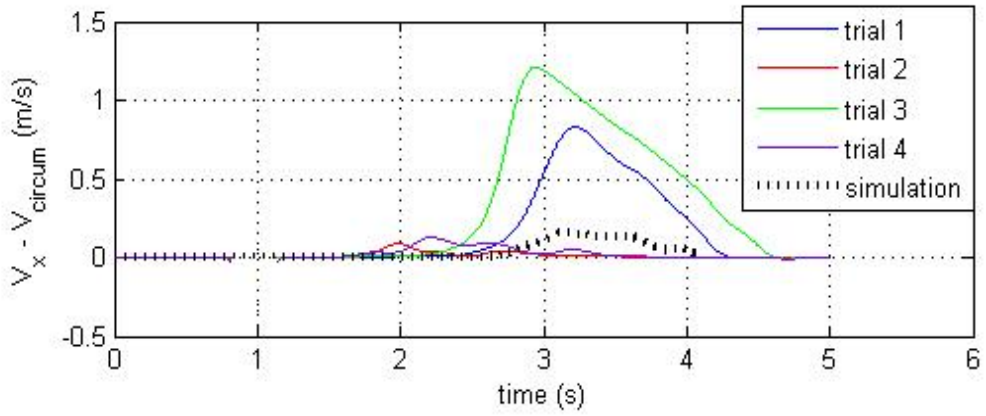

Figure 8.10. Simulation output of Case #2: slip

8.3.3. Simulation of Case #3 (Brake pressure = 180 kPa)

Input brake torque

The input brake torque for the simulation of Case #3 is shown in Fig. 8.11. It is the average value of the brake torques gathered from the four trials of the experiments presented previously in Section 7.4.

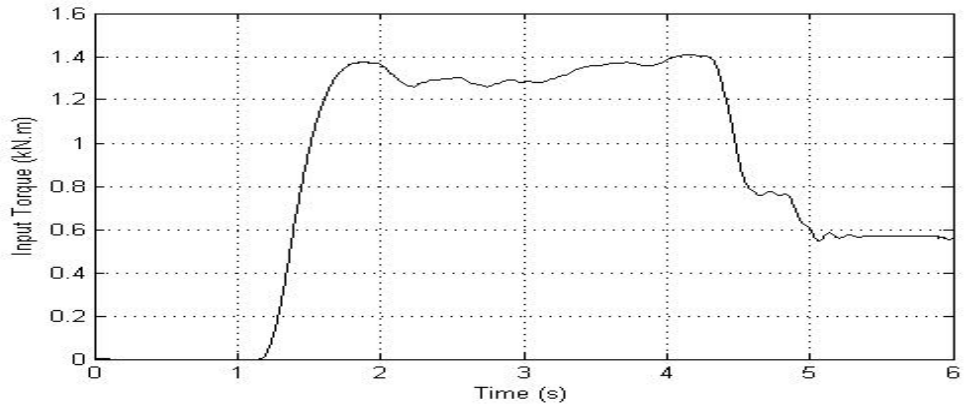

Figure 8.11. Input brake torque for simulation of Case #3

Output deceleration

Fig. 8.12 presents the calculated deceleration from the RBD simulation and the experimental results of Case #3. The output deceleration of the RBD simulation was found to compare very well with the experimental values. Once again, the ability of the RBD program to deal appropriately with such severe dynamics cases is illustrated through this case.

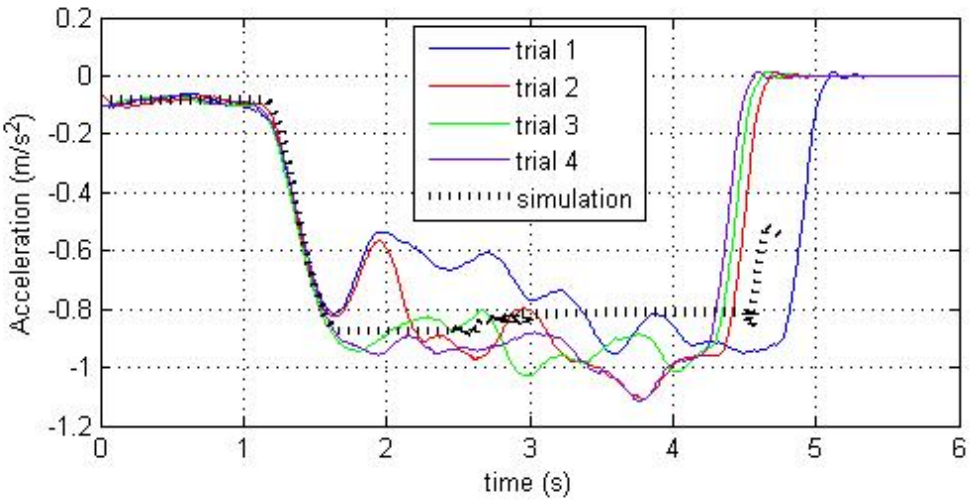

Figure 8.12. Simulation output of Case #3: deceleration

Output speed profile and angular velocity

The output speed profile and the wheelset angular velocity of the simulation and the experimental results of Case #3 are exhibited in Fig. 8.13. The nominal initial speed was set as 2.9 m/s in the simulation. From Fig. 8.13, it can be seen that the RBD program calculated speed profile and angular velocity agree very well with the experimental results. The RBD program has also predicted the occurrence of skid due to large brake torque applied, which is appropriate and consistent with the experimental observations.

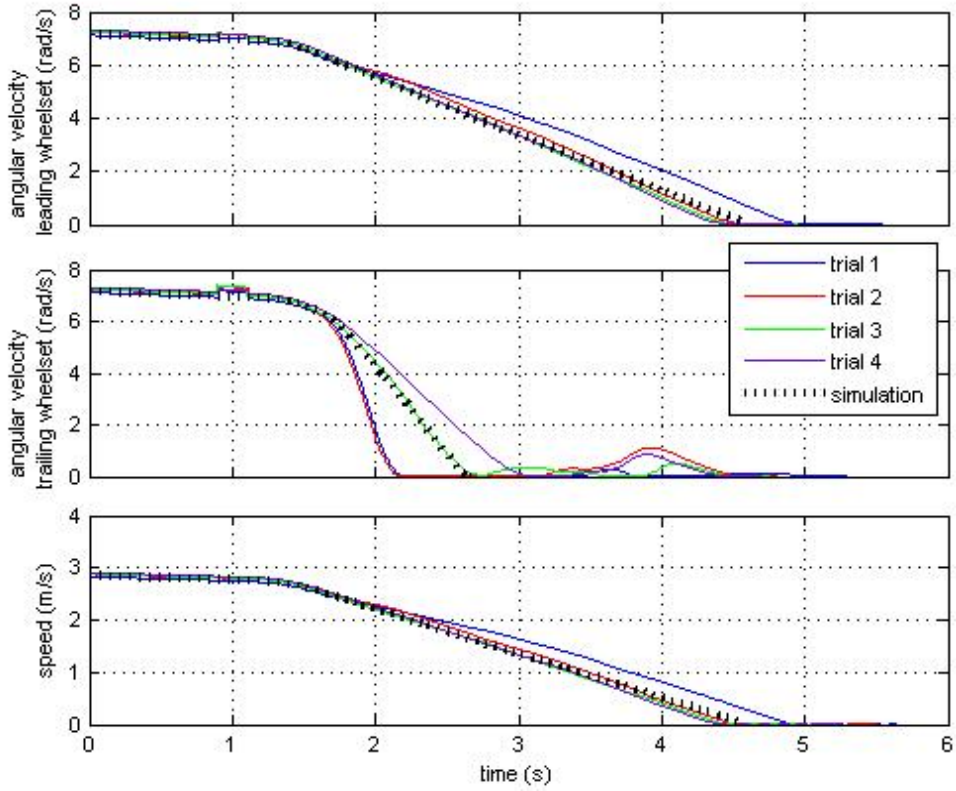

Figure 8.13. Simulation output of Case #3: speed profile and angular velocity

Output slip

Fig. 8.14 shows the slip calculated by the RBD program and the experimental result for Case #3.

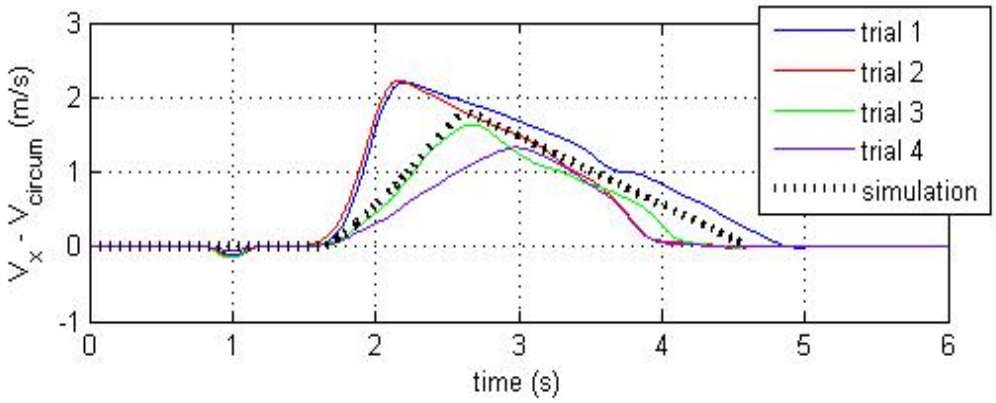

Figure 8.14. Simulation output of Case #3: slip

The RBD program predicted one hundred percent slip (skid) occurring at the speed of 1.8 m/s, at t=2.7s, very close to the values obtained during trial 3 of the experiment Case #3. The order of magnitude of the slip which occurred in this case is approximately 70 times larger than the trials in Case#1. For such larger cases of slip, the creepage – creep force relationship used in the RBD program (standard Pollach method) appears appropriate.

8.4. SUMMARY AND CONCLUSION

Computer simulation of the experiment using the RBD program has been performed and the simulation results have been compared to the data gathered from the experiment. Important conclusions drawn are as follows:

- RBD program simulates the longitudinal dynamics of the bogie used in the experiment under the application of brake very well. The results of the simulation are generally very close to the data obtained from the experiment.

- Although the RBD program did not calculate the instantaneous peak of the slip during the application of the brake without skid, especially for very low values of slip, the program can generally calculate the acceleration and the speed profile correctly. It seems that the creepage-creep relationship used in the RBD program (the standard Polach method) was able to generally model the overall dynamics but not the detail of wheel-rail contact (creepage-creep forces relationship) for such conditions. This observation opens the possibility for future research opportunities to improve the creepage-creep force relationship during braking, where large instantaneous longitudinal creepage occurs.

- The RBD program could now be regarded as being validated for most practical conditions including severe dynamics/skid.

9. APPLICATION OF THE RBD PROGRAM: EFFECT OF ASYMMETRIC BRAKE FORCES TO BOGIE DYNAMICS

9.1. INTRODUCTION

The RBD program and its formulation developed as part of this thesis could now be regarded as being validated for most practical conditions based on the discussions in chapter 8. This chapter reports on severe bogie dynamics due to the application of asymmetric brake normal forces within a single wheelset in bogies equipped with one-side push brake shoe arrangement. Such a situation could lead to the deterioration of the running performance of the bogie including potential for derailment. Handoko et al. (2004) has reported some limited examination of the effect of asymmetric braking to the curving performance of a wagon negotiating a downhill slope with the brake forces applied to keep the *speed constant*. However, to the best knowledge of the author, no studies of asymmetric braking during *variable speed* have been reported in the literatures. The RBD program has the capability to simulate such severe conditions and in this chapter its potential is reported through examples.

9.2. DEFINITION OF ASYMMETRIC BRAKING

Fig. 9.1 shows the brake rigging arrangement of a simple bogie equipped with one-side push brake shoe arrangement. The braking force produced by the brake cylinder that is mounted on the wagon underframe is distributed to the wheels through a mechanical link arrangement. The mechanical link, called brake rigging, consists of rods and levers suspended from the underframe of the bogies and linked with pins and bushes. This type of brake rigging requires careful installation and regular adjustment to ensure that

the forces are evenly distributed to all wheels. It can be seen from the rigging diagram (Fig.9.1) that any bad adjustment of the brake rigging could lead to uneven distribution of braking forces. Such a situation can occur when either the centre-pin on rod AB is slightly off-centred or if the fixed-end pin in the bolster is disorientated and also when the guiding slot is stuck due to some obstacles or dirt.

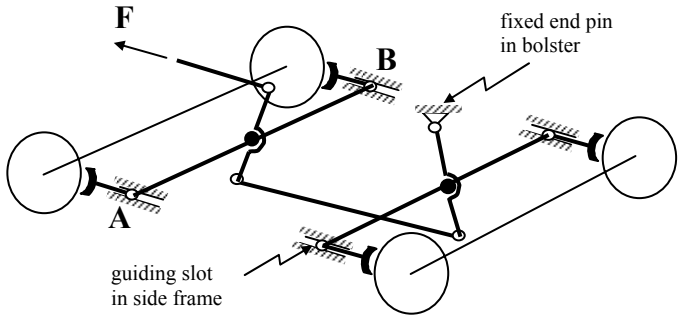

Figure 9.1. Typical Brake rigging arrangement

Fig. 9.2 shows the asymmetric brake shoe normal forces applied to a single wheelset. ΔF is defined as the error in the normal force distribution. It is clear that the asymmetric forces generate yaw torque to the wheelset that could adversely affect the running stability of the bogie. If the distance between the brake shoe is defined as $2b$, the generated yaw torque can be written as

$$T_{yaw} = 2b \cdot \Delta F \qquad (9.1)$$

For simplification, the reaction torque to the bogie frame was ignored (calculation the reaction torque to the bogie frame requires detail geometry data of the brake rigging, which was not available when this investigation was done).

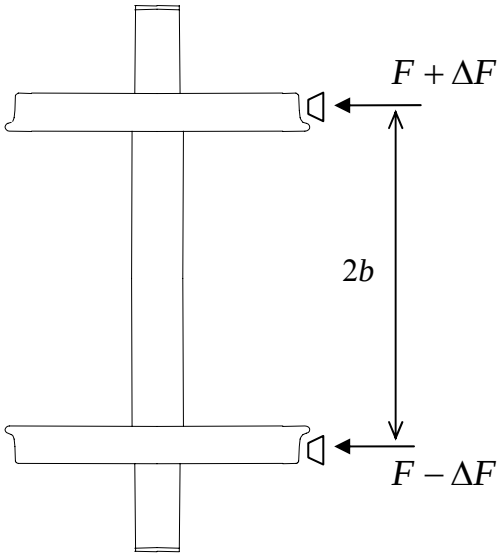

Figure 9.2. Asymmetric brake shoes normal forces

9.3. CASES STUDIED

Several cases of asymmetric brake force (the error ΔF) in the leading wheelset and trailing wheelsets were studied. Table 9.1 shows some selected important cases reported in this chapter. The bogie arrangement, including the mass and the spring constant, was assumed to be the same as that for the bogie model reported in Chapter 5 (see Section 5.2). The wheel-rail friction coefficient was assumed to be 0.3 for all cases. The brake torque applied was assumed to be 20 kNm that produced a constant 1.1 m/s^2 deceleration. These values are considered as common operational parameters in practice. All cases reported correspond to the initial speed of 25 m/s (90 km/h) although other initial speeds were examined. As the initial speed was found to have no significant effect, the cases corresponding to other initial speeds were disregarded in this chapter.

Table 9.1. Cases of Asymmetric Braking

Item	Error Magnitude	Application Time
#1. Asymmetric braking at leading wheelset only	25%	1s, 5s,10s
	50%	1s, 5s, 10s
	75%	1s, 5s,10s
#2. Asymmetric braking at trailing wheelset only	25%	1s, 5s,10s
	50%	1s, 5s, 10s
	75%	1s, 5s,10s

Three levels of error magnitude (25%, 50%, 75%) and application time (normal: 5s / fast: 1s / slow: 10s) were considered as the input control parameters (Table 9.1). Cases of asymmetric braking to the leading and trailing wheelset were also examined, thus a total of eighteen cases were studied. The resulting speed profile and lateral displacement of the wheelsets (leading and trailing) were examined to understand the response of bogies under severe dynamics.

9.4. RESULTS

For simplicity, only detailed results of two (out of the 18) cases for each major items (Items #1 and #2 in Table 9.1) are reported. Results of all cases are compiled in Tables 9.2 and 9.3. Detail plots are included in Appendix IV.

9.4.1. Asymmetric Braking of Leading Wheelset

Fig. 9.3 shows the result of the simulation of the case of 25% error on the leading wheelset at 10s of brake application time (the least severe case of Item #1). From Fig. 9.3 (a), it can be seen that the brake torque linearly increased from zero to 20 kNm within 10 seconds. The application of the brake caused the bogie to come to rest (from its initial speed of 25 m/s) within 22.9 seconds as shown in Fig. 9.3 (c).

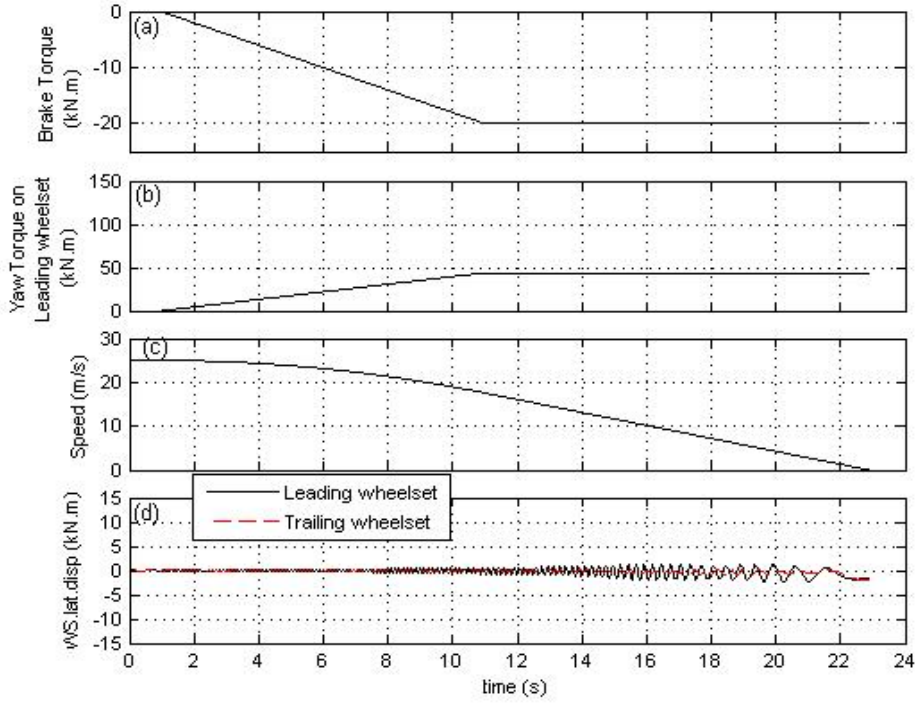

Figure 9.3. 25% error on leading wheelset, 10s brake application time (the least severe case)

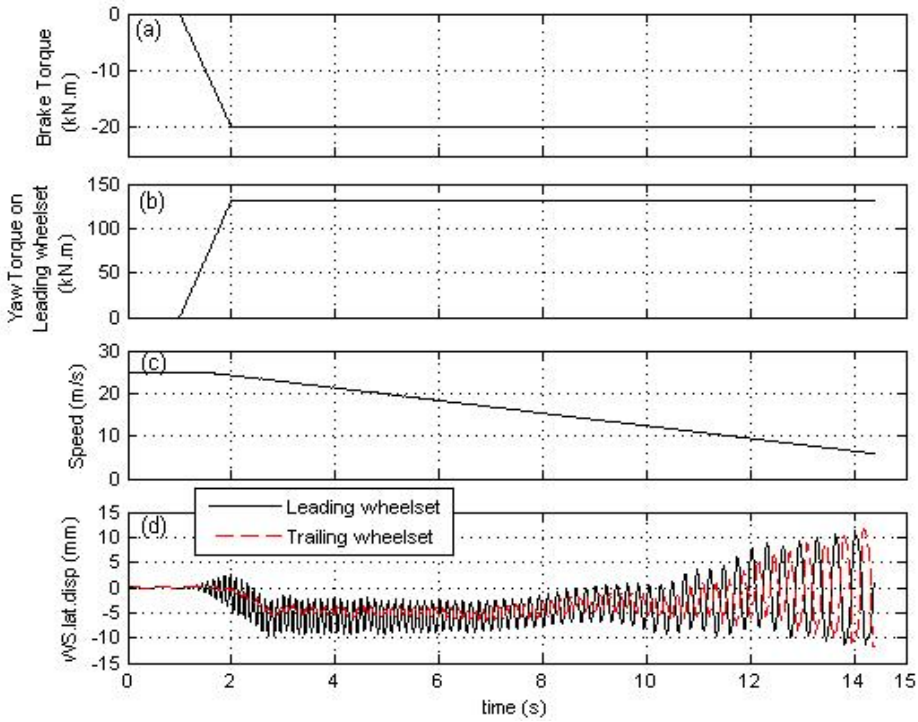

Figure 9.4. 75% error on leading wheelset, 1s brake application time (the most severe case)

Due to 25% error in the distribution of the brake shoe normal forces, yaw torque was generated on the leading wheelset as shown in Fig. 9.3 (b). The maximum yaw torque was 43.92 kNm which occurred when the brake torque attained its maximum value. As revealed in Fig. 9.3 (d), the yaw torque initiated unstable lateral oscillation of the leading wheelset followed by the lateral oscillation of the trailing wheelset. The magnitude of the lateral oscillation of the trailing wheelset remained smaller (maximum 1.5 mm) compared to the lateral oscillation of the leading wheelset (maximum 2.4 mm) throughout the time history.

Fig. 9.4 shows the result of the simulation of the case of 75% error on the leading wheelset at one second of brake application time (the most severe case of Item #1). From Fig. 9.4 (a), it can be seen that the brake torque linearly increased from zero to 20 kNm within one second. The 75% error in the distribution of the brake shoe normal forces generated yaw torque (maximum 131.8 kNm) on the leading wheelset as shown in Fig. 9.4 (b). The yaw torque initiated severe unstable lateral oscillation of the leading wheelset and the trailing wheelset. When the bogie attained the speed of 6.1 m/s, the lateral displacement of the wheelset attained a large enough value to cause abrupt termination of the RBD program. This was due to the diverging contact constraint equations that failed to determine the position and the orientation of the wheel-rail contact point. This condition is regarded as the onset of "*derailment*" in this thesis.

Fig. 9.5 presents several situations of wheel-rail contact predicted by the RBD program during lateral shift of the wheelset. Fig. 9.5 (a) shows the condition when the wheelset is in the centre position (equilibrium state). Fig. 9.5 (b) shows the condition when the wheelset is displaced 5 mm to the right. This figure shows that the clearance between

the flange of the right wheel and the right rail head is narrowing while the clearance between the flange of the left wheel and the left rail head is enlarging.

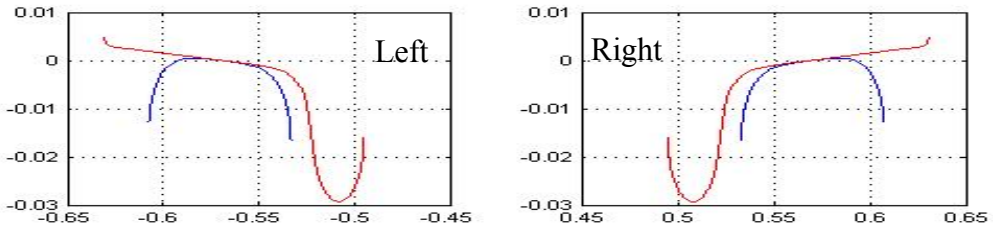

a. centre position

b. 5 mm lateral displacement (towards right rail)

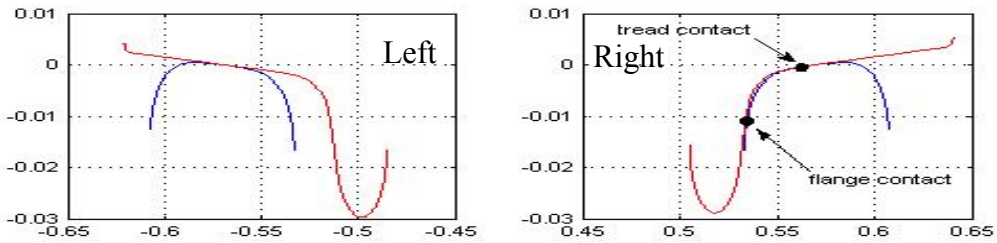

c. 9.5 mm lateral displacement (towards right rail)

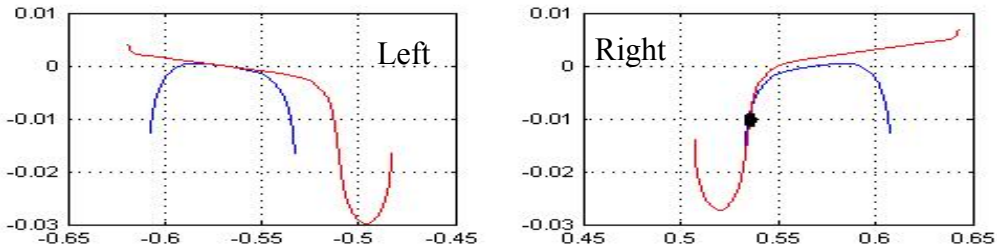

d. loss of right tread contact (on the right rail)

Figure 9.5. Wheelset lateral displacement and W/R contact point

When the lateral displacement attains 9.5 mm, the flange contact between the right wheel and the right rail is encountered while the tread contact is still maintained (Fig. 9.5 (c)). This situation leads to lateral impact. When the wheelset continues moving to the right, the flange of the right wheel starts to climb up the right railhead. As the right wheel continuously climbs up the right railhead, at certain lateral displacement, the tread contact between the right wheel and the right railhead is lost (Fig. 9.5 (d)). It is the point where the contact constraint equation in the RBD program failed to converge. With the profiles used in this thesis, the wheel-climb mechanism of derailment occurred at the lateral displacement of around 11.5 mm.

The results of all cases of the simulation of the asymmetric braking on the leading wheelset are compiled in Table 9.2.

Table 9.2. Results of asymmetric braking on leading wheelset at initial speed 25 m/s

	Input		Output		
Error (%)	Maximum Yaw Torque in Leading Wheelset (kNm)	Application Time (s)	Time to Stop (s)	Maximum Lateral Displacement (mm)	
				Leading Wheelset	Trailing Wheelset
25%	43.92	10s	22.9s	2.4 mm	1.5 mm
		5s	20.4s	2.5 mm	1.7 mm
		1s	18.3s	2.5 mm	1.9 mm
50%	87.84	10s	22.9s	8.3 mm	6.1 mm
		5s	20.4s	9.2 mm	6.5 mm
		1s	18.3s	9.3 mm	7.3 mm
75%	131.76	10s	derailment at v=5.9m/s and t=19.1s	-	-
		5s	derailment at v=6.1m/s and t=16.3s	-	-
		1s	derailment at v=6.1m/s and t=14.4s	-	-

The input (maximum yaw torque and its time of attainment) and output (time to stop and maximum lateral displacement of both the leading and trailing wheelsets) are presented. At 25% error, the lateral oscillation attained only a small value irrespective

of the brake application time. The lateral displacement progressively increased with the increase in yaw torque. At 75% error the program failed to converge at the speed of around 6 m/s, indicating onset of derailment, for all cases of application time.

9.4.2. Asymmetric Brake on the Trailing Wheelset

Fig. 9.6 shows the result of the simulation of the case of 25% error on the trailing wheelset at 10s of brake application time (the least severe case of Item #2). From Fig. 9.6 (a), it can be seen that the brake torque linearly increased from zero to 20 kNm within 10 seconds. The application of the brake caused the bogie to come to rest from 25 m/s within 22.9 seconds as shown in Fig. 9.6 (c). Due to 25% error in the distribution of the brake shoe normal forces, yaw torque was generated on the trailing wheelset as shown in Fig. 9.6 (b). The maximum yaw torque generated was 43.92 kNm which occurred when the brake torque attained its maximum value. As revealed in Fig. 9.6. (d), the yaw torque on the trailing wheelset caused unstable lateral oscillation of the wheelset followed by the lateral oscillation of the leading wheelset. The magnitude of the lateral oscillation of the trailing wheelset was larger (maximum 2.2 mm) compared to the lateral oscillation of the leading wheelset (maximum 1.7 mm).

Fig. 9.7 exhibits the result of the simulation of the case of 75% error on the trailing wheelset at 1s of brake application time (the most severe case of Item #2). Fig. 9.7 (a) shows that the brake torque linearly increased from zero to 20 kNm within 1 second. The 75% error in the distribution of the brake shoe normal forces generated yaw torque (maximum 131.8 kNm) on the trailing wheelset as shown in Fig. 9.7 (b). The yaw torque initiated severely unstable lateral oscillation of the trailing wheelset followed by the leading wheelset.

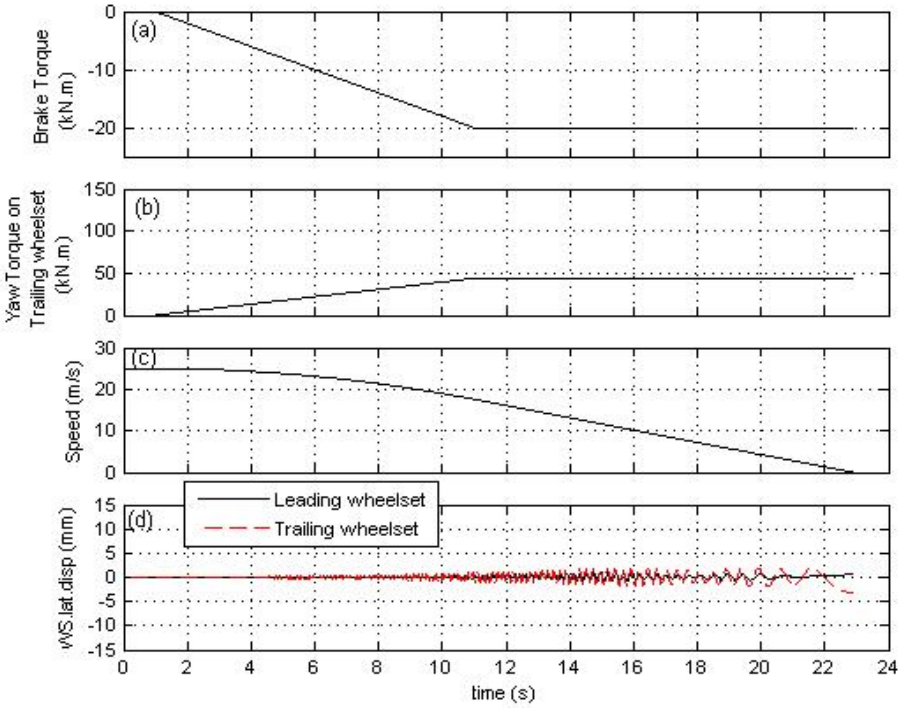

Figure 9.6. 25% error on trailing wheelset, 10s brake application time (the least severe case)

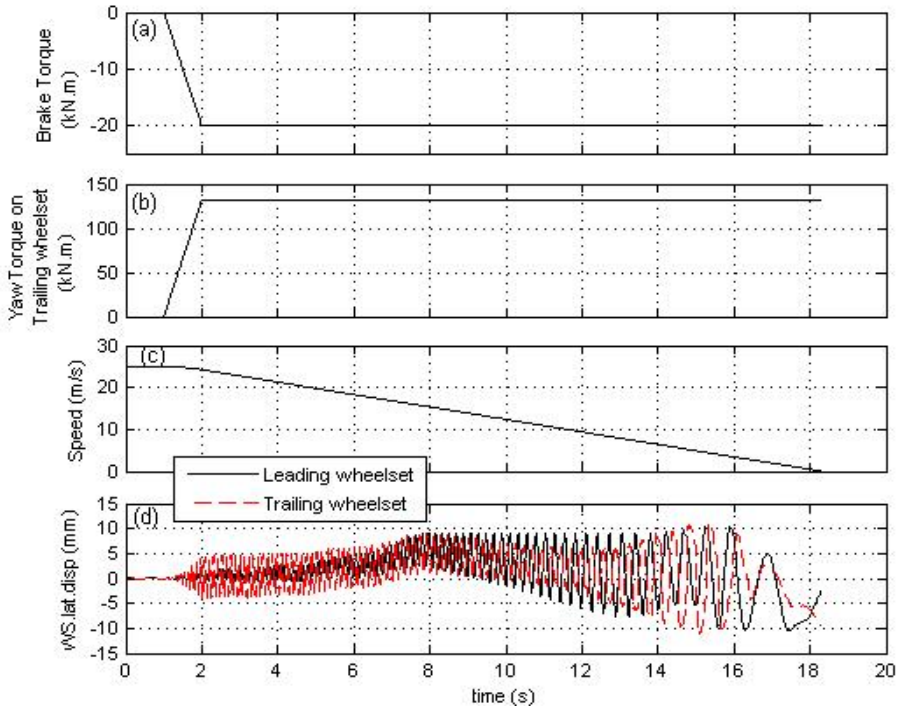

Figure 9.7. 75% error on trailing wheelset, 1s brake application time (the most severe case)

However, as seen in Fig. 9.7, unlike the severe case Item #1, the contact constraint equations in the RBD program during the severe case of Item #2 always converged as illustrated by the stoppage of the bogie (the bogie stopped from 25 m/s within 18.3 seconds as shown in Fig. 9.7 (c)). The magnitude of the lateral oscillation of the trailing wheelset was initially larger compared to the lateral oscillation of the leading wheelset. After 8s, the magnitude of the lateral oscillation of the leading wheelset became larger than that of the trailing wheelset. At the end of the simulation the lateral oscillation of both wheelsets had more or less the same magnitudes (approximately 11 mm), but they never reached the point where the tread contact was lost (11.5 mm).

The results of all cases of the simulation of the asymmetric braking applied to the trailing wheelset are compiled in Table 9.3.

Table 9.3. Results of asymmetric braking on trailing wheelset at initial speed 15 m/s

	Input		Output		
Error (%)	Maximum Yaw Torque on Trailing Wheelset (kN.m)	Application Time (s)	Time to Stop (s)	Maximum Lateral Displacement (mm)	
				Leading Wheelset	Trailing Wheelset
25%	43.92	10s	22.9s	1.6 mm	2.2 mm
		5s	20.4s	1.7 mm	2.4 mm
		1s	18.3s	1.7 mm	2.7 mm
50%	87.84	10s	22.9s	7.4 mm	5.6 mm
		5s	20.4s	7.5 mm	5.9 mm
		1s	18.3s	7.8 mm	6.2 mm
75%	131.8	10s	22.9s	10.9 mm	10.8 mm
		5s	20.4s	11.1 mm	11.2 mm
		1s	18.3s	11.2 mm	11.1 mm

Similar to the asymmetric braking on the leading wheelset, the 25% error caused only small lateral oscillation and the brake application time was revealed not to have much effect to the magnitude of the lateral oscillation of the wheelset. The magnitude of the

lateral displacement of the wheelset was mainly affected by the error that generated yaw torque of the wheelset. Unlike the asymmetric braking on the leading wheelset, the program was found to converge for all cases of asymmetric brake application on the trailing wheelset. Thus, it can be considered that no "*derailment*" occurred for all cases of asymmetric braking on the trailing wheelset considered in this investigation. However, at the error of 75% the lateral displacement was around 11 mm, resulting in flange contact. Any further increase in yaw torque (or more than 75% error) could potentially lead to derailment.

At 25% error, the magnitude of the lateral oscillation of the trailing wheelset where the asymmetric braking was applied remained consistently larger than the magnitude of lateral oscillation of the leading wheelset. However, at larger errors (50% and 75 %), the lateral oscillation of the leading wheelset, at certain periods of the simulation, became larger than the lateral oscillation of the braked trailing wheelset.

9.5. SUMMARY AND CONCLUSION

The effect of asymmetric braking to the dynamics of bogies has been examined using the validated RBD program. The results can be summarised as follows:

- In general, the asymmetric braking due to error in the distribution of brake shoe normal forces adversely affects the lateral dynamics of the wheelset as evidenced by unstable lateral oscillations.

- The case corresponding to 25% error in the distribution of brake shoe normal force on the leading wheelset and/ or trailing wheelset caused only small lateral oscillation of the wheelsets.

- For the cases of asymmetric braking applied to the leading wheelset, the magnitude of lateral oscillation of the leading wheelset remained always larger than the trailing wheelset.

- For the cases of asymmetric braking applied to the trailing wheelset, at small level of error the lateral oscillation of the trailing wheelset was larger than the lateral oscillation of the leading wheelset. However at larger errors (50% and 75 %), the magnitude of lateral oscillation of the leading wheelset, at certain simulation times, could became larger than the magnitude of lateral oscillation of the trailing wheelset.

- The 75% error applied to the leading wheelset has caused the contact constraint equation in the RBD program to fail to converge, a situation that is described as "*derailment*". However derailment did not happen for a similar case of brake shoe forces applied to the trailing wheelset. It is concluded that the error in the brake shoe forces on the leading wheelset is more dangerous than a similar error in the trailing wheelset.

10. SUMMARY AND CONCLUSIONS

Suburban passenger trains are regularly subjected to braking / traction for most of their travel. Similar situations also exist in heavy haul and long haul train operations during their entry and exit of speed restriction zones and/or tight curves. Application of braking/traction torque modifies the speed of travel of trains nonlinearly due to the complex wheel-rail interface characteristics, track geometry and bogie design parameters. In spite of these situations, the current simulation practices largely deal with constant speed conditions with the speed profile input as a priori.

With a view to providing a simulation platform that truly accounts for the traction/braking torque induced dynamics of wagons, this thesis has formulated a model that explicitly accounts for the wheelset pitch degree of freedom. The formulation has been provided with reference to a coordinate system that is fixed in space and time. The formulation has enabled the simulation to be performed in a natural way using the brake/traction torque as the input and the resulting speed profile as the output thus avoiding approximate calculation of the speed profile as a priori.

Using the formulation, a MATLAB computer program titled Rail Bogie Dynamics (RBD) program has been developed and applied to a series of simulations of the dynamics of bogies subjected to the following conditions:

- Without braking / traction torque but including various types of track irregularities:
    - vertical irregularity
    - lateral irregularity

- cross level irregularity

- With braking /traction torque
  - gentle application
  - rapid application
  - very heavy braking torque sufficient to cause skid and derailment potential

The results of the simulations have been verified using a commercial software package VAMPIRE where possible. The cases that could not be simulated in VAMPIRE, for example wheelset skid, have been validated using a full scale laboratory test.

From the research carried out as stated above, the following conclusions are made:

1. General Conclusions

1.1. The formulation developed with reference to a coordinate system that is fixed in space and time appropriately predicts the dynamics of rail bogies.

1.2. The idea of representing the total system differential equations of motion with a set of algebraic constraint equations in an augmented form and solving them using the generalised coordinate partitioning method is proved to be acceptable.

1.3. Rigid body contact represented by surface parameters is sufficiently accurate for the determination of the wheel-rail contact position and orientation.

1.4. Polach method of calculating the creep forces works well in areas of high creepage characterised by wheelset skid.

1.5. The RBD program developed in this thesis could provide reliable prediction of the dynamics of bogies with or without the application of braking/traction torques to an adequate level of accuracy. The RBD program could also handle various track irregularities appropriately.

1.6. The RBD program has the potential to simulate dangerous situations such as the wheelset skid and the onset of wheel climb derailment.

1.7. The RBD program is capable of dealing with bogie dynamics induced by asymmetric brake shoe forces.

1.8. It is possible to design a full-scale laboratory test capable of determining the speed profile as a function of applied brake torque with instrumented bogie and wayside measurement. The experiment could also deal with severe bogie dynamics including wheelset skid.

1.9. Experimental measurement of the normal and the tangential brake shoe forces eliminates the need for assuming the friction coefficient between the brake shoe surface and the wheel tread.

1.10. From the wheelset skid test, it is possible to determine the friction coefficient between the wheel and the railhead.

1.11. The lateral dynamics of the bogie subjected to braking/traction torque is not affected by the time of application of the torque.

1.12. Asymmetric brake shoe forces in general should be avoided. Where such cases cannot be avoided, it should be remembered that the application of

asymmetric brake shoe forces on the leading wheelset is more dangerous (higher derailment potential) than if applied on the trailing wheelset.

1.13. The application of very large braking torque leads to wheelset skid and tends to destabilise the wheelset lateral oscillation.

2. Specific Conclusions

2.1. Runge-Kutta method is good for the numerical integration of the differential equations contained in the augmented system matrix.

2.2. The Newton-Raphson method provides reliable solution to the nonlinear algebraic constraint equations.

2.3. The wheel and the railhead could be represented by two surface parameters each.

2.4. For the wheel and the railhead profile adopted in the simulation, the mean lateral creep force has been found to be independent of the operating speed.

2.5. Serious wheelset skid occurs as the coefficient of friction between the wheel and the rail reduces.

2.6. From the full-scale tests carried out, the following conclusions are obtained:

2.6.1. The QR30 bogie brake beam slider can be modified to facilitate the measurement of the tangential brake shoe forces.

2.6.2. LIMES wayside measurement system provides very accurate measurement of the longitudinal position of the bogie.

2.6.3. The accelerometers developed at CQU are economical and accurate in predicting even low frequency and very small levels of acceleration.

2.6.4. The experiments have proved that the shaft encoders on both wheelsets could provide sufficient information for the calculation of all related dynamics events, thus making the LIMES system redundant.

2.6.5. From the measurement of the normal and tangential brake shoe forces, friction coefficients between the brake shoe and the wheel tread were calculated for all cases. It appeared that, with the increase in brake shoe forces (or brake cylinder pressure), the coefficient of friction between the brake shoe and the wheel tread reduces. For the 130kPa, 150kPa and 180kPa cylinder pressure, the average friction coefficients determined were 0.30, 0.27 and 0.25 respectively.

2.6.6. From the six skid trials reported in this chapter, friction coefficient between the wheel tread and railhead was determined and was found to vary between 0.15 – 0.20. This range is much smaller than the coefficients determined from the tribometer readings (0.50 – 0.55). As the tribometer is considered more relevant for understanding relative changes in friction coefficient, the absolute values of friction coefficient obtained from the tribometer measurement were disregarded. More reliable determination of friction coefficient between the wheel tread and railhead is therefore considered to be the one obtained through the skid trials (0.15 – 0.20).

2.7. The 75% error in the distribution of brake shoe forces applied to the leading wheelset has caused the contact constraint equation in the RBD program to fail to converge, a situation that is described as "*derailment*". However derailment did not happen for a similar case of brake shoe forces applied to the trailing wheelset. It is concluded that the error in the brake shoe forces on the leading wheelset is more dangerous than the same error on the trailing wheelset.

3. Recommendations

Some potential improvements that could be made in future work include but are not limited to:

1. Extending the model for the simulation of the complete wagon.
2. Extending the model to account for curving simulation.
3. Improving the model to allow for inclusion of other suitable methods of creep forces calculation.
4. Writing the RBD program in an efficient programming language to improve the computational time and design it such a way that the program becomes more user friendly.
5. Performing the field test by improving the design of the instrumented bogie to examine the effect of application of braking torque at higher speeds.

REFERENCES

Ahmadian, M. (1998). *Hopf Bifurcation and Hunting Behaviour in A Rail Wheelset with Flange Contact*. Nonlinear Dynamics **15**: 15-30.

Anderson, C. and Abrahamsson, T. (2002). *Simulation of Interaction Between a Train in General Motion and a Track*. Vehicle System Dynamics **38**: 433-455.

Andrews, H. I. (1986). *Railway Traction; The Principles of Mechanical and Electrical Railway Traction*, Elsevier Science Publisher.

Balas, M. Balas, V. Foulloy, L. Galichet, S. (2001). *A Model of The Sliding Wheel During Braking*. 5th International Conference on Railway Bogies and Running Gear, Budapest.

Berghuvud, A. (2002). *Freight Car Curving Performance in Braked Condition*. Journal of Rail and Rapid Transit **216**: 23-29.

Berzeri, M. (2000). *Absolute Nodal Coordinate Formulation: Elastic Forces and Application to Wheel/Rail Interaction*. *PhD Thesis. Department of Mechanical Engineering*. Chicago, University of Illinois.

Boor, C. de. (1978). *A Practical Guide to Spline*, Springer-Verlag.

Bosso, N., Gugliota, A. and Soma, A. (2000). *Simulation of a Freight Bogie with Friction Dampers*. 5th ADAMS/Rail User's Conference, Haarlem, Netherland.

Bureau, Railway Educational. (2002). *Guide to freight car air brakes*, Simmons-Boardman Book, Inc.

Carter, F. W. (1926). *On the action of a locomotive driving wheel*. Proc. Royal Soc. Ser. **A112**: 151-157.

Cocci, G., Presciani, P., Rindi, A. and Volterrani, G. P. J. (2001). *Railway wagon model with anti slip braking system*. 16th European MDI user conference, Berchtesgaden, Germany.

Company, Standard Car Truck. (2000). *Maintenance Manual of Barber 3-piece Bogie*.

de Pater, A. D. (1961). *The Approximate Determination of the Hunting Movement of Railway Vehicles by Aid of the Method of Krylov and Bogoliubov*. Applied Science Res **10**(A): 205-228.

de Pater, A. D. (1987). *The Equations of Motion of A Single Wheelset Moving Along A Perfect Track*. 10th IAVSD Symposium, Prague, CSSR.

de Pater, A. D. (1989). *The lateral stability of railway vehicle with two axle bogies*. 11th IAVSD Symposium,.

de Pater, A. D. Meijers, P. and Shevtsof, I. Y. (1999). *Technical Report no. LTM1196 - Simulation of The Motion of Railway Vehicle Along Curved Tracks*, Laboratory for Engineering Mechanics, Delft University of Technology.

Dukkipati, R. V. (2000). *Vehicle dynamics*, CRC Press, Boca Raton, Fla.

Dukkipati, R. V. and Narayanaswamy, S. (2004). *Improved compatibility between the lateral stability and curving behaviour of modified truck designs*. Heavy Vehicle Systems, Int. J. of Vehicle Design, **11**: 1-25.

Durali, M. and Shadmehri, B. (2003). *Nonlinear Analysis of Train Derailment in Severe Braking*. Journal of Dynamic Systems, Measurement, and Control **125**: 48-53.

Eich-Sollner, E. and Fuhrer, C. (1998). *Numerical Method in Multibody Dynamics*. Stuttgart, B. G. Teubner.

Esveld, C. (2001). *Modern Railway Track*, MRT Production, Netherland.

Evans, J. R. (1999). *Rail Vehicle Dynamics Simulation using VAMPIRE*. Vehicle System Dynamic Supplement **31**: 119-140.

Frylmark, D. and Johnsson, S. (2003). *Automatic Slip Control for Railway Vehicles. Master Thesis. Dept. of Electrical Engineering*. Link¨oping, Swedia, Link¨opings university.

Garg, V. K. and Dukkipati, R. V. (1984). *Dynamic of Railway Vehicle System*, Academic Press.

Gilchrist, A. O. (1998). *The Long Road to Solution of The Railway Hunting and Curving Problems*. Proc. Institution Mechanical Engineering Part F: Journal of Rail and Rapid Transit **212**: 219 - 226.

Grassie, S. L. (1992). *Dynamics models of the track and their uses*. Proceeding of International Conference on Rail Quality and Maintenance for Modern Railway Operation, Delft.

Greenberg, M. D. (1978). *Foundation of Applied Mathematics*. New Jersey, Prentice-Hall, Inc.,.

Handoko, Y., Xia, F. and Dhanasekar, M. (2004). *Effect of Asymmetric Brake Shoe Force Application on Wagon Curving Performance*. Vehicle System Dynamic Supplement **41**: 113-122.

Haque, I., McGirt, P. and Nagurka, M. L. (1996). *A non-linear wheelset model to predict derailment*. Proceeding of the ASME Dynamics System **Vol. 58**: pp. 141-148.

Harder, R. F. (2000). *Dynamic Modelling and Simulation of Three-Piece North American Freight Vehicle suspension with Non-linear Frictional Behaviour Using ADAMS/Rail*. 5th ADAMS/Rail User's Conference, Haarlem, Netherland.

Ikamoto, I. (1998). *How Bogies Work*. *Japan Railway and Transport Review*. **18**.

Iwnicky, S., Ed. (1999). *The Manchester Benchmarks for Rail Vehicle Simulation, Supplement to Vehicle Dynamics Volume 31*, Swetz & Zeitlinger, Netherland.

Jacobson, B. and Kalker, J. J., Eds. (2000). *Rolling contact phenomena*. CSIM Courses and Lectures, Springer-Verlag Wien New York.

Johnson, K. L. (1985). *Contact Mechanics*, Cambridge University Press.

Kalker, J. J. (1967). *On the rolling contact of two elastic bodies in the presence of dry friction*, Delft University.

Kalker, J. J. (1982). *A fast Algorithm for the simplified theory of rolling contact*. Vehicle System Dynamic **2**: 1-13.

Kalker, J. J. (1990). *Three Dimensional Elastic Bodies in Rolling Contact*, Kluwer Academic Publisher.

Kalker, J. J. (1991). *Wheel-Rail Rolling Contact Theory*. Wear **144**: 243-261.

Kerr, A. D. (2000). *On the determination of the rail support modulus k*. International Journal of Solid and Structures **37**: 4335-4351.

Klingel (1883). *Uber den Lauf der Eisenbahnwagen auf Gerarder Bahn*. Organ Fortsch, Eisenb-wes **38**: 113-123. (original not seen, cited from Wickens (2003)).

Kreyszig, E. (1999). *Advanced Engineering Mathematics*, John Willey & Son.

Litvin, F. L. (1994). *Gear Geometry and Applied Theory*. Englewood Cliffs, NJ, Prentice Hall.

Lixin, Q. and Haitao, C. (2001). *Three Dimension Dynamics Response of Car in Heavy Haul Train during Braking Mode*. 7th International Heavy Haul Conference, Brisbane, Australia.

Luo, Y., Yin, H. and Hua, C. (1996). *The Dynamic Response of Railway Ballast to the Action of Trains Moving at Different Speed*. Proc. Inst. Mech. Engrs Part F: Journal Rail and Rapid Transit. **210**: 95-101.

Mace, S., Pena, R., Wilson, N. and DiBrito, D. (1996). *Effects of Wheel-Rail Contact Geometry on Wheelset Steering Forces*. Wear **191**: 204-209.

Macfarlane, I., Ed. (2000). *Brakes*. Railway Safety, Engineers Australia Pty Limited.

Malvezzi, M., Presciani, P., Allotta, B. and Toni, P. (2003). *Probabilistic Analysis of Braking Performance in Railways*. Proc. Institution Mechanical Engineering Part F: Journal of Rail and Rapid Transit **Vol. 217**: 149 - 165.

Marshal, C. F. D. (1938). *History of British Railway Down to the Year 1830*, Oxford University Press. (original not seen, cited from Wickens (1998)).

Matsudaira, T. (1952). *Shimmy of Axle with Pair of Wheelset*. Railway Engineering Res, Japan.

Matsumoto, A., Sato, A., Ohno, Y., Suda, H., Nishimura, Y., Tanimoto, R. and Oka, M. (1999). *Compatibility of Curving Performance and Hunting Stability of Railway Bogie*. Vehicle System Dynamic Supplement **33**: 740-748.

McClanachan, M., Handoko, Y., Dhanasekar, M., Skerman, D. and Davey, J. (2004). *Modelling Freight Wagon Dynamics*. Vehicle System Dynamic Supplement **41**: 438-447.

Mohan, A. (2003). *Nonlinear Investigation of the Use of Controllable Primary Suspensions to Improve Hunting in Railway Vehicles*. Virginia, USA, Virginia Polytechnic Institute and State University.

Muller, S. and Kogel, R. (2000). *The Influence of Mechanical Design Parameters on Roll-Slip Oscillations in Locomotive Drives*. International ADAMS User Conference, Orlando, Florida, USA.

Nagase, K., Wakabayashi, Y. and Sakahara, H. (2002). *A study of the phenomenon of wheel climb derailment: results of basic experiment using model bogies*. Proc. Inst. Mech. Engrs Part F: Journal Rail and Rapid Transit. **216**: 237-247.

Nielsen, J. B. and Theiler, A. (1996). *Tangential Contact Problem With Friction Coefficients Depending on Sliding Velocity*. 2nd Mini Conference on Contact Mechanics and Wear of Rail/Wheel Systems, Budapest.

Ohishi, K., Ogawa, Y., Miyashita, I. and Yasukawa, S. (2000). *Anti-slip Re-adhesion control of electric motor coach based on force control using disturbance observer*. Proceeding of IAS annual meeting (IEEE Industry Application Society), Rome, Italy.

Olson, B. J. (2001). *Nonlinear Dynamics of Longitudinal Ground Vehicle Traction. Mechanical Engineering*. Michigan, USA, Michigan State University.

de Pater, A. D. (1956). *Etude de Mouvement de Lacet d'un Vehicle de Chemin de Fer*. Applied Science Res **6**(A): 263. (original not seen, cited from Gilchrist (1998)).

Polach, O. (1999). *A Fast Wheel-Rail Forces Calculation Computer Code*. Vehicle System Dynamic Supplement **33**: 728-739.

Polach, O. (2001). *Influence of Locomotive Tractive Effort on the Forces Between Wheel and Rail*. Vehicle System Dynamic Supplement **35**: 7-22.

Polach, O. (2005). *Creep Forces in Simulation of Traction Vehicles Running on Adhesion Limit*. Wear **258**: 992-1000.

Profilidis, V. A. (2000). *Railway Engineering*, University Press, Cambridge.

Rabinowicz, E. (1995). *Friction and Wear of Material*, John Willey & Son.

Rail, A. T. (2003). *VAMPIRE version 4.31 User Manual*.

Rail, A. T. (2004). *Vampire, Rail Vehicle Dynamics Software*, http://www.vampire-dynamics.com.

Redtenbacher, F. J. (1885). *Die Gesetze des Locomotived-Baues*. Verlag von Friderich, Mannheim: 22. (original not seen, cited from Wickens (2003)).

Renger, A. (1984). *Lateral Dynamics of complete four-axled vehicles with powered two-axled bogies*. Proc. of 8th IAVSD Symposium.

Riley, K. F., Hobson, M. P. and Bence, S. J. (2002). *Mathematical Methods for Physics and Engineering*, Cambridge University Press.

Rinehart, R. E. (1978). *Hunting Stability of Three Axle Locomotive Truck*. Journal of Engineering for Industry, Transaction of ASME **100**: 483-491.

Ripke, B. and Knothe, K. (1995). *Simulation of High Frequency Wagon-Track Interaction*. Vehicle System Dynamic Supplement **24**: 72-85.

Roberson, R. E. and Schwertassek, R. (1998). *Dynamics of Multibody Systems*. New York, Springer-Verlag.

Schiehlen, W. (1997). *Multibody System Dynamics: Root and Perspectives*. Multibody System Dynamics **1**: 149-188.

Schiehlen, W. O. (1984). *Modelling of Complex Vehicle Systems*. 8th IAVSD Symposium: 548 - 563.

Schupp, G. (2003). *Simulation of Railway Vehicles: Necessities and Application*. Mechanics Based Design of Structures and Machines **31**(3): 297-314.

Shabana, A. A. (1989). *Dynamics of Multibody Systems*, John Willey & Son.

Shabana, A. A. (2001). *Computational Dynamics*, John Willey & Son.

Shabana, A. A., Berzerri, M. and Sany, J. R. (2001). *Numerical Procedure for the Simulation of Wheel/Rail Contact Dynamics*. Journal of Dynamic System, Measurement, and Control **123**: 168-178.

Shabana, A. A. and Sany, J. R. (2001). *An Augmented Formulation for Mechanical Systems with Non-Generalized Coordinates: Application to Rigid Body Contact Problems*. Nonlinear Dynamics **24**: 183 - 204.

Shabana, A. A. and Sany, J. R. (2001). *A Survey of Rail Vehicle Track Simulation and Flexible Multibody Dynamics*. Nonlinear Dynamics **26**: 179-210.

Shen, G. and Pratt, I. (2001). *The Development of A Railway Dynamics Modelling and Simulation Package to Cater for Current Industrial Trends*. Proc. Institution Mechanical Engineering Part F: Journal of Rail and Rapid Transit **215**: 167 - 178.

Shen, Z. Y., Hendrick, J. K. and Elkins, J. K. (1983). *A Comparison of Alternative Creep Force Models for Rail Vehicle Dynamic Analysis*. 8th IAVSD Symposium, Cambridge.

Stichel, S. (1999). *On Freight Wagon Dynamics and Track Deterioration*. Proc. Inst. Mech. Engrs Part F: Journal of Rail and Rapid Transit. **213**: 243-254.

Strang, G. (1980). *Linear Algebra and Its Application*. New York, Academic Press.

Suda, Y. and Anderson, R. J. (1994). *High Speed Stability and Curving Performance of Longitudinal Unsymmetric Trucks with Semi-active Control*. Vehicle System Dynamic **23**: 29-52.

Suda, Y. and Grencik, J. (1996). *The Mechanism of Enhanced Curving Performance of Unsymmetric Suspension Trucks under Acting Traction/Brake Torque*. 14th IAVSD Symposium, University of Michigan, Swets & Zeitlinger.

Sun, Y. Q. (2002). *A Wagon Track System Dynamics Model for The Simulation of Heavy Haul Railway Transportation*. *PhD thesis. Centre for Railway Engineering*, Central Queensland University.

Sun, Y. Q. and Dhanasekar, M. (2001). *A Dynamic Model for the Vertical Interaction of The Rail Track and Wagon System*. International Journal of Solids and Structures **39**: 1337-1359.

Sun, Y. Q. and Dhanasekar, M. (2004). *Importance of Track Modeling to the Determination of the Critical Speed of Wagons*. 18th IAVSD Symposium, Kanagawa, Japan.

Sweet, L. M., Budell, R. A., Karmel, A., Lassman, D. and D.Schulte (1984). *Theory and measurement of derailment quotients*. 8th IAVSD Symposium, Cambridge.

Thijse, B. J. (2002). *Spline2 V6.0 Software*, Delft University of Technology, Laboratory of Material Science, http://www.tm.tudelft.nl/secties/fcm/matphy/software/software.htm.

Tuten, J. M., Law, E. H. and Cooperrider, N. K. (1979). *Lateral Stability of Freight Cars With Axles Having Different Wheel Profiles and Asymmetric Loading*. Journal of Engineering for Industry **101**: 1 - 16.

Vermeulen, P. J. and Johnson, K. L. (1964). *Contact of non-spherical bodies transmitting tangential forces*. Applied Mechanics **31**: 338-340.

Website, K. Industrier. AB. *http://www.kindustrier.se/Products/Boggi/*.

Wehage, R. A. (1980). *Generalized Coordinate Partitioning in Dynamic Analysis of Mechanical System*, University of Iowa.

Wickens, A. H. (1965-6). *The dynamics of railway vehicles on straight track: fundamental consideration on lateral stability*. Proc. Inst. Mech. Eng **180**(3F): 1-16.

Wickens, A. H. (1991). *Steering and Stability of Bogie: Vehicle Dynamics and Suspension Design*. Proc. Inst. Mech. Engrs Part F: Journal of Rail and Rapid Transit. **205**: 109-122.

Wickens, A. H. (1998). *The dynamics of railway vehicles - from Stephenson to Carter*. Proc. Inst. Mech. Eng **212**(Part F): 209-217.

Wickens, A. H. (2003). *Fundamental of Rail Vehicle Dynamics*, Swets & Zetlinger.

Xia, F. (2002). *The Dynamics of The Three-Piece Freight Truck. Department of Informatics and Mathematical Modelling*. Kgs. Lyngby, Technical University of Denmark.

Yabuno, H., Okamoto, T. and Aoshima, N. (2001). *Stabilization Control for The Hunting Motion*. Vehicle System Dynamic Supplement **35**: 41 - 55.

Zboinski, K. (1999). *The Importance of Imaginary Forces and Kinematic-type Non-Linearities for The Description of Railway Vehicle Dynamics*. Proc. Institution Mechanical Engineering Part F: Journal of Rail and Rapid Transit **213**: 199 - 210.

Zhai, W. and Sun, X. (1993). *A detailed Model for Investigating Vertical Interaction between Railway Vehicle and Truck*. 13th IAVSD Symposium.

APPENDIX I

DETERMINATION OF CONSTRAINT JACOBIAN MATRICES OF CONTACT BETWEEN TWO RIGID BODIES

I.1. Contact Constraint Jacobian Matrices

From Eq.(3.56): $\mathbf{C} = \mathbf{R}^i + \mathbf{A}^i\overline{\mathbf{u}}^{ik} - \mathbf{R}^j - \mathbf{A}^j\overline{\mathbf{u}}^{jk}$

$$\begin{aligned}\mathbf{C}_\mathbf{q} &= \left[\frac{\partial \mathbf{C}}{\partial \mathbf{q}}\right] \\ &= \left[\begin{array}{cccc}\mathbf{I} & \dfrac{\partial \mathbf{A}^i}{\partial \boldsymbol{\theta}^i}\overline{\mathbf{u}}^{ik} & -\mathbf{I} & \dfrac{\partial \mathbf{A}}{\partial \boldsymbol{\theta}}\overline{\mathbf{u}}^{ik}\end{array}\right] \\ &= \left[\begin{array}{cccc}\mathbf{I} & -\mathbf{A}^i\tilde{\overline{\mathbf{u}}}^{ik}\overline{\mathbf{G}}^i & -\mathbf{I} & \mathbf{A}^j\tilde{\overline{\mathbf{u}}}^{jk}\overline{\mathbf{G}}^j\end{array}\right]\end{aligned}$$

$$\begin{aligned}\mathbf{C}_\mathbf{s} &= \left[\frac{\partial \mathbf{C}}{\partial \mathbf{s}}\right] \\ &= \left[\begin{array}{cc}\mathbf{A}^i\dfrac{\partial \overline{\mathbf{u}}^{ik}}{\partial \mathbf{s}_l^i} & \mathbf{A}^j\dfrac{\partial \overline{\mathbf{u}}^{jk}}{\partial \mathbf{s}_l^k}\end{array}\right], \quad l = 1,2 \\ &= \left[\begin{array}{cc}\mathbf{A}^i\mathbf{T}^{ik} & \mathbf{A}^j\mathbf{T}^{jk}\end{array}\right], \quad \mathbf{T}^{ik} = \left[\begin{array}{cc}\overline{\mathbf{t}}_1^{ik} & \overline{\mathbf{t}}_1^{ik}\end{array}\right] \quad \textit{and} \quad \mathbf{T}^{jk} = \left[\begin{array}{cc}\overline{\mathbf{t}}_1^{jk} & \overline{\mathbf{t}}_1^{jk}\end{array}\right]\end{aligned}$$

I.2. Orientation Constraint Jacobian Matrices

From Eq.(3.58): $\mathbf{C}_l = \overline{\mathbf{n}}^{jkT}\mathbf{A}^{j\mathrm{T}}\mathbf{A}^i\overline{\mathbf{t}}_l^{ikT}, \quad l = 1,2$

The orientation constraint in respect to the generalised coordinates $\mathbf{q}$ is:

$$\begin{aligned}\mathbf{C}_{l,\mathbf{q}} &= \left[\frac{\partial \mathbf{C}_l}{\partial \mathbf{q}}\right], \quad l = 1,2 \\ &= \left[\begin{array}{cccc}\mathbf{0} & \overline{\mathbf{n}}^{jkT}\mathbf{A}^{jt}\dfrac{\partial \mathbf{A}^i}{\partial \boldsymbol{\theta}^i}\overline{\mathbf{t}}_l^{ik} & \mathbf{0} & \overline{\mathbf{t}}_l^{ikT}\mathbf{A}^{it}\dfrac{\partial \mathbf{A}^j}{\partial \boldsymbol{\theta}^j}\overline{\mathbf{n}}^{jk}\end{array}\right], \quad l = 1,2\end{aligned}$$

Note that: $\overline{\mathbf{n}}^{ikT}\mathbf{A}^{j\mathrm{T}}\mathbf{A}^i\overline{\mathbf{t}}_l^{ik} = \overline{\mathbf{t}}_l^{ikT}\mathbf{A}^{i\mathrm{T}}\mathbf{A}^j\overline{\mathbf{n}}^{jk}$

Applying some mathematical manipulation we get:

$$\dot{\mathbf{A}}^i \overline{\mathbf{t}}_l^{ik} = \mathbf{A}^i \left(\overline{\boldsymbol{\omega}}^i \times \overline{\mathbf{t}}_l^{ik} \right)$$

$$\frac{\partial \mathbf{A}^i}{\partial \boldsymbol{\theta}^i} \dot{\boldsymbol{\theta}}^i \overline{\mathbf{t}}_l^{ik} = \mathbf{A}^i \left(\overline{\mathbf{G}}^i \dot{\boldsymbol{\theta}}^i \times \overline{\mathbf{t}}_l^{ik} \right)$$

$$\frac{\partial \mathbf{A}^i}{\partial \boldsymbol{\theta}^i} \dot{\boldsymbol{\theta}}^i \overline{\mathbf{t}}_l^{ik} = -\mathbf{A}^i \tilde{\overline{\mathbf{t}}}_l^{ik} \overline{\mathbf{G}}^i \dot{\boldsymbol{\theta}}^i$$

$$\frac{\partial \mathbf{A}^i}{\partial \boldsymbol{\theta}^i} \overline{\mathbf{t}}_l^{ik} = -\mathbf{A}^i \tilde{\overline{\mathbf{t}}}_l^{ik} \overline{\mathbf{G}}^i$$

Using the same principle we also get:

$$\frac{\partial \mathbf{A}^j}{\partial \boldsymbol{\theta}^j} \overline{\mathbf{n}}^{jk} = -\mathbf{A}^j \tilde{\overline{\mathbf{n}}}^{jk} \overline{\mathbf{G}}^j$$

Thus, the orientation constraint in respect to the generalised coordinates $\mathbf{q}$ can be written as:

$$\mathbf{C}_{l,\mathbf{q}} = \left[\mathbf{0} \quad -\overline{\mathbf{n}}^{jkT} \mathbf{A}^{jt} \mathbf{A}^i \tilde{\overline{\mathbf{t}}}_l^{ik} \overline{\mathbf{G}}^i \quad \mathbf{0} \quad -\overline{\mathbf{t}}_l^{ikT} \mathbf{A}^{it} \mathbf{A}^j \tilde{\overline{\mathbf{n}}}^{jk} \mathbf{G}^j \right], \quad l = 1,2$$

The orientation constraint in respect to the surface parameter $\mathbf{s}$ can be written as:

$$\mathbf{C}_{l,\mathbf{s}} = \left[\frac{\partial \mathbf{C}_l}{\partial \mathbf{s}} \right], \quad l = 1,2$$

$$= \left[\overline{\mathbf{n}}^{jkT} \mathbf{A}^{j\mathbf{T}} \mathbf{A}^i \frac{\partial \overline{\mathbf{t}}_l^{ik}}{\partial \mathbf{s}^{ik}} \quad \overline{\mathbf{t}}_l^{ikT} \mathbf{A}^{i\mathbf{T}} \mathbf{A}^j \frac{\partial \overline{\mathbf{n}}^{jk}}{\partial \mathbf{s}^{jk}} \right], \quad l = 1,2$$

APPENDIX II

TRIBOMETER MEASUREMENT OF RAIL FRICTION COEFFICIENT

Tool: QR Tribometer (Type: Salient's Hand-Pushed Tribometer)

Date: 15 November 2005

Start: 4:05 pm

Finish: 5:00 pm

Precondition: Surface of rails have been cleaned using piece of clothes prior to measurement

Number of measurement: 5 times each rail for every condition (Dry, Wet, Soap Solution)

DRY CONDITION

Meas. No	Friction Coefficient	
	Right Rail (East Rail)	Left Rail (West Rail)
1	0.52	0.51
2	0.52	0.50
3	0.55	0.50
4	0.53	0.51
5	0.54	0.53

WET CONDITION

Meas. No	Friction Coefficient	
	Right Rail (East Rail)	Left Rail (West Rail)
1	0.53	0.51
2	0.52	0.50
3	0.54	0.49
4	0.53	0.50
5	0.53	0.51

SOAP SOLUTION APPLIED ON RAIL SURFACE

Meas. No	Friction Coefficient	
	Right Rail (East Rail)	Left Rail (West Rail)
1	0.45	0.44
2	0.44	0.43
3	0.46	0.45
4	0.43	0.46
5	0.45	0.44

APPENDIX III

SAMPLES OF MINIPROF RESULTS
OF WHEEL AND RAIL PROFILE MEASUREMENT

III.1. Left Rail Profile Measurement

Header fields	
ID	Value
ProgramName	MiniProf Pocket
ProgramVer	2.1.4.0
MPTypeNo	299
MPSerNo	795
Date	09-11-2005
Time	11:38:14
Chars	Win
Stock	Greenwood
MPCalTime	06:31:04
MPCalDate	07-09-2005
Reference	AS60.mpt
Line	Test Track
Location	
Direction	
Rail	Left
Curve Dirn	
Comment	1
SFAR0000.Par.Type.Value	2
XYPoints	481
W1	9.3357
W1_AlarmStatus	3
W2	11.8481
W2_AlarmStatus	3
W3	11.2239
W3_AlarmStatus	3
Gauge	1074.2199
Gauge_AlarmStatus	3
RailAngle	-0.7219
RailAngle_AlarmStatus	3
ColumnDef	X,Y,A,N,C
Xoffset	0.0000
Yoffset	0.0000
RefPoint1	0.0000, 0.0000
RefPoint2	10.0000, 0.0000
RefPoint3	0.0000, 5.0000
RefPoint4	0.0000, 0.0000
RefPoint5	10.0000, 0.0000
RefPoint6	0.0000, 5.0000
RefPoint7	0.0000, 0.0000
RefPoint8	10.0000, 0.0000
RefPoint9	0.0000, 5.0000
ProfileFilename	20051109-0001.ban
ProfileFilepath	d:\miniprof\profiles\ucq test track\
ProfileIndex	-1

Plot: Left Rail Profile Pos1

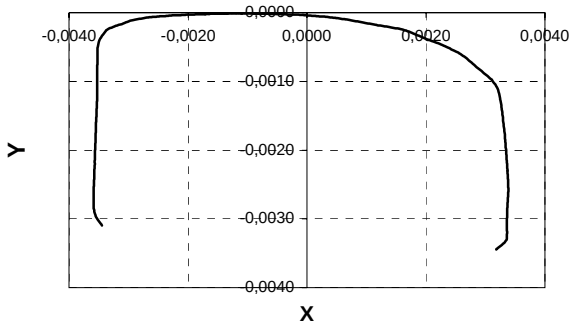

III.2. Right Rail Profile Measurement

Header fields

ID	Value
ProgramName	MiniProf Pocket
ProgramVer	2.1.4.0
MPTypeNo	299
MPSerNo	795
Date	09-11-2005
Time	12:10:31
Chars	Win
Stock	Greenwood
Reference	AS60.mpt
Line	Test Track
Location	
Direction	
Rail	Right
Curve Dirn	
Comment	2R
SFAR0000.Par.Type.Value	2
XYPoints	489
W1	8.2222
W1_AlarmStatus	3
W2	9.1859
W2_AlarmStatus	3
W3	9.6213
W3_AlarmStatus	3
Gauge	1075.1020
Gauge_AlarmStatus	3
RailAngle	-1.4799
RailAngle_AlarmStatus	3
ColumnDef	X,Y,A,N,C
Xoffset	0.0000
Yoffset	0.0000
RefPoint1	0.0000, 0.0000
RefPoint2	10.0000, 0.0000
RefPoint3	0.0000, 5.0000
RefPoint4	0.0000, 0.0000
RefPoint5	10.0000, 0.0000
RefPoint6	0.0000, 5.0000
RefPoint7	0.0000, 0.0000
RefPoint8	10.0000, 0.0000
RefPoint9	0.0000, 5.0000
ProfileFilename	20051109-0052.ban
ProfileFilepath	d:\miniprof\profiles\ucq test track\
ProfileIndex	-1

Plot: Right Rail Profile Pos1

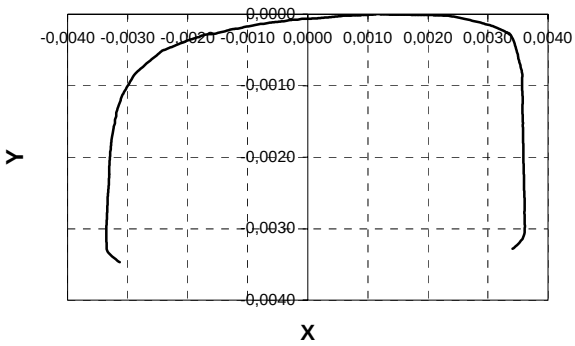

III.3. Left Wheel Profile Measurement

Header fields	
ProgramName	MiniProf Pocket
ProgramVer	2.1.4.0
MPTypeNo	130
MPSerNo	435
Date	10-11-2005
Time	10:51:35
Chars	Win
Stock	Greenwood
MPCalTime	03:35:38
MPCalDate	30-09-2005
Reference	
CarNo	uni,test
AxleNo	n402004
WheelID	WH1,t1
XYPoints	534
Sd	29.3427
Sd_AlarmStatus	3
Sh	28.8603
Sh_AlarmStatus	3
qR	9.2549
qR_AlarmStatus	3
DiameterFlange	854.7532
DiameterFlange_AlarmStatus	3
FlangeAngleMax	70.2922
FlangeAngleMax_AlarmStatus	3
FlangeAngleMaxPos	28.0230
FlangeAngleMaxPos_AlarmStatus	3
Hollowing	0.0000
Hollowing_AlarmStatus	3
HollowingPos	59.8894
HollowingPos_AlarmStatus	3
DiameterTaperline	797.0326
DiameterTaperline_AlarmStatus	3
ColumnDef	X,Y,A,N,C
ProfileFilename	20051110-0001.whl
ProfileFilepath	d:\university profiles\
ProfileIndex	-1
Xoffset	0.0000
Yoffset	0.0000
RefPoint1	0.0000, 0.0000
RefPoint2	10.0000, 0.0000
RefPoint3	0.0000, 5.0000
RefPoint4	0.0000, 0.0000
RefPoint5	10.0000, 0.0000
RefPoint6	0.0000, 5.0000
RefPoint7	0.0000, 0.0000
RefPoint8	10.0000, 0.0000
RefPoint9	0.0000, 5.0000

Plot: Rear Wheel Profile Left Pos1

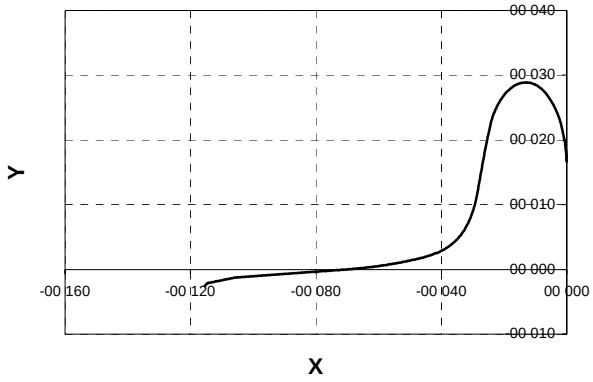

III.4. Right Wheel Profile Measurement

Header fields	
ProgramName	MiniProf Pocket
ProgramVer	2.1.4.0
MPTypeNo	130
MPSerNo	435
Date	10-11-2005
Time	11:11:03
Chars	Win
Stock	Greenwood
Reference	
CarNo	uni,test
AxleNo	N402004
WheelID	WH,2.T1
XYPoints	541
Sd	29.2953
Sd_AlarmStatus	3
Sh	29.0995
Sh_AlarmStatus	3
qR	9.2844
qR_AlarmStatus	3
DiameterFlange	853.0339
DiameterFlange_AlarmStatus	3
FlangeAngleMax	70.4741
FlangeAngleMax_AlarmStatus	3
FlangeAngleMaxPos	27.7960
FlangeAngleMaxPos_AlarmStatus	3
Hollowing	0.0000
Hollowing_AlarmStatus	3
HollowingPos	59.7680
HollowingPos_AlarmStatus	3
DiameterTaperline	794.8348
DiameterTaperline_AlarmStatus	3
ColumnDef	X,Y,A,N,C
ProfileFilename	20051110-0005.whl
ProfileFilepath	d:\university profiles\
ProfileIndex	-1
Xoffset	0.0000
Yoffset	0.0000
RefPoint1	0.0000, 0.0000
RefPoint2	10.0000, 0.0000
RefPoint3	0.0000, 5.0000
RefPoint4	0.0000, 0.0000
RefPoint5	10.0000, 0.0000
RefPoint6	0.0000, 5.0000
RefPoint7	0.0000, 0.0000
RefPoint8	10.0000, 0.0000
RefPoint9	0.0000, 5.0000

Plot: Rear Wheel Profile Right Pos1

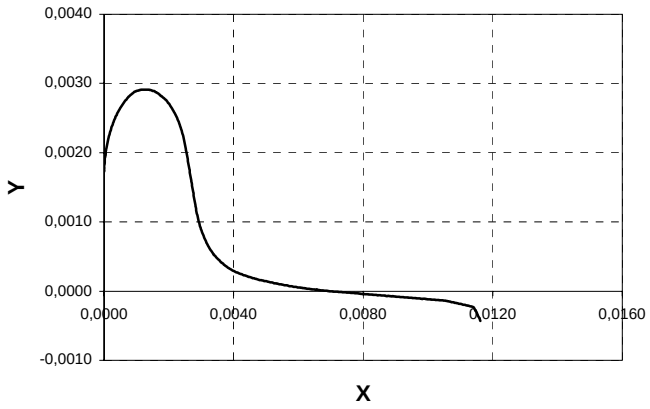

APPENDIX IV

RESULTS OF ASYMMETRIC BRAKING SIMULATION

IV.1 Error on Leading Wheelset

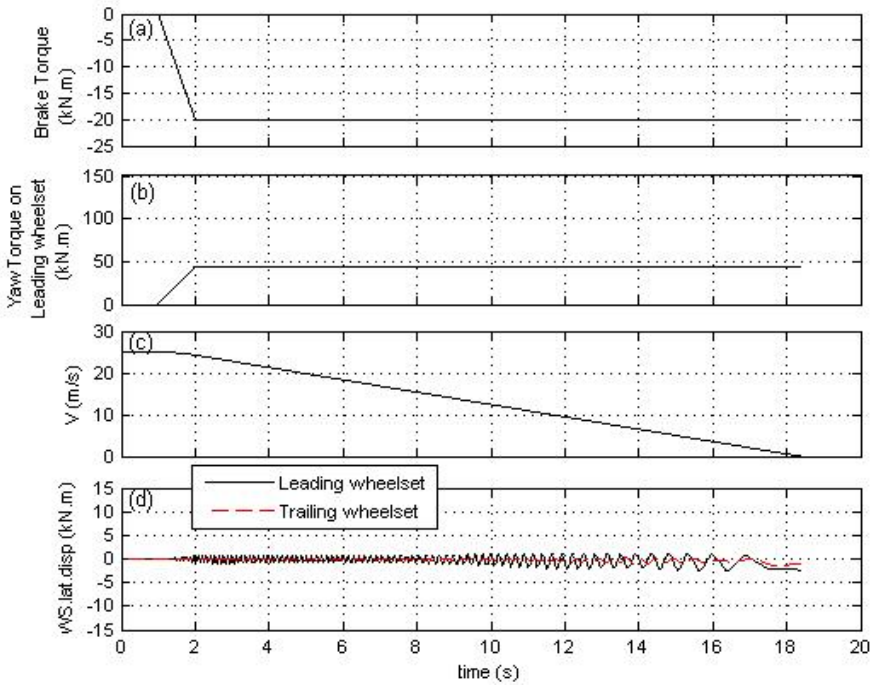

Figure IV.1. 25 % error on leading wheelset, 1s brake application time

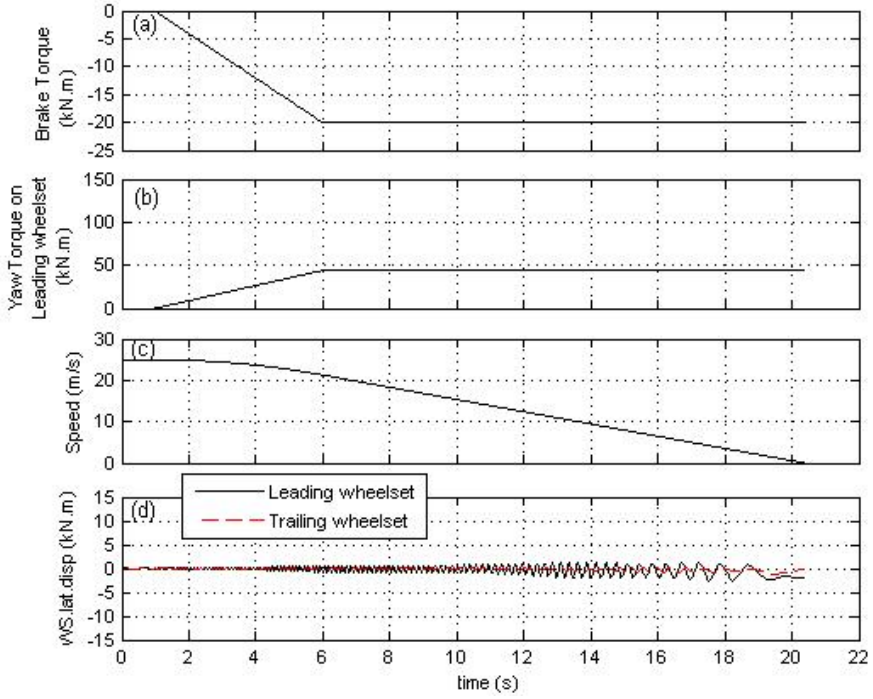

Figure IV.2. 25 % error on leading wheelset, 5s brake application time

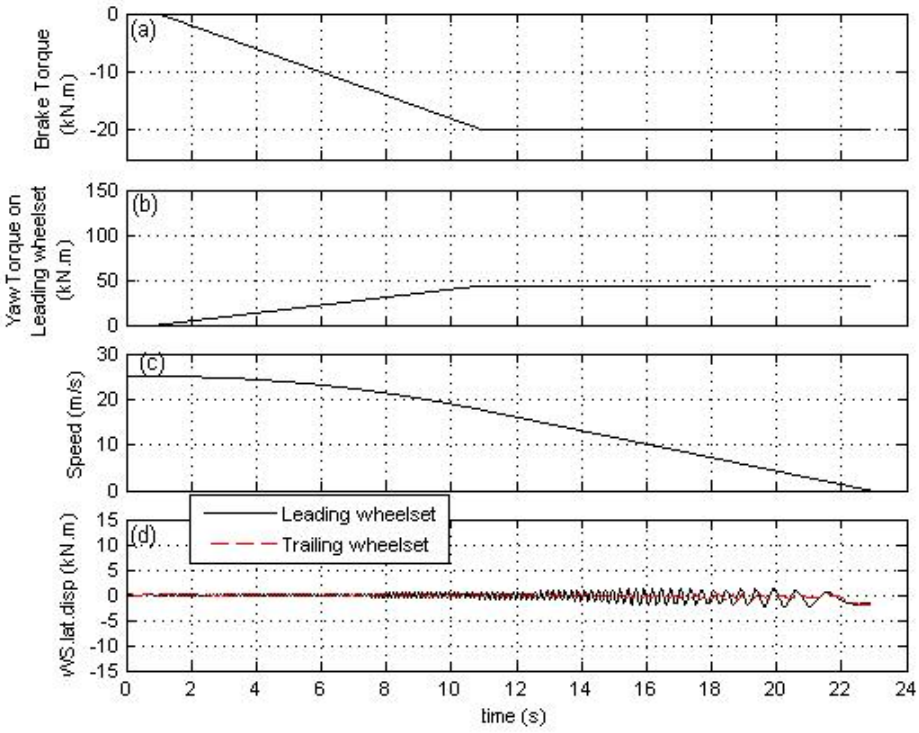

Figure IV.3. 25 % error on leading wheelset, 10s brake application time

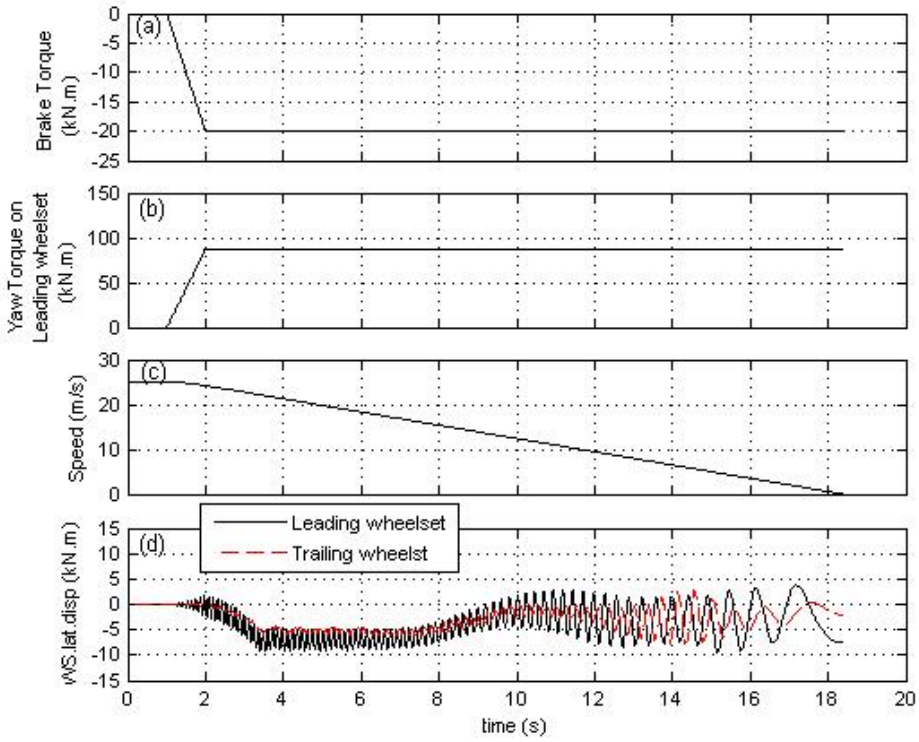

Figure IV.4. 50 % error on leading wheelset, 1s brake application time

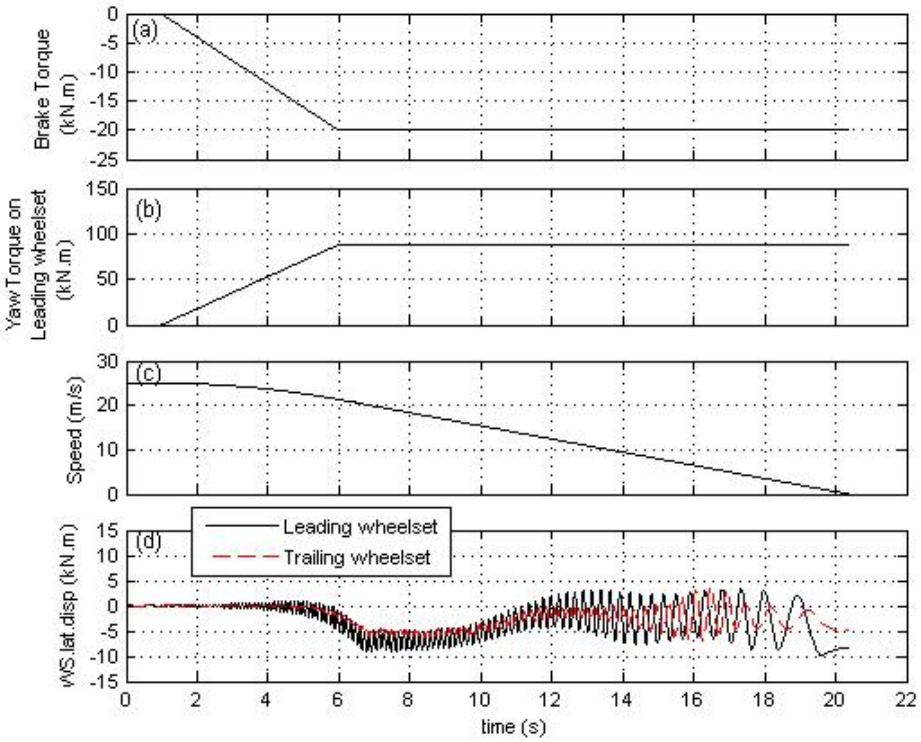

Figure IV.5. 50 % error on leading wheelset, 5s brake application time

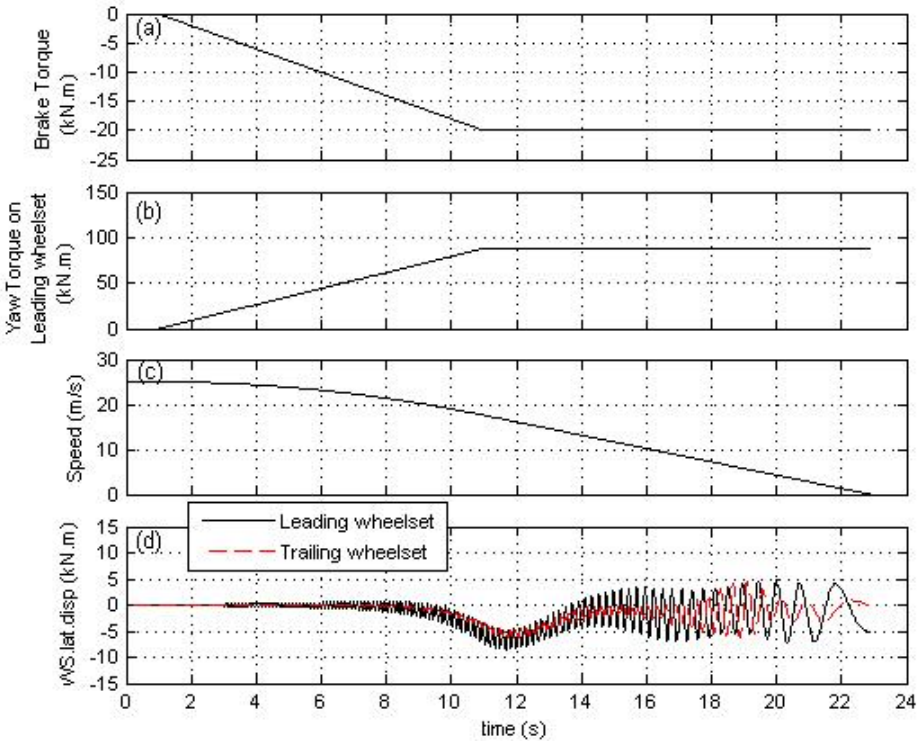

Figure IV.6. 50 % error on leading wheelset, 10s brake application time

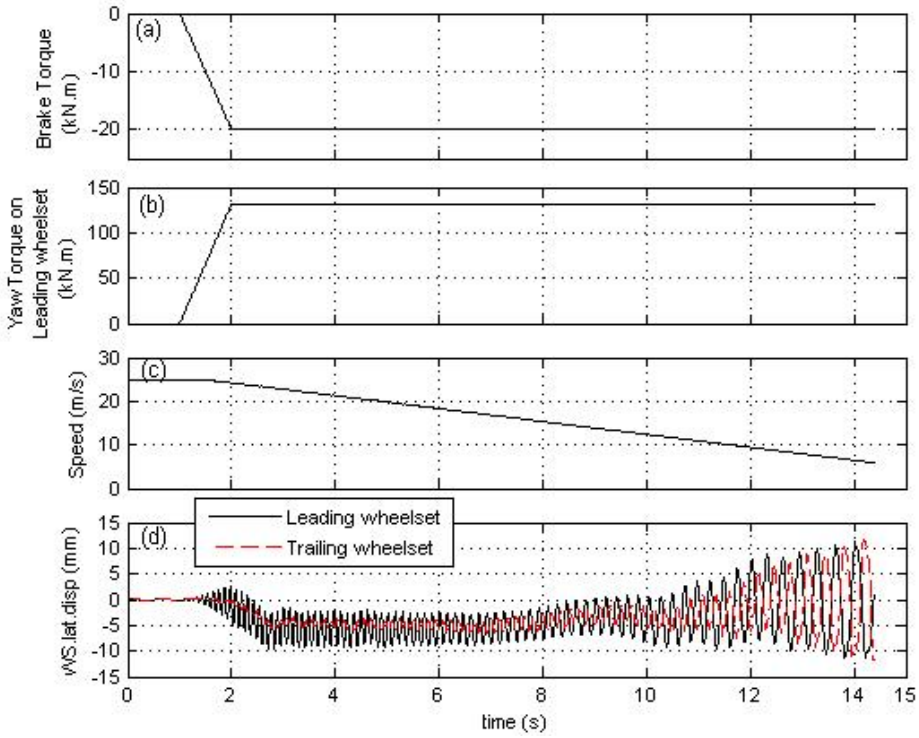

Figure IV.7. 75 % error on leading wheelset, 1s brake application time

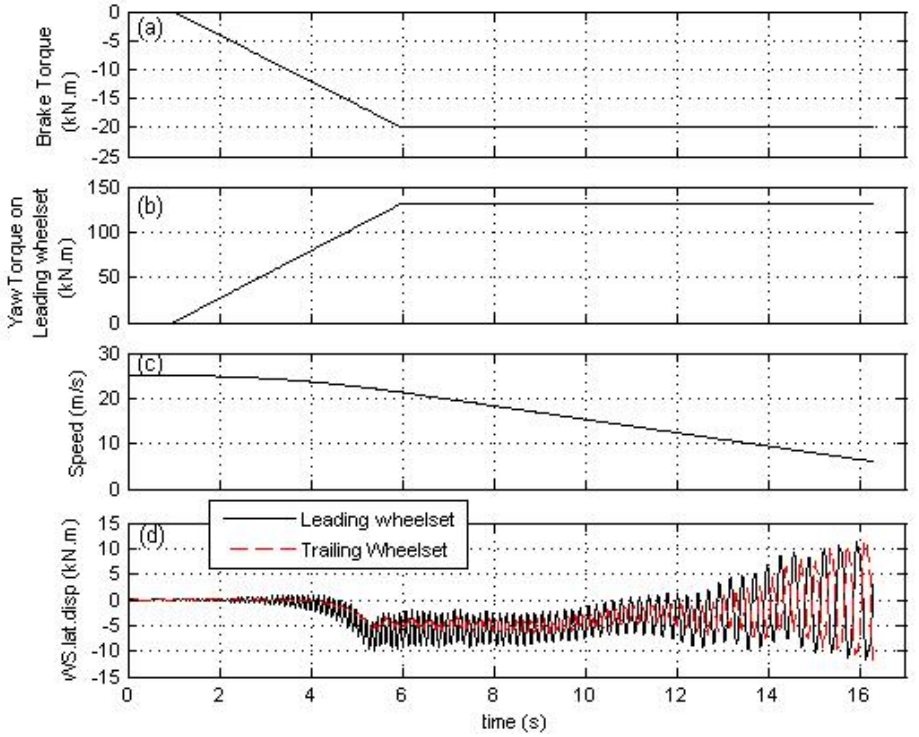

Figure IV.8. 75 % error on leading wheelset, 5s brake application time

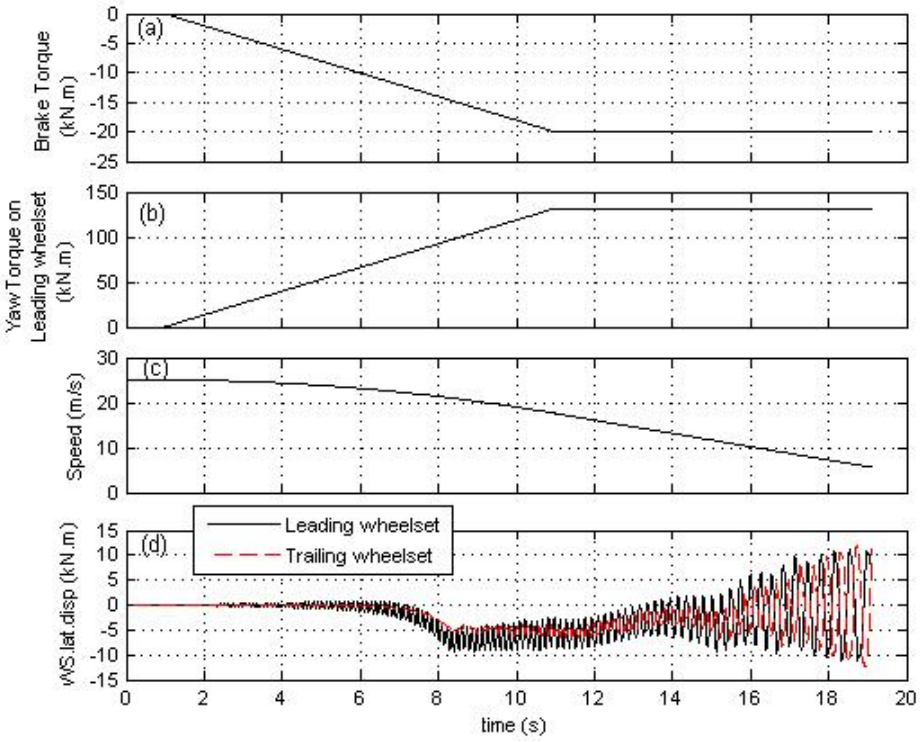

Figure IV.9. 75 % error on leading wheelset, 10s brake application time

IV.2 Error on Trailing Wheelset

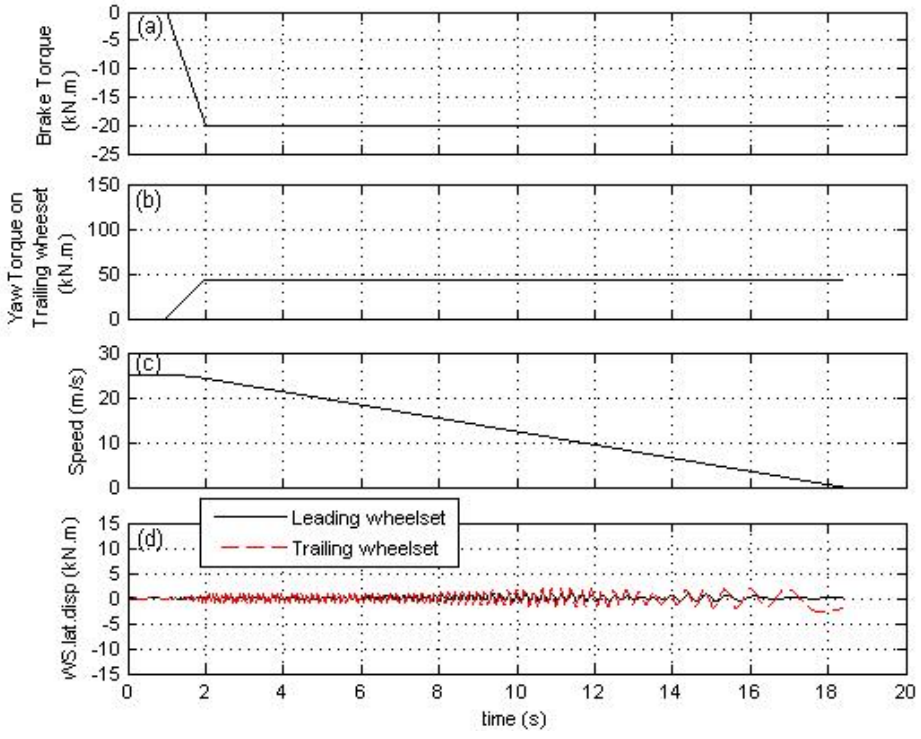

Figure IV.10. 25 % error on trailing wheelset, 1s brake application time

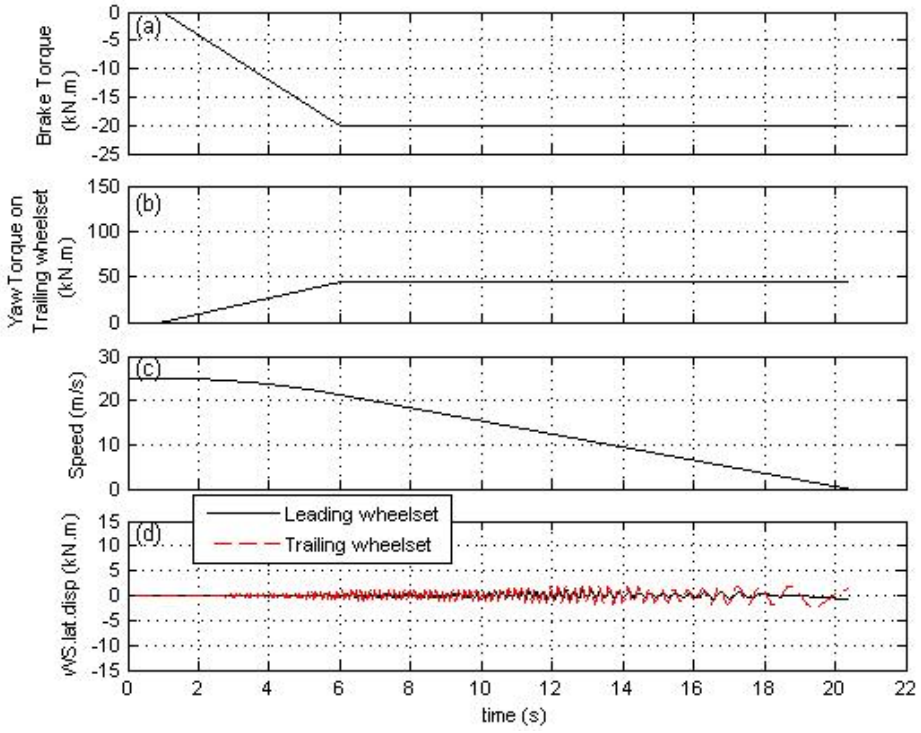

Figure IV.11. 25 % error on trailing wheelset, 5s brake application time

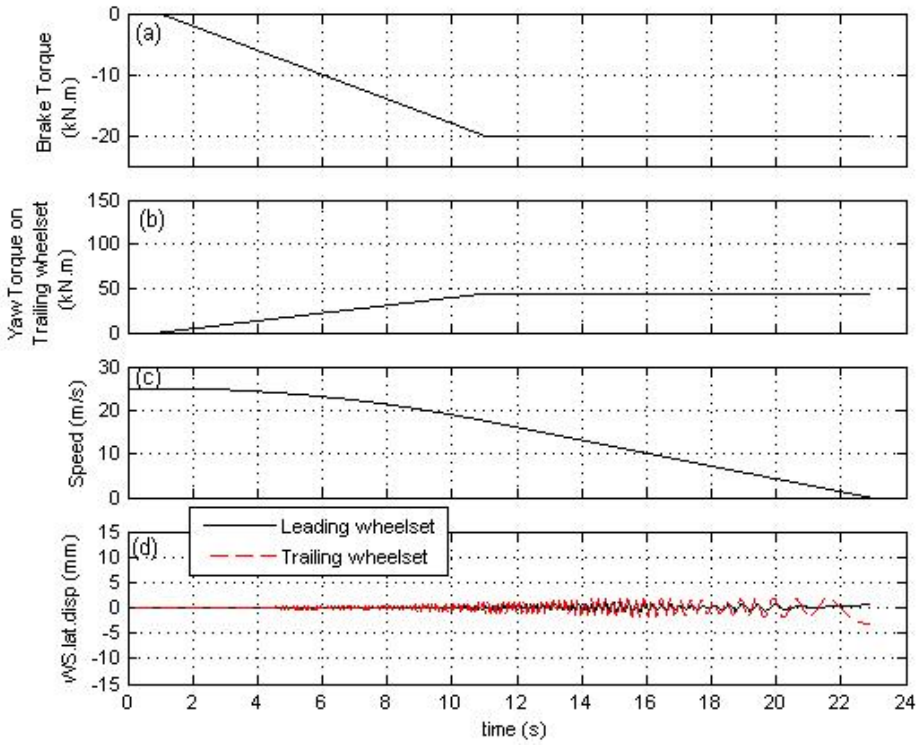

Figure IV.12. 25 % error on trailing wheelset, 10s brake application time

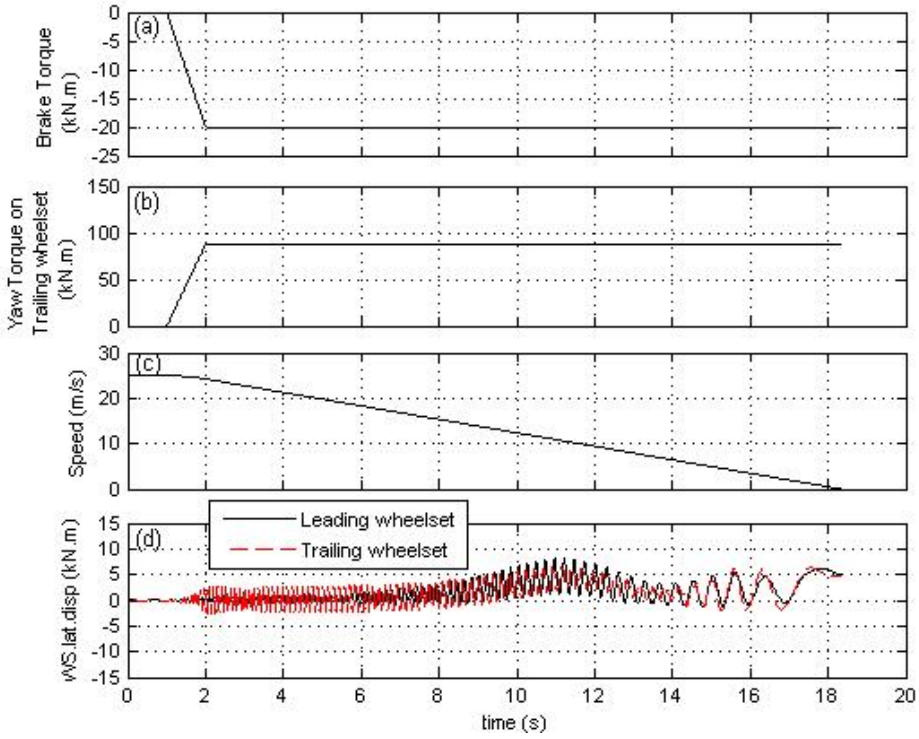

Figure IV.13. 50 % error on trailing wheelset, 1s brake application time

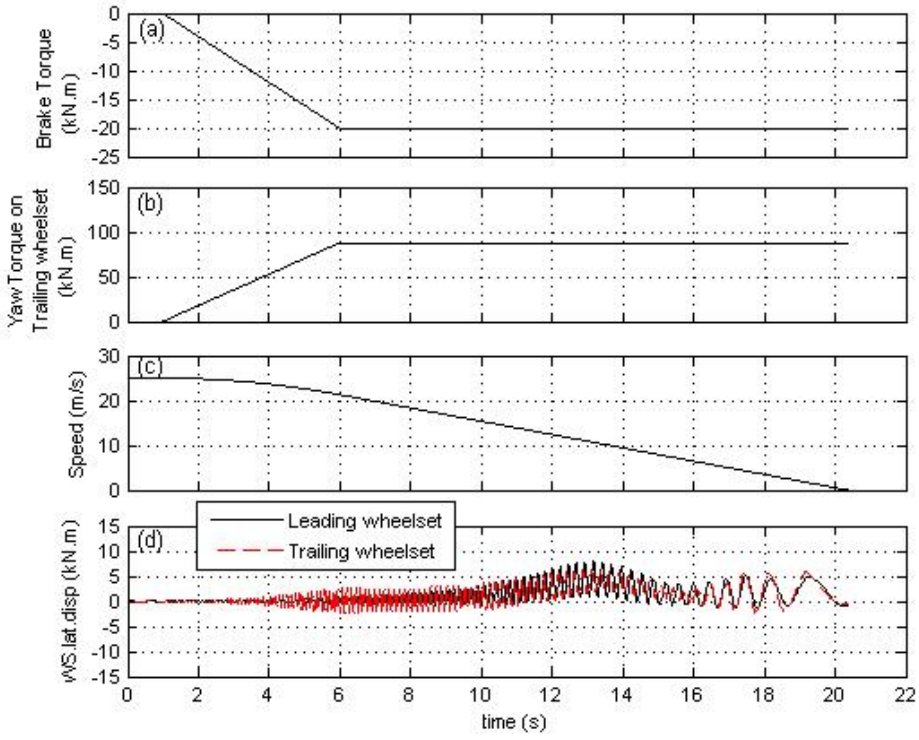

Figure IV.14. 50 % error on trailing wheelset, 5s brake application time

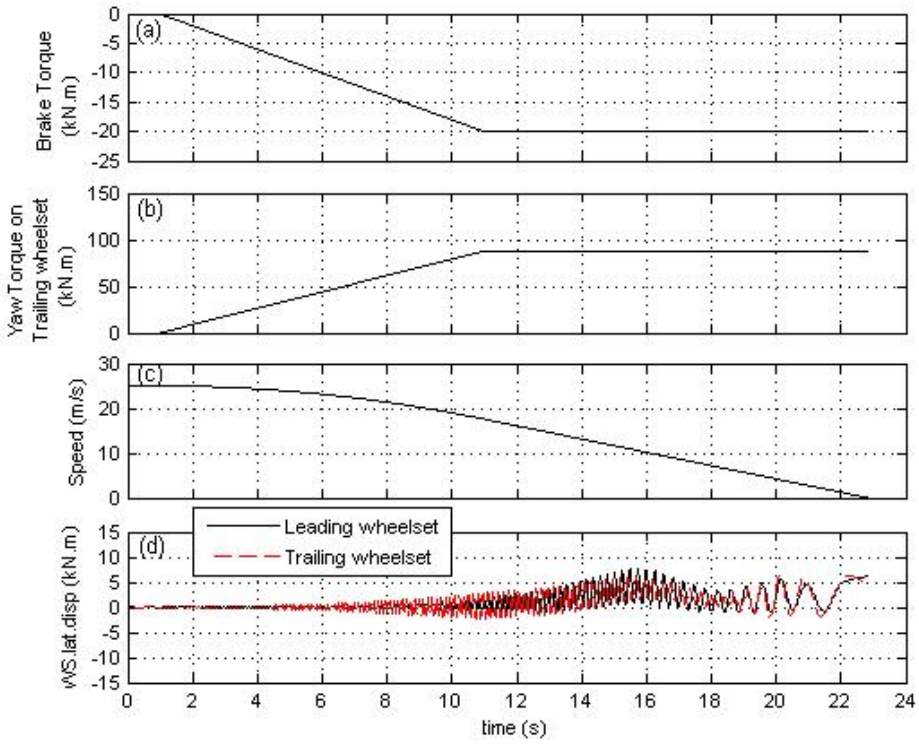

Figure IV.15. 50 % error on trailing wheelset, 10s brake application time

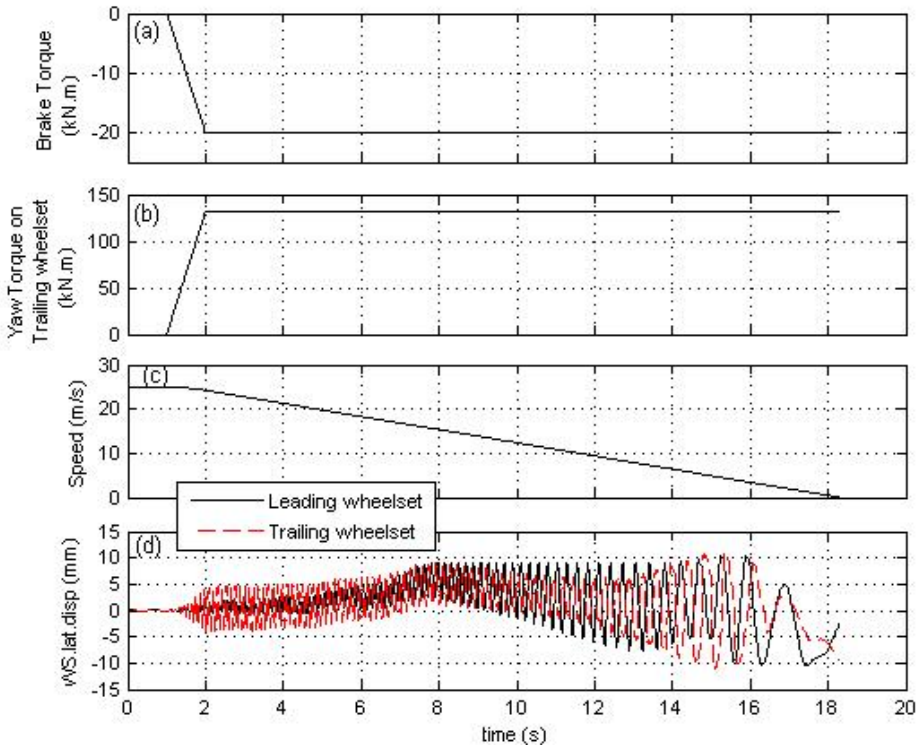

Figure IV.16. 75 % error on trailing wheelset, 1s brake application time

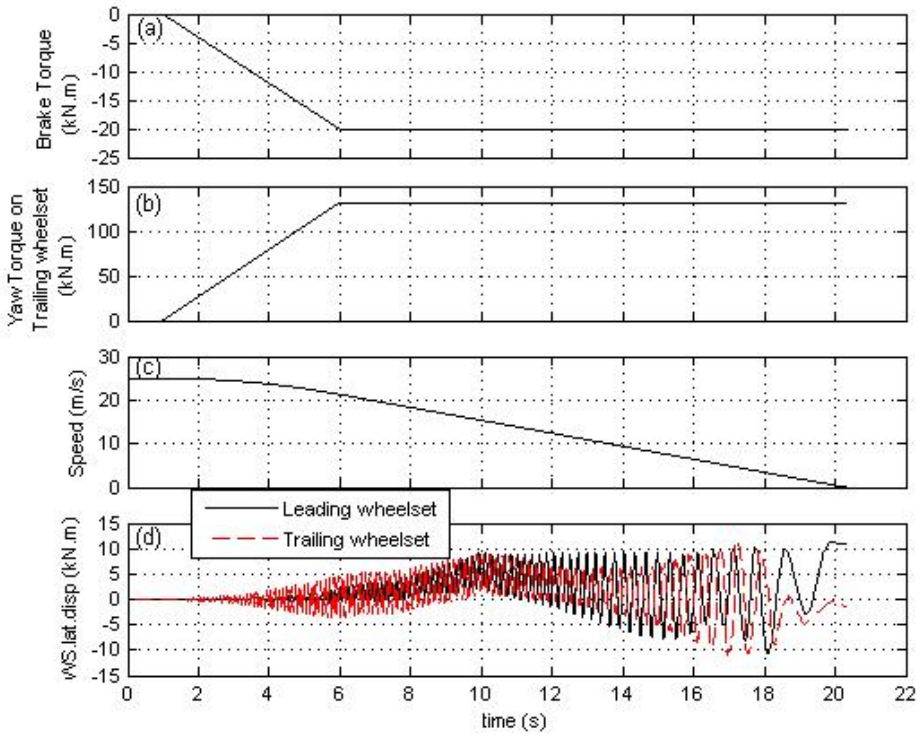

Figure IV.17. 75 % error on trailing wheelset, 5s brake application time

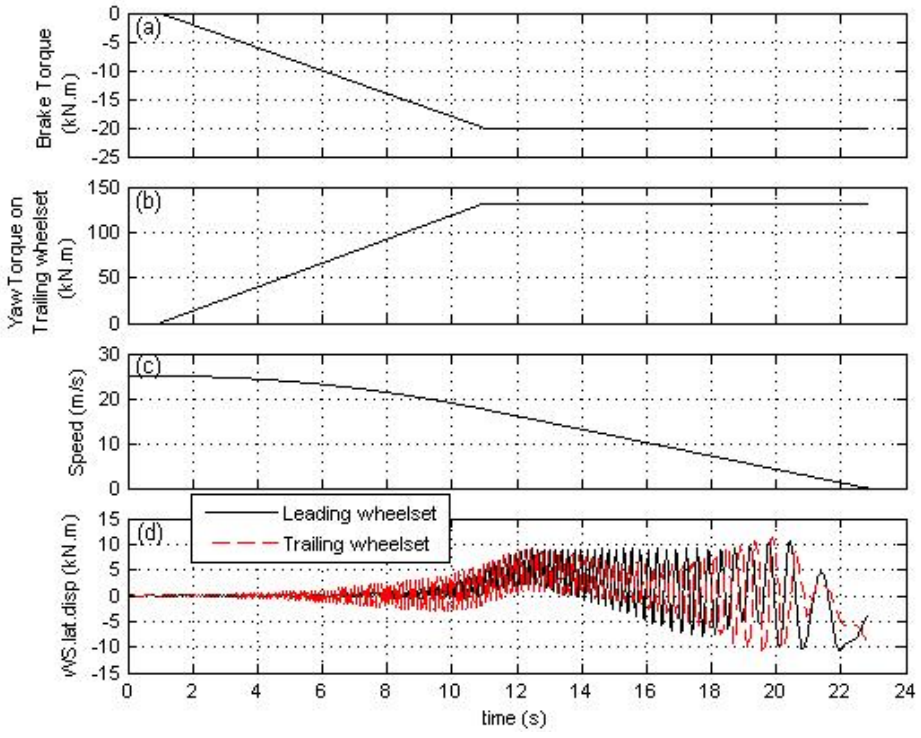

Figure IV.18. 75 % error on trailing wheelset, 10s brake application time